

**Kinetic Study and Development of Ligand-Accelerated Clip Reactions and Synthesis of a
Tetrahydrofuran Analog of FR901464**

by

Ivanna Pohorilets

BS Chemistry, Syracuse University, 2016

Submitted to the Graduate Faculty of the
Dietrich School of Arts and Sciences in partial fulfillment
of the requirements for the degree of
Doctor of Philosophy

University of Pittsburgh

2021

UNIVERSITY OF PITTSBURGH

DIETRICH SCHOOL OF ARTS AND SCIENCES

This thesis was presented

by

Ivanna Pohorilets

It was defended on

August 25, 2021

and approved by

Paul Floreancig, Professor, Department of Chemistry

Peng Liu, Associate Professor, Department of Chemistry

Lin Zhang, Professor, Department of Pharmacology & Chemical Biology

Committee Chair: Kazunori Koide, Professor, Department of Chemistry

Copyright © by Ivanna Pohorilets

2021

Kinetic Study and Development of Ligand-Accelerated Clip Reactions and Synthesis of a Tetrahydrofuran Analog of FR901464

Ivanna Pohorilets, PhD

University of Pittsburgh, 2021

Fluorescence has found many uses in the areas of analytical, organic, biological, and physical chemistry. Herein, fluorescence was used to study the kinetics of Tsuji-Trost reaction under biologically relevant conditions. The Tsuji-Trost reaction was studied using a fluorogenic substrate, which allowed for high throughput, accurate data collection and revealed three kinetic regimes. The turnover limiting step was found to depend on the substrate concentration and reaction temperature.

Florescence was also used to develop and optimize palladium-catalyzed clip reaction. Currently, deallylation is deemed to be too slow to be viable uncaging reaction and more rapid, palladium-catalyzed propargylic C-O or C-N bond cleavage is typically used. These studies avoid using phosphine ligands, known to accelerate the reaction. Here, new phosphine ligands were synthesized and tested under biological conditions. This palladium-catalyzed deallylation with phosphine as an added ligand was found to be 35 times faster than previously reported phosphine-free palladium-catalyzed depopargylation.

Next, the synthesis of tetrahydrofuran FR901464 analog is discussed. FR901464, a natural product splicing regulator with low nanomolar activity against various cancer cell lines. FR901464 analogs regulate the alternative splicing of the myeloid cell leukemia 1 pre-mRNA. We describe the synthesis of the first tetrahydrofuran FR901464 analog. The key step in the synthesis is electrophilic, N-bromosuccinimide-mediated cyclization. The new analog was shown to inhibit

cancer cell growth with low micromolar potency, indicating the importance of the tetrahydropyran ring.

Table of Contents

Acknowledgments	xxi
1.0 Kinetics and inverse temperature dependence of a Tsuji–Trost reaction in aqueous buffer	1
1.1 Introduction	1
1.2 Previous kinetic studies of the Tsuji-Trost reaction.....	5
1.3 Tsuji-Trost reaction under aqueous conditions.....	7
1.4 Bioorthogonal organometallic (BOOM) chemistry	10
1.5 Summary	13
1.6 Results and Discussion	13
1.6.1 Introduction	13
1.6.2 Initial Investigation with Previously Optimized Conditions: Effect of Substrate Concentration.....	17
1.6.3 Effect of Phosphine Concentration.....	19
1.6.4 Effect of Phosphate Ion Concentration	20
1.6.5 Effect of NaBH ₄ Concentration.....	24
1.6.6 Effect of Palladium Concentration	25
1.6.7 Effect of Substrate Concentration	26
1.6.8 Effect of DMSO Concentration.....	27
1.6.9 Competition Experiment	29
1.6.10 Identification of the Nucleophile.....	30
1.6.11 Density Functional Theory Calculations.....	33

1.6.12 Detailed Mechanism of Allyl Association.....	35
1.7 Conclusions	37
2.0 Development of Ligand-Accelerated Clip Reactions	39
2.1 Transition-metal-catalyzed bioorthogonal reactions	39
2.1.1 Ruthenium-catalyzed cleavage reactions	40
2.1.2 Platinum-catalyzed cleavage reactions.....	46
2.1.3 Gold catalyzed cleavage reactions	50
2.1.4 Palladium catalyzed cleavage reactions	52
2.1.4.1 Palladium catalyzed depropargylation	53
2.1.4.2 Palladium catalyzed deallylation.....	58
2.1.5 Conclusion.....	61
2.2 Results and discussion	63
2.2.1 Synthesis and evaluation of new TFP analogs.....	66
2.2.2 Synthesis and evaluation of second generation TFP analogs	70
2.2.3 Synthesis and evaluation of palladium-phosphine complexes	75
2.2.4 Optimal phosphine to palladium ratio	79
2.2.5 Rate constant	79
2.2.6 Copper does not interfere with palladium catalyzed decaging in the presence of TFP analogs.....	81
2.2.7 The scope of palladium-catalyzed deallylation.....	83
2.3 Conclusions	86
2.4 Future Plan.....	87
3.0 Synthesis of a Tetrahydrofuran Analog of FR901464.....	88

3.1 Introduction	88
3.1.1 Discovery of FR901464	88
3.1.2 Mode of action	89
3.1.3 Alternative splicing and FR901464	91
3.1.4 Natural product splicing regulators	93
3.1.5 Synthetic strategy	94
3.1.6 FR901464 structure activity relationship (SAR) studies	94
3.1.7 Drug-conjugates	96
3.2 Results and discussion	99
3.2.1 Right fragment synthesis	99
3.2.2 Efforts towards more versatile right fragment analog through a Wacker-type oxy-palladation.....	100
3.2.3 Electrophilic cyclization.....	102
3.2.4 Synthesis of a tetrahydrofuran analog of FR901464	107
3.3 Biological Assay	108
3.4 Conclusions	110
Appendix A. Supporting Information.....	111
Appendix A.1 Kinetics and inverse temperature dependence of a Tsuji–Trost reaction in aqueous buffer	111
Appendix A.1.1 Instrumentation and reagents	111
Appendix A.1.2 Experimental Procedures	112
Appendix A.1.2 Computational Details.....	117
Appendix A.2 Development of Ligand-Accelerated Clip Reactions	118

Appendix A.2.1 Experimental Procedures	118
Appendix A.2.2 Raw Data Tables.....	123
Appendix A.2.3 Chemistry General Procedures	146
Appendix A.2.4 Chemistry Experimental Procedures.....	148
Appendix A.3 Synthesis of a Tetrahydrofuran Analog of FR901464	170
 Appendix A.3.1 Growth Inhibition.....	170
 Appendix A.3.2 Chemistry Experimental Procedures.....	170
Appendix B. NMR Spectra.....	179
Bibliography	253

List of Tables

Table 1. Calculated plateau of APE from fitting to a one-phase decay as reaction continues indefinitely; data over time also shown in Figure 1.....	15
Table 2. Synthesis of coumarin based probes.....	83
Table 3. Conditions for Wacker-type oxi-palladation.....	102
Table 4. Optimization of NBS-mediated cyclization.....	107
Table 5. Antiproliferative activity of MAMD and meayamycin.....	109
Table 6. Raw data for Figure 20 (deallylation and depropargylation with and without serum).	123
Table 7. Calculated %yield for Figure 20 (deallylation and depropargylation with and without serum).	123
Table 8. Raw data for Figure 21 (the rate of deallylation in phosphate buffer).	123
Table 9. Raw data for Figure 21 (the rate of deallylation in phosphate buffer) continued.	124
Table 10. Calculated %yield for Figure 21 (the rate of deallylation in phosphate buffer).124	
Table 11. Calculated %yield for Figure 21 (the rate of deallylation in phosphate buffer) continued.....	125
Table 12. Raw data for Figure 21 (the rate of depropargylation in phosphate buffer).	125
Table 13. Raw data for Figure 21 (the rate of depropargylation in phosphate buffer) continued.....	126
Table 14. Calculated %yield for Figure 21 (the rate of depropargylation in phosphate buffer).....	126

Table 15. Calculated %yield for Figure 21 (the rate of depropargylation in phosphate buffer) continued.....	127
Table 16. Raw data for Figure 22 (deallylation and depropargylation without Pd and phosphine premixing).....	127
Table 17. Calculated %yield for Figure 22 (deallylation and depropargylation without Pd and phosphine premixing).....	127
Table 18. Raw data for Figure 22 (deallylation and depropargylation with Pd and TFP premixing).....	128
Table 19. Calculatd %yield for Figure 22 (deallylation and depropargylation with Pd and TFP premixing).....	128
Table 20. Raw data for Figure 22 (the optimal concentration of TFP and mono-hydroxyethyl- TFP at 37 °C in DMEM with 10% BCS).....	128
Table 21. Raw data for Figure 23 (deallylation in the presence of second generation of phosphines in DMEM with serum)	129
Table 22. Raw data for Figure 23 (deallylation in the presence of second generation of phosphines in DMEM with serum) continued.....	130
Table 23. Calculated %yield for Figure 23 (deallylation in the presence of second generation of phosphines in DMEM with serum)	131
Table 24. Calculated %yield for Figure 23 (deallylation in the presence of second generation of phosphines in DMEM with serum) continued.	132
Table 25. Raw data for Figure 23 (depropargylation in the presence of second generation of phosphines in DMEM with serum).	132

Table 26. Raw data for Figure 23 (depropargylation in the presence of second generation of phosphines in DMEM with serum) continued.....	133
Table 27. Calculated %yield for Figure 23 (depropargylation in the presence of second generation of phosphines in DMEM with serum).....	133
Table 28. Calculated %yield for Figure 23 (depropargylation in the presence of second generation of phosphines in DMEM with serum) continued.....	134
Table 29. Raw data for Figure 24 (decaging reactions with second-generation phosphines without premixing).....	134
Table 30. Calculated %yield for Figure 24 (decaging reactions with second-generation phosphines without premixing).	135
Table 31. Raw data for Figure 25 (reactivation of palladium-phosphine complexes with additional phosphine).	135
Table 32. Raw data for Figure 25 (deallylation with premixed palladium-phosphine complexes and additional phosphines).....	136
Table 33. Raw data for Figure 25 (deallylation with premixed palladium-phosphine complexes and additional phosphines) continued.....	136
Table 34. Raw data for Figure 26 (the correlation between palladium concentrations and optimal 3iPhos1 concentrations).....	137
Table 35. Raw data for Figure 27 (kinetics of palladium catalyzed deallylation).	138
Table 36. Calculated [resorufin] μM for Figure 27 (kinetics of palladium catalyzed deallylation).	139
Table 37. Calculated [RAE] μM for Figure 27 (kinetics of palladium catalyzed deallylation).	141

Table 38. Raw data for Figure 28 (copper does not interfere in the presence of iPhos1)..	143
Table 39. Raw data for Figure 28 (copper does not interfere in the presence of 3iPhos1).	144
Table 40. Raw data for Figure 29 (substrate scope of deallylation based on the pK_a of the leaving group).....	144
Table 41. Calculated %yield for Figure 29 (substrate scope of deallylation based on the pK_a of the leaving group). ..	145
Table 42. Raw data for Figure 30 (substrate scope of deallylation based on the sterics of the alkene). ..	145
Table 43. Calculated %yield for Figure 30 (substrate scope of deallylation based on the sterics of the alkene).....	145

List of Figures

Figure 1. Consumption of APE as a function of time	16
Figure 2. Representative Eyring plot.	16
Figure 3. (a) Eyring plot under the previously developed reaction conditions with various APE concentrations.	18
Figure 4. (a) Eyring plot with various TFP concentrations.	20
Figure 5. (a) Eyring plot with various phosphate concentrations.	21
Figure 6. Effects of DMSO and phosphate ions on TFP-palladium binding.....	23
Figure 7. Various NaBH₄ concentrations.....	24
Figure 8. Palladium concentration dependence.	25
Figure 9. APE concentration dependence.....	26
Figure 10. Various DMSO concentrations.....	29
Figure 11. Competition experiments with APE and external alkene.....	30
Figure 12. Formation of P-allyl TFP.	31
Figure 13. Same excess experiments with TFP.	32
Figure 14. Eyring plot with increased palladium.....	33
Figure 15. Optimized structures and activation energies of the transition states of allyl association (TS1), oxidative addition (TS2), and nucleophilic attack (TS3).	34
Figure 16. The computed energy profile of the association of the allyl phenyl ether to the (TFP)₂Pd(0) complex (Pd-1) to form the π complex (Pd-2).	36
Figure 17. Summary of chapter 1.....	38
Figure 18. Summary of clip reaction discussed in this section.	62

Figure 19. The rate of deallylation and depropargylation in phosphate buffer.....	64
Figure 20. The influence of DMEM and serum on the rate of deallylation and depropargylation.....	65
Figure 21. The rate of deallylation and depropargylation in the presence of hydroxymethyl- TFP analogs in phosphate buffer.....	68
Figure 22. Deallylation and depargylation of RAE or RPE in the presence of hydroxymethyl-TFP analogs in phosphate buffer, respectively at 37 °C in DMEM with 10% BCS.....	69
Figure 23. The rate of decaging reactions with second generation phosphines in DMEM with serum (premixed).....	73
Figure 24. Decaging reactions with second-generation phosphines without premixing.	75
Figure 25. Deallylation of RAE with palladium-phosphine complexes.	78
Figure 26. The correlation between palladium concentrations and optimal 3iPhos1 concentrations.	79
Figure 27. Kinetics of palladium catalyzed deallylation.....	80
Figure 28. Copper interference with lead phosphines.....	82
Figure 29. Substrate scope of deallylationbased on the pK_a of the leaving group.....	84
Figure 30. Substrate scope of deallylation based on the sterics of the alkene.	86
Figure 31. Chemical structures of FR901463, FR901464 and FR901465.....	89
Figure 32. Chemical structure of the biotin derivative of spliceostatin A.	90
Figure 33. Mechanism of covalent coupling of Spliceostatin A to the nucleophilic zinc finger of PHF5A.	90
Figure 34. Pathways of alternative splicing.....	91

Figure 35. Alternative splicing with FR901464 analogs.....	92
Figure 36. Natural product splicing regulators.....	93
Figure 37. Convergent synthesis of FR901464 analogs.	94
Figure 38. SAR summary of FR901464.	95
Figure 39. Structures of selected ADCs.	97
Figure 40. Examples of drugs conjugated to sugars.	98
Figure 41. Structure of Spliceostatin A.....	99
Figure 42. NOESY of tetrahydrofuran 3.21.	105
Figure 43. Plausible reaction mechanism for the NBS-mediated cyclization to form tetrahydrofuran 3.21.....	106
Figure 44. Antiproliferation assay.....	109
Figure 45. MAMD (black) and 3.25 (red) overlayed.	110

List of Schemes

Scheme 1. Initial report of palladium-mediated allylation by Tsuji.	2
Scheme 2. Improvement of palladium-mediated alkylation with a phosphine ligand.	2
Scheme 3. Tsuji-Trost reaction mechanism.	4
Scheme 4. Asymmetric allylic alkylation as a key step in the synthesis of Aeurginosin 98B.	5
Scheme 5. Linear substrates studied by Lloyd-Jones and the proposed resting state.	6
Scheme 6. Kinetic study of palladium-catalyzed allylation by Shintani and Hayashi.	7
Scheme 7. Unique reactivity in palladium-catalyzed reactions in water. a) Tsuji-Trost reaction with an alcohol. b) Tsuji-Trost reaction with allylic carbonates. c) Tsuji-Trost reaction with allylation of uracils.	9
Scheme 8. Water mediated reduction of palladium(II) to palladium(0).	10
Scheme 9. The first alkene-based chemodosimeter for palladium imaging.	11
Scheme 10. The first alkyne-based chemodosimeter for palladium imaging.	11
Scheme 11. Chemodosimeters for carbon monoxide detection.	12
Scheme 12. Deallylation of nonfluorescent allyl Pittsburgh Green ether to fluorescent Pittsburgh Green.	14
Scheme 13. General catalytic cycle of a Tsuji-Trost reaction with proposed TLSs.	19
Scheme 14. Meggers [Cp[*]Ru(cod)-Cl] ruthenium catalyst.	41
Scheme 15. New Meggers' ruthenium catalysts.	42
Scheme 16. Photoactivatable Meggers catalyst.	43
Scheme 17. Biocompatible ruthenium system.	44
Scheme 18. Mascareñas' mitochondria specific ruthenium catalysts.	45

Scheme 19. Serum stable Meggers catalyst.	46
Scheme 20. Depropargylation of N-propargyl 5-fluorouracil with cis platinum.	47
Scheme 21. Cis platinum depropargylation in cancer cells.	48
Scheme 22. Platinum-catalyzed deallylation developed in the Koide lab.	49
Scheme 23. Gold catalyzed depropargylation.	51
Scheme 24. Gold-catalyzed depropargylation of peptides.	52
Scheme 25. Palladium -catalyzed deprotection of cysteines.	53
Scheme 26. Palladium-catalyzed generation of neuramic acid.	54
Scheme 27. Palladium-catalyzed depropargylation for the protein activation.	55
Scheme 28. Palladium-catalyzed dealkylation of 5-fluoro-uracil pro-drugs.	56
Scheme 29. Activation of gemcitabine prodrugs by palladium catalysis.	56
Scheme 30. Palladium-catalyzed decaging of floxuridine.	57
Scheme 31. De-caging of doxorubicin prodrugs with a palladium-devices.	58
Scheme 32. Rhodamine-based chemodosimeter used in intracellular palladium-catalyzed deallylation.	58
Scheme 33. Alkene-based probe for mitochondria imaging.	59
Scheme 34. De-caging of allyloxycarbonyl modified doxorubicin.	60
Scheme 35. Palladium-catalyzed deprotection in peptide synthesis.	61
Scheme 36. RAE and RPE decaging.	63
Scheme 37. Synthesis of hydroxymethyl-TFP analogs.	66
Scheme 38. Synthesis of second generation phosphine ligands.	71
Scheme 39. Synthesis of palladium-phosphine complexes.	76
Scheme 40. Synthesis of sterically hindered resorufin analogs.	85

Scheme 41. First generation synthesis of right fragment	100
Scheme 42. Synthetic scheme for Wacker-type oxy-palladation.....	101
Scheme 43. NBS-mediated cyclization.	103
Scheme 44. Reduction of bromide.	104
Scheme 45. Cross coupling of tetrahydrofuran analog of FR901464.....	108

List of Equations

Equation 1. Observed rate reported by Lloyd-Jones and coworkers..... 6

Equation 2. Observed rate reported by Shintani, Hayashi and coworkers..... 7

Acknowledgments

First and foremost, I would like to thank my parents for their continued support and for moving to another continent in the pursuit of a better life for me. I will be forever grateful. They showed me, by their example, that stepping out of the comfort zone is, although difficult, can be very important. My parents listened to me for hours after a bad day and provided comforting words when I needed it the most. I also need to thank the rest of my family and friends, especially my grandparents, who have cheered for me every step of the way. Last but not least, I want to thank Ostap, Tux, and Tiger for making even the worst day better when I get home every day.

I would like to thank Professor Kazunori Koide for accepting me into his laboratory and his mentorship in developing my skills as a scientist. I would also like to thank my committee members, Professor Paul Floreancig, Professor Peng Liu, and Professor Lin Zhang for serving on my dissertation committee. Thank you for the time you spent reviewing my documents and for your guidance. I want to thank Professor John Schmitz at UPMC Hillman Cancer Center for performing cell viability experiments and our helpful discussions.

I also need to thank Dr. Damodaran Achary and Dr. Bhaskar Godugu for their help interpreting NMR and MS spectra and maintaining these important facilities. Additionally, I would like to thank all administrative and other staff members for answering hundreds of questions through these five years.

Thank you to all of the past and current members of the Koide group for their support and mentorship in the past five years. Specifically, I would like to acknowledge Dr. Robert Bressin and Dr. Dianne Pham for their contributions to my training. I would also like to thank Dr. Adriana Gambino, Dr. Hina Khan, Jacob Beard, and Jincy K. Vinod for reviewing this document and

providing their feedback. Thank you to Miho Naruse for her help with statistical analysis and for brightening my days by sending me cat videos. I am grateful for the scientific discussions, friendships, and fun days that I had with all past and current members of the Koide group. Thank you for all of your help and support through these five years. I appreciate everyone that I got to meet during my studies at Pitt. I am grateful for the new friendships that flourished here. I could not have done this alone. Thank you for being a part of this chapter in my journey.

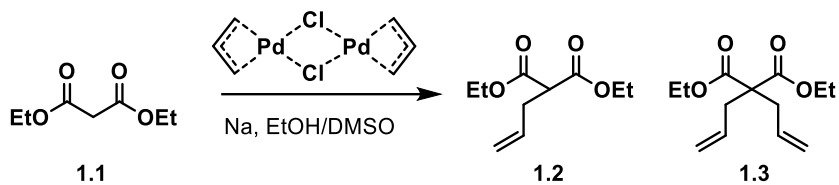
1.0 Kinetics and inverse temperature dependence of a Tsuji–Trost reaction in aqueous buffer

A significant portion of this chapter was published as: Pohorilets, I.; Tracey, M. P.; LeClaire, M. J.; Moore, E. M.; Lu, G.; Liu, P.; Koide, K., *ACS Catal.* **2019**, 9, 11720–11733. In this work, M. J. LeClaire and M. P. Tracey performed experiments and analysis for Eyring plots and identified the nucleophile. E. M. Moore and I carried out concentration dependence experiments and performed data analysis. I performed the competition experiment. Computational experiments were performed by Dr. G. Lu and Professor P. Liu.

Reprinted (adapted) with permission from *ACS Catal.* **2019**, 9, 11720–11733. Copyright 2019 American Chemical Society.

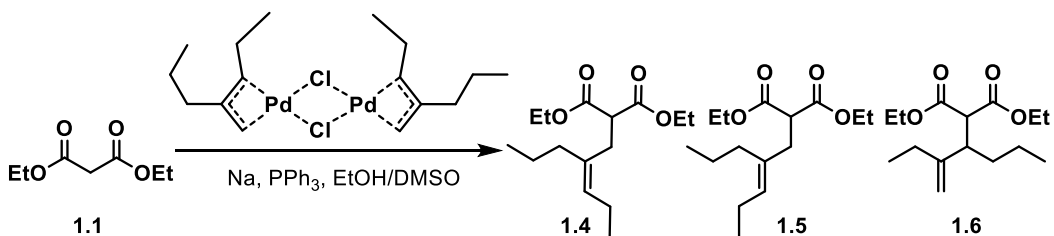
1.1 Introduction

The Tsuji-Trost reaction is a palladium (Pd)-catalyzed substitution reaction comprising of an electrophilic allylic group, a leaving group, and a nucleophile. The Smidt group reported the use of a palladium-catalyzed oxidation of alkenes to carbonyls in 1962.¹ In 1965, the Tsuji group published a pioneering report using malonate **1.1** as the nucleophile with bis-allyl palladium chloride dimer under basic conditions. This initial report required stoichiometric amounts of the palladium species, which acted as both the palladium source and the electrophilic allylic group (Scheme 1).²



Scheme 1. Initial report of palladium-mediated allylation by Tsuji.

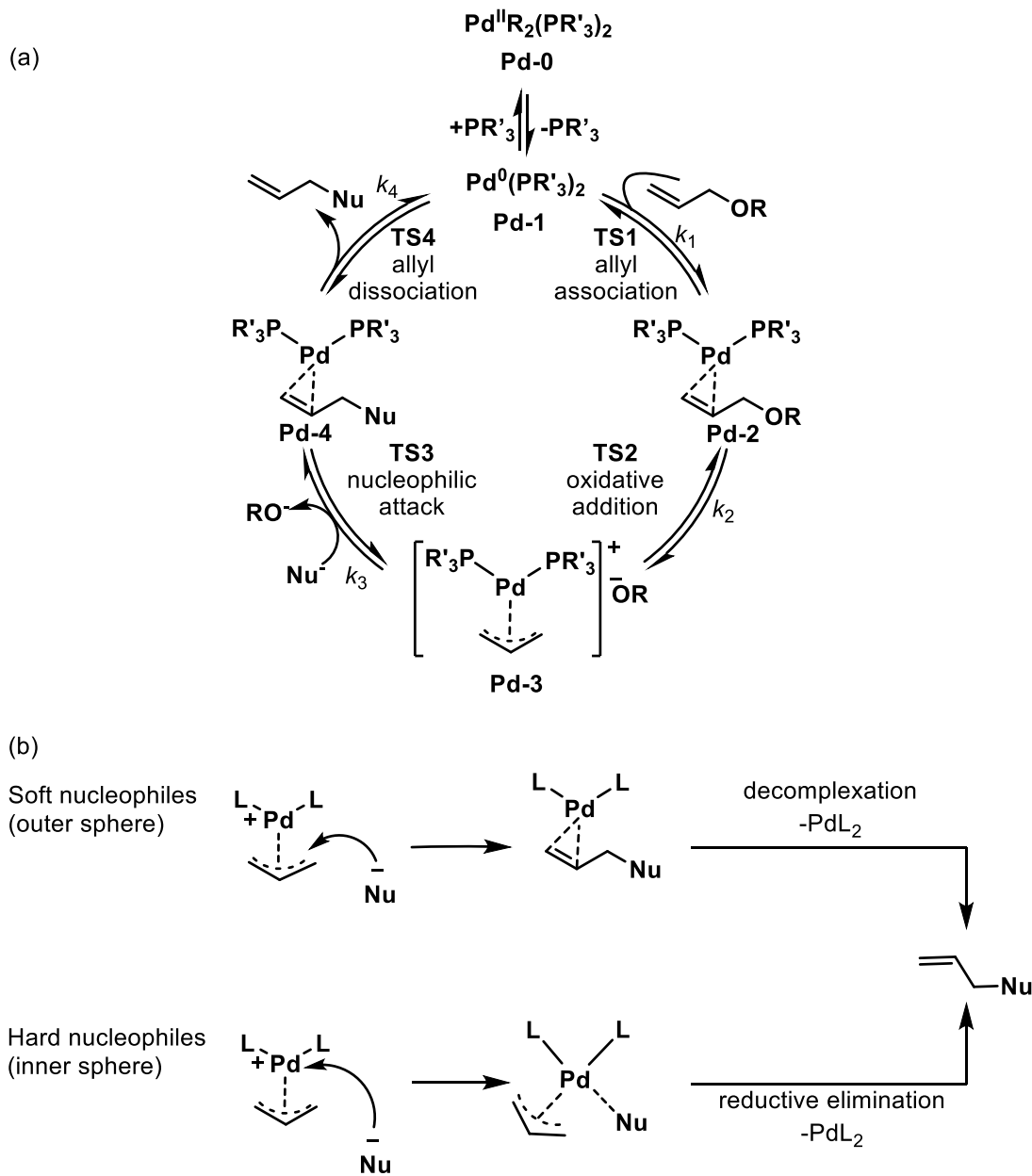
In 1973, while working on preparing acyclic sesquiterpene homologs, the Trost group improved on Tsuji's discovery;³ they reported that the reaction was accelerated to a near instantaneous rate at room temperature in the presence of triphenylphosphine (Ph_3P) ligand (Scheme 2). The addition of the ligand not only accelerated the rate of the reaction to minutes, but also expanded the scope (e.g., methyl(methylsulfonyl)acetate and methyl methylsulfinylacetate were used). This result motivated subsequent developments of new and improved phosphine ligands. For example, chiral phosphine ligands were later developed for asymmetric allylic alkylation, which quickly gained popularity in synthetic chemistry.⁴



Scheme 2. Improvement of palladium-mediated alkylation with a phosphine ligand.

The mechanism and kinetics of the Tsuji-Trost reaction has been extensively studied.⁵⁻⁷ The accepted mechanism is shown in Scheme 3a. The catalytically active, palladium(0), first associates with the alkene to give the 16-electron species, **Pd-2**. The subsequent oxidative addition of **Pd-2** between the allyl group and the leaving group produces an activated π -allyl palladium

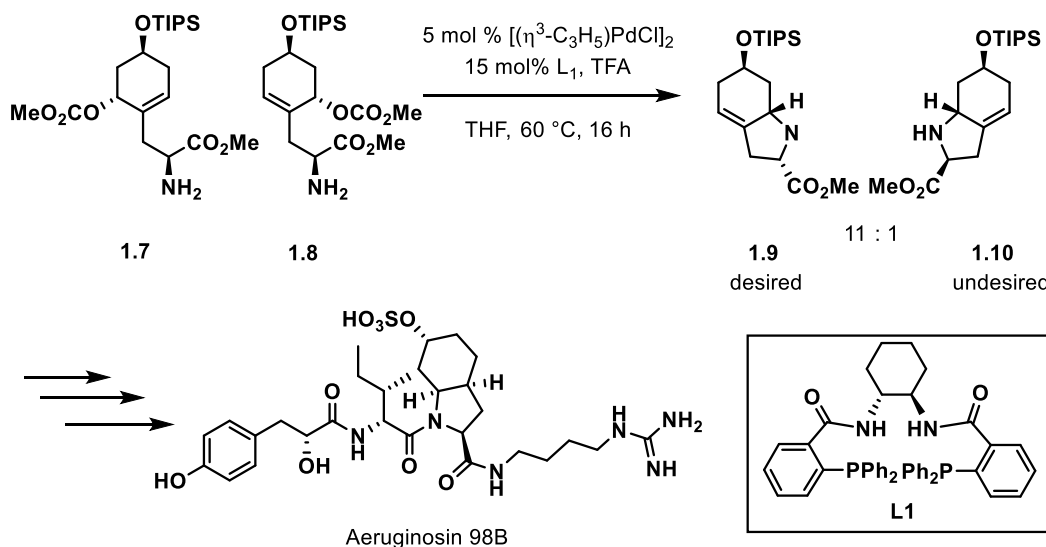
complex, **Pd-3**, which is susceptible to a nucleophilic attack. The nucleophile can attack the carbon or the metal center (also known as outer sphere and inner sphere, respectively) (Scheme 3b).⁸⁻⁹ Soft nucleophiles, with $pK_a < 20$, attack the carbon center directly through the outer sphere. On the contrary, hard nucleophiles attack the metal center via the inner sphere, and the carbon-carbon bond formation occurs after reductive elimination to generate **Pd-4**. Upon allyl dissociation, the desired product is formed and the active palladium(0) species, **Pd-1**, is regenerated, closing the catalytic cycle.



Scheme 3. Tsuji-Trost reaction mechanism. (a) the catalytic cycle. (b) the mechanisms of nucleophilic attack.

The Tsuji-Trost reaction is a valuable transformation in synthetic chemistry and has been used as key steps in many total syntheses.^{4,8} Although Ph₃P is a common ligand for the Tsuji-Trost reaction, other ligands with different steric and electronic properties have been developed to tune the reactivity and selectivity of the reaction.¹⁰ For example, in the total synthesis of aeruginosin

98B, the Trost group utilized a highly diastereoselective palladium-catalyzed intramolecular asymmetric allylic alkylation (Scheme 4).¹¹ The Trost group tested various enantiopure and racemic phosphorus ligands to obtain the desired diastereomer **1.9** (Scheme 4). The racemic mixture of ligand **L1** produced **1.9** in highest yield and diastereoselectivity (**1.9:1.10 = 11:1**). The synthesis of aeruginosin 98B highlights how careful selection of the phosphine ligand is crucial for good yields and selectivity.

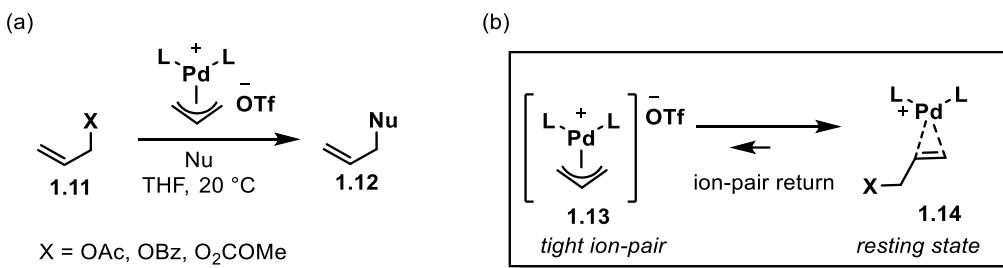


Scheme 4. Asymmetric allylic alkylation as a key step in the synthesis of Aeurginosin 98B.

1.2 Previous kinetic studies of the Tsuji-Trost reaction

Following extensive study, the turnover-limiting step (TLS) for the Tsuji-Trost reaction has been found to be substrate dependent. In 2008, the Lloyd-Jones group observed counterintuitive kinetics when studying Tsuji-Trost allylation reaction with acyclic substrates in

the presence of additives (Scheme 5a).¹² They reported L₂Pd(η²-allyl) complex **1.14** (Scheme 5b) as the resting state of the catalytic cycle. While studying the trends in electrophilicity and ion-pairing, the Lloyd-Jones group reported a rate equation that is zeroth order with respect to their electrophile, allyl acetate, and first order with respect to palladium and nucleophile (Equation 1). The findings indicated that the TLS was the nucleophilic attack on the π-allylpalladium complex (**Pd-3** to **Pd-4**, Scheme 3). Furthermore, the counterion had a pronounced effect on the rate of the reaction. In this study, the Lloyd-Jones group assumed a steady-state amount of the electrophilic π-allylpalladium complex.



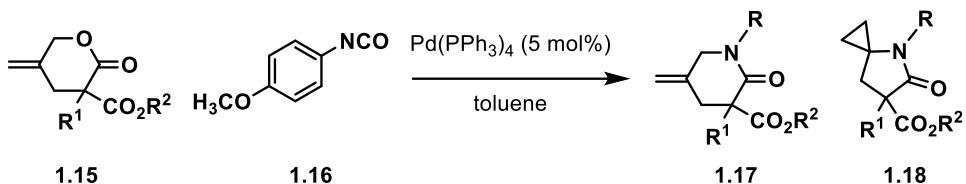
Scheme 5. Linear substrates studied by Lloyd-Jones and the proposed resting state.

Equation 1. Observed rate reported by Lloyd-Jones and coworkers.

$$\frac{d[1.12]}{dt} = k[\text{Pd}][\text{Nu}]$$

Shintani, Hayashi, and coworkers established that the oxidative addition was the rate limiting step for the reaction of a cyclic substrate and a lactone **1.15** (Scheme 6).¹³ The reaction was shown to be the zeroth order with respect to isocyanate **1.16** and first order with respect to lactone **1.15** and palladium (Equation 2). They also observed that more electron-rich triaryl

phosphines afforded faster reaction rates, indicating that the rate-limiting step was the oxidative addition.



Scheme 6. Kinetic study of palladium-catalyzed allylation by Shintani and Hayashi.

Equation 2. Observed rate reported by Shintani, Hayashi and coworkers.

$$\frac{d[1.17]}{dt} = k[1.15][\text{Pd}]$$

It should be noted that kinetic studies discussed by Lloyd-Jones, Shintani and Hayashi, and others were in organic solvents.¹²⁻¹³ However, the Tsuji-Trost reaction is not limited to organic solvents; the performed reaction is not water-sensitive and can be executed with water as a co-solvent.¹⁴

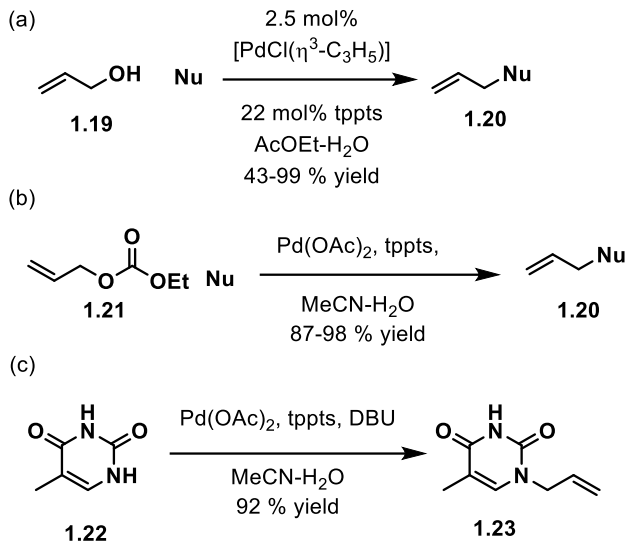
1.3 Tsuji-Trost reaction under aqueous conditions

Water is deemed to be the “solvent of nature” because all biochemical processes happen in aqueous environments.¹⁴ Water is also a useful solvent for chemical transformations used in synthetic chemistry; it makes reactions biomimetic and biocompatible.

Water is one of the most polar solvents (dielectric constant of 78.3 at 25 °C) known.¹⁵ Chemically, it is considered amphoteric, as it can promote electrophilic and nucleophilic reactions,

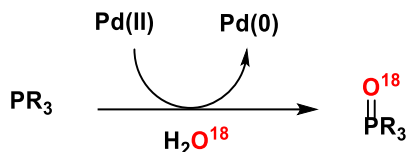
as well as assist in both, acid and base catalysis. Most importantly, water is compatible with many organic reactions such as, the Baeyer-Villiger oxidation,¹⁶ the Hoffman elimination,¹⁷ the Wolff-Kishner reduction,¹⁸ the Curtius rearrangement,¹⁹ Diels-Alder cycloadditions,²⁰ and organometallic reactions, including those catalyzed by palladium.¹⁴ Sharpless and coworkers, coined the term “on water”,²¹ which refers to transformations in aqueous suspensions and occurs more quickly than in organic solvents due to the insolubility of the reagents. Resurgence of water as a solvent for organic reactions took place when Bertozzi coined the concept of bioorthogonal chemistry.²²⁻²⁴ The term describes reactions that take place in biologically complex media that consists of water, while remaining highly chemoselective and biocompatible.

When water is used as the solvent in palladium-catalyzed reactions, unique reactivities are observed, possibly due to the polarity of water. For example, alcohols, such as **1.19**, can be used as leaving groups (Scheme 7a),²⁵ allylic carbonates (**1.21**) can react in the absence of base (Scheme 7b),²⁶ and allylation of uracils (**1.22**) and thiouracils turns out to be more selective toward mono-allylation (Scheme 7c).²⁷ Although the Tsuji-Trost reaction is synthetically useful and has broad application, it has limitations.⁸ The modest catalytic efficiency often requires moderate catalyst loading (5–10 mol %)²⁸, and phosphine-free systems are usually inept.²⁹ Catalyst loading can potentially be lowered by using water as a co-solvent because the palladium catalyst can be recycled under reaction conditions.¹⁴ The catalyst will stay in the aqueous layer, while product and starting material will remain in the organic layer.



Scheme 7. Unique reactivity in palladium-catalyzed reactions in water. a) Tsuji-Trost rection with an alcohol.
b) Tsuji-Trost reaction with allylic carbonates. c) Tsuji-Trost reaction with allylation of uracils.

Water is also known to assist in the reduction of palladium(II) to palladium(0) in the presence of phosphine ligands. In 1992, the Fumiyuki and Verkade groups discovered that the oxygen atom that transforms phosphine to phosphine oxide during the reduction of palladium(II) comes from water (Scheme 8).³⁰⁻³² In 1999, Grushin reported that bidentate phosphine ligands can undergo mono-oxidation in the presence of palladium and 1,2-dibromoethane under aqueous conditions.³³ Furthermore, the Verkade group showed that palladium(II) can be reduced to palladium(0) under aqueous conditions using strong organic bases in the presence of catalytic amount of fluoride.³⁴ Schunn reported that potassium metal can also reduce triethylphosphine palladium complex from palladium(II) to palladium(0) under aqueous conditions.³⁵

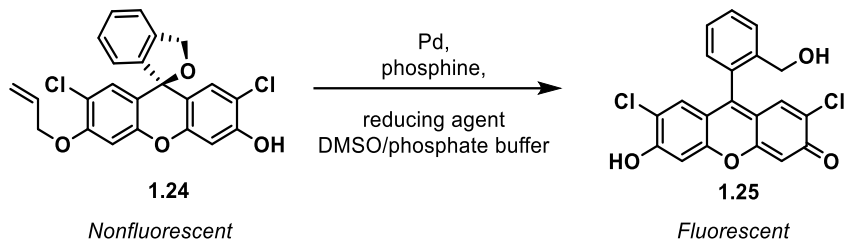


Scheme 8. Water mediated reduction of palladium(II) to palladium(0).

1.4 Bioorthogonal organometallic (BOOM) chemistry

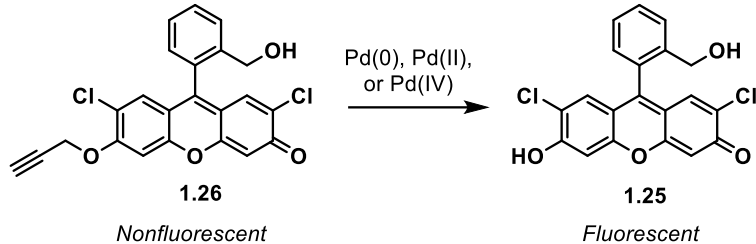
The palladium-catalyzed Tsuji-Trost reaction found its use outside of synthetic organic chemistry^{2-3, 8} in the development of chemosensors,³⁶⁻³⁸ signal amplification,³⁹ and BOOM chemistry.⁴⁰⁻⁴⁴ BOOM chemistry emerged as a viable method to uncage bioactive compounds inside and outside of live cells.⁴⁵⁻⁴⁶ Tsuji-Trost reactions designed to contain fluorophores as leaving groups have been extensively used in BOOM chemistry.^{36, 40}

In 2007, the Koide group demonstrated the utility of chemodosimeter allyl Pittsburgh Green ether (APE) **1.24**, based on a 2',7'-dichlorofluorescein derivative Pittsburgh Green **1.25** (Scheme 9).⁴⁷ Chemodosimeters are small non-fluorescent molecules that undergo irreversible reactions with analytes to form fluorescent compounds.⁴⁸ As we have shown, alkylation of the phenol moiety of Pittsburgh Green (and similar chemodosimeters) made them essentially non-fluorescent. However, upon exposure to palladium, an increase in fluorescence can be observed due to the release of the fluorophore.



Scheme 9. The first alkene-based chemodosimeter for palladium imaging.

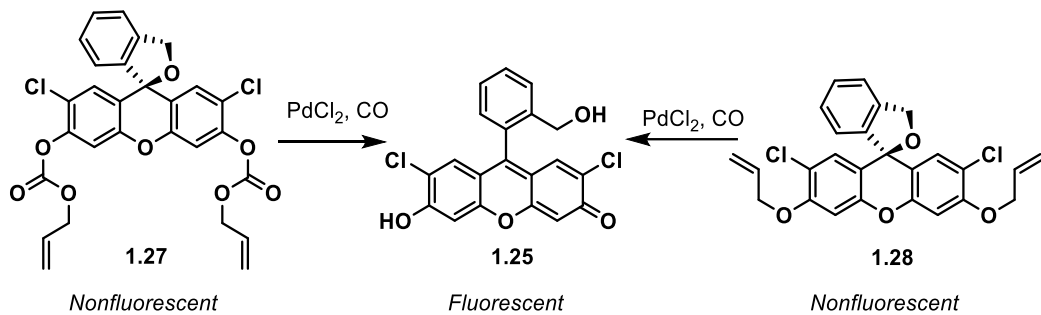
In 2010, Ahn and coworkers reported the first alkyne-based fluorogenic chemodosimeter **1.26** and demonstrated its use in zebrafish for palladium imaging (Scheme 10).⁴⁹ Upon exposure of **1.26** to nano- to micromolar palladium concentrations, Ahn and coworkers demonstrated that Propargyl Pittsburgh Green **1.26** was dealkylated, and fluorescence microscopy showed increased fluorescence inside zebrafish.



Scheme 10. The first alkyne-based chemodosimeter for palladium imaging.

In 2016, the Lu group synthesized an allyloxycarbonyl (alloc) protected fluorescein **1.27**, which served as a Tsuji-Trost based carbon monoxide probe (Scheme 11).⁵⁰ Its applications were demonstrated in live cell imaging, which were performed in Dulbecco's Modified Eagle's Medium (DMEM) supplemented with 10% fetal bovine serum (FBS). In 2018, the Lu group developed probe **1.28** with the ability to monitor exogenous and endogenous carbon monoxide in nude mice.⁵¹ In 2017, Feng and coworkers reported the first bioluminescent probe, allyl-luciferin,

to detect carbon monoxide in living cells in phosphate buffered saline (PBS) buffer.⁵² Furthermore, 5-fluorouracil,⁵³ gemcitabine,⁵⁴ and doxorubicin⁵⁵ prodrugs have been developed using fluorescent precursors to study biological reactivity of the catalytic system.



Scheme 11. Chemodosimeters for carbon monoxide detection.

In the development of chemosensor for palladium and prodrug uncaging (i.e., clip chemistry), the concentrations of the substrate have been chosen arbitrarily. This is problematic because these studies may assume that the kinetic profile of a palladium-catalyzed deallylation remains the same regardless of substrate concentrations. To better understand the reaction and guide future optimization, it is imperative to identify a turnover limiting step under specific reaction conditions. It has been shown that the turnover-limiting step of Tsuji-Trost reaction changes depending on the substrate structure.¹²⁻¹³ However, it is unclear what influences the identity of TLS at micromolar substrate concentrations often used in chemosensor development, signal amplification, and BOOM chemistry.

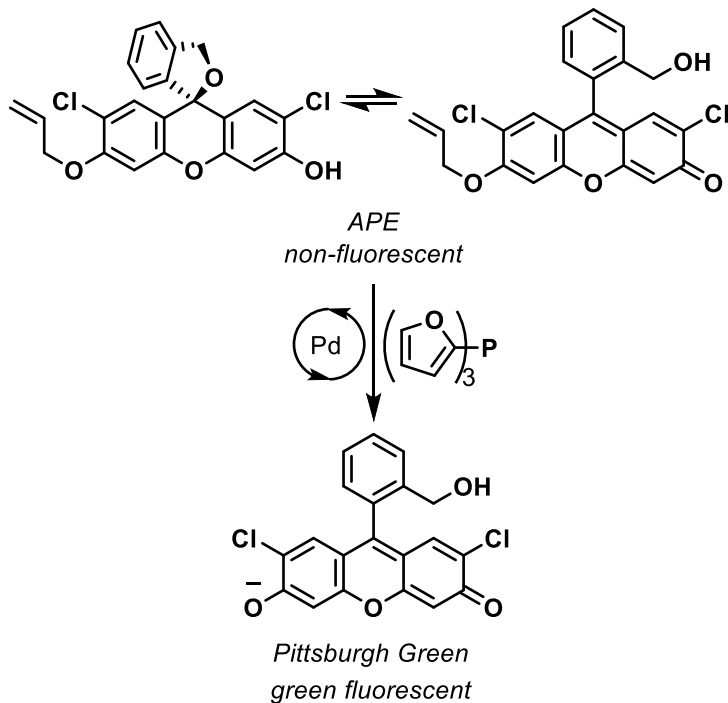
1.5 Summary

Identifying the TLS in the Tsuji-Trost reaction under different conditions is necessary for the development of faster and more controlled reactions. The studies led by Lloyd-Jones, Shintani and Hayashi, and many others were performed with millimolar (mM) concentrations of substrates and at a single temperature.¹²⁻¹³ This is acceptable for synthetic chemistry, but not applicable to biological systems. It is unknown how the TLS depends on substrate concentrations in a micromolar range or the temperature. Given the applicability of Tsuji-Trost reaction in both chemosensor development and BOOM chemistry, a study of the reaction mechanism and kinetics at low substrate concentrations is relevant, especially in aqueous conditions.

1.6 Results and Discussion

1.6.1 Introduction

The Koide group previously reported the palladium-catalyzed deallylation of fluorogenic chemodosimeter APE (Scheme 12) in 5% DMSO/pH 7 buffer.⁴⁷ Pittsburgh Green represents typical leaving groups in Tsuji-Trost reactions because the pK_a value of the phenolic hydroxyl group is 4.27,⁴⁷ reflecting the acidity of carboxylic acids or electron-deficient phenols. As the Semagina group demonstrated, the use of APE for mechanistic studies can provide new insights because the reaction can be both continuously and accurately monitored by fluorescence at low micromolar concentrations.⁵⁶



Scheme 12. Deallylation of nonfluorescent allyl Pittsburgh Green ether to fluorescent Pittsburgh Green.

The reaction proceeded faster when Ph_3P was replaced with tri(2-furyl)phosphine (TFP)⁵⁷ and when the phosphate concentration was increased from 0.05 M to 1.23 M.⁵⁸ The use of NaBH_4 did not have an impact on the conclusion of this research but facilitated kinetic studies; it eliminated the deactivation of palladium(0) by air oxidation when high throughput experiments were carried out under an air atmosphere.⁵⁹ If palladium nanoparticles are formed under the reaction conditions, it would complicate the interpretation of data. However, because the solvents in this study are DMSO and water and palladium concentrations are in the 10 nM to 4 μM range, palladium species are most likely monomeric.⁶⁰

Figure 1a shows the consumption of 50 or 25 μM APE over time. Fitting the consumption of APE to a one-phase decay model revealed that the reaction rapidly slowed as the substrate concentration approached 4 μM (Table 1). When the reaction started with 5 μM APE, the reaction

progressed at a similar rate as when the above reaction slowed after the substrate concentration reached 4 μM , excluding product inhibition and indicating that the TLS may change at this concentration (Figure 1b, Table 1). If the TLS remains the same during the course of the reaction, a single kinetic profile should be observed from 50 to 0 μM . As this was not the case, we turned to Eyring plots to quantify energetic contributions in the reaction.

Table 1. Calculated plateau of APE from fitting to a one-phase decay as reaction continues indefinitely; data over time also shown in Figure 1. Conditions: 5, 25, or 50 μM APE, 1 μM $\text{Pd}(\text{NO}_3)_2$, 80 μM TFP, 10 mM NaBH_4 , 10% DMSO v/v 1.23 M phosphate pH 7 buffer.

Initial APE concentration, μM	Calculated plateau of APE (M) as reaction proceeds infinitely
5	$8.0 \pm 4.0 \times 10^{-7}$
25	$4.1 \pm 0.7 \times 10^{-6}$
50	$4.1 \pm 1.3 \times 10^{-6}$

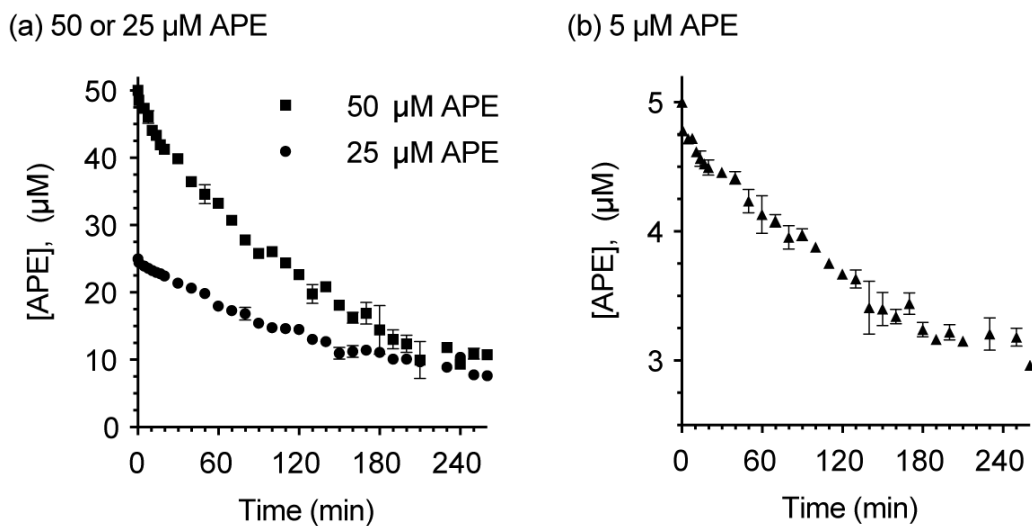


Figure 1. Consumption of APE as a function of time. Conditions: (a) 25 or 50 μM APE, 1 μM $\text{Pd}(\text{NO}_3)_2$, 80 μM TFP, 10 mM NaBH_4 , 10% v/v DMSO/1.23 M phosphate pH 7 buffer, 298 K, $n = 3$. (b) 5 μM APE, 1 μM $\text{Pd}(\text{NO}_3)_2$, 80 μM TFP, 10 mM NaBH_4 , 10% v/v DMSO/1.23 M phosphate pH 7 buffer, 298 K, $n = 3$.

Reprinted (adapted) with permission from *ACS Catal.* 2019, 9, 11720–11733. Copyright 2019 American Chemical Society.

Preparation of an Eyring plot involves plotting the natural log of the reaction rate constant against the inverse temperature to afford a line where the slope is $-\Delta H^\ddagger/R$ and the y-intercept is $\ln(k_b/T) + \Delta S^\ddagger/R$ (Figure 2). ΔH^\ddagger values are intrinsically independent of the concentrations of reactants, while ΔS^\ddagger values are often dependent. Because it was not possible to measure the concentrations of reactive species involved in the TLS, we will not discuss experimental ΔS^\ddagger values extensively. We measured the fluorescence stemming from the reaction product (Pittsburgh Green, Scheme 12) after 30 min, at which point a vast majority of the substrate remained intact. This choice allowed for high throughput and accurate data collection under analytically and biologically relevant, highly diluted conditions in a 96-well format.

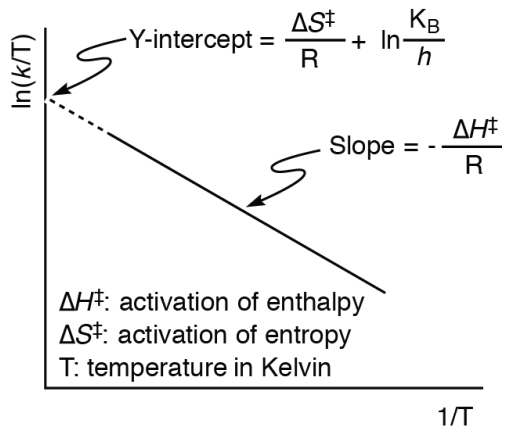


Figure 2. Representative Eyring plot. Reprinted (adapted) with permission from *ACS Catal.* 2019, 9, 11720–11733. Copyright 2019 American Chemical Society.

1.6.2 Initial Investigation with Previously Optimized Conditions: Effect of Substrate Concentration

We first wished to establish a benchmark Eyring plot under previously optimized conditions⁵⁸ at 293–358 K. With 12.5 μM APE, we uncovered three regimes (Figure 3a). Regime 1, regime 2, and regime 3 showed $\Delta H^\ddagger > 0$, $\Delta H^\ddagger \sim 0$, and $\Delta H^\ddagger < 0$, respectively. The concave-down shape may indicate two changes in TLS.^{61–64} These benchmark values for ΔH^\ddagger provided a standard against which we could evaluate effects on the TLS by changing conditions, using the generally accepted mechanism (Scheme 3a).

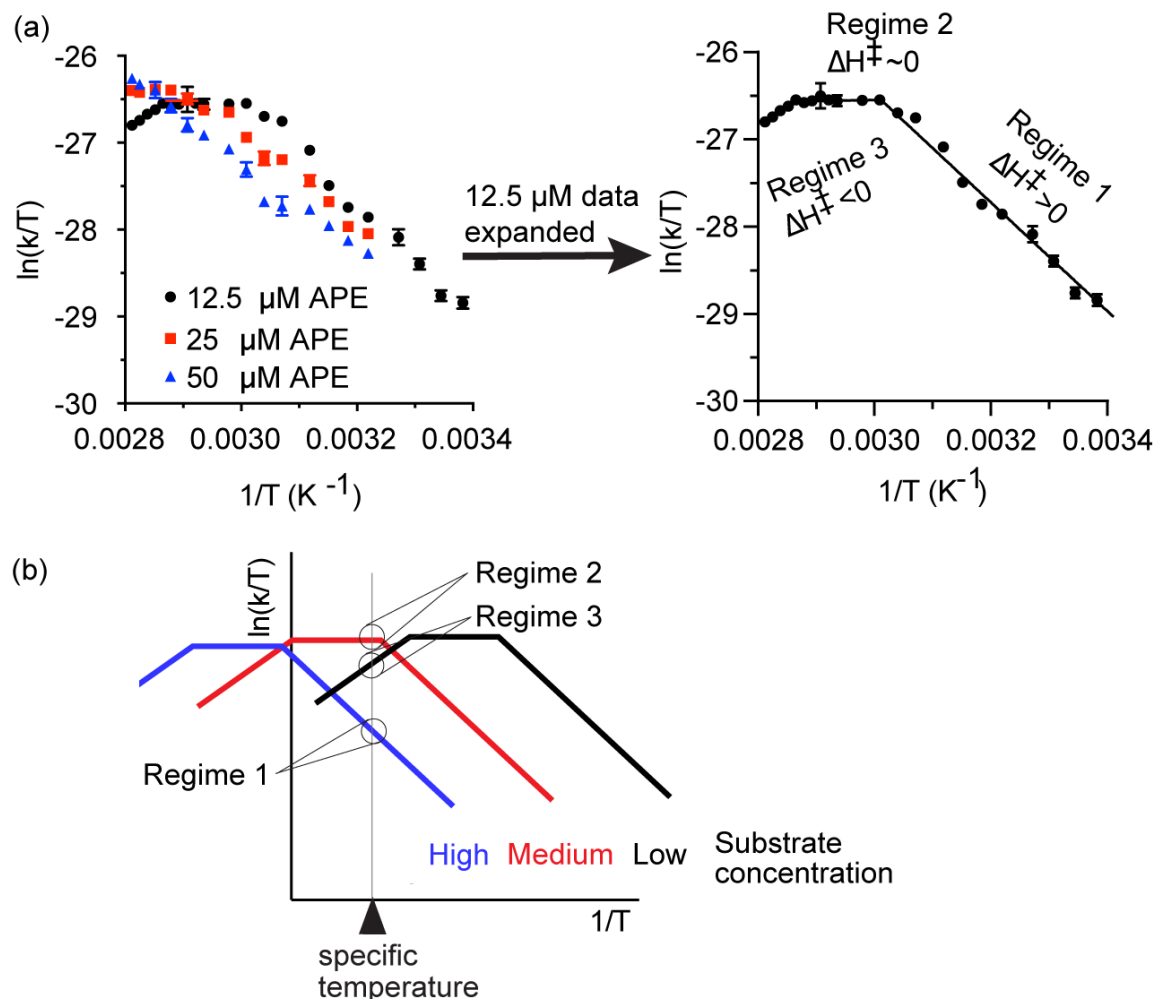


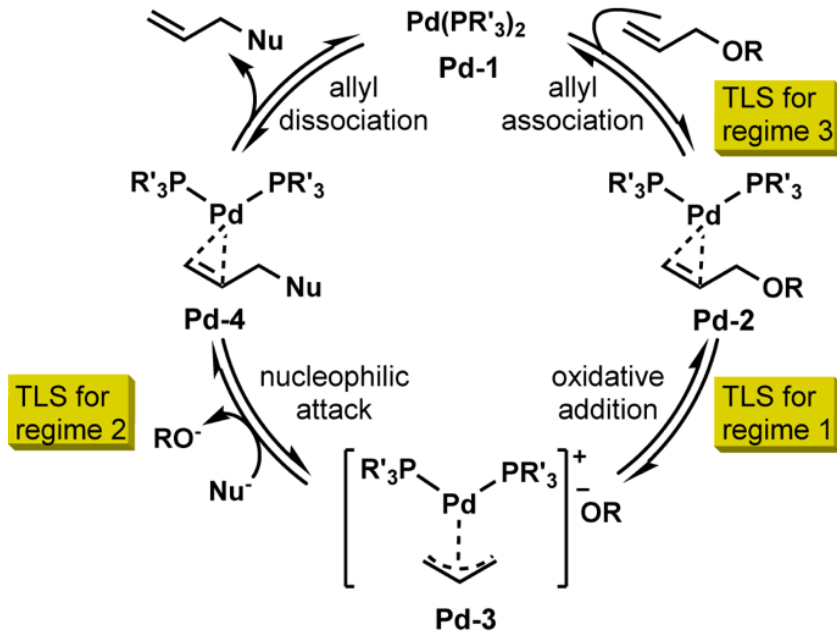
Figure 3. (a) Eyring plot under the previously developed reaction conditions with various APE concentrations. Conditions. (b) Changing regime with reaction progress at a single temperature. Reprinted (adapted) with permission from *ACS Catal.* 2019, 9, 11720–11733. Copyright 2019 American Chemical Society.

We then used APE at 25 and 50 μM concentrations; the APE concentrations had little impact on ΔH^\ddagger in regime 1 (42–55 kJ mol^{-1} ; Figure 3a) but had notable impact on the inversion temperature (T_{inv}). Specifically, when the APE concentration was lower, the T_{inv} was lower (Figure 3b). This observation can account for the change observed in Figure 1; as the reaction proceeds, the kinetic profile at a specific reaction temperature shifts from regime 1 to regime 2, finally to regime 3 (Figure 3b, “specific temperature”). The existence of regime 2 was uncertain at this point, because this regime might be the transition between regime 1 and regime 3. However, further studies shown below support the existence of regime 2 as an independent regime.

For regime 1, we propose that the TLS is the oxidative addition (i.e., **Pd-2** to **Pd-3**, Scheme 13) because this step converts the stronger C-O bond to the weaker Pd-O and Pd-C bonds.⁶⁵ For regime 2, the TLS is entropically controlled; this may be attributed to the nucleophilic attack toward **Pd-3**, as will be discussed later. Regime 3 is inversely temperature-dependent ($\Delta H^\ddagger < 0$), which is scarce in literature and not well understood.^{66–78} We propose that the TLS for regime 3 is the association of the TFP-ligated palladium species to the allyl group (i.e., **Pd-1** to **Pd-2**) as the coordinatively unsaturated 14-electron species **Pd-1** gains electrons to form a more stable 16-electron species **Pd-2**. As shown later, increasing palladium concentration eliminates this regime, supporting the association as the TLS of this regime.

Altogether, the identities of TLSs depend on both the temperatures and the substrate concentrations, and at elevated temperatures with very low substrate concentrations, the ΔH^\ddagger has

a negative value. To better understand the contributions of each reaction component on the kinetics, we began to systematically perturb the benchmark reaction conditions.



Scheme 13. General catalytic cycle of a Tsuji-Trost reaction with proposed TLSs. Reprinted (adapted) with permission from *ACS Catal.* 2019, 9, 11720–11733. Copyright 2019 American Chemical Society.

1.6.3 Effect of Phosphine Concentration

Numerous studies have shown that phosphine structures substantially impact palladium catalysis;⁷⁹⁻⁸¹ however, fewer have demonstrated correlations between phosphine concentration and reaction rate.⁸²⁻⁸³ We studied the deallylation with 60, 120, and 180 μM TFP; with 12.5 μM APE (Figure 4a), the results did not differ significantly at the three TFP concentrations. The correlation between the TFP concentration and deallylation rate showed initial linear relationship

at 318 K (regime 1), 339 K (regime 2), and 353 K (regime 3) (Figure 4b). At these three temperatures, the rate declined with higher concentrations of TFP. This may be because the equilibrium between less ligated and more highly ligated palladium species shift toward the latter at higher TFP concentrations.^{82, 84}

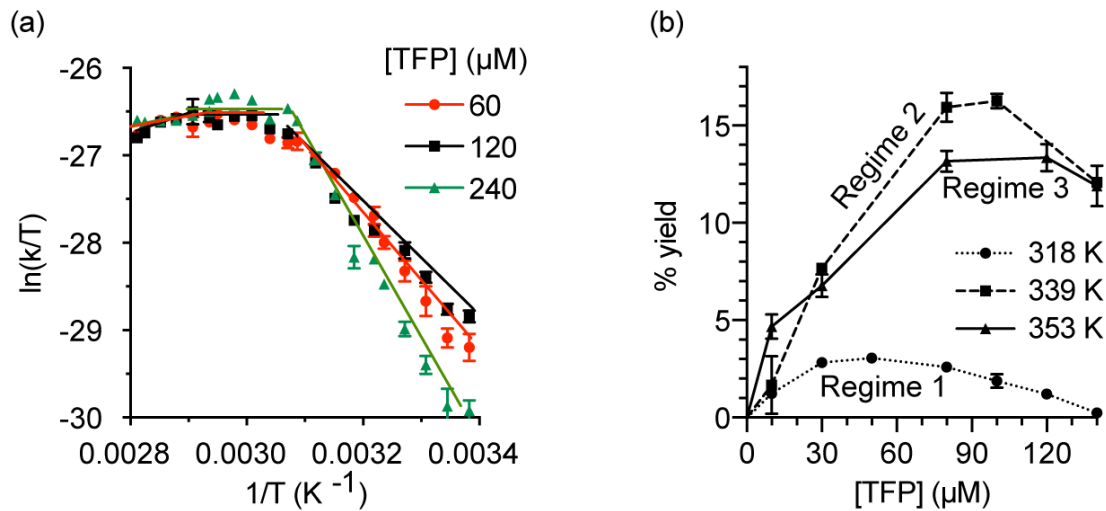


Figure 4. (a) Eyring plot with various TFP concentrations. Conditions: 9.4 nM Pd(NO₃)₂, 10 mM NaBH₄, 12.5 μM APE, 5% v/v DMSO/1.23 M phosphate pH 7 buffer, 30 min. $n = 3$. (b) TFP-concentration dependence. Conditions: 0–140 μM TFP, 9.4 nM Pd(NO₃)₂, 10 mM NaBH₄, 12.5 μM APE, 5% v/v DMSO/1.23 M phosphate pH 7 buffer, 30 min. $n = 3$. Reprinted (adapted) with permission from ACS Catal. 2019, 9, 11720–11733. Copyright 2019 American Chemical Society.

1.6.4 Effect of Phosphate Ion Concentration

The Baran and Gaunt groups independently reported an unspecified but positive role of phosphate ions in palladium catalysis.^{85–86} In more closely related systems, π-allylpalladium-organic phosphate complexes were reactive intermediates, but the reactions were carried out in

aprotic solvents (e.g., toluene or THF).⁸⁷⁻⁸⁸ We wondered whether inorganic phosphates, originally intended to be used as the buffer salts, affect the deallylation kinetics in water. It should be noted that phosphate ions were not a nucleophile toward an electrophilic allyl species.⁵⁸ With 12.5 μM substrate, we were unable to conclude whether and how phosphate ion concentrations influence the kinetic profile (Figure 5a).

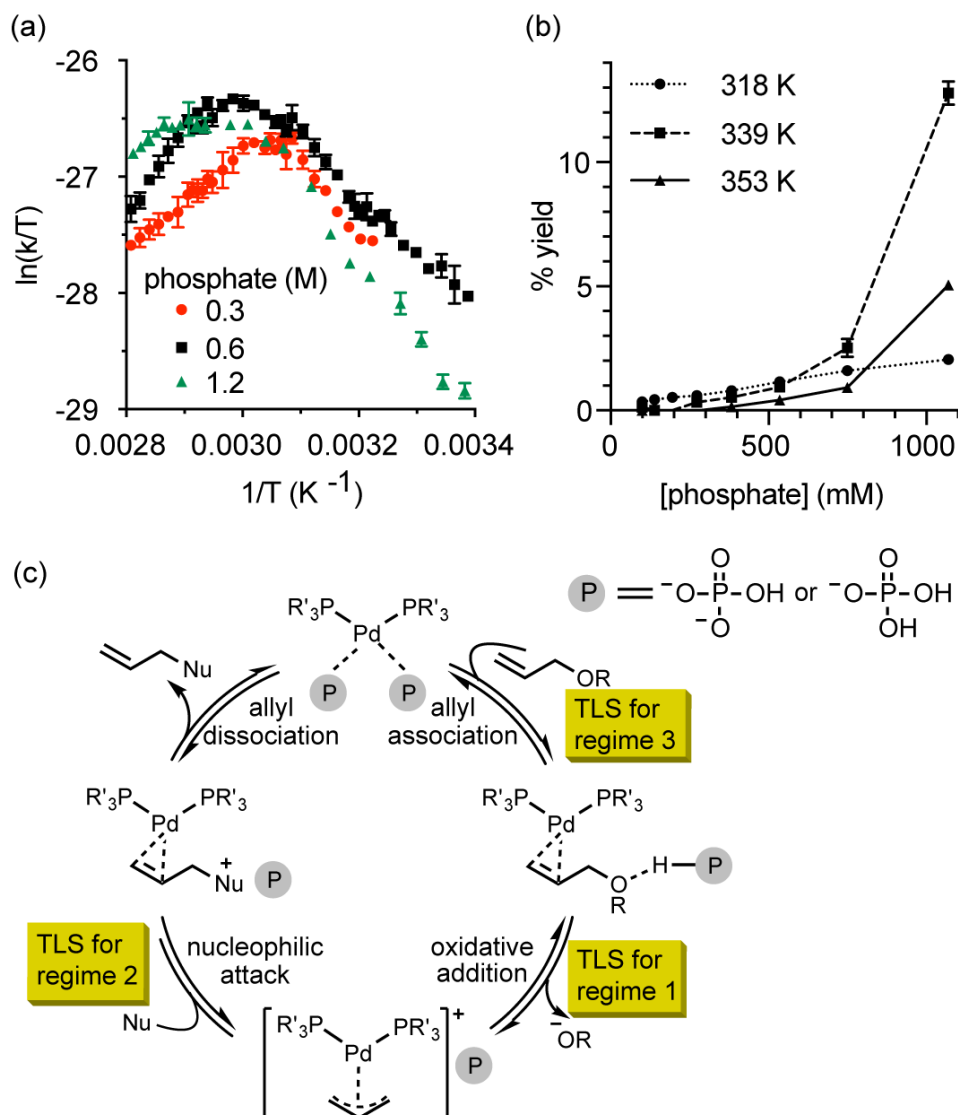


Figure 5. (a) Eyring plot with various phosphate concentrations. Conditions: 12.5 μM APE, 9.4 nM $\text{Pd}(\text{NO}_3)_2$, 120 μM TFP, 10 mM NaBH_4 , 5% v/v DMSO/0.3, 0.6, or 1.2 M phosphate pH 7 buffer, 293–358 K, $n = 4$, 30

min. (b) phosphate concentration dependence. Conditions: 12.5 μ M APE, 5 nM Pd(NO₃)₂, 80 μ M TFP, 5% v/v DMSO/100–1070 mM phosphate pH 7 buffer, $n = 3$, 30 min. (c) A working hypothesis for the roles of phosphate ions. Reprinted (adapted) with permission from *ACS Catal.* 2019, 9, 11720–11733. Copyright 2019 American Chemical Society.

Therefore, we resorted to a slightly different approach; the reaction was monitored at various phosphate concentrations at three temperatures corresponding to three regimes (Figure 5b). In this experiment, we did not use NaBH₄ because it would change the pH at low phosphate concentrations and because NaBH₄ was found to be unnecessary (see the section below). In regime 1 (318 K), the reaction rate was the first order with respect to phosphate. In regimes 2 and 3 (339 and 353 K, respectively), the rates appeared to be nearly second order with respect to phosphate concentrations. Therefore, in regime 1 where the TLS may be the oxidative addition step, one molecule of a phosphate ion may be involved in the transition state. In regime 2 or regime 3 where the TLS may be the nucleophilic attack or palladium-olefin association, two phosphate ions may be involved.

Crystal structures of palladium(II)-diphosphate complexes have been previously reported,⁸⁹⁻⁹⁰ but palladium(0)–phosphate complexes have not been synthesized. A working hypothesis is depicted in Figure 5c; in the allyl association step, the palladium species may be bound to two phosphate ions, which are dissociated as the olefin binds the metal. The rate acceleration by phosphate ions may be due to the shift in equilibrium between phosphate-bound palladium as a pre-catalyst and DMSO-bound palladium as a resting state complex toward the precatalyst. In the oxidative addition step, either H₂PO₄⁻ or HPO₄²⁻ may form a hydrogen bond with the allylic oxygen atom to facilitate the C–O bond cleavage. Hydrogen-bond-driven activation

of allylic ethers has been previously reported in methanol.⁹¹ Their DFT calculations showed that hydrogen bonding could lower the activation energy by more than 20 kcal mol⁻¹.⁹¹

In the oxidative addition step, the counteranion may be rapidly exchanged from the phenolic oxide anion to a phosphate ion (Figure 5c). Because the nucleophile in the next step is a neutral species (as discussed in section below), a phosphate ion can lower the transition state energy by forming an ion pair with the incipient positive charge on the nucleophile. This would account for the phosphate-mediated acceleration of the deallylation in regime 2.

The palladium-phosphine binding can be reversible;⁹²⁻⁹⁴ thus, we asked whether phosphate ions could act as a competitive ligand against TFP toward palladium. As Figure 6 shows, lowering the phosphate concentration did not change the optimal concentration of TFP, indicating that these two species are probably not competing as palladium ligands.

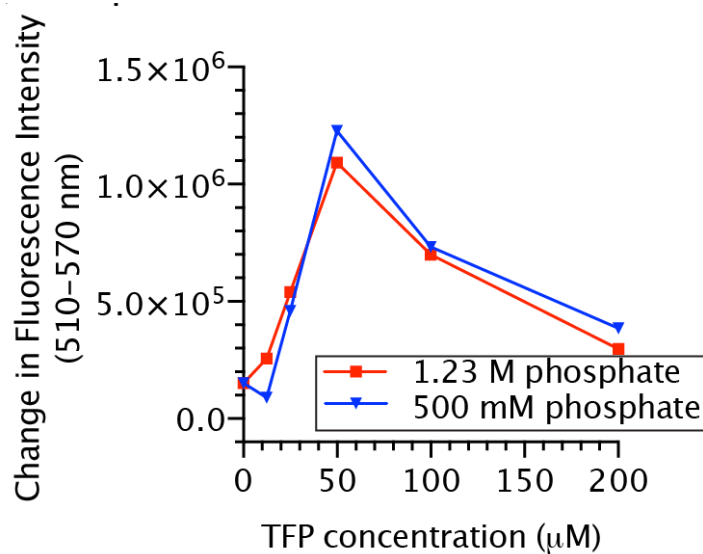


Figure 6. Effects of DMSO and phosphate ions on TFP-palladium binding. Conditions: 470 nM $\text{Pd}(\text{NO}_3)_2$, 10 mM NaBH_4 , 20 μM APE, 5% v/v DMSO/phosphate pH 7 buffer, 298 K, 60 min. Reprinted (adapted) with permission from *ACS Catal.* 2019, 9, 11720–11733. Copyright 2019 American Chemical Society.

1.6.5 Effect of NaBH₄ Concentration

The reduction of palladium(II) with >10 mM NaBH₄ is not the TLS because the deallylation rate was independent of NaBH₄ concentration.⁵⁸ Little was known about the energetic contributions of NaBH₄ below 10 mM. With 12.5 μM APE (Figure 7a), the Eyring plots were similar in the 0–10 mM NaBH₄ concentration range. To understand the impact of NaBH₄ concentrations, we focused on three temperatures (318, 339, and 353 K) corresponding to regimes 1, 2, and 3. As Figure 7b shows, in regime 1 (318 K), the concentrations of NaBH₄ had no impact on the kinetics of the deallylation reaction. In regimes 2 and 3, higher concentrations of NaBH₄ retarded the reaction. Although it is unclear how NaBH₄ does so, it has become evident that NaBH₄ is probably not involved in TLSs in any regimes. The insights from these experiments may be applicable to synthetic organic chemistry, chemosensing, and bioorthogonal chemistry in which NaBH₄ cannot be used.

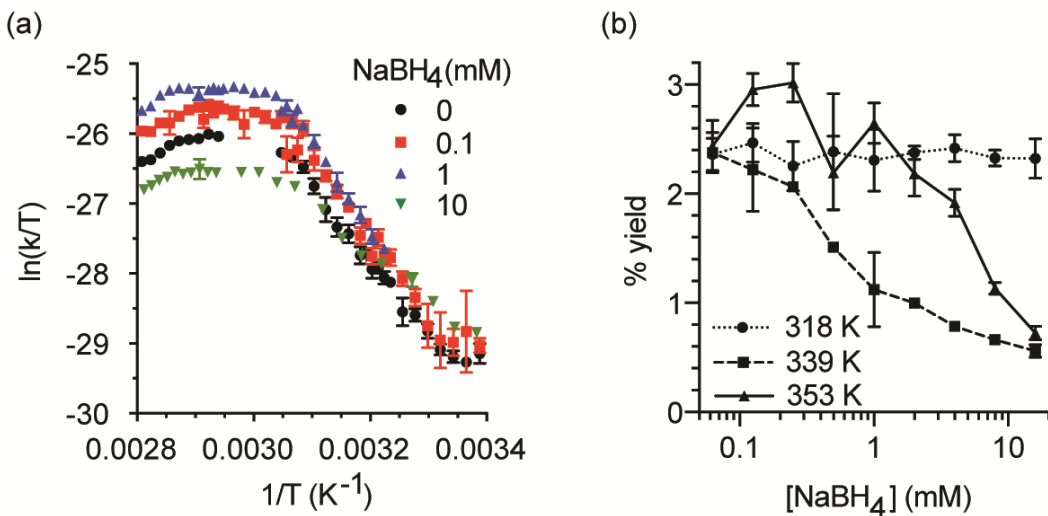


Figure 7. Various NaBH₄ concentrations. (a) Eyring plots. Conditions: 9.4 nM Pd(NO₃)₂, 120 μM TFP, 0–10 mM NaBH₄, 5% v/v DMSO/1.2 M phosphate pH 7 buffer, 293–358 K, 30 min, $n = 5$. (b) NaBH₄-

concentration-dependence. Conditions: 0–16 mM NaBH₄, 12.5 μM APE, 60 μM TFP, 10 nM Pd(NO₃)₂, 5% v/v DMSO/1.2 M phosphate pH 7 buffer, 60 min, *n* = 3. Reprinted (adapted) with permission from *ACS Catal.* 2019, 9, 11720–11733. Copyright 2019 American Chemical Society.

1.6.6 Effect of Palladium Concentration

Fluorescence was measured at 0–9.4 nM palladium concentrations (Figure 8a). The yields after 30 min under three regimes were linearly proportional to palladium concentration (i.e., first order with respect to palladium concentration), indicating that catalytically active palladium species involved in TLSs are most likely monomeric. However, we acknowledge that the current high throughput protocol is not compatible with the measurement of product formation with higher concentrations of palladium; with more palladium, non-linear behavior may be observed.

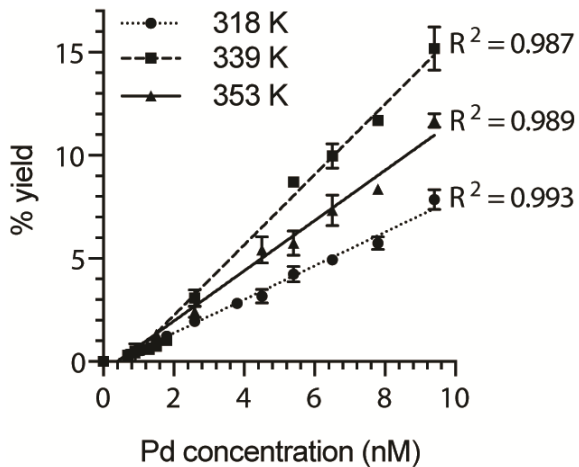


Figure 8. Palladium concentration dependence. Conditions: 0–9.4 nM Pd(NO₃)₂, 10 mM NaBH₄, 12.5 μM APE, 60 μM TFP, 5% v/v DMSO/1.2 M phosphate pH 7 buffer, 30 min, *n* = 4. Reprinted (adapted) with permission from *ACS Catal.* 2019, 9, 11720–11733. Copyright 2019 American Chemical Society.

1.6.7 Effect of Substrate Concentration

The rate of the reaction was investigated at different APE concentrations (3–48 μM) (Figure 9a and Figure 9b). The substrate concentration was linearly correlated with the % yield under all regimes, suggesting that all the TLSs involve the substrate in the transition state as the general catalytic cycle indicates. It is possible that the linearity may be limited to the 3–48 μM APE range, because Michaelis-Menten kinetics are still plausible at higher concentrations.⁹⁵ Unfortunately, the APE concentration range could not be broadened under the current conditions with 5% DMSO due to limited solubility.

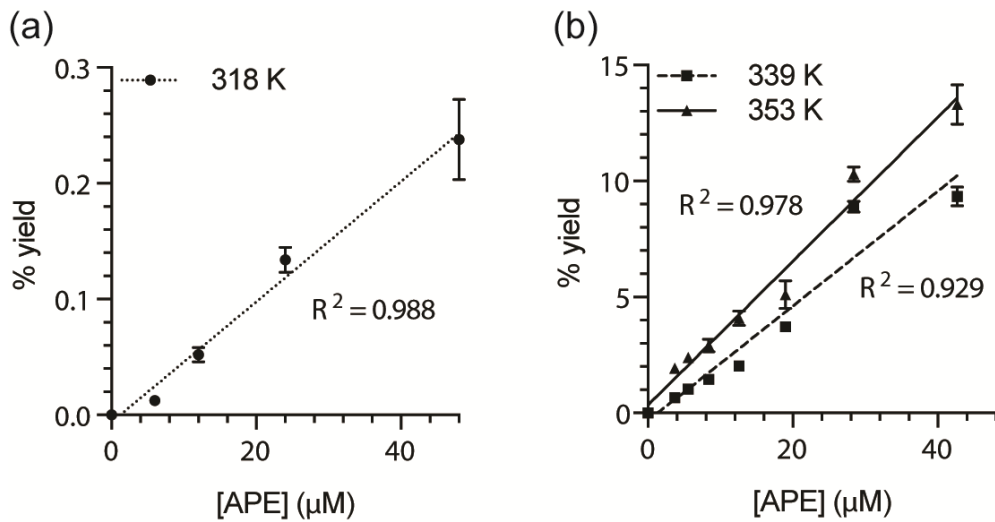


Figure 9. APE concentration dependence. Conditions: 3–48 μM APE, 10 nM $\text{Pd}(\text{NO}_3)_2$, 10 mM NaBH_4 , 60 μM TFP, 5% v/v DMSO/1.23 M phosphate pH 7 buffer, 60 min, $n = 4$. Reprinted (adapted) with permission from *ACS Catal.* 2019, 9, 11720–11733. Copyright 2019 American Chemical Society.

1.6.8 Effect of DMSO Concentration

DMSO has been used as a co-solvent in aqueous palladium-catalyzed reactions to solubilize hydrophobic reactants.^{54, 96} Because DMSO could bind to palladium,⁹⁷⁻⁹⁸ we wondered whether DMSO could impact the deallylation rate. Figure 10a shows the benchmark Eyring plot with 12.5 μM APE in 5% DMSO. When 10% DMSO was used instead, regime 2 disappeared. The arrows indicate that DMSO decelerates and accelerates the deallylation above and below the first T_{inv} , respectively.

We titrated DMSO under regime 1 (318K), regime 2 (339K), and regime 3 (353K) with 12.5 μM APE (Figure 10b). Generally, high DMSO concentrations slowed the kinetics of deallylation under all regimes. Regime 2 was the most sensitive to DMSO concentration, with the optimal concentration of 2%. The positive correlation with up to 2% DMSO in regime 2 may require further studies to understand. Nonetheless, these results suggest that regime 2 is probably not a transition between regimes 1 and 3. Figure 10c summarizes the findings in Figure 10a and Figure 10b.

If DMSO acts as a ligand in the current system, the optimal concentrations of TFP should be higher with more DMSO. Indeed, this was the case in regime 1 (Figure 10d), indicating that DMSO may act as a competitive ligand in the oxidative addition step to reversibly generate a resting species. The rate of deallylation for regimes 2 and 3 (Figure 10e and Figure 10f) was very slow with 10% DMSO, making it difficult to determine the optimal TFP concentration. With 5% DMSO, the rate of the reaction started to decline as TFP concentration reached 200 μM at both 339 and 353 K. No decline in reactivity was observed with 2.5% DMSO at these temperatures. At this point, the role of DMSO in regimes 2 and 3 is not clear.

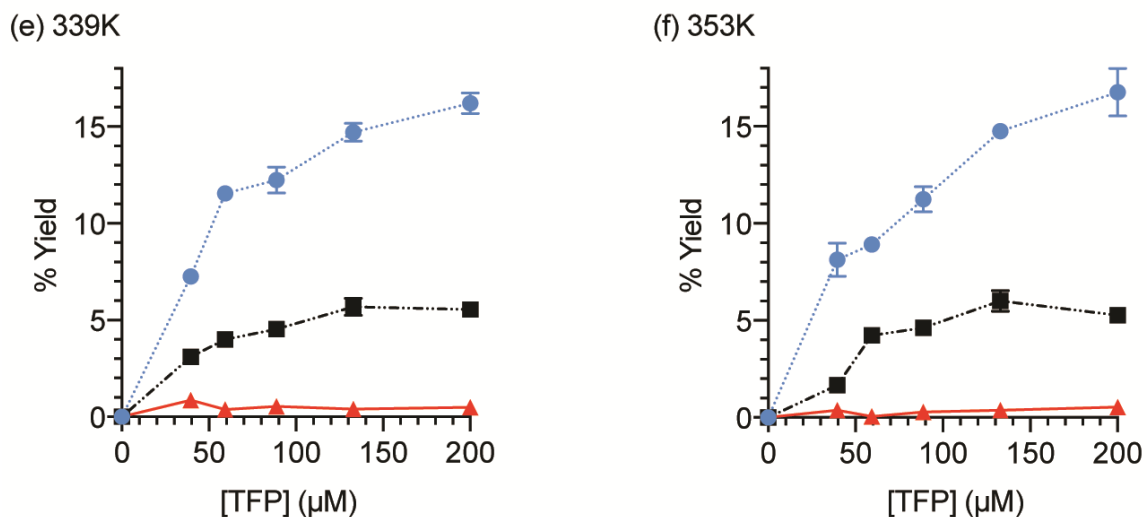
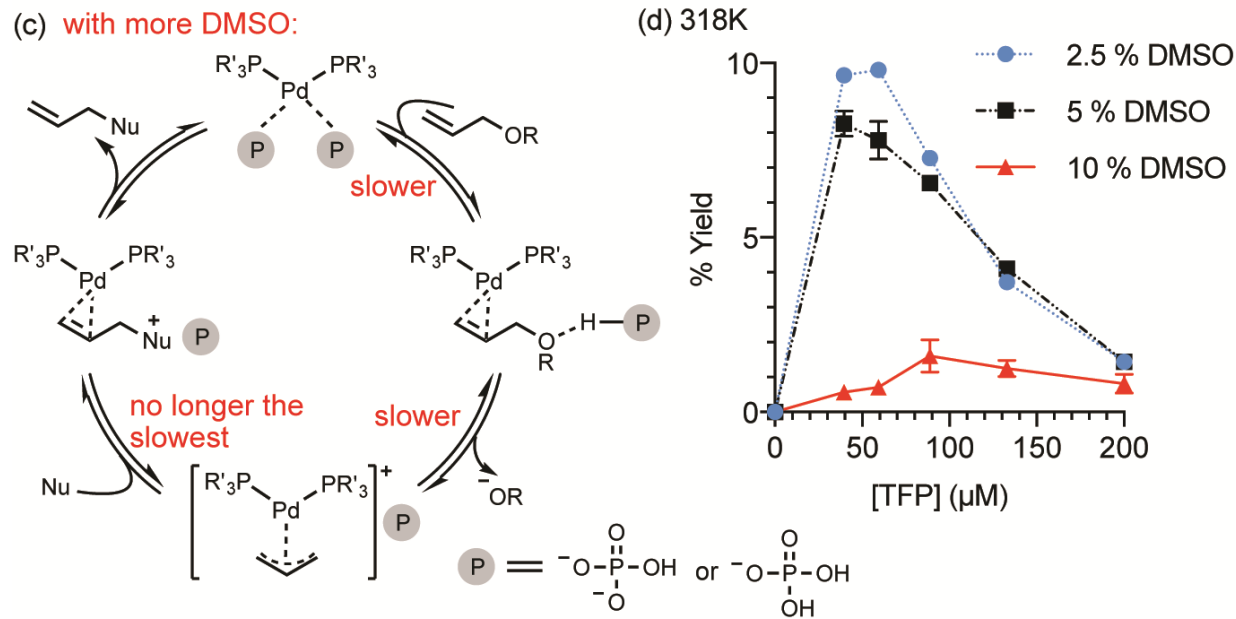
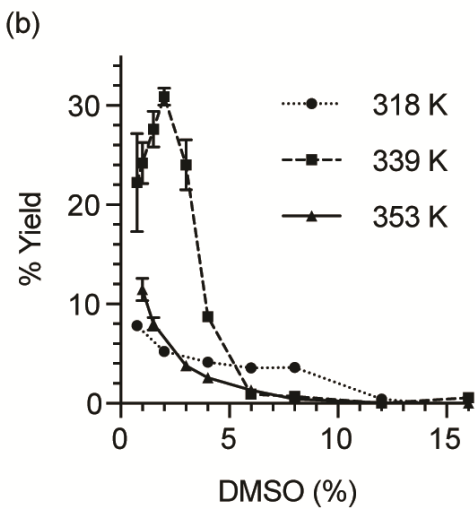
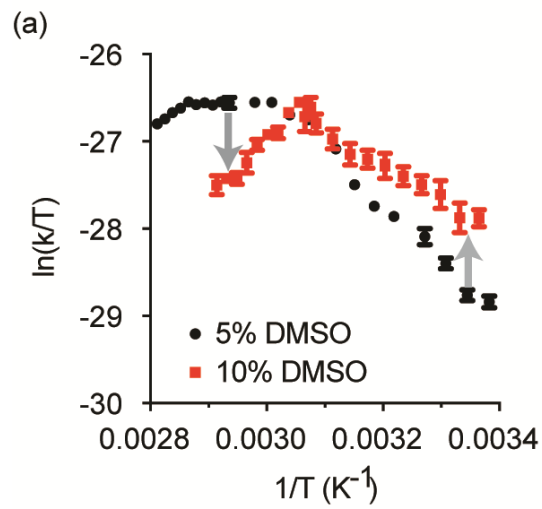


Figure 10. Various DMSO concentrations. (a) 9.4 nM Pd(NO₃)₂, 12.5 μM APE, 120 μM TFP, 10 mM NaBH₄, 5% v/v DMSO/1.2 M phosphate pH 7 buffer, 293–358 K, *n* = 3 or 5. (b) Conditions: 0.75–16% v/v DMSO/1.2 M phosphate pH 7 buffer, 10 mM NaBH₄, 12.5 μM APE, 60 μM TFP, 10 nM Pd(NO₃)₂, 60 min, *n* = 4. (c) Summary of the DMSO impact. Effect of DMSO on TFP-palladium binding. (d-f) Conditions: 0–200 μM TFP, 10 nM Pd(NO₃)₂, 10 mM NaBH₄, 10 μM APE, 2.5–10% v/v DMSO/1.1 M phosphate pH 7 buffer, 30 min. *n* = 3. Reprinted (adapted) with permission from *ACS Catal.* 2019, **9**, 11720–11733. Copyright 2019

American Chemical Society.

How does the higher concentration of DMSO decelerate the TLS of regime 3 by increasing the entropic penalty, as indicated by the arrow in Figure 10a? Our working hypothesis is that the alkene substrate and the catalyst may be more solvated by DMSO, requiring a greater loss of entropy to associate with each other.^{99–100} Although DMSO accelerates the η¹-η³ isomerization in a phosphine-free system,¹⁰¹ it is not clear whether the phosphine-free system is relevant to the current system. Regardless, this result indicates that a rational approach toward accelerating bioorthogonal Tsuji-Trost reaction may be to minimize solvation of substrates and catalysts, for example, by exploiting hydrophobic effects, to facilitate the association of the two species under highly diluted conditions.

1.6.9 Competition Experiment

If the association of palladium species to the olefin is the slowest step in the catalytic cycle under regime 3, the presence of an external alkene should compete for the palladium, retarding the reaction. Based on this hypothesis, competition experiments under regimes 1, 2, and 3 were performed (Figure 11) with 12.5 μM APE in presence and absence of 12.5 μM phenyl allyl ether.

No change in fluorescence was observed under regimes 1 and 2 upon addition of the external alkene. Under regime 3, however, the rate of the reaction decreased by half in presence of the alkene. These results support our hypothesis that the association is the TLS in regime 3.

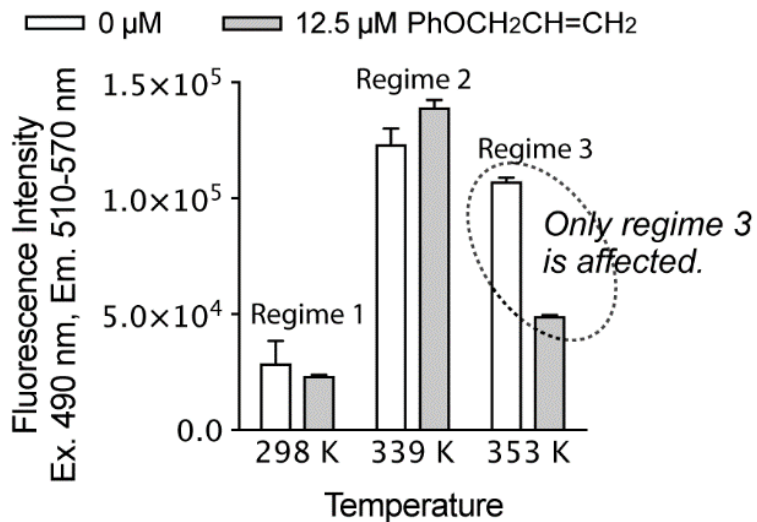


Figure 11. Competition experiments with APE and external alkene. Conditions: 0 or 12.5 μM phenyl allyl ether, 12.5 μM APE, 9.4 nM $\text{Pd}(\text{NO}_3)_2$, 120 μM TFP, 10 mM NaBH_4 , 5 % DMSO/1.23 M phosphate pH 7 buffer, $n = 3$, 30 min. Reprinted (adapted) with permission from *ACS Catal.* 2019, 9, 11720–11733. Copyright 2019 American Chemical Society.

1.6.10 Identification of the Nucleophile

To model the reaction with density functional theory (DFT) calculations, we needed to identify the nucleophile of the reaction. Previous investigations revealed that the phosphate ions were not the nucleophile.⁵⁸ Spurred on by this, a reaction mixture was analyzed by LC-MS. A peak corresponding to P-allylated TFP (Figure 12) was found, indicating that TFP is the primary nucleophile. This is similar to the precedence in the literature, in which Ph_3P was allylated under

Tsuji-Trost reaction conditions.¹⁰² As such, we further investigated TFP as the reaction nucleophile through decreasing both APE and TFP simultaneously to mimic reaction progress (Figure 13). The “same excess” models¹⁰³⁻¹⁰⁵ would afford a single line if the TFP is acting as the nucleophile. In effect, each decreasing concentration of APE was paired with the equally lower concentration of TFP to mimic the reaction progressing under the assumption that TFP is the only nucleophile. If TFP is not consumed, the reactions with 60, 50, and 40 μM TFP would show different rates as indicated by Figure 4b. Further increasing the TFP concentration (120, 110, or 100 μM) at the same APE concentrations afforded the same effect as shown in Figure 4b.

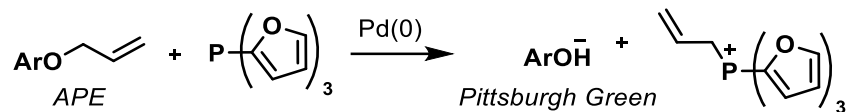


Figure 12. Formation of P-allyl TFP.

In the same-excess experiments, we found that unlike the kinetic data in Figure 1, the reaction continued at the same rate instead of slowing down over time (Figure 13). To investigate this seemingly contradictory result, we prepared an Eyring plot with the increased $\text{Pd}(\text{NO}_3)_2$ concentrations (3.6 μM instead of 9.4 nM; Figure 14). The higher $\text{Pd}(\text{NO}_3)_2$ concentration eliminated regime 3 at high temperatures, because the 400-fold higher concentration of palladium would lower the entropic penalty for the alkene association. It is noteworthy that the higher palladium concentration increased the ΔH^\ddagger value from 55 ± 2 to 94 ± 2 kJ mol⁻¹ in the 293–326K range.

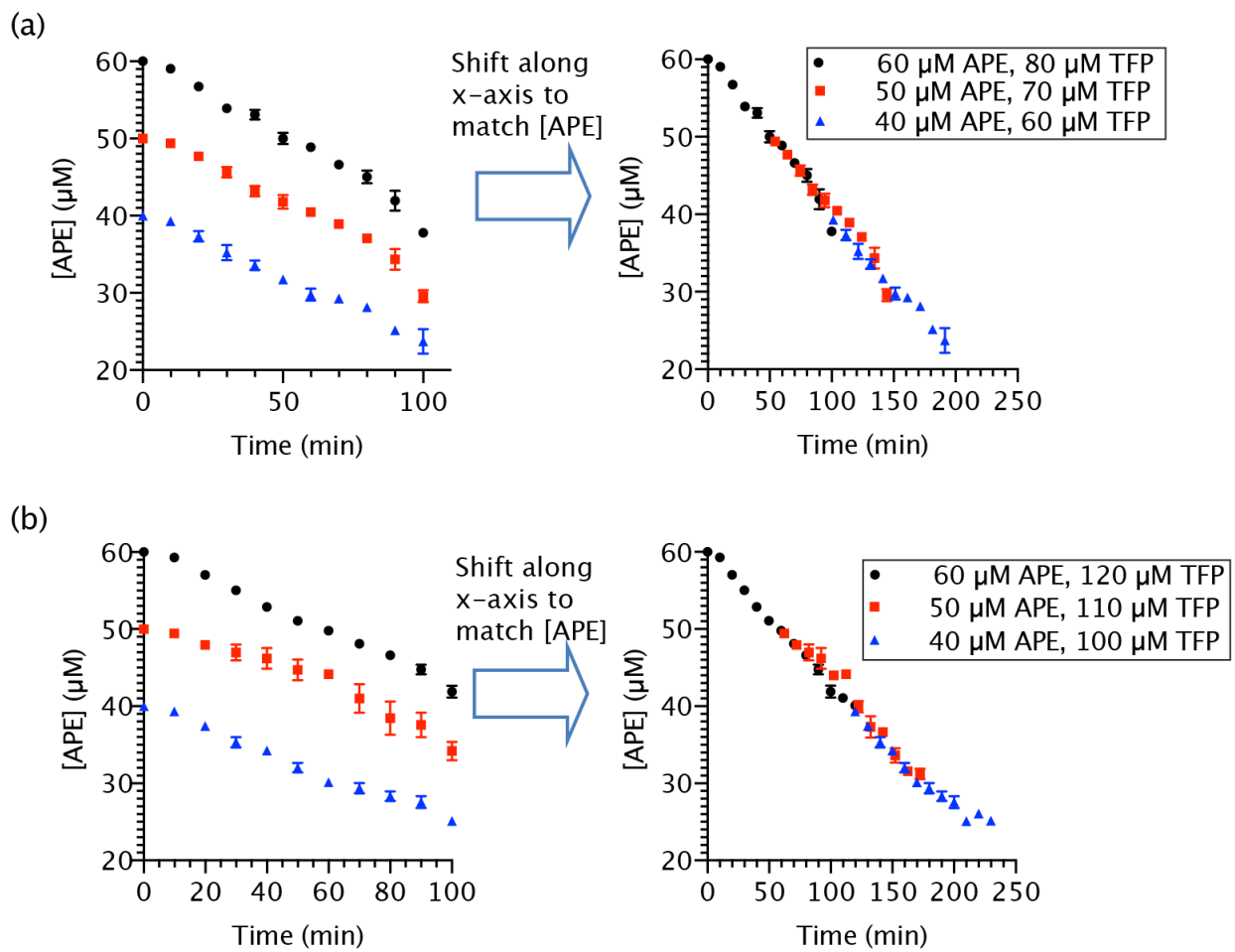


Figure 13. Same excess experiments with TFP. On right, graphs are adjusted to match concentration of APE at given time points. Reprinted (adapted) with permission from *ACS Catal.* 2019, 9, 11720–11733. Copyright 2019 American Chemical Society.

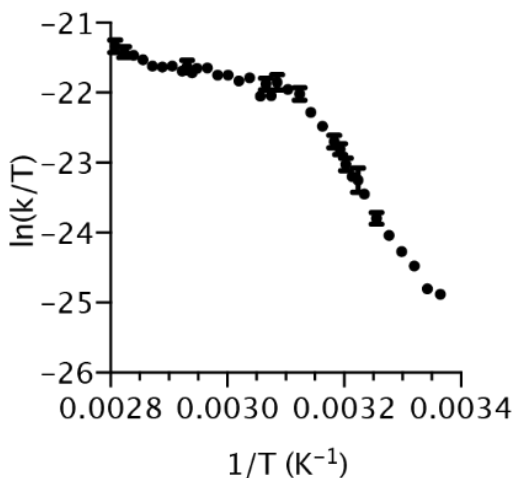


Figure 14. Eyring plot with increased palladium. Conditions: 3.6 μM Pd $\text{Pd}(\text{NO}_3)_2$, 12.5 μM APE, 120 μM TFP, 10 mM NaBH_4 , 5% v/v DMSO/1.23 M phosphate pH 7 buffer, 295–357 K, 30 min, $n = 4$ or 5. Reprinted (adapted) with permission from *ACS Catal.* 2019, 9, 11720–11733. Copyright 2019 American Chemical Society.

1.6.11 Density Functional Theory Calculations

DFT calculations were performed to provide further insights into the TLSs of the palladium-catalyzed deallylation reaction (for previous computational studies of Tsuji-Trost-type reactions, see the cited references^{91, 106–109}). The activation enthalpies and entropies of three key steps of the reaction of allyl phenyl ether with the $\text{Pd}(\text{TFP})_2$ catalyst were calculated using Gaussian 09.¹¹⁰ The calculations were performed using B3LYP/LANL2DZ–6-31G(d) for geometry optimization and M06/SDD–6-311+G(d,p) for single point energy calculations. Thermal corrections to the enthalpies and entropies were calculated using the gas-phase harmonic vibrational frequencies at 298K. Solvation effects were taken into account in the single point energy calculations using the SMD solvation model¹¹¹ and water as the solvent. A few possible

nucleophiles were considered in the DFT calculations, including TFP, H_2PO_4^- , and OH^- . Among all the nucleophiles considered in the calculations, TFP has the lowest computed activation Gibbs free energies for the nucleophilic attack of the palladium-allyl intermediate (Figure 15), in agreement with the aforementioned experiments. The computed gas-phase ΔS^\ddagger values are expected to have large deviations from experimental data,¹¹² though the computed activation enthalpies (ΔH^\ddagger) of the three key steps in the catalytic cycle shed light on the experimentally proposed TLSs at different temperatures.

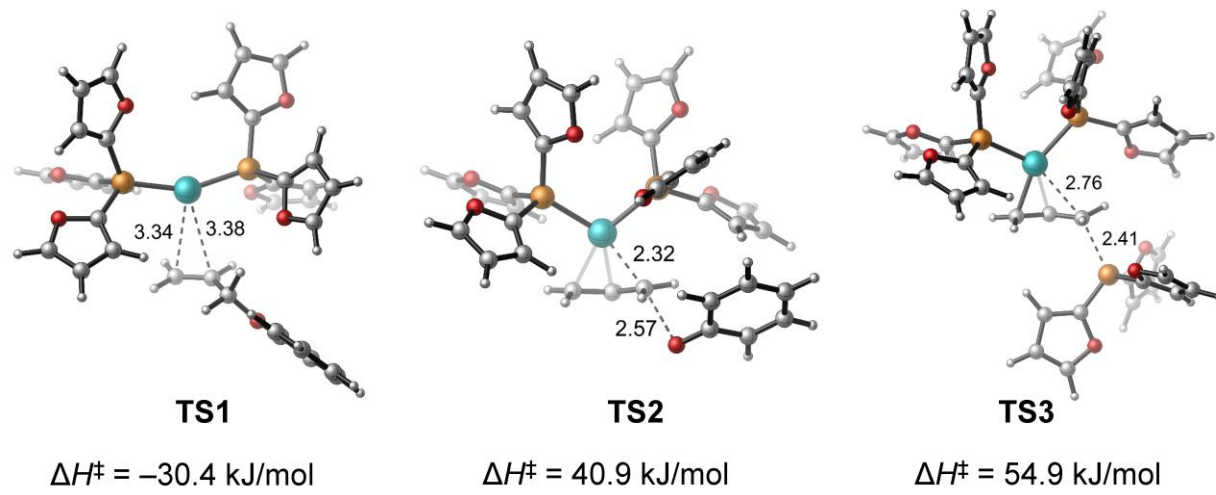


Figure 15. Optimized structures and activation energies of the transition states of allyl association (TS1), oxidative addition (TS2), and nucleophilic attack (TS3). The computed ΔH^\ddagger of TS1, TS2, and TS3 are with respect to Pd-1, Pd-2, and Pd-3, respectively (see Scheme 3). Reprinted (adapted) with permission from ACS Catal. 2019, 9, 11720–11733. Copyright 2019 American Chemical Society.

DFT calculations indicated that the allyl association step (**TS1**) is the most favorable enthalpically with a negative ΔH^\ddagger ($-30.4 \text{ kJ mol}^{-1}$), supporting the proposed assignment for the TLS of regime 3 (Figure 15). Here, the activation enthalpy is calculated with respect to the separate reactants (the two coordinated $\text{Pd}(\text{TFP})_2$ catalyst, **Pd-1**, and the allyl phenyl ether). The negative

activation enthalpy for this step is due to the exothermic formation of a van der Waals complex prior to the allyl association transition state (**TS1**) (see below for detailed discussions). The computed ΔH^\ddagger of the oxidative addition step (**TS2**, 40.9 kJ mol⁻¹) is in reasonable agreement with the experimental value of 55±2 kJ mol⁻¹ measured at 293-326K (regime 1). The nucleophilic attack of the palladium-allyl complex by TFP (**TS3**) occurs via theoutersphere pathway (Figure 15). The DFT calculations significantly overestimated the ΔH^\ddagger of the nucleophilic attack (54.9 kJ mol⁻¹), compared to the experimental ΔH^\ddagger in regime 2 (326-347K). The difference between the computational and experimental values is possibly due to the challenges of calculating solvation effects of the cationic palladium-allyl species,¹¹³ as the DFT calculations and the experiments were performed in different media (water vs. phosphate buffer) and the effects of the counter anion were not considered in the calculations. Taken together, the computational results support the hypothesis that three different TLSs are operating at different temperatures, although quantitative prediction of ΔH^\ddagger in phosphate buffer solution remains challenging.

1.6.12 Detailed Mechanism of Allyl Association

The computed energy profile of the association of the allyl phenyl ether to the Pd(0)(TFP)₂ complex (**Pd-1**) to form the π complex (**Pd-2**) is shown in Figure 16. The reaction first forms van der Waals (vdW) complex **Pd-2a**, which is 37.0 kJ mol⁻¹ more stable than the separate reactants (**Pd-1** and allyl phenyl ether) in terms of enthalpies. Due to entropic effects, this vdW complex is less stable than the separate reactants in terms of Gibbs free energies. It should be noted that under the low concentrations in the present experimental study, formation of the vdW complex is expected to be even less favorable. Thus, the resting state before the allyl association should be the separate reactants (**Pd-1** and allyl phenyl ether), rather than the vdW complex **Pd-2a**. From the

vdW complex, the association of the double bond in the allyl phenyl ether to the palladium to form the π complex **Pd-2** occurs via **TS1**. The enthalpy of **TS1** is 6.6 kJ mol^{-1} higher than that of the vdW complex and is 30.4 kJ mol^{-1} lower than that of the resting state (**Pd-1**). Thus, the overall enthalpy of activation of allyl association from **Pd-1** to **TS1** is negative ($\Delta H^\ddagger = -30.4 \text{ kJ mol}^{-1}$).

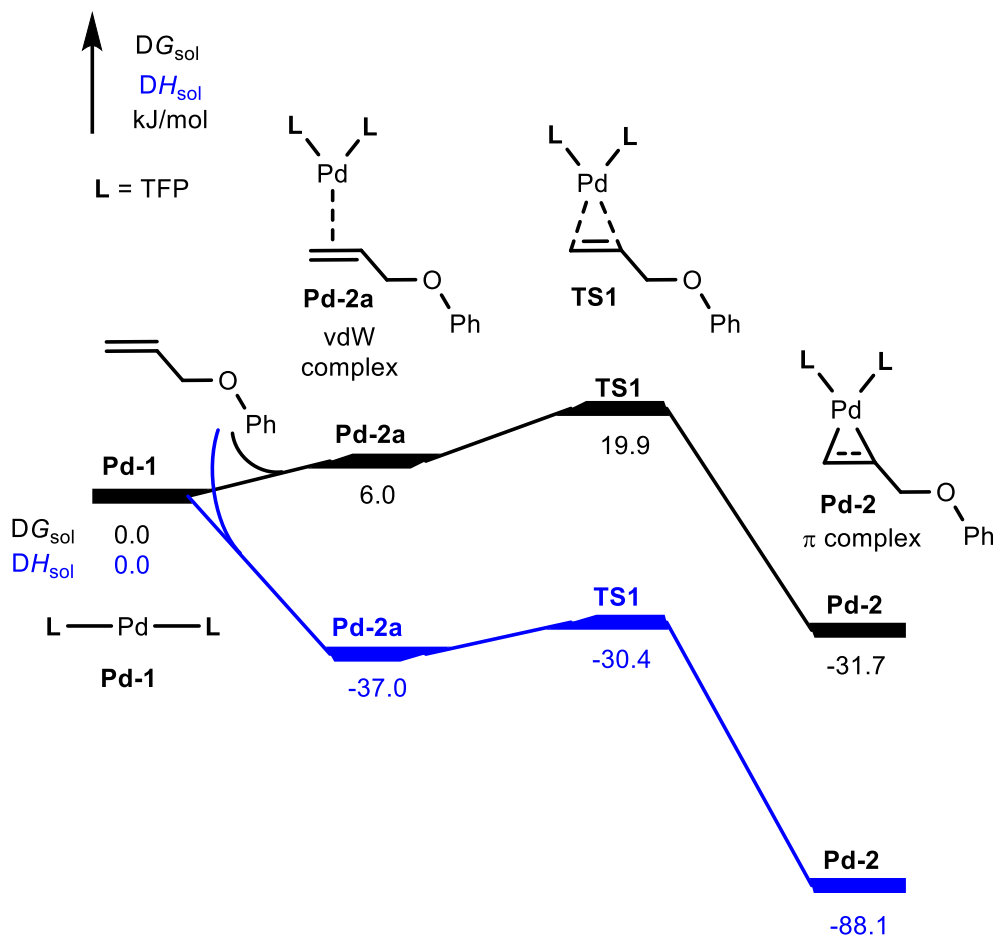


Figure 16. The computed energy profile of the association of the allyl phenyl ether to the $(\text{TFP})_2\text{Pd}(0)$ complex (**Pd-1**) to form the π complex (**Pd-2**). Reprinted (adapted) with permission from *ACS Catal.* 2019, 9, 11720–11733. Copyright 2019 American Chemical Society.

1.7 Conclusions

The sensitive and high throughput fluorometric method allowed for measuring the activation enthalpy energies at micromolar concentrations of the substrate. The TLS was found to depend on the substrate concentration and the temperature (Figure 17a). Three regimes were observed at low substrate concentration (Figure 17b). The associated TLSs were assigned as the oxidative addition (regime 1; $\Delta H^\ddagger > 0$), nucleophilic attack (regime 2; $\Delta H^\ddagger \sim 0$), and association (regime 3; $\Delta H^\ddagger < 0$). It is possible that regime 2 is a transition between regime 1 and regime 3, although our data support the existence of regime 2. The generality of the current findings must be examined in the future with other substrates and phosphines. Nonetheless, this work may provide kinetic insights into Tsuji-Trost reactions under biological or analytical conditions. For example, with a substrate and palladium at low micromolar to nanomolar concentrations, the TLS may be the association step. More broadly, the trend depicted in Figure 3b indicates that the kinetic profile can change from regime 1 to regime 2 and even to regime 3 as the substrate is consumed. It also suggests that the reaction may proceed in different regimes at different temperatures. Thus, a blueprint for developing a faster allylic C-O bond cleavage may be to determine the regime under which the reaction operates in order to rationally optimize the reaction conditions accordingly.

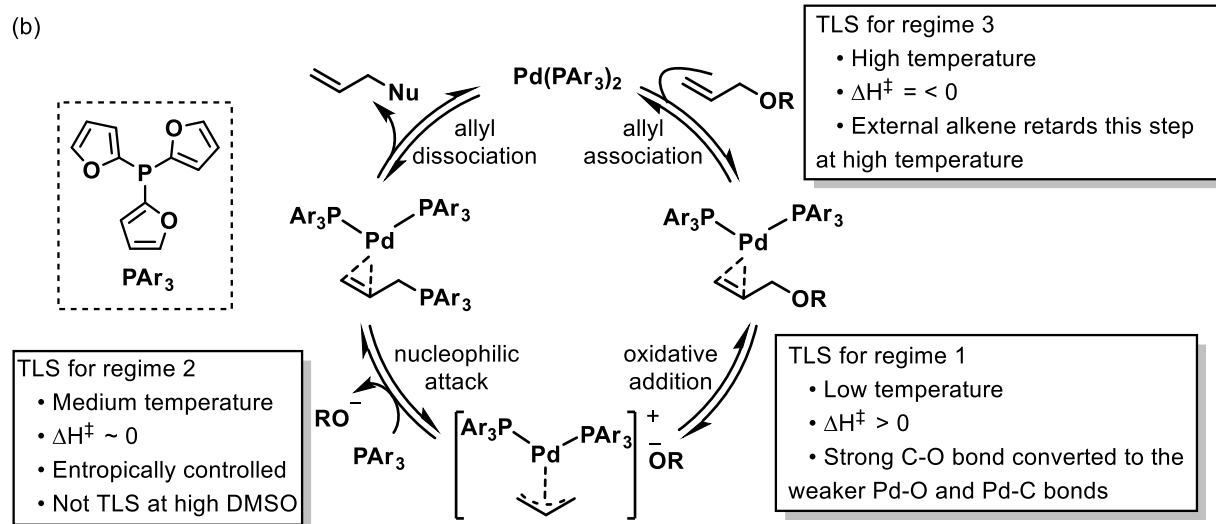
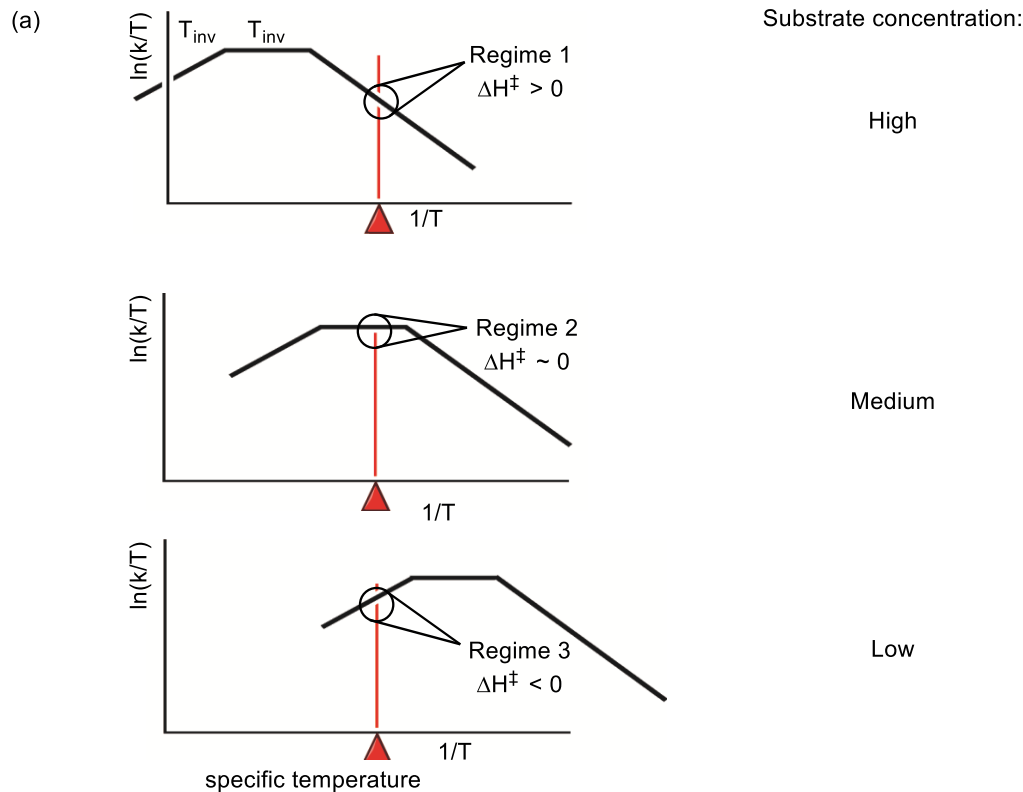


Figure 17. Summary of chapter 1. (a) TLS dependence on the substrate concentration. (b) Catalytic cycle with proposed TLSs and evidence to support it.

2.0 Development of Ligand-Accelerated Clip Reactions

2.1 Transition-metal-catalyzed bioorthogonal reactions

Transition metal catalysis is widely used in organic synthesis,¹¹⁴⁻¹¹⁵ but it lags behind in chemical biology. This could be due to the notion that metal reagents are deactivated by water, air, and components in biological media, such as glutathione (GSH), thiol-containing proteins, nucleobases, etc.¹¹⁶ Recently, a growing number of transition metal catalysts have been shown to be compatible with aqueous conditions,⁴² leading to metal-mediated bioorthogonal reaction development. This, however, proved to be challenging because reactions must be fast and inert towards a multitude of competing functionalities.¹¹⁶ Applying these reactions to the living setting adds more complexity because the transition metals must be active under dilute conditions, be nontoxic, and cell-permeable.^{42, 117-119}

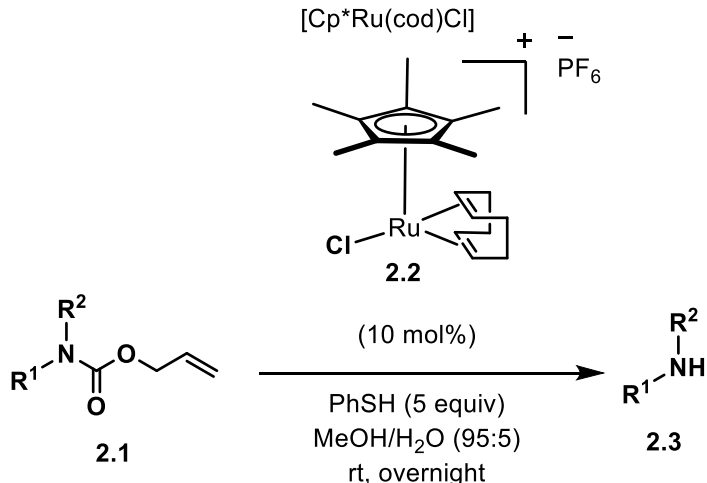
The copper (Cu)-catalyzed bioorthogonal ligation, independently discovered by the groups of Sharpless and Meldal,¹²⁰⁻¹²³ is a representative transition metal-catalyzed bioorthogonal reaction.¹²⁴ This reaction has not been widely applied in living systems due to the toxicity of copper ions and has predominately been used to label in the extracellular space. This discovery led to many attempts to uncover other bioorthogonal transition metal-mediated reactions, which expanded the toolbox for selective cleavage of covalent bonds, also referred to as clip reactions.¹²⁵ In such transformations, a masked group can be converted into active functionality in a presence of a transition metal catalyst. The catalyst and the protecting group must be orthogonal and inert to other functional groups present in the reaction media. It holds great potential for many applications in medicine and chemical biology, including triggered drug release and biomolecule

uncaging. However, transitioning this chemistry to living cells has been very difficult due to intrinsic toxicities associated with these metals and because biomolecules such as thiols and amines are known to poison transition metal catalysts.¹¹⁶ Nevertheless, transition metals, such as ruthenium (Ru), platinum (Pt), gold (Au), and palladium have been used for biological applications. This section will discuss the emergence of transition metal-catalyzed clipping reactions and how careful ligand fine-tuning can reduce the toxicity and the deactivation of catalysts.¹²⁶⁻¹²⁸

2.1.1 Ruthenium-catalyzed cleavage reactions

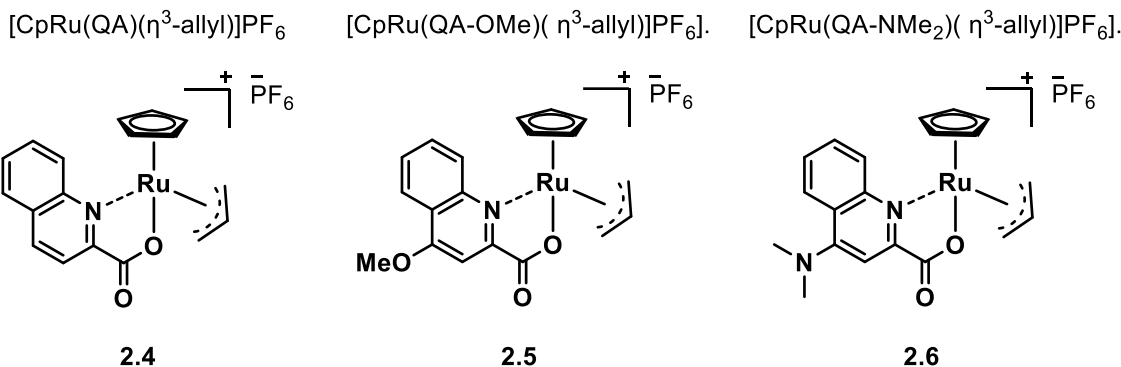
Ruthenium-catalyzed deallylation reactions are one of the most explored metal-catalyzed clip reaction to date. The Meggers group pioneered this work, producing a variety of ruthenium complexes that are efficient and stable under biological conditions (presence of water, air, and thiols) and inside living HeLa cells.¹²⁹ Their reported ruthenium complex, $[\text{Cp}^*\text{Ru}(\text{cod})\text{-Cl}]$ ($\text{Cp}^* = \eta^5\text{-pentamethylcyclopentadienyl}$, $\text{cod} = \eta^4\text{-1,5-cyclooctadiene}$) **2.2**, catalyzed the cleavage of various allyl carbamates **2.1** to their respective amines **2.3**. (Scheme 14). The catalyst was stable to both water and air at room temperature. However, this method suffered from low efficiency (turnover number (TON) = 4), long reaction times, and required the addition of toxic thiophenols, which act as nucleophiles. The addition of an external nucleophile was especially necessary at room temperature. Additionally, the catalyst was reported to be quickly deactivated (within less than 30 minutes) in the presence of cell extract and glutathione. Nonetheless, the catalyst was able to facilitate the reaction in HeLa cells in PBS buffer. This deprotection was found to be quite

general as it worked for electron-rich or electron-poor substrates and with primary or secondary amines.



Scheme 14. Meggers $[\text{Cp}^*\text{Ru}(\text{cod})\text{Cl}]$ ruthenium catalyst.

In 2014, the Meggers group was able to overcome the dependence on thiophenol and broaden the application.¹³⁰ Ruthenium half-sandwich complexes that are known to be efficient Tsuji–Trost catalysts were screened. Kitamura's type of ruthenium catalysts containing quinoline ligands, $[\text{CpRu}(\text{QA})(\eta^3\text{-allyl})]\text{PF}_6$ (cp = cyclopentadienyl, QA = 2-quinolinicarboxylate) **2.4**, provided full conversion in 3 hours (Scheme 15). Homologous Cp^* and 2-pyridinecarboxylato (PA) derivatives of **2.4**, which were reported to catalyze S-allylation reactions, were also screened, however, catalyst **2.4** was found to be superior under the reaction conditions.

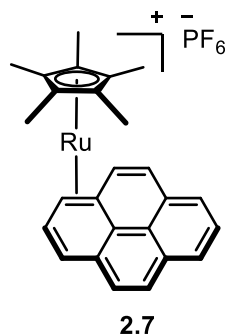
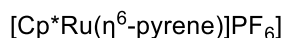


Scheme 15. New Meggers' ruthenium catalysts.

It was postulated that the reduced reactivity of the Cp^* complexes was due to steric hindrance introduced by the five methyl groups.¹³⁰ It was also hypothesized that fast deactivation of the catalyst was due to the π -accepting ability of the bidentate ligand. Indeed, catalytic activity was further improved by reducing the π backbonding of the bidentate ligand. The efficiency of the reaction was improved by introducing π -donating substituents, such as methoxy (**2.5**) or dimethylamino (**2.6**) groups onto the quinoline ligand (Scheme 15); (TON of 90, 150, and 270 was reported for **2.4**, **2.5**, and **2.6**, respectively). The application of this catalytic system was shown via successful deprotection of a fluorescent probe in HeLa cells. It is not clear if the imaging experiments were done in PBS buffer or DMEM with FBS.

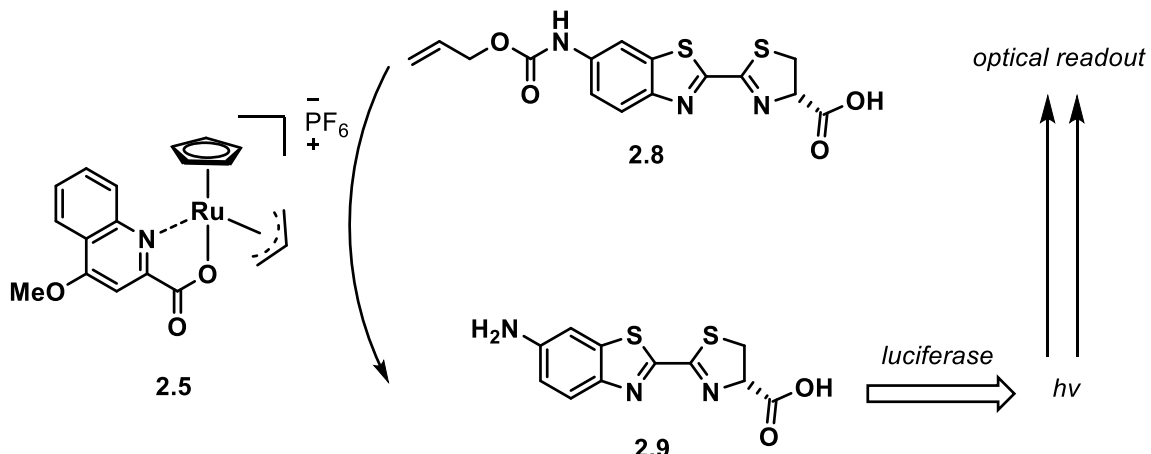
Furthermore, photoactivatable version $[\text{Cp}^*\text{Ru}(\eta^6\text{-pyrene})]\text{PF}_6$ **2.7** was developed, which enabled spatial and temporal control (Scheme 16).¹³¹ These $\text{Ru}(\eta^6\text{-arene})$ sandwich complexes are solvent-coordinated catalysts $[\text{Cp}^*\text{Ru}(\text{solvent})_3]^+$ capable of catalyzing various transformations. The pre-catalyst is known to be photochemically labile and can be activated upon irradiation with $\lambda \geq 330 \text{ nm}$ for 5 min. This released method still required nucleophilic thiols; a correlation between the % yield and the nucleophilicity of the thiol was observed. The toxic thiophenol was replaced with glutathione; the glutathione present in cells was strong enough to promote the turnover in the

catalytic process eliminating the need for external nucleophile. Zeroth order rate was reported with respect to glutathione, indicating that it does not diminish the activity of the ruthenium catalyst. Cell imaging experiments showed that ruthenium sandwich complex was membrane permeable and could be successfully activated to catalyze deallylation.



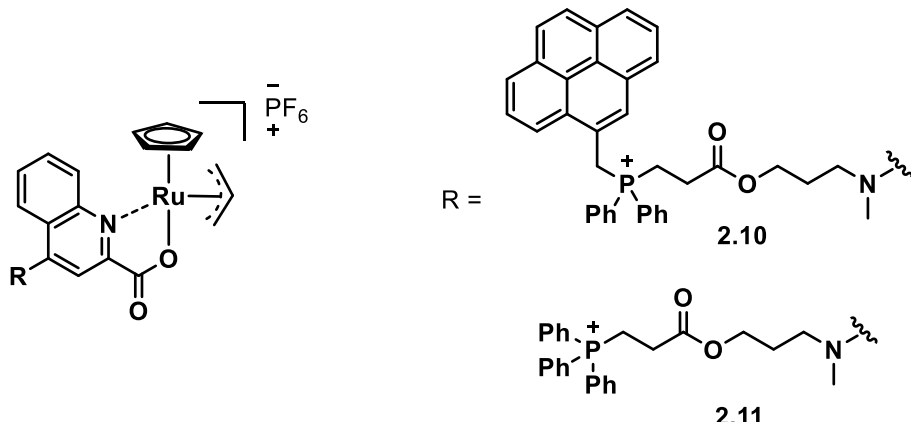
Scheme 16. Photoactivatable Meggers catalyst.

The Wender and Waymouth groups reported a biocompatible system using ruthenium complex **2.5** (Scheme 17).¹³² Here, ruthenium catalyst activated alloc-protected aminoluciferin (**2.8**), a bioluminescence pro-probe and released the active luminophore (**2.9**), aminoluciferin, in the presence of luciferase-transfected cells. Upon release of the probe, this system provided for “turn on” bioluminescence, which resulted in better signal-to-background ratios and real-time evaluation of the catalytic activity. The system allowed for high throughput screening in cells suspended in PBS buffer. The catalyst lacked cell permeability and resided preferentially on the 4T1 cell membrane or in the extracellular space. Detailed investigation showed that the presence of thiols was critical for high reactivity and selectivity.



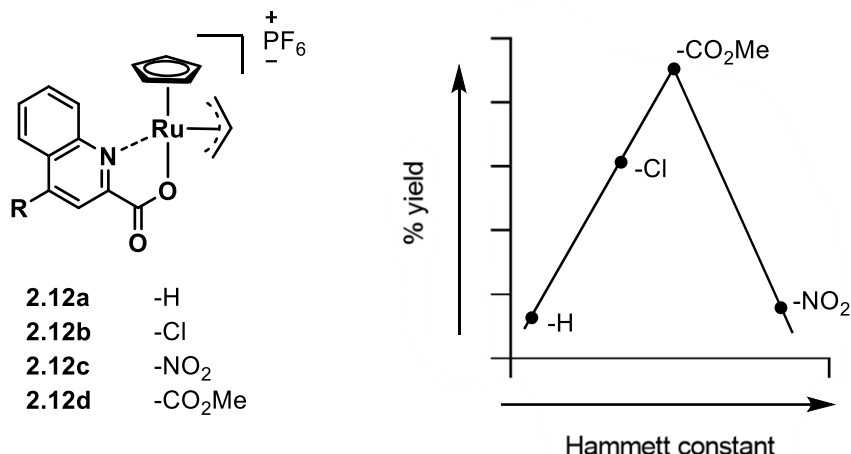
Scheme 17. Biocompatible ruthenium system.

The Mascareñas group showed that Kitamura's ruthenium complexes can be engineered to target certain cellular compartments (Scheme 18).¹²⁷ An introduction of triphenylphosphonium derivative **2.11**, which exhibits a single positive charge, resonance-stabilized over three phenyl groups, and a large hydrophobic surface area, led to accumulation in mitochondria. Accumulation of these cations was driven by the membrane potential across the mitochondrial inner membrane. The QC ligand was conjugated to triphenylphosphonium through a relatively hydrophobic alkyl chain. Modified ruthenium complexes **2.10** and **2.11** were inferior to previously reported ruthenium catalysts, likely due to sterics and poor solubility. However, these new analogs had better intracellular retention compared to catalysts described in the section above and were able to accumulate in mitochondria to facilitate the decaging reaction. It should also be noted that cell imaging experiments were performed in DMEM with serum. Additionally, **2.11** was the first reported non-toxic ruthenium complex.



Scheme 18. Mascareñas' mitochondria specific ruthenium catalysts.

The Volker and Meggers groups further improved upon their ruthenium complex containing quinoline ligands **2.4–2.6** shown in Scheme 15. It has been previously shown that higher electron density at the ruthenium center was important for catalytic activity.¹²⁸ Since there was no way to increase electron density at the metal center, new substituents were added to the quinoline-2-carboxylato ligand **2.12a–d** (Scheme 19). The data were analyzed by plotting the uncaging reaction yield against the Hammett constants. The reactivity-structure analysis revealed that mildly electronegative ruthenium complex **2.12d** (Scheme 19) increased the efficiency of the reaction. This study shows that the suitable electronic density on the metal center is required for maximum activity. The new generation ruthenium complex exhibited increased stability and catalytic potential in blood serum (30% yield). TON of >300 was achieved, with a reaction rate of 580 M⁻¹s⁻¹ in phosphate buffer. This study showed that electronic properties must be considered when designing organometallic catalysts.



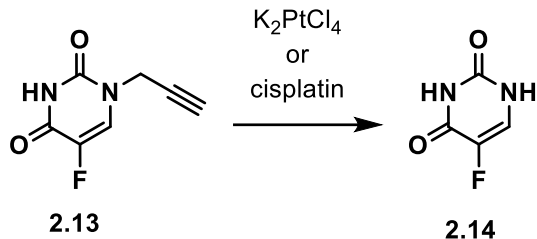
Scheme 19. Serum stable Meggers catalyst.

2.1.2 Platinum-catalyzed cleavage reactions

Platinum has been extensively used for catalysis,¹³³ but has not been used much in chemical biology due to intrinsic toxicity. Cisplatin is used in the clinic to treat cancer.¹³⁴⁻¹³⁶ Thus, platinum might have a lot of potential as a catalyst for click reactions in the context of cancer treatment (uncaging of cancer prodrugs). Cisplatin is very reactive (half-life of 30 hours),¹³⁷⁻¹³⁸ accumulates in tumors, and not present in human biology, making it a good candidate for bioorthogonal chemistry.¹³⁹⁻¹⁴⁰

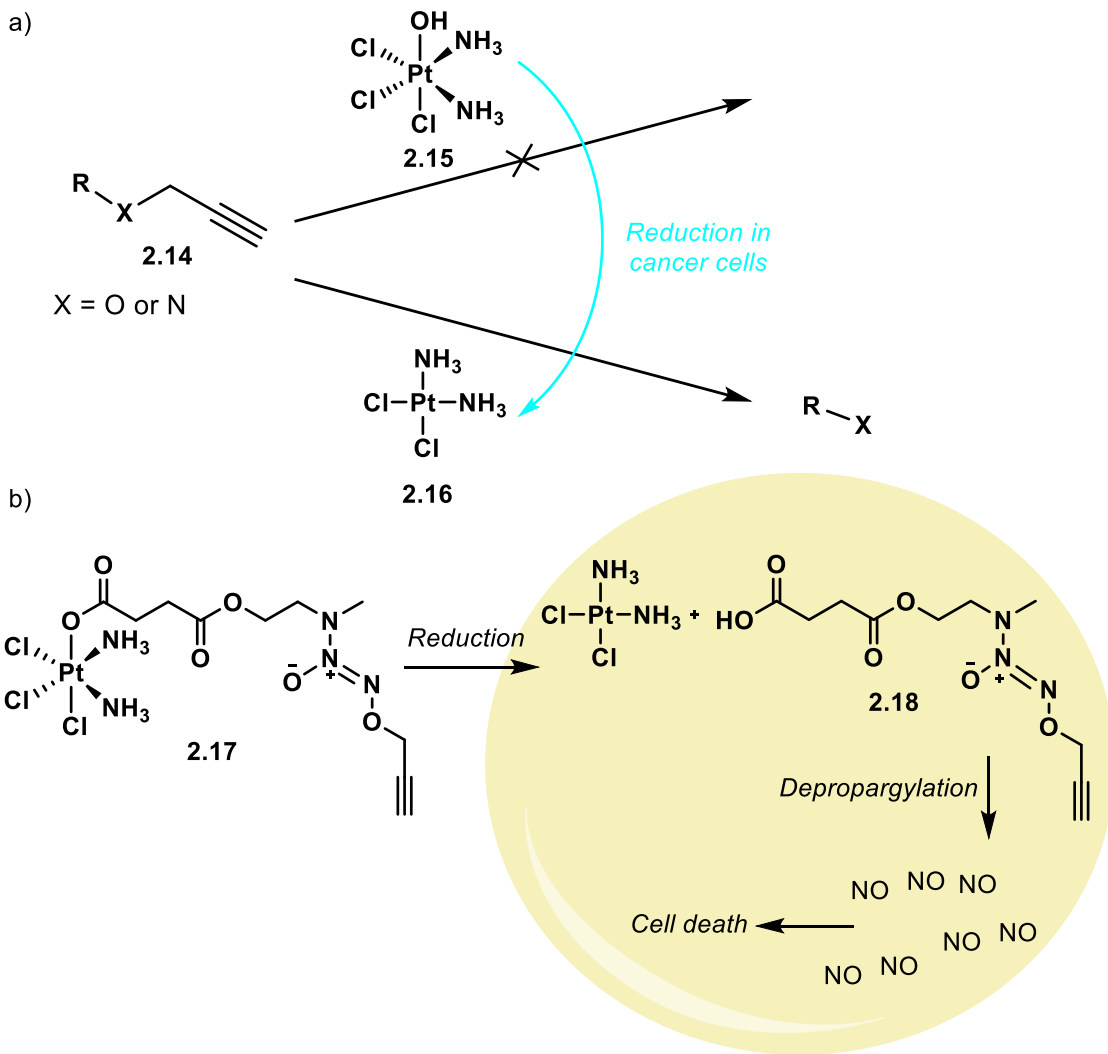
In 2020, Bernardes, Fior, and Oliveira groups developed a depropargylation reaction (Scheme 20) that used platinum complexes [K_2PtCl_4 or cisplatin].¹⁴¹ During the initial investigations water was found to be crucial for this transformation. Mechanistic studies suggested that water activated platinum complex via chloride ligand dissociation. Furthermore, platinum(II) was proposed to be the active catalyst. Substoichiometric amounts of platinum lead to slow reaction times (72 hours) with a TON of 3.3. The reaction time was decreased to 4 hours in the

presence of 2 equivalents of platinum salt. The rate and the efficiency of the reaction were, however, hindered with the addition of DMEM and serum. Nonetheless, this methodology was used to activate the propargylated derivative of 5-fluorouracil in zebrafish.



Scheme 20. Depropargylation of N-propargyl 5-fluorouracil with cis platinum.

The same year, the Huang group reported platinum(II)-catalyzed depropargylation of various caged molecules(Scheme 21a).¹⁴² Screening of numerous platinum complexes indicated that platinum(II), not platinum(IV) catalyzed the reaction. As in the previous study, water was found to be essential for this reaction.

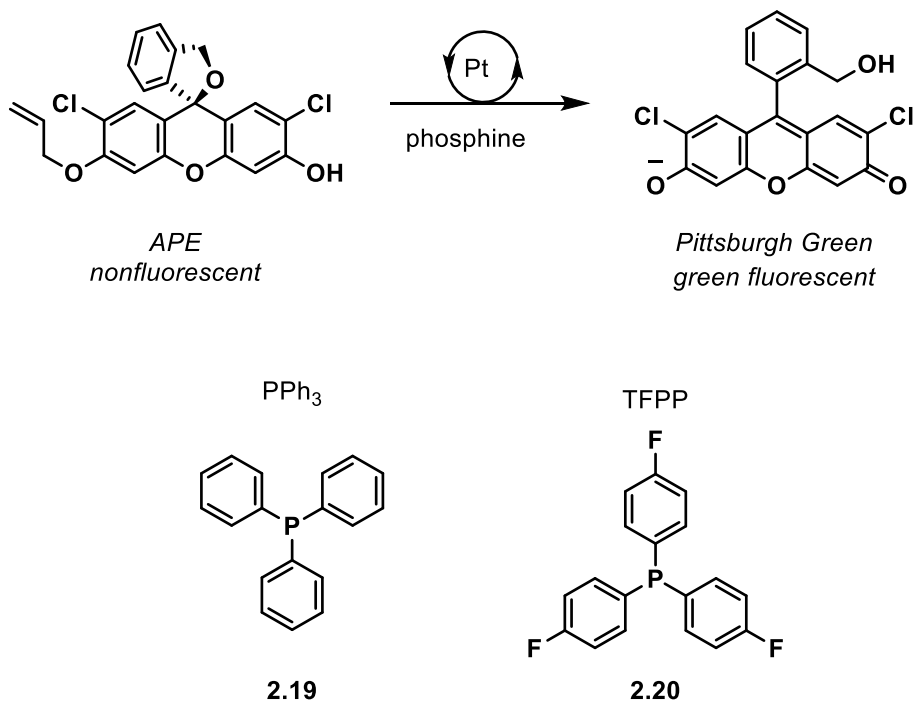


Scheme 21. Cis platinum depopargylation in cancer cells.

Platinum(IV) complexes are kinetically inert prodrugs¹³⁵ that can be converted to active platinum(II) upon reduction by high concentrations of cytoplasmic reductants such as ascorbic acid in cancer cells.¹⁴³⁻¹⁴⁷ NO is a potential cancer therapeutic, as several kinds of NO donors have been shown to have antiproliferative activity.¹⁴⁸⁻¹⁵¹ Thus, a prodrug containing masked platinum(IV) and O²-propargyl N-methylethanalamine diazeniumdiolate connected by succinic acid **2.17** was developed (Scheme 21b). The prodrug had no toxicity in normal cells; upon

platinum(IV) reduction to platinum(II) in cancer cells, the metal was able to catalyze depropargylation and subsequent NO release, which led to cancer cell death.

Platinum has also been shown to catalyze deallylation reactions. The Koide group reported platinum-catalyzed deallylation of the fluorometric probe, APE (Scheme 22).¹⁵² The method was catalytic in the presence of PPh_3 ,⁵⁷ but was more responsive to palladium.⁴⁷ It was applied to the detection of platinum in buffers and serum.



Scheme 22. Platinum-catalyzed deallylation developed in the Koide lab.

In 2020, the Koide group reported a platinum-catalyzed deallylation method utilizing tris(4-fluorophenyl)phosphine (TFPP; Scheme 22).¹⁵³ This method was specific for platinum over palladium. Platinum-catalyzed deallylation in the presence of TFPP was more efficient compared to PPh_3 . Different oxidation state platinum species were premixed with the ligand and showed the

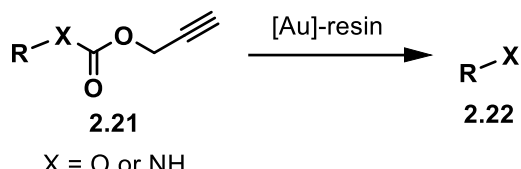
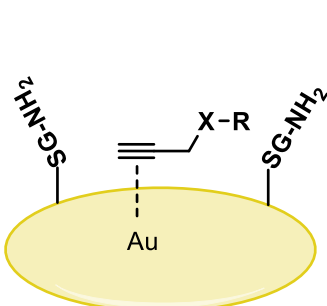
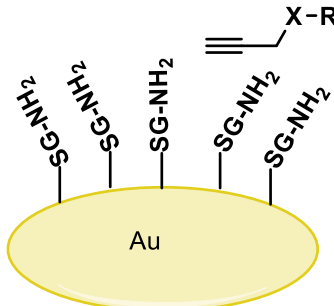
same reactivity towards APE, indicating that platinum(0) is likely the active catalyst in this system. Cisplatin in combination with TFPP was shown to catalyze deallylation in serum and in living tumor cells.

2.1.3 Gold catalyzed cleavage reactions

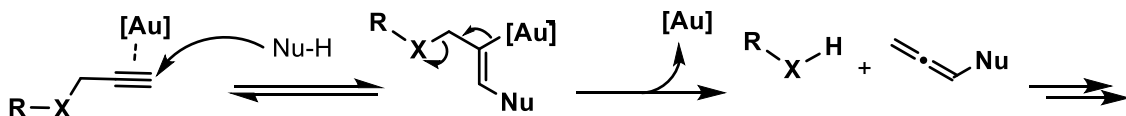
Gold is another metal capable of promoting depropargylation that has not been widely studied. In the past decade, gold catalysis gained a lot of attention in organic synthesis due to its preference to coordinate to alkynes in the presence of other functional groups.¹⁵⁴⁻¹⁶⁰ The chemistry of gold in chemical biology is overshadowed by near-covalent S-Au bonding.¹⁶¹⁻¹⁶³

Santamaría and Unciti-Broceta hypothesized that synthesizing gold nanoparticles in solid support would protect the metal nanostructures from thiols while allowing alkynes to enter and react under biological conditions (Scheme 23a).¹⁶⁴ Gold (III) species embedded on a TentaGel® resin removed propargyl group in PBS buffer with and without serum.¹⁶⁵ Although low yields were observed (up to 25% yield), serum helped to facilitate the reaction. Thiols suppressed the reactivity, while amines boosted catalytic activity. The gold-nanoparticle was sensitive to glutathione concentrations. It facilitated the reaction until a saturation threshold was reached and prevented gold coordination to the alkyne (Scheme 23b). The authors proposed that gold acts as a π -acid to activate the nucleophilic addition onto the alkyne (Scheme 23c). This led to a release of the leaving group and the formation of allenyl byproducts that can isomerize or hydrolyze under the reaction conditions. The gold-nanoparticle was used to decage various prodrugs in cells. Furthermore, a fluorescent probe was successfully released in the brain of a zebrafish.

a)

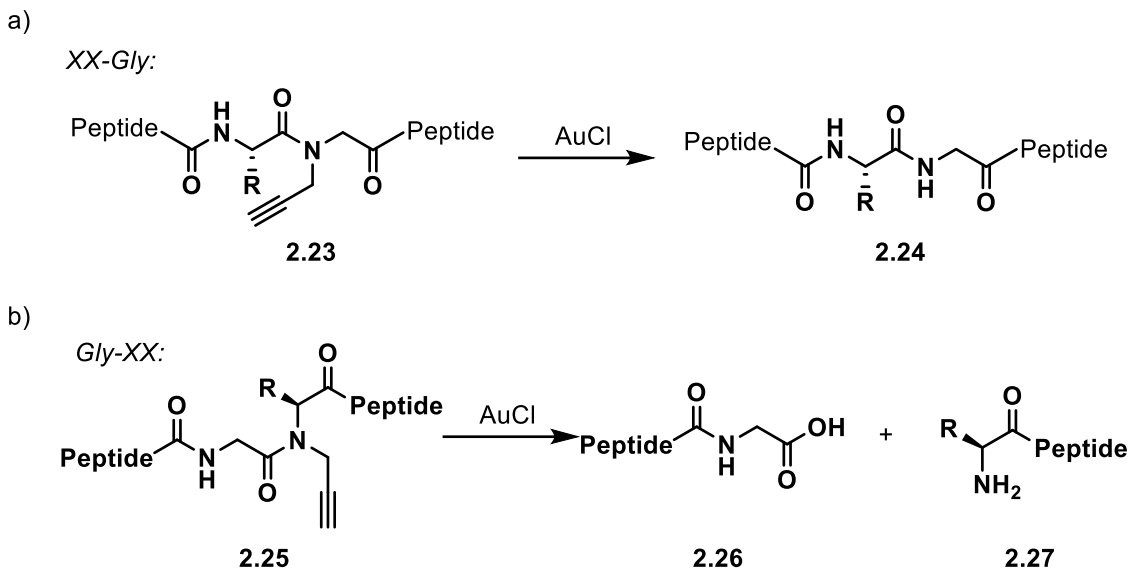
b) *Low concentrations of glutathione:**High concentrations of glutathione:*

c)



Scheme 23. Gold catalyzed depropargylation.

Gold(I)-catalyzed depropargylation of amides in peptides in PBS buffer was reported by the Brik group (Scheme 24).¹⁶⁶ This method was compatible with secondary and tertiary amides as well as a carbamate. Site-selective amide bond cleavage was discovered in this study, which depended on the position of the modified site. The sequence corresponding to XX-Gly led to depropargylation (Scheme 24a) while switching the sequence to Gly-XX lead to the amide bond cleavage (Scheme 24b).



Scheme 24. Gold-catalyzed depropargylation of peptides.

2.1.4 Palladium catalyzed cleavage reactions

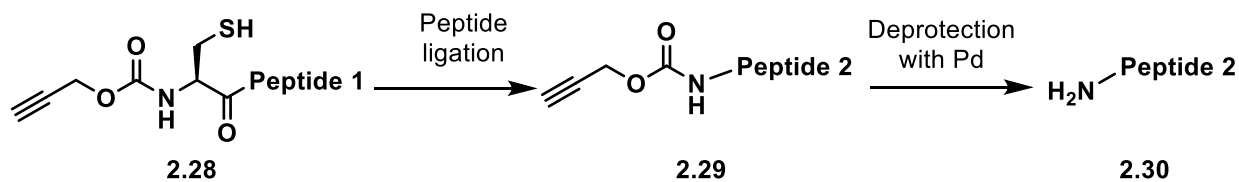
Ruthenium-catalyzed clip reactions have been extensively studied and shown to work under biological conditions. However, palladium might be more attractive because it has been shown to catalyze a variety of reactions in synthetic organic chemistry in water.¹⁴ Sterics and electronics of palladium complexes can be tuned through ligand modifications. Palladium is less toxic than some other transition metals;¹⁶⁷ thus, it has the potential to be used in biology and medicine.¹⁶⁸ Allylic and propargylic palladium-catalyzed C-O or C-N bond cleavage do not require biologically incompatible reagents. Allylic and propargylic ethers, amines, and carbamates are also stable under biological conditions. Early studies of palladium-catalyzed decaging suggest that depropargylation is faster than deallylation.^{45-46, 53, 54} However, these studies do not use phosphine

ligands, which are known to accelerate the rate of Tsuji-Trost reaction in synthetic chemistry.¹⁶⁹⁻

170

2.1.4.1 Palladium catalyzed depropargylation

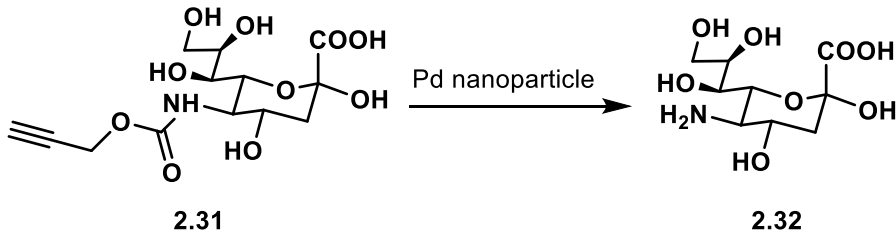
Native chemical ligation is widely used in the synthesis of proteins. It uses N-terminal thiol modified amino acid (cysteine) from one peptide and C-terminal thioester from another peptide, which reacts to form an amide bond.¹⁷¹ The key for this approach is to use protecting groups for the N-terminal cysteine in the middle fragments, due to two reactive groups, N-terminal cysteine and C-terminal thioester.¹⁷²⁻¹⁷³ Current protecting groups suffer from the use of harsh removal conditions,¹⁷⁴ the need for peptide isolation prior to deprotection,¹⁷⁵ or special preparations.¹⁷⁶ Furthermore, many deprotections suffer from long and non-efficient reactions. The Brik group used [Pd(allyl)Cl₂] for rapid removal of the propargyloxycarbonyl-protecting group from the N-terminal cysteine **2.28** (Scheme 25).¹⁷⁷ Although successful, this method required 40 equivalents of palladium and the addition of 1,4-dithiothreitol to quench the palladium species and to release any palladium bound to the peptide.



Scheme 25. Palladium -catalyzed deprotection of cysteines.

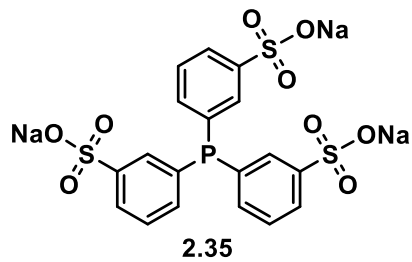
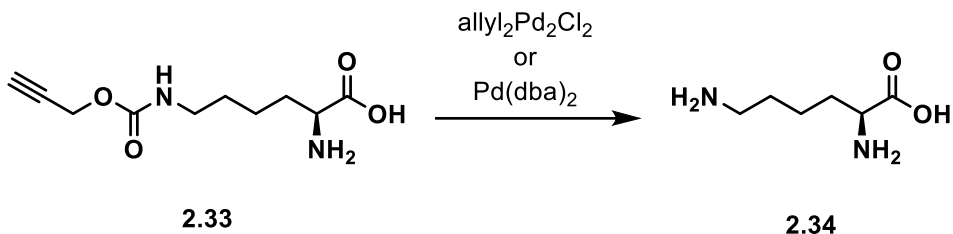
Clip reactions can also be used as a tool for cell surface engineering. Neuramic acid **2.32** (Scheme 26) is rarely found in nature, however, there is some evidence supporting its presence in

nerve cells and cancer cells. How neuramic acid is installed into glycans and its exact functions remain unknown due to its high reactivity *in vivo*. The Chen group reported a palladium-catalyzed decaging strategy for the *in-situ* generation of neuramic acid **2.32** on live cells in 4-(2-hydroxyethyl)-1-piperazineethanesulfonic acid (HEPS) buffer (Scheme 26).⁹⁶ This conversion mimicked the enzymatic de-N-acetylation of N-acetylneuramic acid. This was the first example of the formation of the core nine-carbon atom sugar on the surface of live cells.



Scheme 26. Palladium-catalyzed generation of neuramic acid.

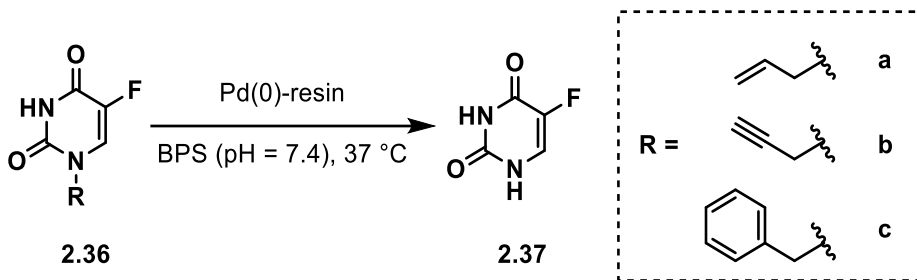
Palladium-catalyzed depropargylation for protein activation in live cells was also developed by the Chen group (Scheme 27).¹⁷⁸ Biocompatible palladium catalysts, Pd(dba)₂ and allyl₂Pd₂Cl₂, successfully cleaved the N-propargyl carbamate of lysine **2.33** in various cell lines and proteins. In this study, the authors noted that the addition of phosphine ligand, 3,3',3''-phosphanetriyltris(benzenesulfonic acid) trisodium salt (TPPTS) **2.35** to Pd(NO₃)₂ species increased the efficiency of deallylation, but not depropargylation. Phosphine ligands are known to increase the rate of deallylation in organic synthesis but are rarely used in biology to avoid possible toxicity.¹⁶⁹⁻¹⁷⁰



Scheme 27. Palladium-catalyzed depropargylation for the protein activation.

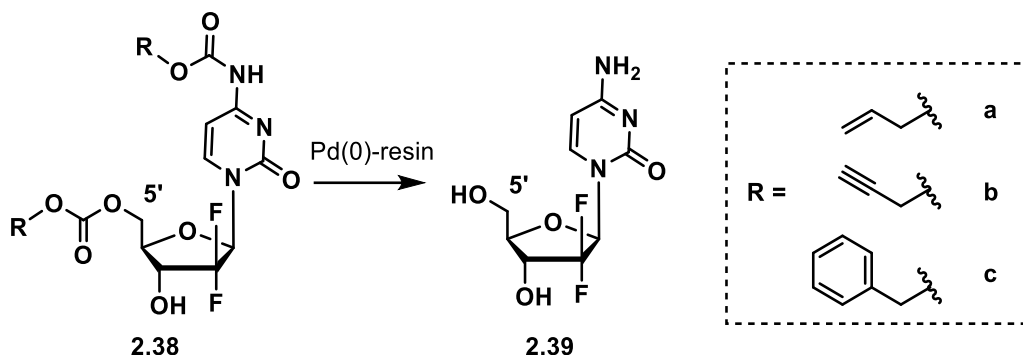
In the last decade, palladium catalyzed clip reactions also found its use in prodrug development.⁴⁶ Prodrugs – molecules with little or no pharmacological activity have been used to mediate the toxicity of active drugs. Tsuji-Trost reactions with drugs as the leaving group proved to be useful in prodrug synthesis.

In 2014, Unciti-Broceta, Bradley, and coworkers described the palladium-catalyzed dealkylation of 5-fluoro-1-propargyl-uracil **2.36** to generate the anti-cancer agent 5-fluorouracil **2.37** (Scheme 28).⁵³ Allyl, propargyl, and benzyl groups were introduced to mask the active N1 position, affording inactive **2.36a–c**. Upon uncaging of the prodrug, 5-fluorouracil **2.37** was released without any loss of its anti-cancer activity, leading to a disruption of normal cellular functions.



Scheme 28. Palladium-catalyzed dealkylation of 5-fluoro-uracil pro-drugs.

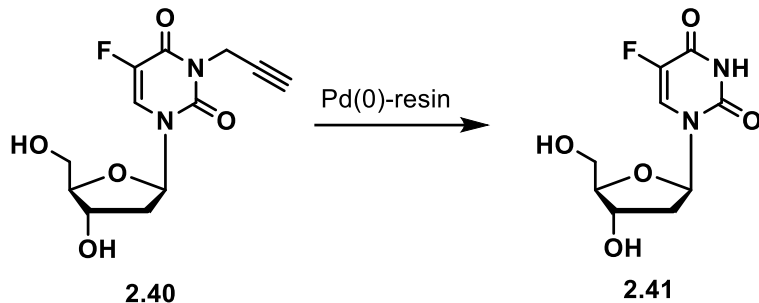
In the same year, Unciti-Broceta, Bradley, and coworkers developed gemcitabine prodrugs **2.38** with a protected 5'-OH or amine groups (Scheme 29).⁵⁴ The unmasked drug was shown to be cytotoxic, killing not only cancer cells but healthy cells as well. With controlled delivery of palladium nanoparticles to tumor sites, the prodrug could be selectively uncaged in cancer cells to produce active **2.39**, lowering the possibility of off-target effects.



Scheme 29. Activation of gemcitabine prodrugs by palladium catalysis.

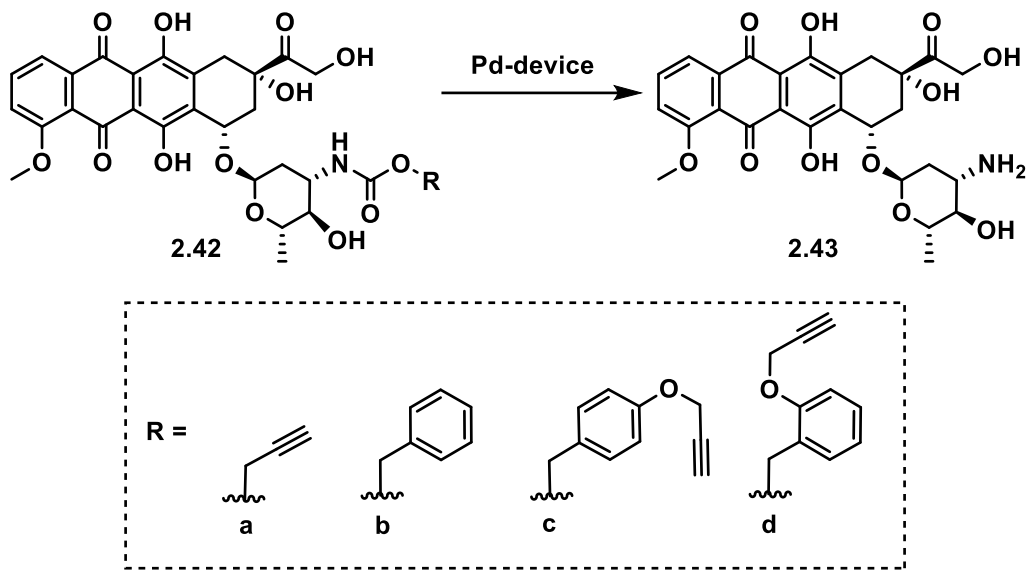
Unciti-Broceta, Weiss, and coworkers applied the same strategy to the anticancer drug floxuridine **2.41**, a potent antineoplastic drug used to treat advanced solid tumors (Scheme 30).¹⁷⁹ Cytotoxicity was significantly reduced with the installation of the propargyl group in the N3

position of the uracil ring, which serves as the enzymatic point of recognition. Cytotoxic properties were rescued in cancer cell culture in the presence of palladium at low pH and under both, normoxic and hypoxic conditions.



Scheme 30. Palladium-catalyzed decaging of floxuridine.

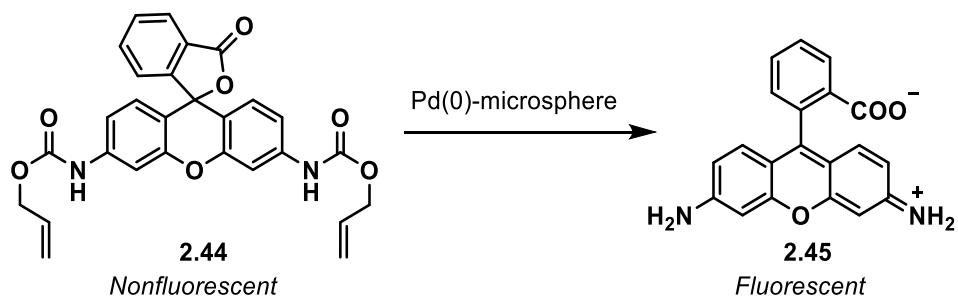
In 2018, the groups of Leung and Unciti-Broceta demonstrated that palladium devices were able to uncage doxorubicin prodrugs **2.42a–d** inside the zebrafish with no adverse effects (Scheme 31).¹⁸⁰ The devices were made of a copolymer consisting of a low crosslinked polystyrene matrix on which polyethylene glycol was grafted. Palladium devices were injected directly into tumors to promote controlled dealkylation of prodrugs and subsequent doxorubicin release. The prodrugs had no activity and did not accumulate across the body in the absence of palladium.



Scheme 31. De-caging of doxorubicin prodrugs with a palladium-devices.

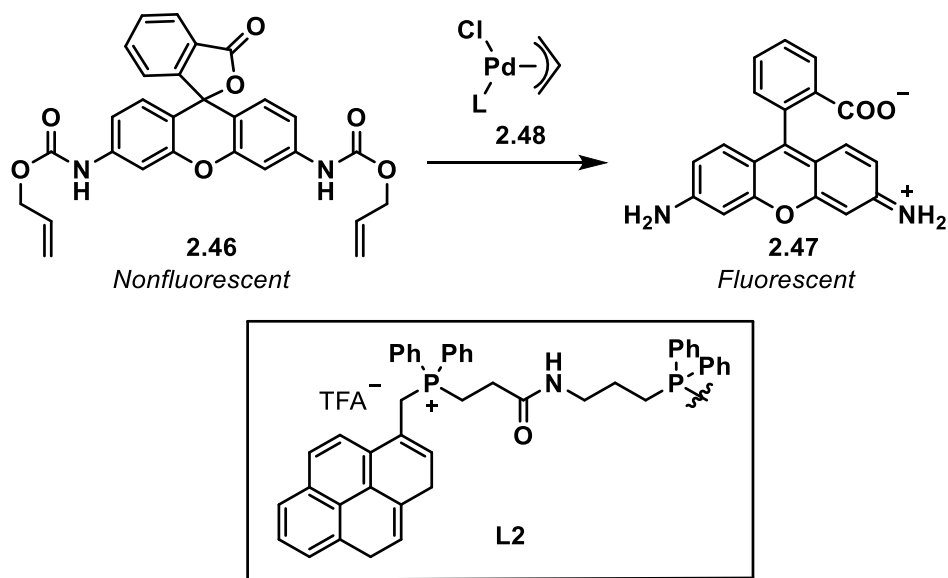
2.1.4.2 Palladium catalyzed deallylation

In 2011, the first palladium-mediated deallylation in cells was reported by Bradley and coworkers (Scheme 32).⁴⁵ Upon trapping of palladium nanoparticles within polystyrene microspheres, the palladium-loaded complex was able to enter the cell and catalyze the cleavage of allyl carbamate groups in chemodosimeter **2.44** to produce rhodamine 110 dye **2.45**.



Scheme 32. Rhodamine-based chemodosimeter used in intracellular palladium-catalyzed deallylation.

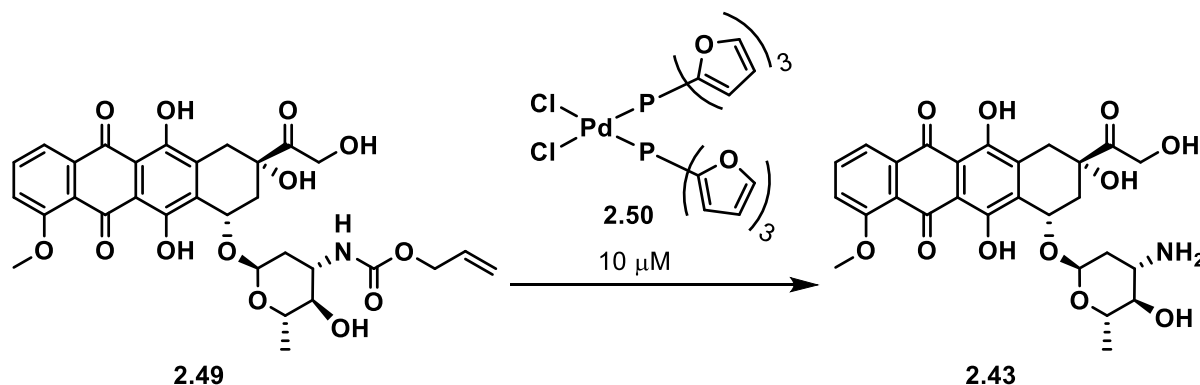
In 2018, the Mascareñas group designed another rhodamine probe that could react intracellularly (Scheme 33).¹⁸¹ While testing for palladium sources other than palladium(0) nanoparticles for cleavage, they discovered a palladium-complex **2.48** that favored accumulation in the mitochondria. The ligand **L2** is the key to the observed cellular localization. The pyrene and phosphonium groups are speculated to have the desirable combination of charge and hydrophobicity for mitochondrial localization. The combination of **L2** and palladium-complex **2.48** can therefore be used to selectively image mitochondria in live cells suspended in DMEM with 5% FBS.



Scheme 33. Alkene-based probe for mitochondria imaging.

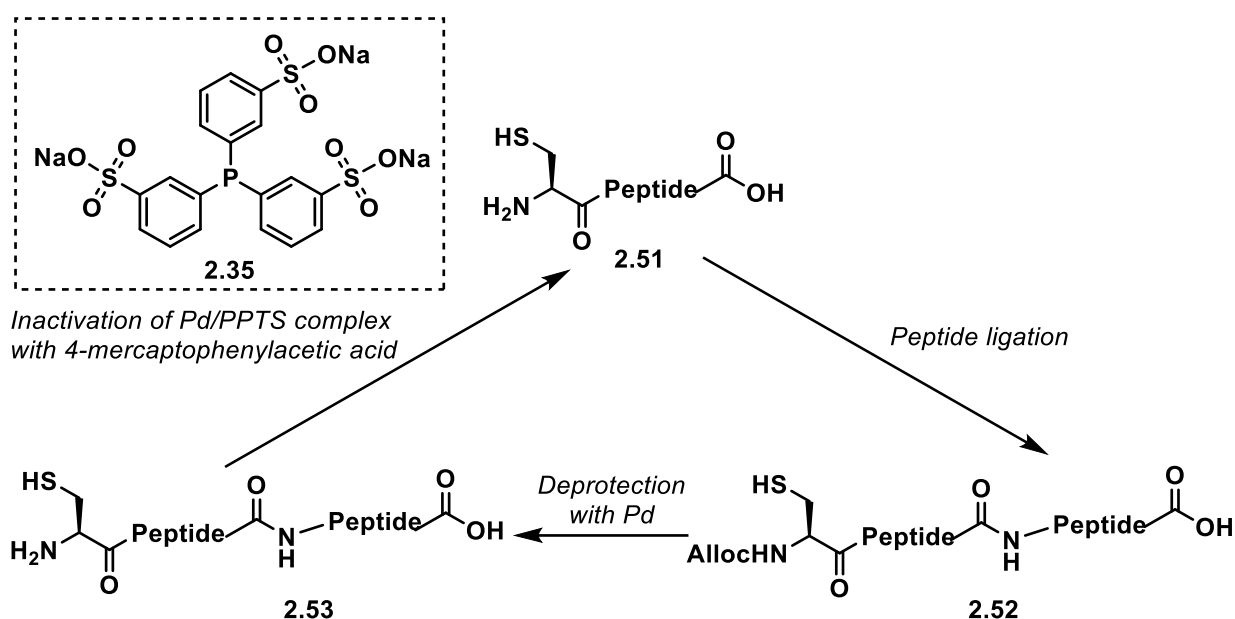
In 2017, the Weissleder group described a palladium nanoparticle containing $\text{PdCl}_2(\text{TFP})_2$ in a biocompatible poly(lactic-co-glycolic acid)-*b*-polyethyleneglycol platform.⁵⁵ While screening for phosphine ligands, they observed the superior rate of dealkylation in the presence of TFP in phosphate buffer. However, all palladium-phosphine complexes failed to catalyze the deallylation

in Minimum Essential Medium with serum. The Weissleder group demonstrated the utility of combining palladium nanoparticles and TFP by successfully uncaging alloc-modified doxorubicin **2.49** in cells at rates superior to those with Ph₃P (Scheme 34) in MEM with serum.



Scheme 34. De-caging of allyloxycarbonyl modified doxorubicin.

Palladium-catalyzed uncaging is often used in amino acid and peptide synthesis.¹⁸² Depropargylation, although useful, is not very efficient. The Okamoto laboratory reported the first one-pot multiple peptide ligation, which used palladium(0)/TPPTS complex to uncage alloc protected cystine **2.52** (Scheme 35).¹⁸³ The addition of the phosphine allowed for a reduction of palladium from 15–40 equivalents¹⁷⁷ to only 2 equivalents in water. In this study, 4-mercaptophenylacetic acid was used as a nucleophile and to quench the palladium complex after alloc deprotection.



Scheme 35. Palladium-catalyzed deprotection in peptide synthesis.

2.1.5 Conclusion

Transition metal-catalyzed bioorthogonal reactions are very useful in peptide synthesis and prodrug development. Gold- and platinum-catalyzed alloc/allyl and propargyloxycarbonyl deprotections (Figure 18a–b) have been overlooked by the field, while ruthenium- and palladium-catalyzed reactions have been extensively investigated (Figure 18c–d). Palladium-catalyzed uncaging reactions may be more attractive because palladium salts are less toxic. Currently, deallylation is deemed to be too slow to be viable as a clip reaction and more rapid, palladium-catalyzed propargylic C–O or C–N bond cleavage is typically used. It should be noted that phosphine ligands are usually omitted in these studies. Additionally, palladium-catalyzed depropargylation required 3–24 h under biologically relevant conditions,^{53, 178} warranting further improvement on the kinetics. The studies published by the Weissleder,⁵⁵ Mascareñas,¹⁸¹ and

Okamoto¹⁸² groups showed that the addition of phosphines increases the rate of deallylation; furthermore, careful engineering of the ligand can allow subcellular targeting and efficient catalysis. Additionally, these clip reactions (Figure 18) are typically optimized in phosphate buffer or water, however, DMEM and serum would be more applicable for biological studies.

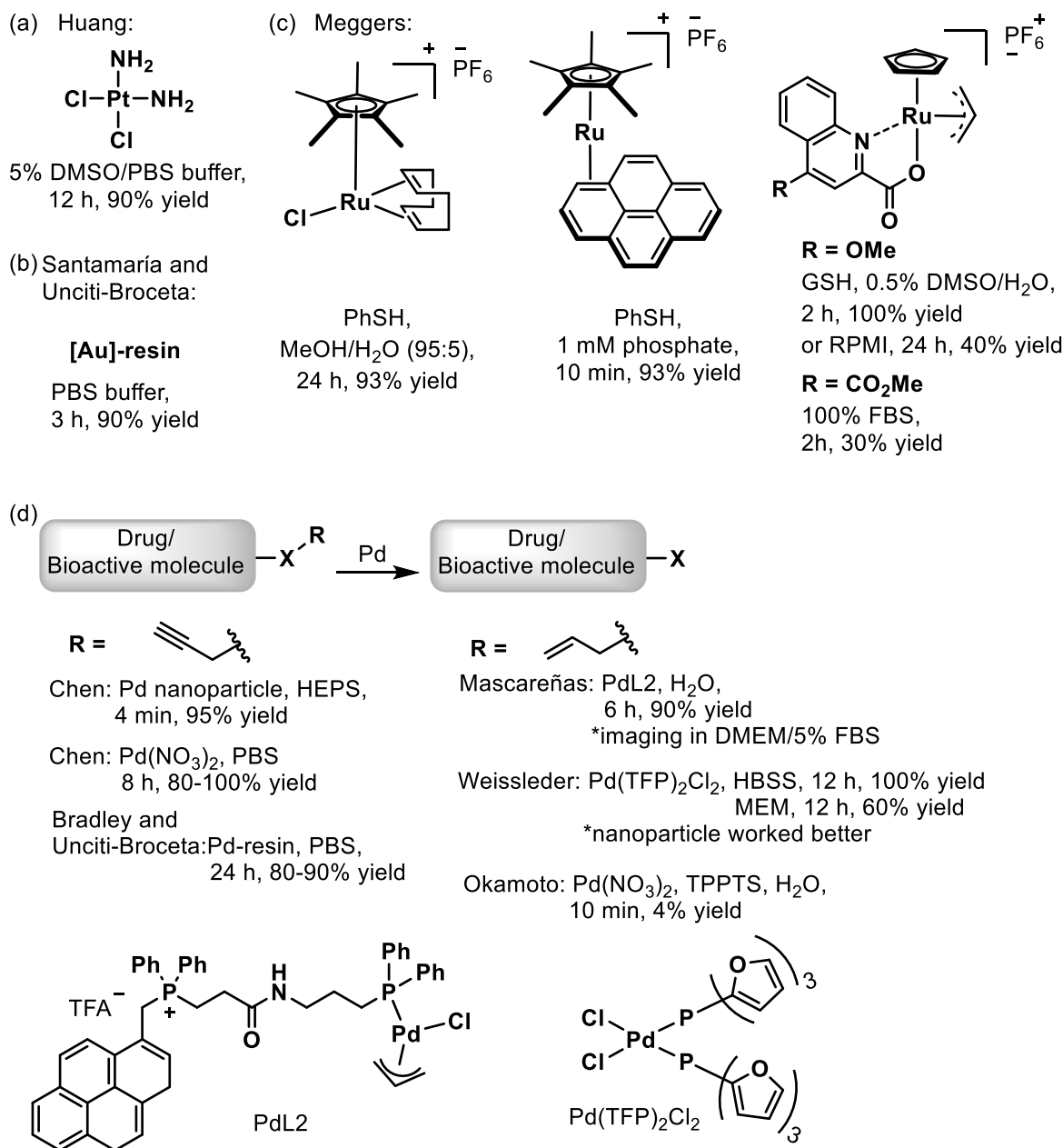
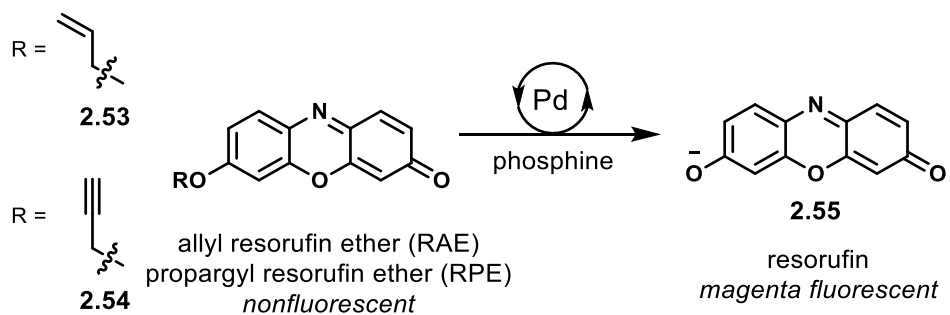


Figure 18. Summary of clip reaction discussed in this section.

2.2 Results and discussion

Fluorometric systems can provide opportunities for enabling rapid development of catalysis-based methods. To exploit fluorescence-based techniques, we chose to use resorufin propargyl ether (RPE) and resorufin allyl ether (RAE) (Scheme 36). Cleavage of the propargyl or allyl ethers is fluorogenic, producing fluorescent resorufin. In the previous study, the palladium-catalyzed deallylation of APE in pH 7 phosphate buffer was the fastest with TFP as the ligand.⁵⁷



Scheme 36. RAE and RPE decaging.

We also studied the deallylation of RAE in pH 7 phosphate buffer (Figure 19); the deallylation did not proceed without a phosphine ligand. In contrast, the depropargylation of RPE proceeded without the phosphine ligand (Figure 19), and was faster with TFP.

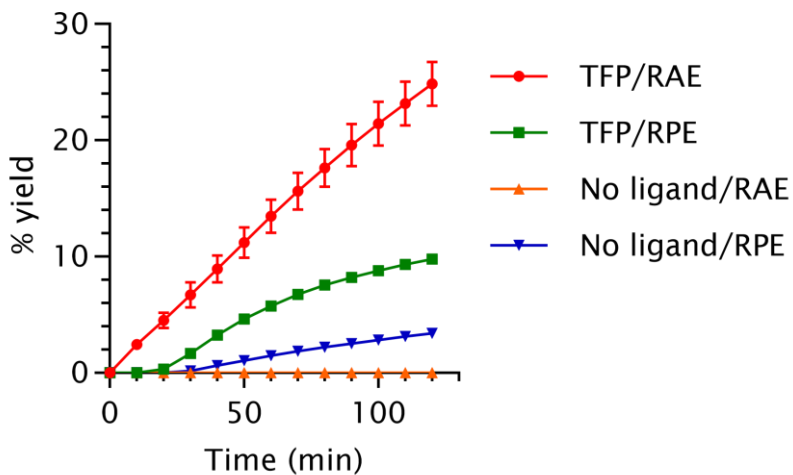


Figure 19. The rate of deallylation and depargylation in phosphate buffer. Conditions: 0 or 40 μM TFP, 20 μM RAE or RPE, 10 μM $\text{Pd}(\text{OAc})_2$, 1 % DMSO 50 mM phosphate pH 7 buffer, 25 °C, $n = 3$.

The rate of the reaction with RAE decreased when the medium was switched to DMEM (Figure 20a). No depargylation of RPE was observed in DMEM. The rate of deallylation was decelerated by the addition of fetal bovine serum (FBS) to DMEM (final concentration of FBS was 10% v/v) (Figure 20b). DMEM and serum contain many components, such as thiols, that can bind to transition metals and deactivate the active catalyst.¹¹⁶ We premixed $\text{Pd}(\text{OAc})_2$ and TFP in 14% v/v DMSO in H_2O prior to introducing $\text{Pd}(\text{OAc})_2$ to DMEM with 10 % serum to no avail as precipitate formed even at 1:6 v/v DMSO: H_2O mixture.

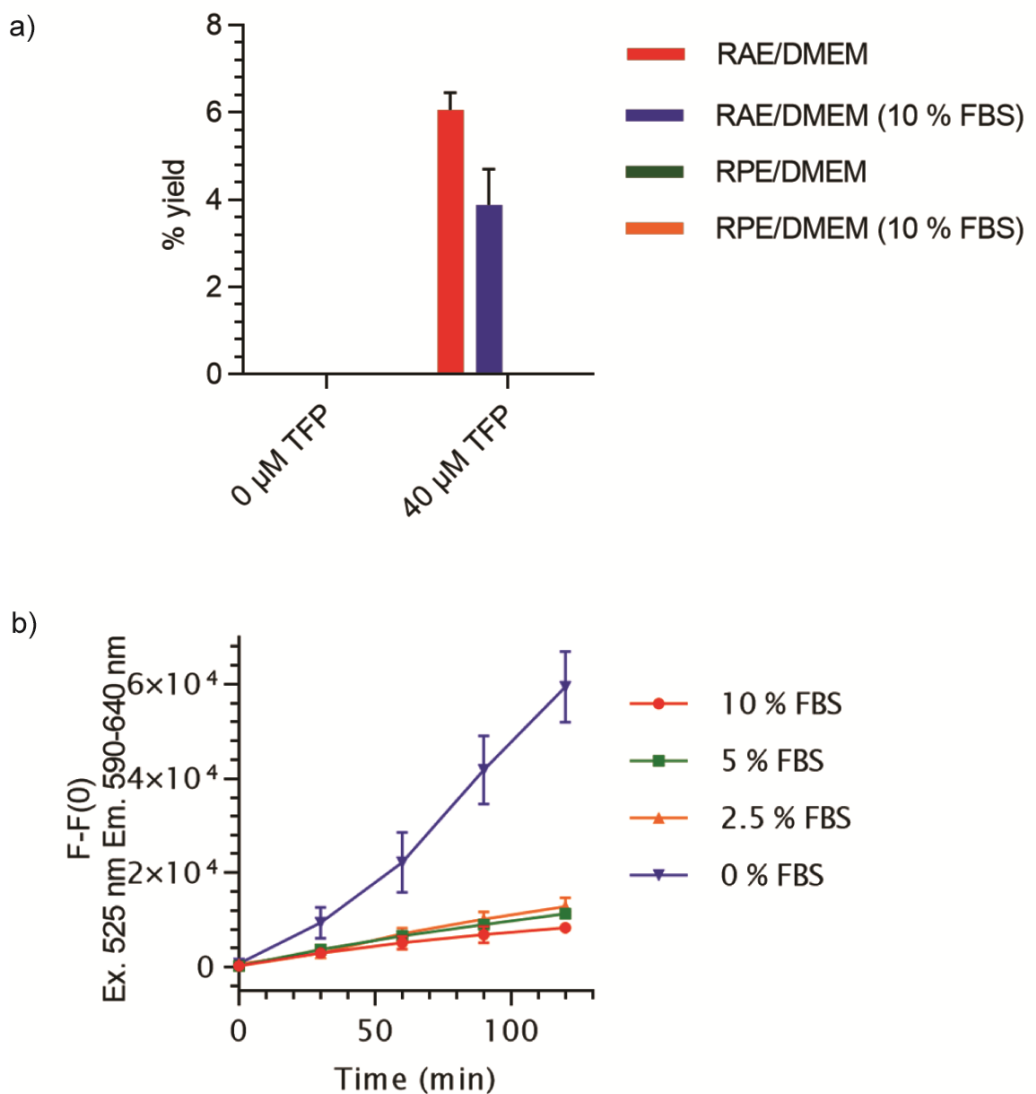
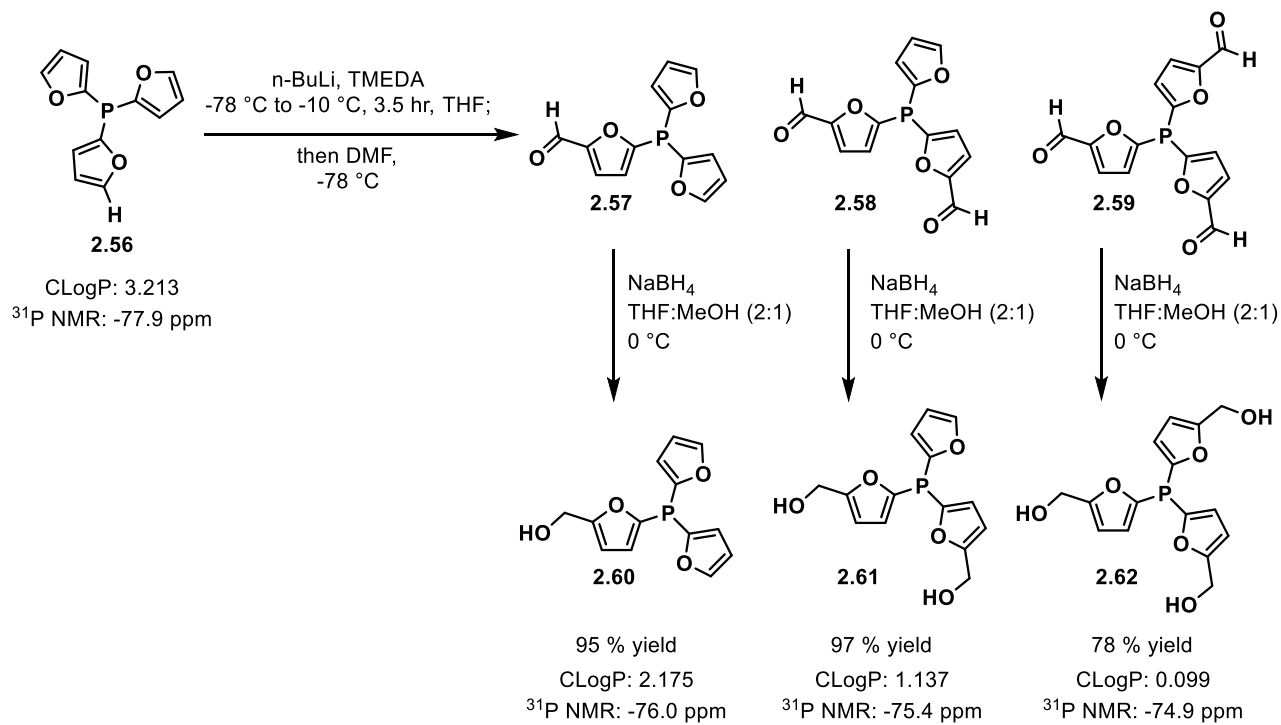


Figure 20. The influence of DMEM and serum on the rate of deallylation and depropargylation. (a) Dealylation and depropargylation with and without serum. Conditions: 0 or 40 μM TFP, 20 μM RAE or RPE, 10 μM $\text{Pd}(\text{OAc})_2$, 1 % DMSO/25 mM phosphate pH 7 buffer/ DMEM with 0 or 10 % FBS, 37 °C, 1 h, $n = 3$. (b) The rate of dealylation at different serum concentrations. Conditions: 40 μM TFP or TFP-(CH₂OH)₁, 20 μM RAE, 10 μM Pd, 1% DMSO in DMEM with either 25 mM phosphate buffer or 25 mM HEPES buffer, 10, 5, 2.5, 0 % FBS, 25 °C, 2 h, $n = 3$.

2.2.1 Synthesis and evaluation of new TFP analogs

Given the literature indicating that albumin, the most abundant protein in serum, has strong affinity for hydrophobic molecules,¹⁸⁴⁻¹⁸⁵ we hypothesized that TFP might be sequestered by the protein. As such, we synthesized more water soluble TFP analogs by introducing hydroxymethyl group (Scheme 37). TFP was deprotonated in the presence of *n*-BuLi and TMEDA.¹⁸⁶ The anion reacted with DMF to make the aldehyde precursors **2.57–2.59** upon acid hydrolysis. The corresponding aldehydes were reduced with NaBH₄ to give hydroxymethyl-TFP analogs **2.60–2.62**.



Scheme 37. Synthesis of hydroxymethyl-TFP analogs.

An introduction of hydroxymethyl substituents accelerated the reaction in 50 mM phosphate pH 7 buffer for both, RAE and RPE (Figure 21). A positive correlation was observed between the number of hydroxymethyl groups and reactivity, with iPhos3 (**2.62**) being the best. Importantly, Figure 21 indicates that O-allyl ether cleavage is 14 times faster after 1 hour than O-propargyl ether cleavage when the ligands were used.

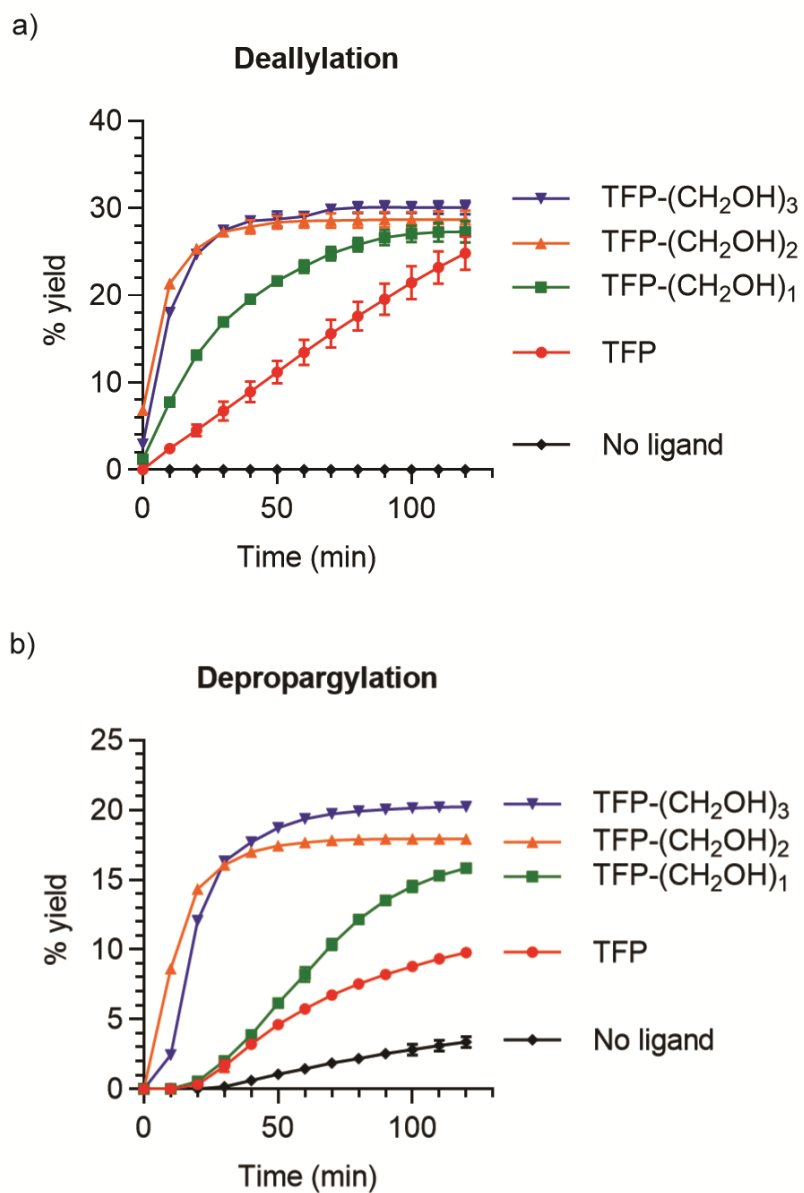


Figure 21. The rate of deallylation and depropargylation in the presence of hydroxymethyl-TPP analogs in phosphate buffer. Conditions: 40 µM TFP, TFP-(CH₂OH)_n (*n* = 1, 2, 3), 20 µM RAE or RPE, 10 µM Pd(OAc)₂, 1 % DMSO in 50 mM phosphate pH 7 buffer, 25 °C, *n* = 3.

We then asked whether this discovery could be translated into a more biologically relevant, cell-culture medium, such as DMEM with 10% serum. Low yields were observed with all phosphines when the ligands and palladium were added to the reaction mixture separately (Figure 22a). Furthermore, none of the newly synthesized TFP analogs (**2.60–2.62**) were superior to TFP. We hypothesized that the low efficiency of the clip reactions was likely associated with palladium deactivation by the components in the reaction media.¹¹⁶ DMEM and serum include many thiol-containing amino acids and proteins capable of binding to the active palladium catalyst rendering it inactive. Thus, palladium-phosphine complexes were first pre-formed in DMSO:H₂O, then added to the reaction mixture. We discovered that 60 µM iPhos1 resulted in 35 times the fluorescence compared to the phosphine-free conditions in DMEM with 10% BCS for the deallylation reaction when the reaction mixture was incubated at 37 °C (Figure 22b). The optimal concentration of both TFP and iPhos1 (**2.60**) in DMEM with 10 % serum was found to be around 70 µM (Figure 22c).

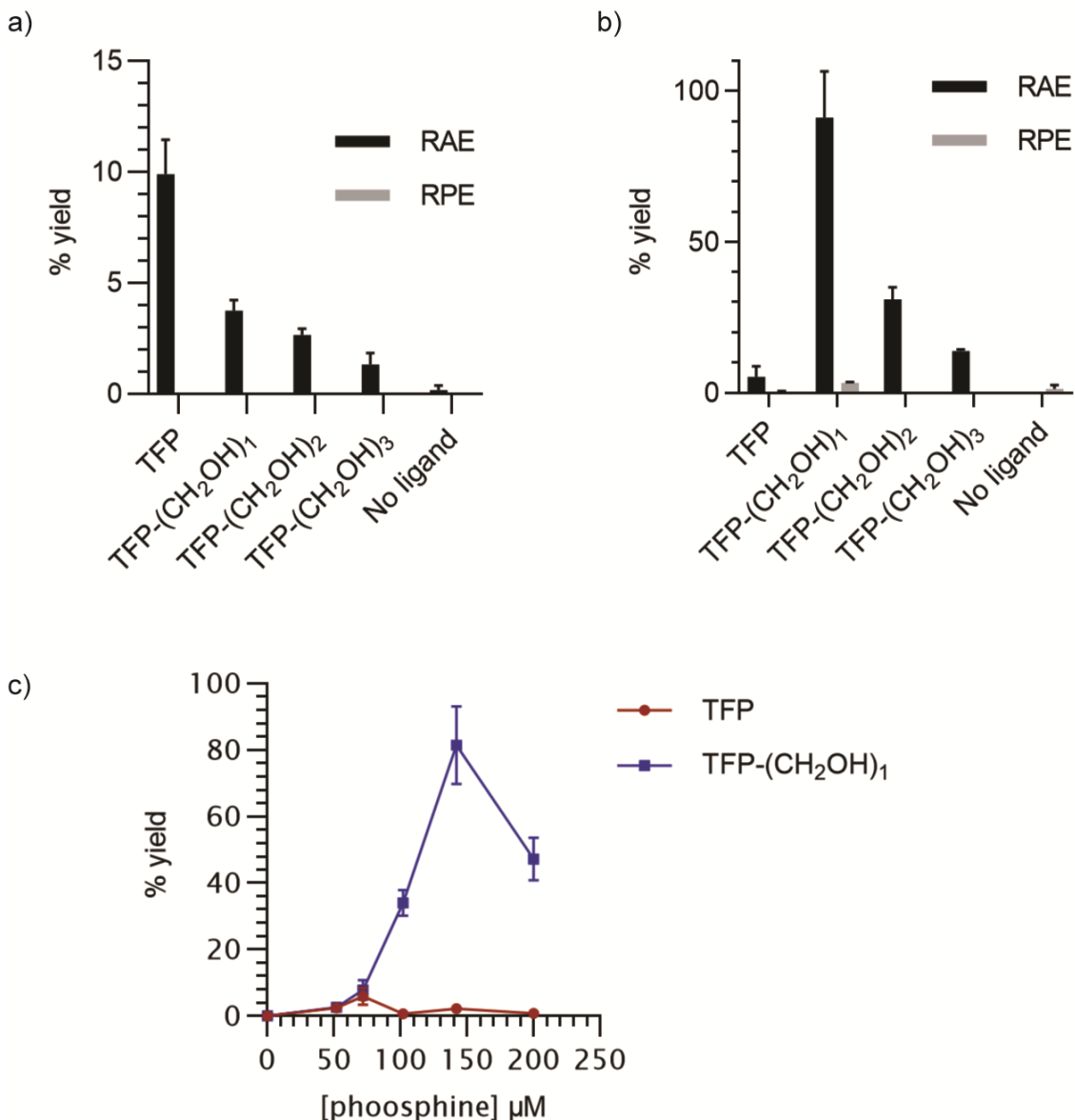
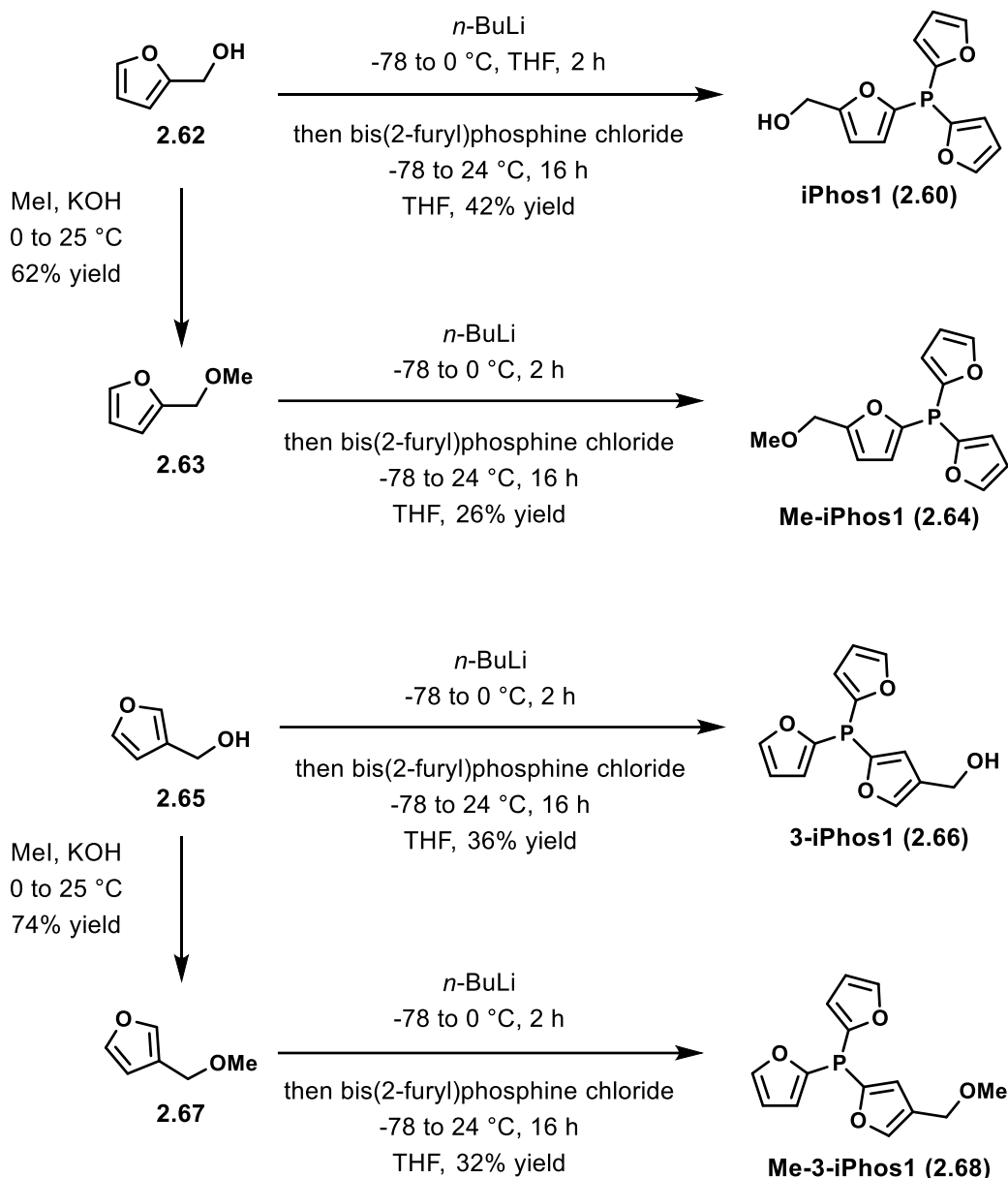


Figure 22. Deallylation and depropargylation of RAE or RPE in the presence of hydroxymethyl-TFP analogs in phosphate buffer, respectively at 37 °C in DMEM with 10% BCS. (a) Deallylation and depropargylation without palladium and phosphine premixing. (b) Deallylation and depropargylation with palladium and TFP premixing. Conditions: 60 μM TFP or TFP-(CH₂OH)_n ($n = 1, 2, 3$), 20 μM RAE or RPE, 10 μM Pd(OAc)₂, 1% DMSO in DMEM with either 25 mM phosphate buffer, 10 % BCS, 37 °C, 1 h, $n = 3$. (c) The optimal concentration of TFP and mono-hydroxyethyl-TFP at 37 °C in DMEM with 10% BCS. Conditions: 100, 71.4, 51.0, 36.4, 26.0, or 0 μM TFP or TFP-(CH₂OH)_n ($n = 1, 2, 3$), 20 μM RAE, 10 μM Pd(OAc)₂, 1% DMSO in DMEM/25 mM phosphate buffer (10 % FBS), 37 °C, 2 h, $n = 2$.

2.2.2 Synthesis and evaluation of second generation TFP analogs

Interestingly, in DMEM with 10 % serum, iPhos1 facilitated the rate of deallylation of RAE more efficiently than iPhos2 and iPhos3, which is a very different trend compared to our earlier observations 50 mM phosphate pH 7 buffer. The differences in ligand reactivities in 50 mM phosphate buffer (Figure 21) and DMEM (Figure 22b) can be attributed to the intrinsic differences in the solvent composition. Amatore and Jutand demonstrated that solvent composition can impact the overall kinetics of palladium-TFP complex formation and its catalytic activity.¹⁸⁷ We hypothesized that components of DMEM or the serum interacted with the hydroxy group on the phosphine making the catalyst bulkier or less reactive towards the alkene. To test this, we decided to synthesize other mono-hydroxymethyl-TFP analog and its methyl ether analogs **2.64**, **2.66**, **2.68** (Scheme 38). Furfuryl alcohol **2.65** or corresponding methyl ethers **2.63**, **2.67** were deprotonated with *n*-BuLi; the anion then reacted with bis(furyl)phosphine chloride to give the desired phosphines **2.64**, **2.66**, and **2.68**.



Scheme 38. Synthesis of second generation phosphine ligands.

Less sterically hindered 3-iPhos1 was superior to iPhos1 in facilitating the deallylation of RAE (Figure 23a). Me-iPhos and Me3-iPhos, were inferior to their hydroxy analogs. To explain this trend, we turned our attention to ^{31}P NMR chemical shifts, which depend on electron density on phosphorus, the bond angles, and π -bonding.¹⁸⁸ When the latter two parameters are kept the

same, ^{31}P NMR chemical shifts can be correlated with the lone pair donation on phosphorus and its Lewis basicity.¹⁸⁹ Thus, we plotted the % yield vs. the chemical shift to check for any correlations (Figure 23b). To our surprise, statistical analysis ($R^2 = 0.3130$) indicated no correlation between the ^{31}P NMR chemical shift and the efficiency of RAE deallylation. These results suggest that either other parameters influence the chemical shift or both solubility and sterics are important in designing phosphine ligands.

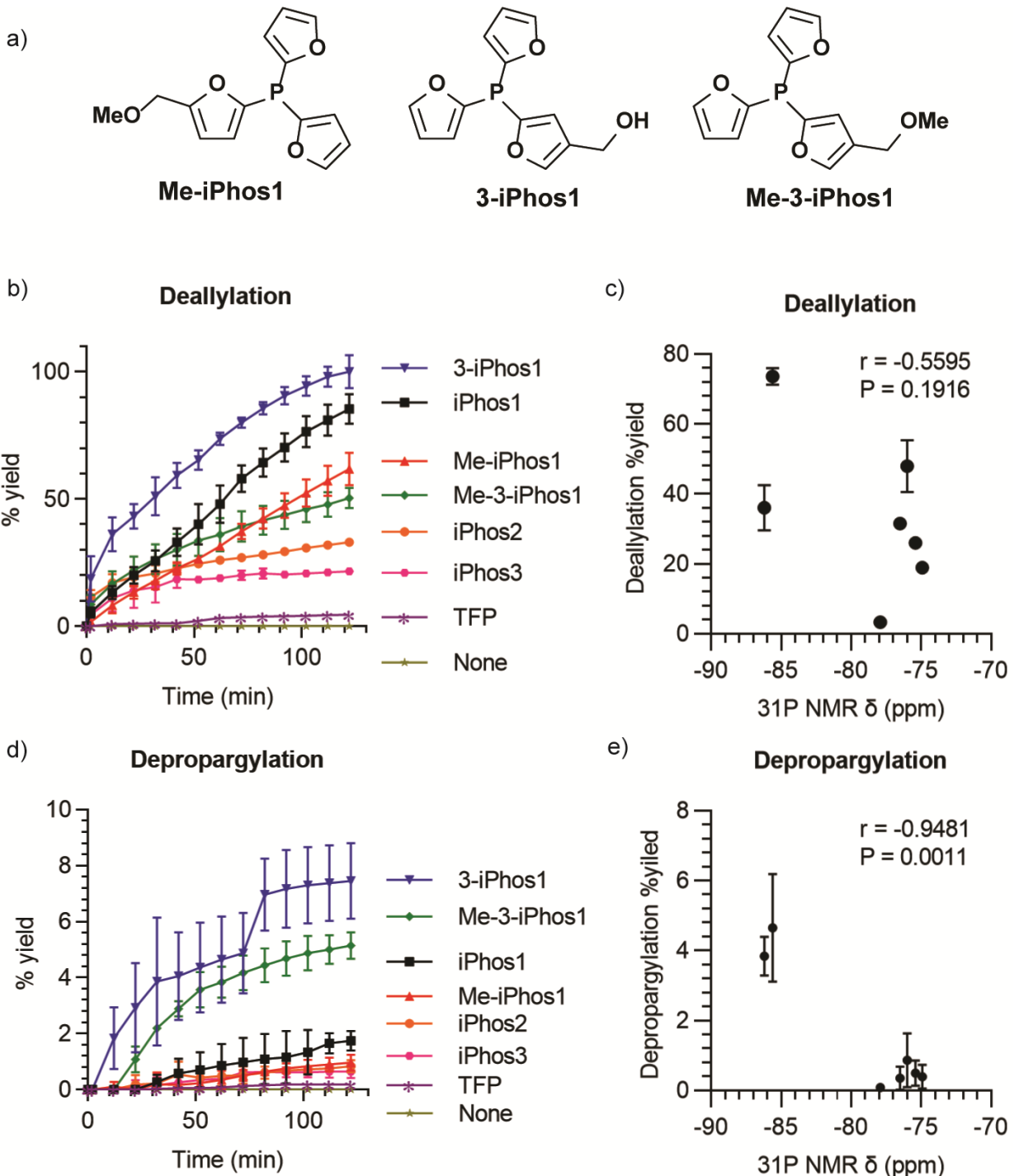


Figure 23. The rate of decaging reactions with second generation phosphines in DMEM with serum (premixed). (a) The rate of deallylation. (b) The correlation between the yield of deallylation and ^{31}P NMR chemical shift. (c) The rate of depropargylation. (d) The correlation between the yield of deallylation and ^{31}P

NMR chemical shift. Conditions: 0 or 60 μ M phosphine, 20 μ M RAE or RPE, 10 μ M Pd(OAc)₂, 1% DMSO in DMEM with 25 mM phosphate buffer, 10 % FBS, 24 °C, 2 h, n = 3.

Intriguingly, 3-iPhos1 and Me3-iPhos1 were also able to facilitate depropargylation in DMEM with 10 % FBS (Figure 23c). The mechanism of palladium-catalyzed depropargylation under biological conditions is not well studied. The Domingos group reported the first mechanistic study of palladium-catalyzed depropargylation at micromolar substrate and palladium concentrations.¹⁹⁰ However, this mechanistic study did not include phosphines. In the presence of the base, ligand, or nucleophilic solvent palladium(II) is believed to be reduced to palladium(0) by a base through an intramolecular ligand exchange reduction or by an attack of a nucleophile, followed by a reductive elimination pathway.^{54, 119, 191-192} The active palladium(0) is then assumed to undergo oxidative addition with the propargyl group to produce an allenylpalladium intermediate, which undergoes hydrolysis to form acetol and regenerate palladium(0). Based on the ³¹P NMR, it can be extrapolated that 3-iPhos1 (**2.66**) and Me-3-iPhos1 (**2.68**) (with chemical shifts of δ = -85.7 and δ = -86.2 ppm, respectively) are the most electron-rich phosphines. Statistical analysis indicated that there is a correlation between the ³¹P NMR chemical shift and the efficiency of RPE depropargylation ($R^2 = 0.8989$). These results suggest that oxidative addition may be the rate-determining step for the palladium-catalyzed depropargylation reaction in biological media. However, further studies are necessary to determine the role of these new phosphines.

We found that the kinetics of the reaction can be improved when premixed palladium and phosphine are added to the reaction mixture containing the probe in DMEM and serum. The second-generation phosphines were less sensitive to DMEM and serum (Figure 24). Although lower yields were observed when palladium and phosphines were not pre-mixed in DMSO-H₂O.

Lower yields are likely observed due to palladium deactivation by the components found in DMEM and serum.¹¹⁶

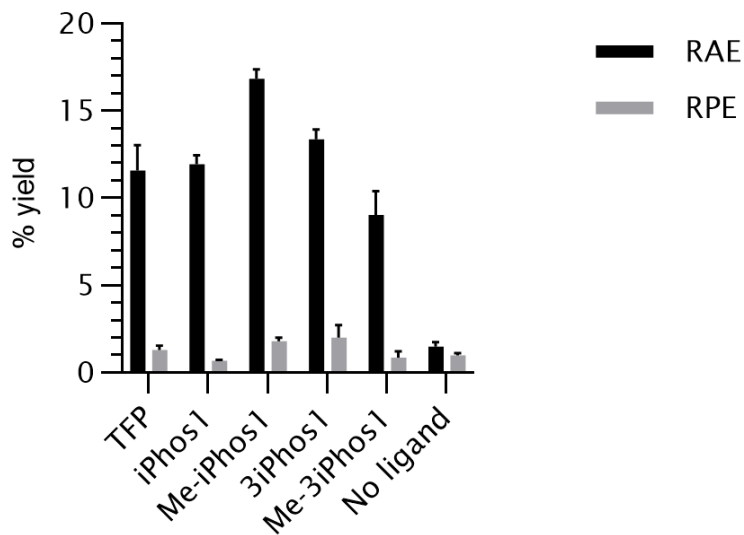
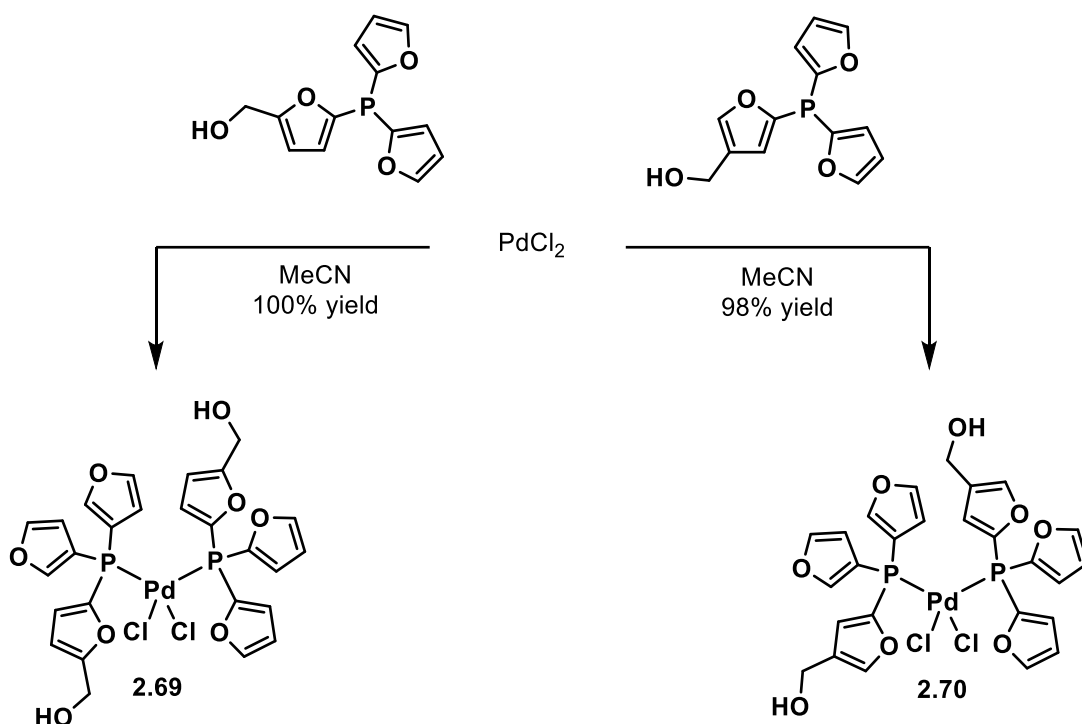


Figure 24. Decaging reactions with second-generation phosphines without premixing. Conditions: 60 μ M phosphine, 20 μ M RAE or RPE, 10 μ M Pd(OAc)₂, 1% DMSO in DMEM with 25 mM phosphate buffer, 10 % FBS, 37 °C, 1 h, n = 3.

2.2.3 Synthesis and evaluation of palladium-phosphine complexes

Palladium complexes **2.69** and **2.70** were synthesized in MeCN to test if the premixing step could be eliminated (Scheme 39). Palladium-phosphine complexes facilitated deallylation in DMEM with serum (Figure 25a). We hypothesized that addition of extra phosphine would reactivate the palladium catalyst and restart the reaction. However, the reaction did not restart upon exposure to additional phosphine. Furthermore, the initially fast reaction started to stall after 30

minutes, and a low fluorescence increase, indicative of low yields, was observed. Similar observation was reported by the Weissleder group; all palladium-phosphine complexes failed to catalyze the deallylation in Minimum Essential Medium with serum.⁵⁵ These results further show that palladium can be deactivated by the components in the media via dynamic ligand exchange and phosphines are unable to re-form the active palladium catalyst.

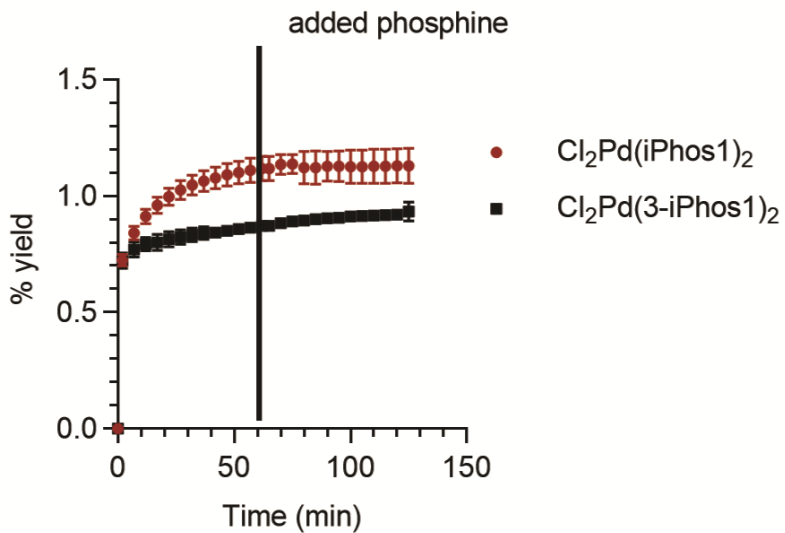


Scheme 39. Synthesis of palladium-phosphine complexes.

Studies performed by Amatore and Jutand suggest that in the presence of only 2 equivalents of phosphine, palladium(II) is readily reduced to highly unstable palladium(0) species;¹⁹³ consistent with the initial quick reaction followed by the catalyst deactivation observed in Figure 25a. On the contrary, with additional equivalents of phosphine ligand, $\text{Pd}(\text{OAc})_2$ formed a more stable $\text{Pd}(\text{OAc})_2(\text{PR}_3)_2$ complex. Thus, $\text{Pd}(\text{OAc})_2$ or palladium-phosphine complexes **2.69** and

2.70 were incubated in the presence of additional phosphine for 45 minutes prior to the addition to the solution containing the probe (Figure 25b). Pd(OAc)₂ premixed with 3iPhos1 and iPhos1 catalyzed deallylation more efficiently than palladium complexes **2.69** and **2.70** premixed with additional phosphine ligand. This can be attributed to the differences between the acetate and the chloride ligands. The complexes such as PdCl₂(PPh₃)₂ are very stable in solutions in THF and DMF.¹⁹⁴ Additionally, bivalent PdX₂(PPh₃)₂ complexes can be readily reduced to zerovalent palladium when ligand X contains oxygen.¹⁹³ Mechanistic studies suggest that this reaction proceeds via an inner-sphere reduction and is rate-determining.¹⁹⁵ Stable, bivalent, PdX₂(PPh₃)₂, complexes that do not contain oxygenated ligand require water and phosphine to form palladium(0) complexes. Thus, reducing bivalent PdCl₂(PR₃)₂ complex likely requires a ligand exchange between the chloride and the water ligands. Unfortunately, many attempts to synthesize Pd(OAc)₂(phosphine)₂ complexes in MeCN and THF led to palladium black formation. Furthermore, PdCl₂ was not soluble enough to be tested under given conditions to directly compare acetate and chloride ligands.

a)



b)

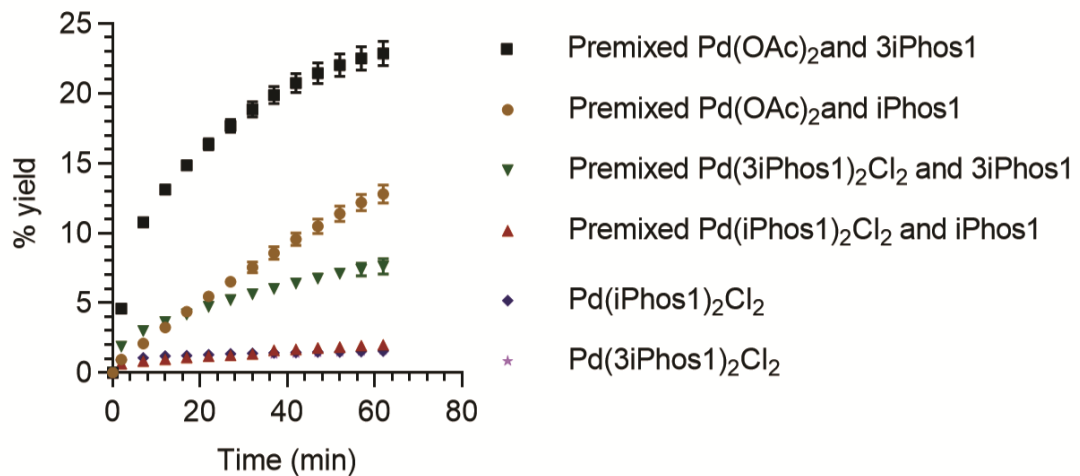


Figure 25. Deallylation of RAE with palladium-phosphine complexes. (a) Reactivation of palladium-phosphine complexes with additional phosphine. Conditions: 20 μM RAE, $\text{Cl}_2\text{Pd}(\text{iPhos1})_2$, 10 or 0 μM $\text{Cl}_2\text{Pd}(3\text{-iPhos1})_2$ or $\text{Pd}(\text{OAc})_2$, 60 μM iPhos and 3-iPhos, 1% DMSO/DMEM with 25 mM phosphate pH 7 buffer, 10% FBS, 25 °C, $n = 3$. (b) Deallylation with premixed palladium-phosphine complexes and additional phosphines. Conditions: 20 μM RAE, 10 or 0 μM $\text{Cl}_2\text{Pd}(\text{iPhos1})_2$, $\text{Cl}_2\text{Pd}(3\text{-iPhos1})_2$ or $\text{Pd}(\text{OAc})_2$, 0 or 60 μM iPhos and 3-iPhos, 1% DMSO/DMEM with 25 mM phosphate pH 7 buffer, 10% FBS, 25 °C, $n = 3$.

2.2.4 Optimal phosphine to palladium ratio

The optimal phosphine concentration and palladium to phosphine ratio were determined in DMEM with serum at 37 °C (Figure 26). No clear correlation between high palladium and phosphine concentrations was observed. Typically, once optimal phosphine concentration is reached, the rate of the reaction decreases because the equilibrium between less ligated and more highly ligated palladium species shift toward the latter at higher phosphine concentrations.^{82, 84} However, our system was more sensitive toward the lower phosphine concentrations, necessary to form the active palladium complex.

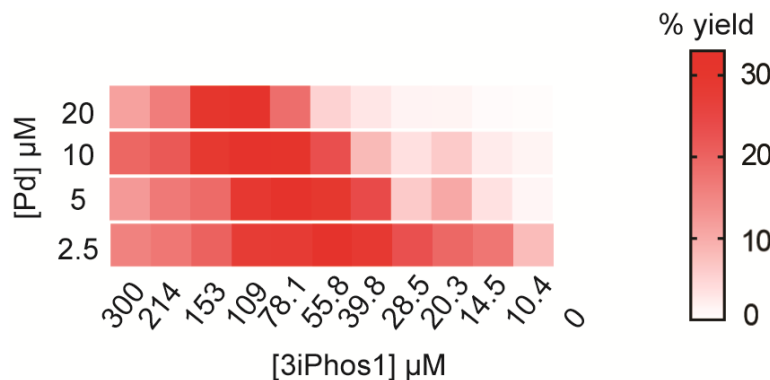


Figure 26. The correlation between palladium concentrations and optimal 3iPhos1 concentrations.

Conditions: 20 μM probe, 20, 10, 5, 2.5 μM Pd(OAc)₂, 300, 214, 153, 109, 78.1, 55.8, 39.8, 28.5, 20.3, 14.5, 10.4, or 0 μM phosphine, 1 % DMEM/25 mM phosphate pH 7 buffer (10 % FBS), n = 3, 37 °C.

2.2.5 Rate constant

With the fluorometrically measured concentrations of resorufin (Figure 27a), RAE concentrations were calculated (Figure 27b) and ln[RAE]versus time (s) was plotted (Figure 27c)

to obtain observed rate constants k' as the slope of the linear plot (Figure 27d). An increase in fluorescence over time was measured upon the addition of $\text{Pd}(\text{OAc})_2$ and the phosphine to RAE to determine the second-order rate constant. The fluorescence readout was converted to the amount of resorufin using the standard curve. Based on the pseudo first-order kinetic studies (Figure 27d), the second-order rate constant k of the reaction was calculated to be $257 \pm 10.3 \text{ M}^{-1}\text{s}^{-1}$.

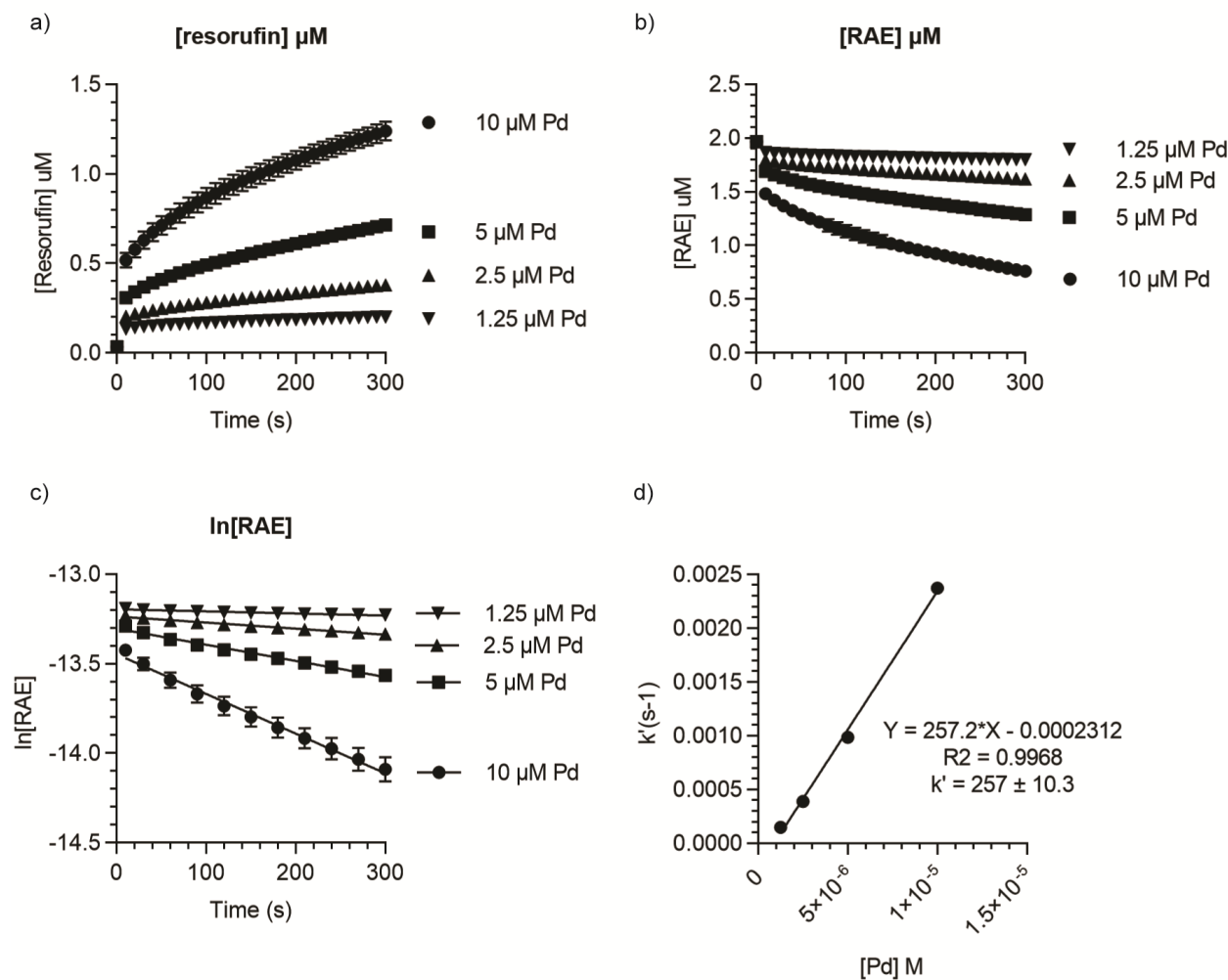


Figure 27. Kinetics of palladium catalyzed deallylation. Conditions: 2 μM RAE, 10, 5.0, or 2.5. 1.25 μM $\text{Pd}(\text{OAc})_2$, 60, 30, 15, or 7.5 μM phosphine, 1 % DMEM/25 mM phosphate pH 7 buffer (10 % FBS), $n = 3, 37$ °C.

2.2.6 Copper does not interfere with palladium catalyzed decaging in the presence of TFP analogs.

Copper is an essential metal in biology.¹⁹⁶ In combination with some phosphine ligands, copper is known to facilitate depropargylation inside the cells.¹⁵³ Thus, we tested whether copper would interfere with our palladium catalyzed reaction and facilitate the decaging of RPE (Figure 28). Both, RAE and RPE, reacted with Pd(OAc)₂. However, CuSO₄ alone, or in combination with Pd(OAc)₂ did not lead to any additional reaction. Therefore, our method does not suffer from copper interference even at high concentrations.

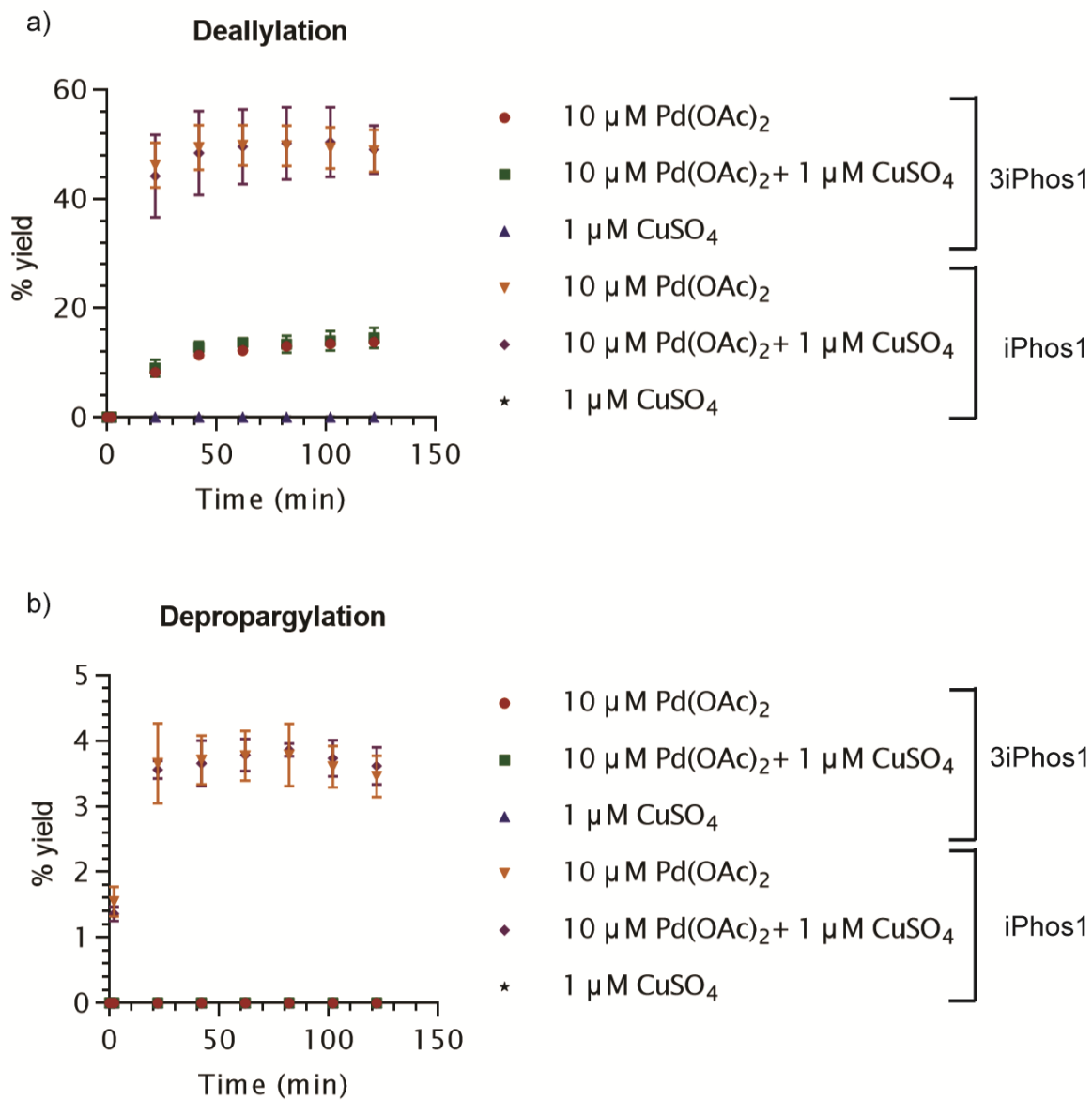


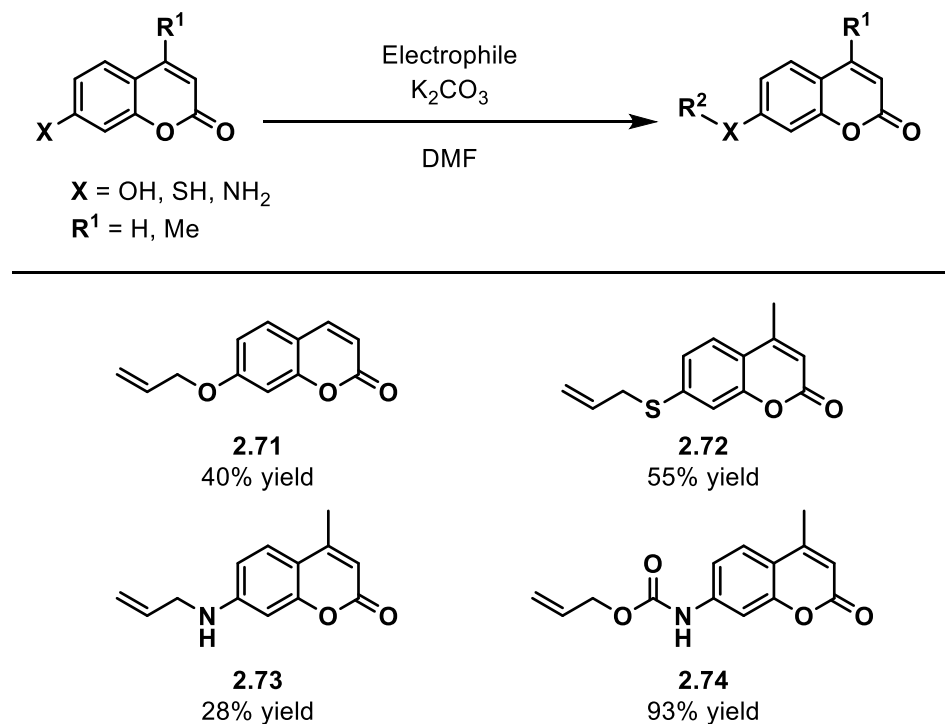
Figure 28. Copper interference with lead phosphines. (a) Copper does not interfere in the presence of iPhos1. (b) Copper does not interfere in the presence of 3iPhos1. Conditions: 20 μM RAE, 10 μM Pd(OAc)₂, 1.0 μM CuSO₄, 60, 30, 15, or 7.5 μM phosphine, 1 % DMEM/25 mM phosphate pH 7 buffer (10 % FBS), n = 3, 24

°C.

2.2.7 The scope of palladium-catalyzed deallylation.

With optimized conditions in hand, we turned our attention to the scope of the reaction. The efficiency of the allylic and propargylic C–O bond cleavage depends on the pKa of the leaving group (a fluorophore in our case).⁴⁷ Thus, coumarin based probes containing functional groups with various pK_a were synthesized (Table 2). We decided to continue to use fluorophores as the leaving groups due to high sensitivity, which allowed us to run reactions at low concentrations.

Table 2. Synthesis of coumarin based probes.



A variety of coumarin-based fluorophores and other probes previously synthesized in our lab with pK_a ranging from 3.9 to 30 were tested (Figure 29).¹⁹⁷⁻²⁰¹ To our surprise, no correlation between the pK_a of the leaving group and the yield was observed for the substrates that were

successfully uncaged. Components in the reaction media may be interacting with the substrates to facilitate the reaction; similar to the phosphate buffer in the chapter above. However, aniline based analog **2.73** showed no reaction indicating that there is a pK_a limit for this transformation.

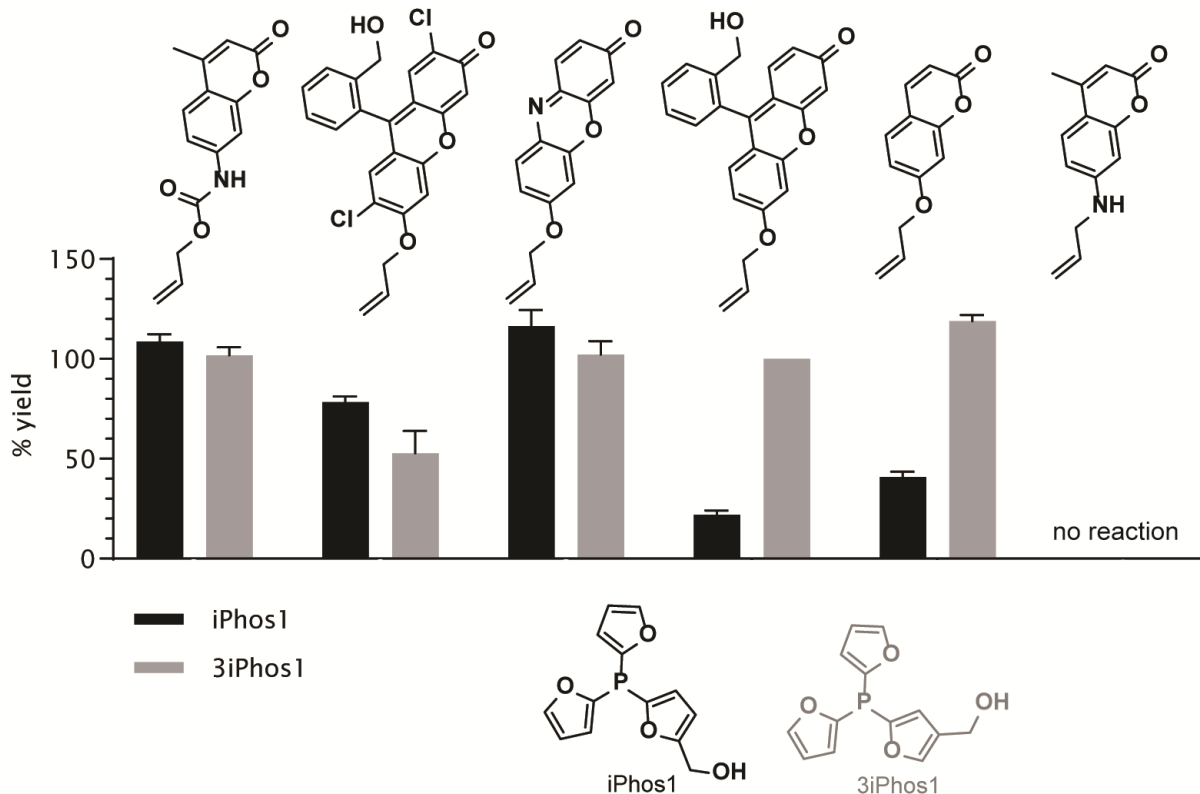
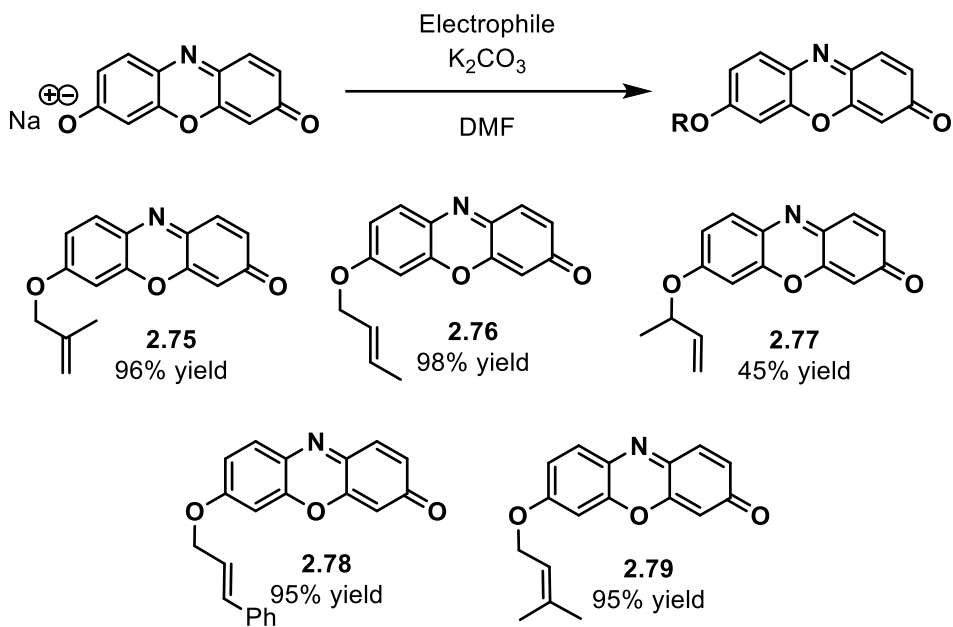


Figure 29. Substrate scope of deallylation based on the pK_a of the leaving group. Conditions: 10 μM probe, 20 μM Pd(OAc)₂, 120 μM phosphine, 1 % DMSO/DMEM/25 mM phosphate pH 7 buffer (10 % FBS), 1 h, n = 3, 37 °C.

Resorufin based probes **2.75–2.79** with varying sterics around the olefin were synthesized from resorufin sodium salt and corresponding electrophiles (Scheme 40). Additional methyl or phenyl substituents were installed to test whether handles could be attached to the probes to make more selective caged molecules.



Scheme 40. Synthesis of sterically hindered resorufin analogs.

The sterics of the alkene influenced the rate of the reaction (Figure 30).²⁰² Least sterically hindered RAE performed the best. Substrates with one methyl **2.75–2.77** or phenyl **2.78** group attached to the alkene or the allylic methylene were approximately 50% less efficient than RAE. The tri-substituted alkene **2.79** was unreactive under the reaction conditions. We suspect that the sterically hindered olefin impedes the association of palladium-phosphine complex and the alkene, which may be the turnover limiting step for this substrate.²⁰²

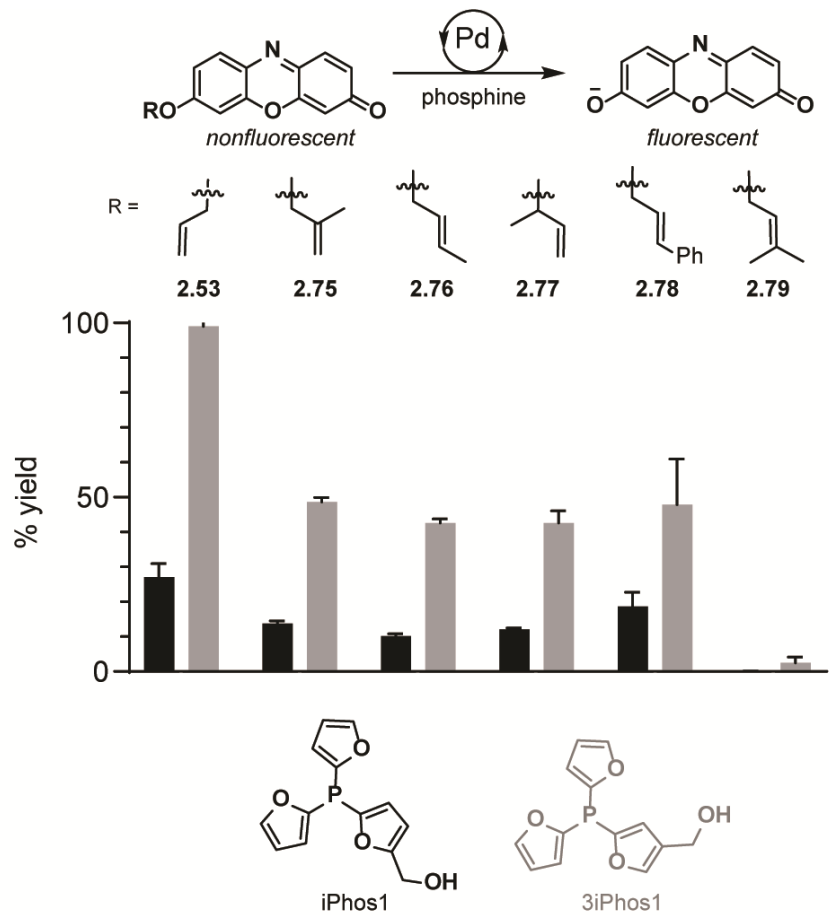


Figure 30. Substrate scope of deallylation based on the sterics of the alkene. Conditions: 10 μM probe, 20 μM $\text{Pd}(\text{OAc})_2$, 120 or 0 μM phosphine, 1 % DMEM/25 mM phosphate pH 7 buffer (10 % FBS), 1 h, n = 3, 37 °C.

2.3 Conclusions

Novel TFP analogs were synthesized and tested in biological media (DMEM with 10% serum). This palladium-catalyzed deallylation with phosphine as an added ligand was 35 times faster than previously reported phosphine-free palladium-catalyzed depropargylation in serum-containing cell culture media. The second-order rate constant k of the reaction was calculated to

be $257 \pm 10.3 \text{ M}^{-1}\text{s}^{-1}$. This method is not very sensitive to the pK_a of the leaving group and is able to facilitate deallylation of sterically hindered substrates.

2.4 Future Plan

Further cell imaging studies are necessary to test whether this combination of palladium and new TFP analogs can facilitate deallylation and depargylation *in vivo*. These phosphines must be cell-permeable to facilitate the reaction inside the cells. Furthermore, phosphines are typically avoided due to possible toxicity; thus, further cell toxicity studies are also necessary.

Additionally, palladium has been shown to accumulate in the kidneys of rats exposed to heavy metal through drinking water.²⁰³ Thus, our method has the potential to be used to selectively release prodrugs to treat kidney cancer. This will allow for targeted treatment and may lower the side effects associated with cancer drugs due to off-target effects.

In Figure 30, we showed that our palladium-phosphine method is, although sensitive, still capable of facilitating the deallylation of sterically hindered substrates. This indicates that our allylic C-O bond cleaving method allows for an attachment of a handle, such as an antibody.²⁰⁴ Therefore, it can be used as a removable linker and a protecting group for the antibody-drug conjugates (ADCs; discussed in the section below) allowing bioorthogonal release of toxic cargoes at tumor sites.

3.0 Synthesis of a Tetrahydrofuran Analog of FR901464

3.1 Introduction

3.1.1 Discovery of FR901464

While searching for natural products with anticancer activity that poses new modes of action, Fujisawa Pharmaceutical Company discovered and isolated FR901463, FR901464, and FR901465 (Figure 31) from the fermentation broth of *Pseudomonas* sp. No. 2663.²⁰⁵⁻²⁰⁶ All three natural products exhibited antitumor activity in A549 (human lung adenocarcinoma), HCT116 (human colon carcinoma), MCF-7 (human breast adenocarcinoma), P388 (murine leukemia), and SW480 (human colon adenocarcinoma). FR901464 was identified as the most potent antitumor agent out of the three natural products, with GI₅₀ of 0.61–3.33 nM. The antitumor activities of the three natural products were evaluated in mice bearing A549, Colon 38 (murine colon adenocarcinoma), Meth A (murine fibrosarcoma), and P388 tumors. Of the three compounds, FR901464 was the most effective.

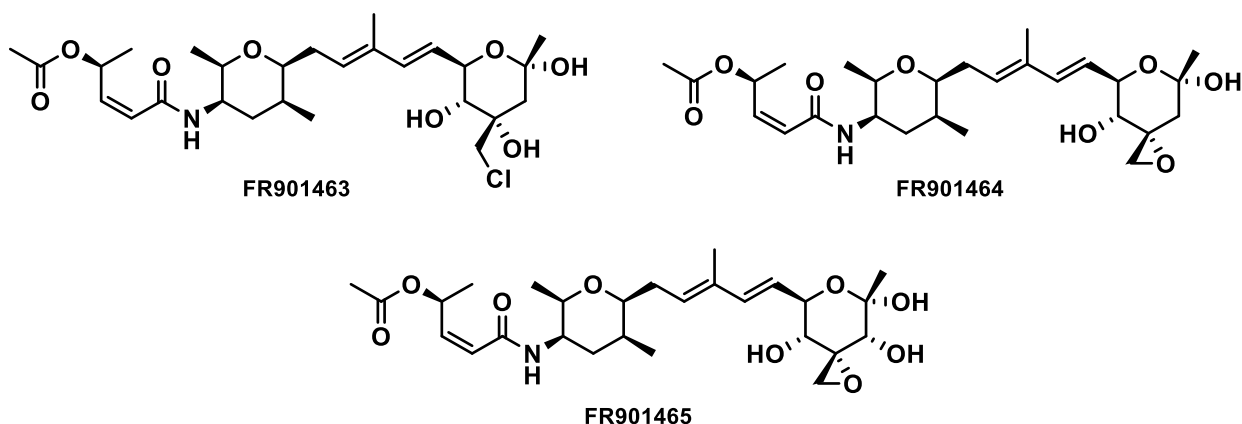


Figure 31. Chemical structures of FR901463, FR901464 and FR901465.

3.1.2 Mode of action

The Nakajima group used 5-bromo-2'-deoxyuridine (BrdU) cell labeling assay to elucidate the mode of action. Incorporation of BrdU in FR901464-treated M-8 cells against numerous control cell cycle inhibitors with known mechanisms of action (adriamycin, camptothecin, and Taxol®) was evaluated. A decrease in cells entering S phase and exiting from G₂/M phase was observed in FR901464-treated M-8 cells. It was determined that FR901464 induced G₁ and G₂/M phase cell cycle arrest. A similar effect on cell cycle distribution was observed for other cancer cell lines.

Additionally, cell shrinkage, associated with induced DNA fragmentation, was observed in cells treated with FR901464. Thus, chromatin status in the FR901464-treated cells was examined, as a sign of DNA fragmentation, using the photometric enzyme immunoassay. An enrichment of nucleosomes was observed in cytoplasm of FR901464 treated cell, indicating the degradation of chromatin.

The Yoshida group used biotinylated spliceostatin A (Figure 32), a methylated derivative of FR901464, and pull-down studies to identify the molecular target of FR901464.²⁰⁷ Splicing factor 3b subunit 1 (SF3B1) was identified as the biological target of FR901464 and its analogs. SF3B1 is a protein of the U2 small nuclear ribonucleoprotein (snRNP). It is required for binding to the branchpoint sequence during splicing.²⁰⁸

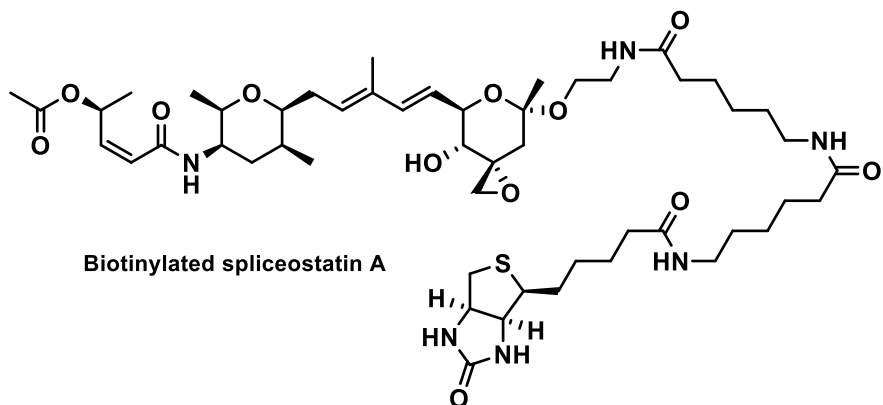


Figure 32. Chemical structure of the biotin derivative of spliceostatin A.

In 2021, the Pena group discovered that the SF3B subunit PHF5A was also the target of FR901464.²⁰⁹ A crystal structure of Spliceostatin A and SF3B revealed that the epoxide of FR901464 analogs reacts with one of the four cysteine residues of PHF5A's zinc finger (Figure 33). This finding may explain high potency of select FR901464 analogs that contain the epoxide moiety.

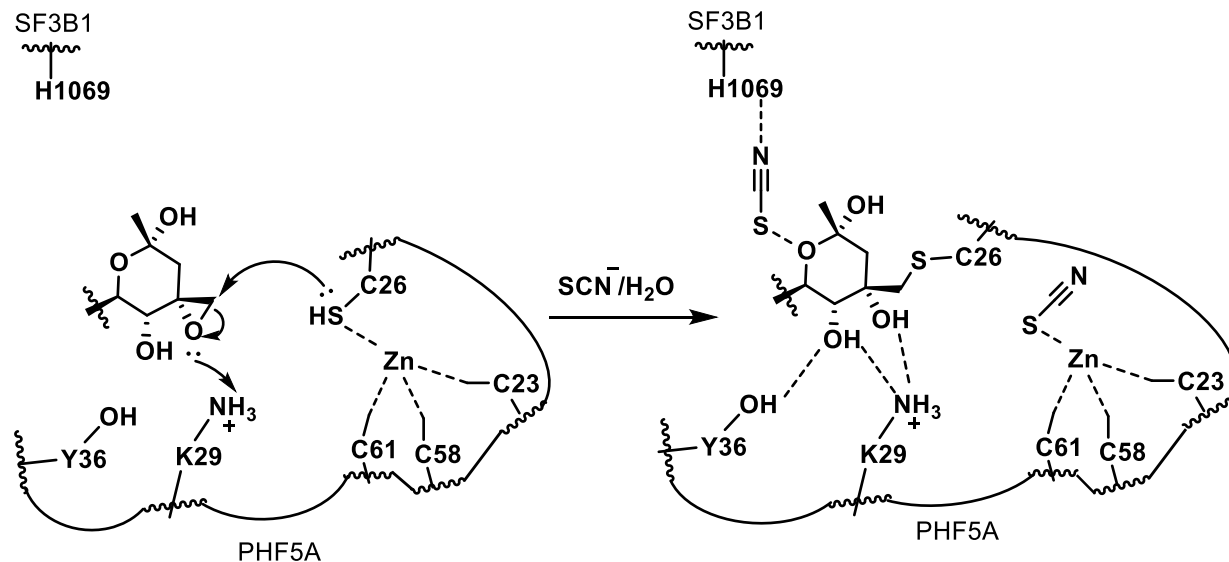


Figure 33. Mechanism of covalent coupling of Spliceostatin A to the nucleophilic zinc finger of PHF5A.

3.1.3 Alternative splicing and FR901464

Alternative splicing is the main source of diversity of the proteome in eukaryotes.²¹⁰

Alternative splicing creates protein diversity through the differential use of splice sites (Figure 34).

Exons are alternatively spliced to generate various forms of mRNA from the same pre-mRNA.

High-throughput sequencing studies suggest that 95–100% of human pre-mRNA that consists of multiexon yield multiple mRNAs.²¹¹

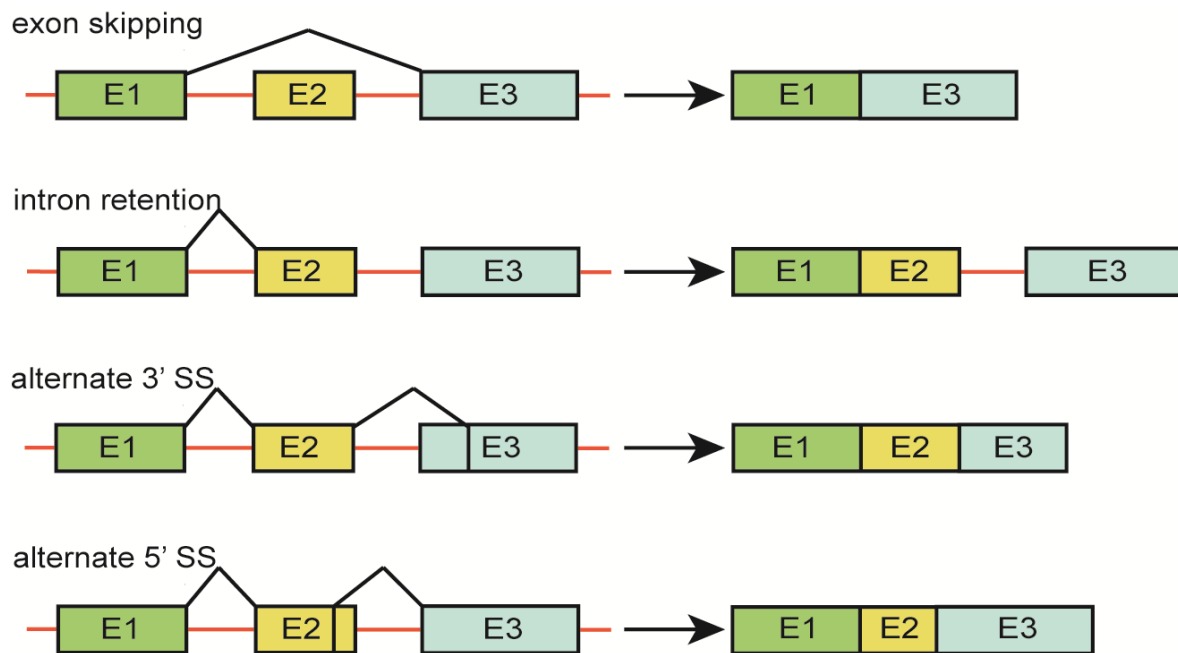


Figure 34. Pathways of alternative splicing.

FR901464 binding to SF3B1 in the U2-snRNP disrupts branch site recognition, which as a result, leads to a shift in alternative splicing of myeloid cell leukemia-1 gene (*Mcl-1*; Figure 35).²¹²⁻²¹⁴ The *Mcl-1* pre-mRNA encodes the long antiapoptotic *Mcl-1_L* and the short proapoptotic *Mcl-1_S*. Overexpression of *Mcl-1_L* is observed in melanoma,²¹⁵ advanced renal cell carcinoma,²¹⁶

breast,²¹⁷⁻²¹⁹ colon²²⁰⁻²²¹ and many others cancers²²²⁻²²⁶ and linked to intrinsic and acquired resistance to various FDA-approved anticancer drugs.^{216, 227-233}

Knocking down *Mcl-1* improves response to anticancer drugs in different cell lines.^{232, 234-235} Various small molecule inhibitors of pan-Bcl-2 family protein have been reported to have anti-*Mcl-1* activity.²³⁶⁻²⁴¹ Furthermore, small molecule inhibitors of *Mcl-1* have shown promising results in various cancer cell lines, but many suffered from side effects related to mitochondria functions.^{224, 238, 242-246}

Treatment with FR901464 shifts splicing preferentiality toward proapoptotic *Mcl-1s* (Figure 35). By reversing the dominant isoform from *Mcl-1L* to *Mcl-1s*, FR901464 and analogs, in combination with Bcl-XL inhibitor ABT-737, leads to cell death.²¹³ FR901464 analogs are capable of restoring sensitivity for otherwise ineffective FDA-approved anticancer drugs due to *Mcl-1L* overexpression.²⁴⁷

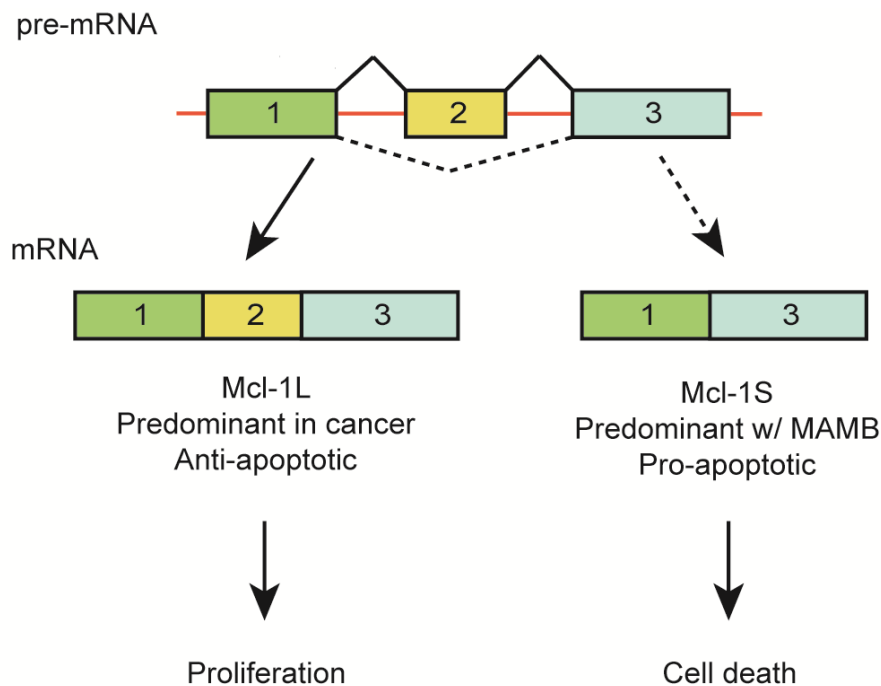


Figure 35. Alternative splicing with FR901464 analogs.

3.1.4 Natural product splicing regulators

An increasing amount of data linking splicing and disease led to the interest in the development of small molecules targeting the spliceosome. Several natural products, FR901464,²⁰⁵ herboxidiene,²⁴⁸ pladienolide B²⁴⁹, and thailanstatin A²⁵⁰, have been found to modulate splicing through binding of SF3B1 (Figure 36).^{207, 251-252} The unique mode of action for these natural products in combination with the interest in small molecules targeting the spliceosome as led to total synthesis efforts and analog development in several laboratories.²⁵³⁻²⁷⁶ These natural products have structural similarities, such as the diene, acetate, and epoxide. Some compounds of this class have been evaluated in the clinical trials, but had little success.²⁷⁷⁻²⁷⁹

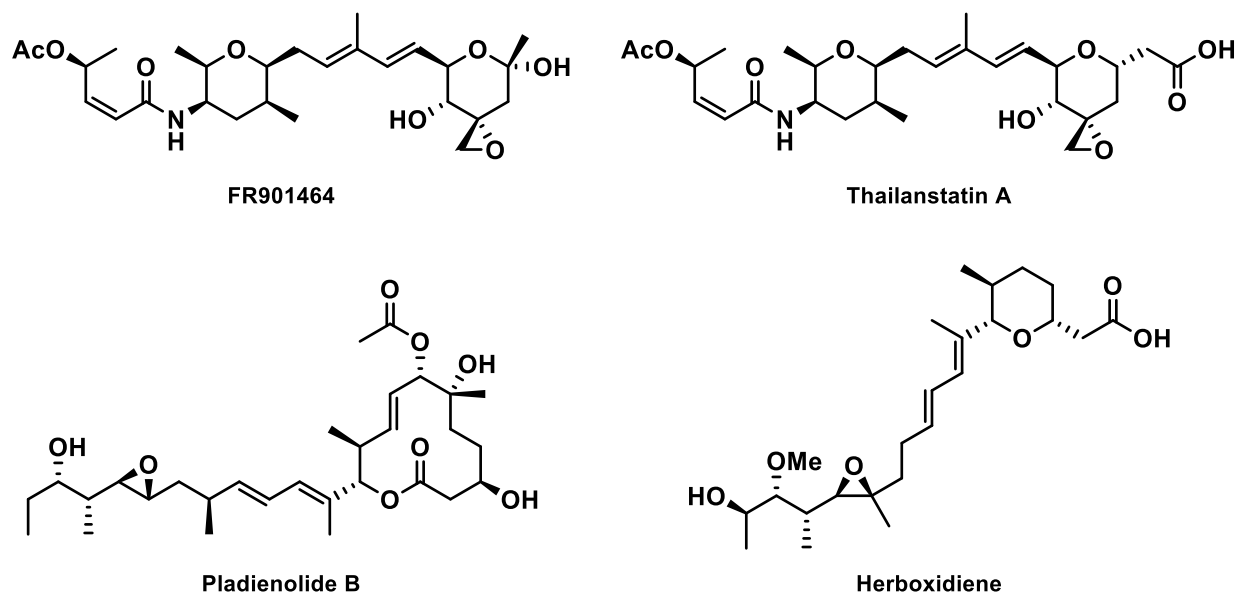


Figure 36. Natural product splicing regulators.

3.1.5 Synthetic strategy

The synthetic strategy from the Koide group follows a convergent route that disconnects the molecule into three main intermediates: the sidechain, the left fragment, and the right fragment (Figure 37). The side-chain acid and the left fragment amine are combined via an amide bond coupling. The resulting diene is then coupled with the right fragment alkene through olefin metathesis to give the final product. This synthetic strategy was adopted because it allows for facile functionalization of the functional groups for further analog development.

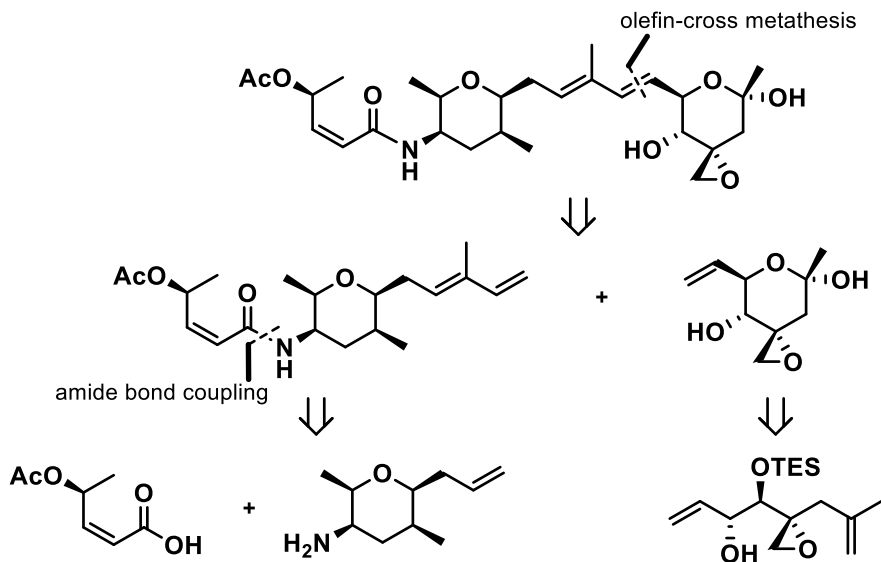


Figure 37. Convergent synthesis of FR901464 analogs.

3.1.6 FR901464 structure activity relationship (SAR) studies

Continued interest in FR901464 due to its antiproliferative activity in cancer cells led to extensive SAR studies.^{254-255, 258, 260, 262, 280-284} These studies outline key functional groups

necessary for the cytotoxic activity of FR901464 (Figure 38). The right pyran ring can exist in an open or close form. The hemiketal was shown to collapse under various conditions.²⁵⁸ Replacing the hydroxy group on C1 with a hydrogen produced an analog equipotent to FR901464.²⁵⁴ This indicated that the cyclic structure of the right pyran ring as the active form of FR901464. Methylation of the hydroxy group lead to the synthesis of more stable spliceostatin A.²⁸¹ Furthermore, replacing the hydroxy group with a methyl increased the half-life of the pyran ring and the potency of the small molecule by 100-fold.²⁵⁸ This analog was named meayamycin.

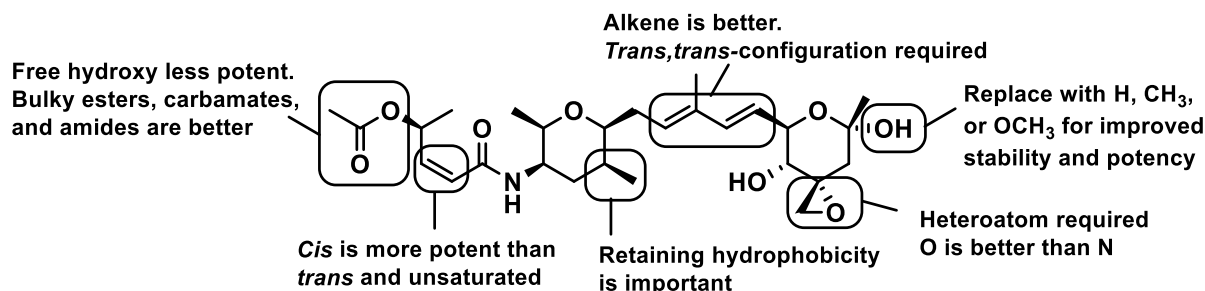


Figure 38. SAR summary of FR901464.

Replacing the epoxide with cyclopropane led to loss of activity.²⁵⁴ Exocyclic alkene²⁸¹ and various non-epoxy analogs²⁶⁰ were found to be less potent. The Nicolaou group synthesized an aziridine analog, which remained potent.²⁶² A recently published crystal structure of SF3B in complex with spliceostatin A revealed that FR901464 analogs are covalent binders; the epoxide acts as the electrophilic warhead of the molecule to form a covalent bond with PFH5A (Figure 33).²⁰⁹

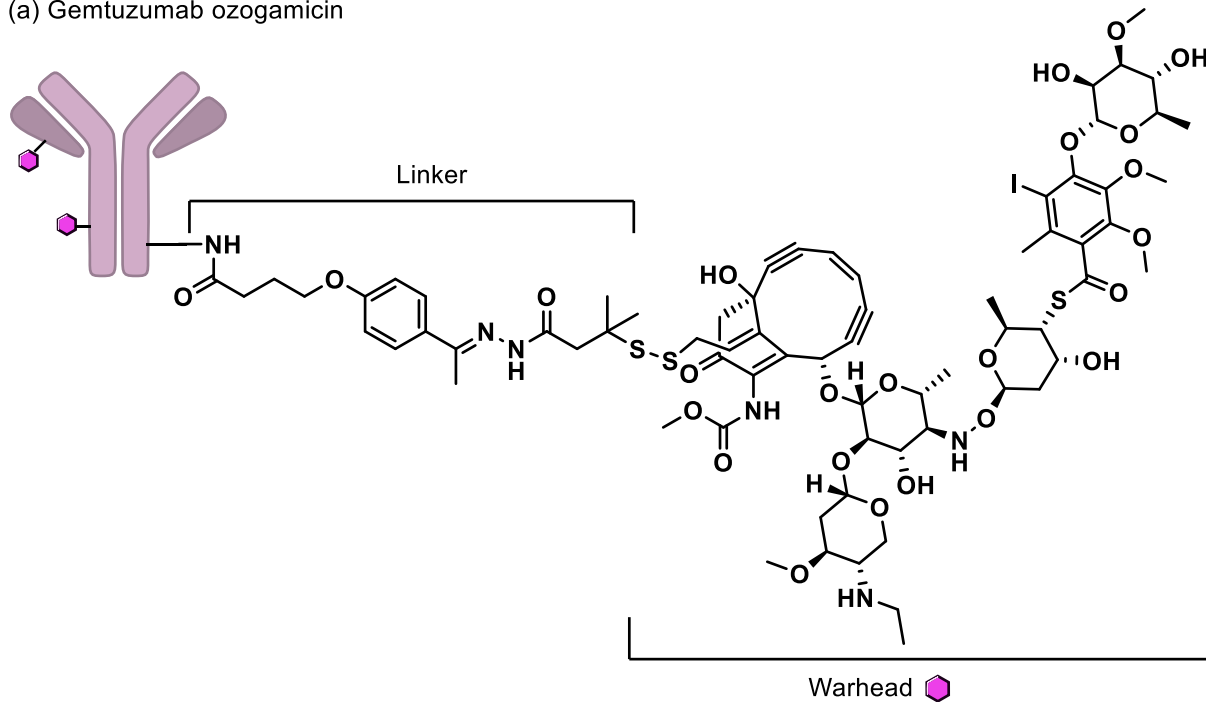
Modifications of the left pyran ring led to reduced potency.^{260, 285} Initial modifications of the side chain suggested that it is not as sensitive to alterations compared to the epoxide.²⁵⁴ Saturation or isomerization of the enoate led to diminished potency.²⁶⁰ Sterically bulky acetyl

esters were comparable in potency.²⁸³ Replacing the acetyl ester with more metabolically stable morpholine carbamate led to a more potent analog meayamycin B.²⁶⁰

3.1.7 Drug-conjugates

ADCs are biopharmaceutical drugs that consist of recombinant monoclonal antibodies (mAb) and cytotoxic drugs (warheads) covalently bound through a linker.²⁸⁶ This class of drugs is designed to target and kill cancer cells over healthy cells. Highly cytotoxic, small-molecule drugs are intended to kill cells, while mAb provides selectivity and stability. Cytotoxic drugs that either damage DNA or block mitosis are typically used as warheads for ADCs. Gemtuzumab ozogamicin was the first ADC that received regulatory approval by the US Food and Drug Administration (FDA). It consisted of an anti-CD33 mAb conjugated to calicheamicin (Figure 39a) and was designed to treat acute myeloid leukemia.²⁸⁷ The development and subsequent approval of trastuzumab deruxtecan (Figure 39b) demonstrated that new types of warheads can be used to overcome resistance.²⁸⁸ These advancements paved the way for clinical trials of more cytotoxic and selective ADCs with new types of warheads.

(a) Gemtuzumab ozogamicin



(b) Trastuzumab deruxtecan

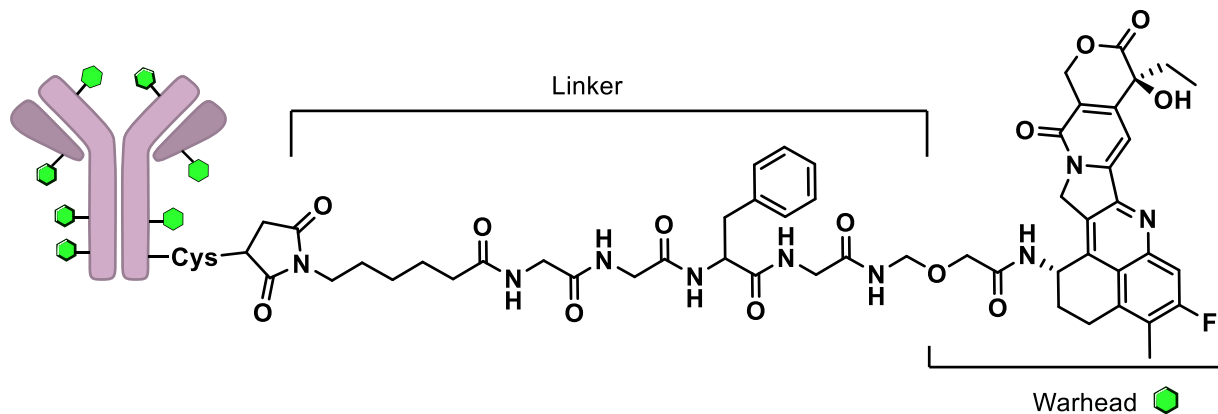


Figure 39. Structures of selected ADCs.

Glycoconjugation, the linking of a drug to a sugar, is another promising strategy for targeted cancer therapy because cancerous cells require more glucose compared to normal tissue.²⁸⁹ However, this strategy suffers from rapid clearing and lower toxicity of drug conjugates. The Chen group reported the development of paclitaxel conjugated to glucose (Figure 40a).²⁹⁰ This

drug-conjugate showed selective cytotoxicity against cancer cell lines and reduced toxicity toward normal cell lines. However, lower cytotoxicity was also reported toward cancer cell lines with low expression levels of glucose transporters. The Mikuni and Mandai groups reported the synthesis of docetaxel conjugated to galactose (Figure 40b).²⁹¹ The drug conjugate had superior water solubility and antitumor activity equivalent to docetaxel. However, it was excreted more readily and the uptake by cancerous cells was not studied.

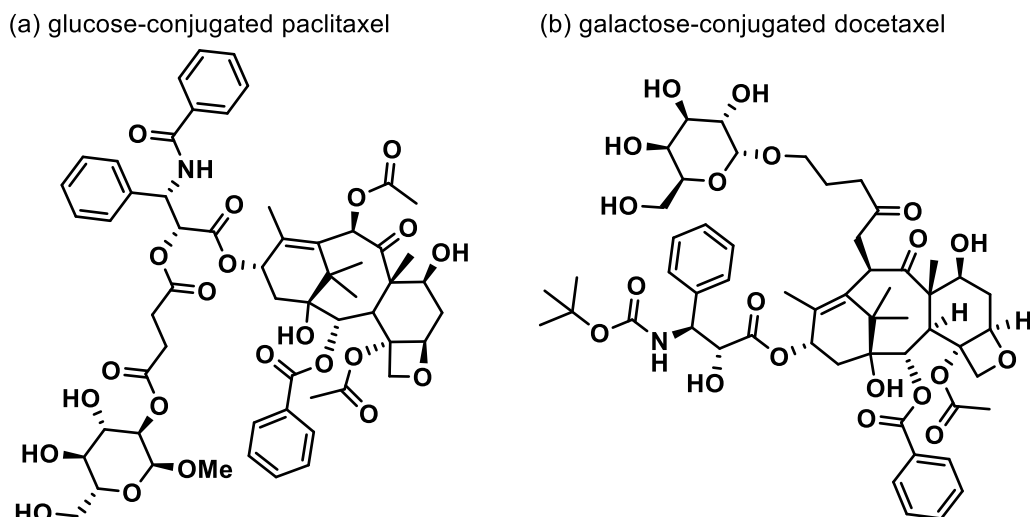
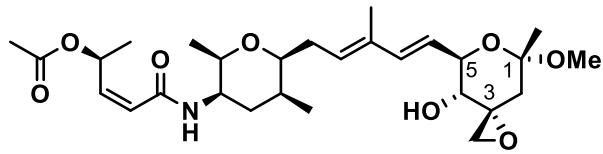


Figure 40. Examples of drugs conjugated to sugars.

We were interested in conjugating FR901464 to an antibody or a sugar to improve drug delivery to tumors while reducing drug exposure to normal tissues. The crystal structure of SF3B in complex with spliceostatin A showed that the axial position at C1 (Figure 41) could handle further modifications.²⁰⁹ Furthermore, this position has been previously conjugated to biotin (Figure 32) without loss in activity.²⁰⁷



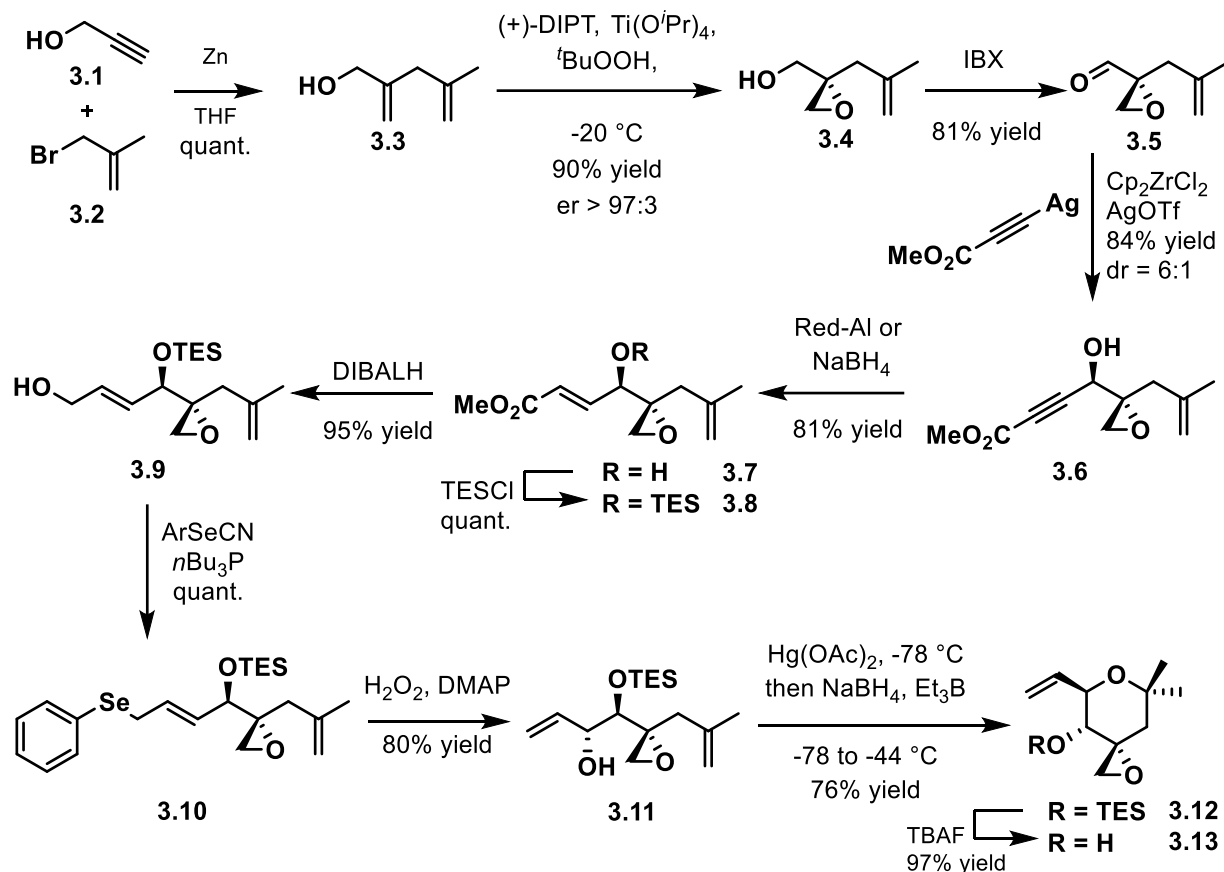
Spliceostatin A

Figure 41. Structure of Spliceostatin A.

3.2 Results and discussion

3.2.1 Right fragment synthesis

The efforts towards the synthesis of the conjugatable analogs were based on the same convergent scheme previously developed for other analogs. The right fragment was synthesized according to the published first-generation synthesis (Scheme 41).²⁵⁷⁻²⁵⁸ Zinc-mediated coupling of propargyl alcohol and methallyl bromide affords the diene **3.3**, which is epoxidized using Sharpless' conditions. The alcohol **3.4** is oxidized with IBX and the subsequent aldehyde **3.5** undergoes Zr/Ag-promoted alkanylation to give an ester **3.6**, which can be selectively reduced to the enoate **3.7** in the presence of Red-Al. The secondary alcohol is protected as silyl ether **3.8**, and the ester is reduced by DIBALH to give the primary allylic alcohol **3.9**. Grieco-type substitution of allylic alcohol yields selenide **3.10**, which upon oxidation with H₂O₂ undergoes [2,3]-seleno Mislow-Evans rearrangement to give the key secondary allylic alcohol **3.11**. Finally, Hg-mediated cyclization gives pyran **3.12**, which is deprotected to yield the right fragment epoxide **3.13**.

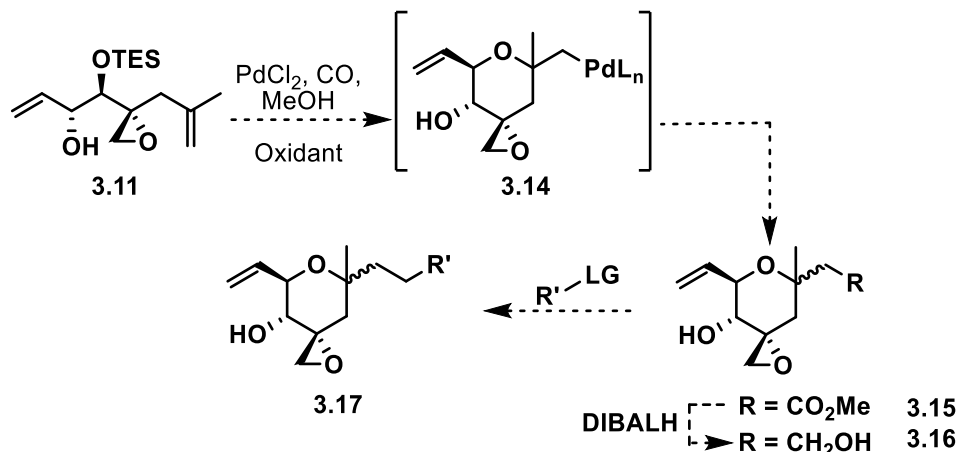


Scheme 41. First generation synthesis of right fragment.

3.2.2 Efforts towards more versatile right fragment analog through a Wacker-type oxy-palladation.

The Hg-mediated cyclization requires stoichiometric amounts of toxic $\text{Hg}(\text{OAc})_2$. This step is not scalable because large amounts of toxic waste will be produced as a result. We envisioned that this cyclization could be achieved through a Wacker-type oxy-palladation to afford the key palladium(II) intermediate **3.14**, which will subsequently undergo carbonylation with carbon monoxide and esterification in the presence of methanol to afford the methyl ester **3.15** (Scheme

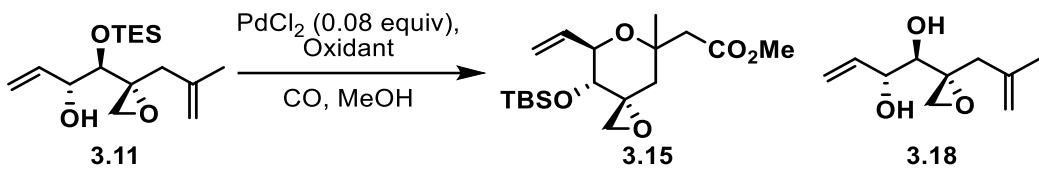
42). Reduction of **3.15** would produce the primary alcohol **3.16** that can be coupled with an electrophile to produce new right fragment analogs. Classical Wacker-type oxy-palladation conditions usually afford 1:1 mixture of diastereomers.²⁹²⁻²⁹³ Thus, we were interested in developing diastereoselective cyclization after we determine the optimal reaction conditions.



Scheme 42. Synthetic scheme for Wacker-type oxy-palladation.

We started with classical Wacker-type oxy-palladation conditions.²⁹²⁻²⁹³ Secondary alcohol **3.11** was exposed to catalytic amounts of PdCl_2 and an equivalent of CuCl_2 (Table 3, entry 1). Starting material was consumed, but a complex mixture of products was observed. Decreasing the substrate concentration had little effect on the reaction (Table 3, entries 1–3). Other oxidants were screened (Table 3, entries 4–7), but only led to TES deprotection to yield the diol **3.18** or no reaction. Different palladium sources were also assessed, but did not lead to the formation of the desired product (Table 3, entries 8–10).

Table 3. Conditions for Wacker-type oxi-palladation.

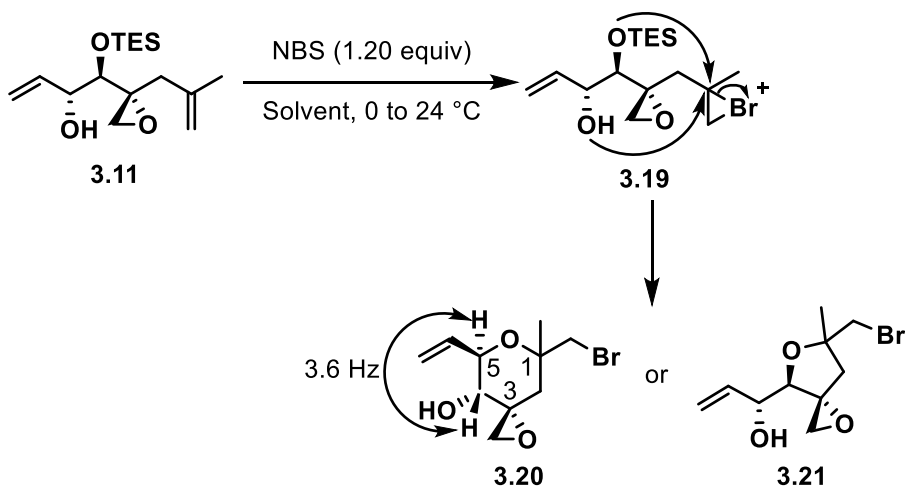


Entry	Oxidant (equiv)	Palladium reagent	Conc. of 3.11 (M)	Temp. °C	Comment
1	CuCl ₂ (1.00)	PdCl ₂	0.37	24	Complex mixture
2	CuCl ₂ (1.00)	PdCl ₂	0.28	24	Complex mixture
3	CuCl ₂ (1.00)	PdCl ₂	0.14	-78 to 24	Complex mixture
4	Oxone® (1.00)	PdCl ₂	0.14	24	TES deprotection
5	AgOAc (1.00)	PdCl ₂	0.14	24	No reaction
6	PhI(OAc) ₂ (1.00)	PdCl ₂	0.14	24	No reaction
7	Benzoquinone (1.50)	PdCl ₂	0.14	24	No reaction
8	None	Pd(OAc) ₂	0.14	24	TES deprotection
9	Benzoquinone (1.50)	(PPh ₃) ₂ PdCl ₂	0.14	24	No reaction
10	Benzoquinone (1.50)	(PPh ₃) ₂ Pd(OAc) ₂	0.14	24	TES deprotection

3.2.3 Electrophilic cyclization

We hypothesized that a tetrahydropyran ring could form via an electrophile-mediated cyclization reaction. Upon treatment of **3.11** with N-bromosuccinimide (NBS), a facile cyclization took place (Scheme 43). The reaction with NBS proceeded with high diastereoselectivity, but TES group was removed in the process. It was not clear if TES deprotection happened before or after

the cyclization. If TES group was deprotected prior to the cyclization it could react with the bromonium ion to give a tetrahydrofuran **3.21**.

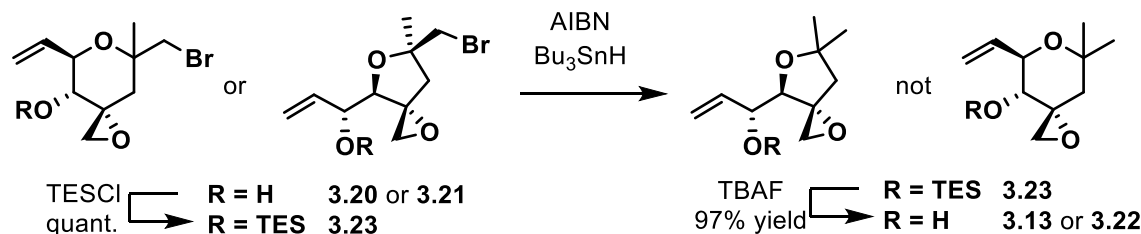


Scheme 43. NBS-mediated cyclization.

From NMR spectra, it was difficult to determine whether five- or six-membered ring was formed. We attempted to derivatize the bromide for X-ray crystallography. However, all derivatives were isolated as oils. We suspected that five-membered ring was formed due to an unusual coupling constant between protons 4 and 5. In FR901464 and meayamycin B, the $J_{4,5}$ was around 10.0 Hz,²⁵⁸ however, the newly formed bromide was observed to have the $J_{4,5}$ of 3.6 Hz. This would indicate a dihedral angle closer to 120° and suggest that the six-membered ring exists in a twist-boat conformation. No other FR901464 analogs were reported to exist in a twist-boat conformation.²⁵⁸

To confirm that the desired six-membered ring was formed, the bromide was debrominated (Scheme 44). The reduction of bromide **3.20** would produce previously reported alcohol **3.13** if electrophilic cyclization yielded the desired tetrahydropyran. Treatment of bromide with Bu₃SnH

and AIBN led to no reaction; however, upon protection as a silyl ether, it was successfully debrominated. ^1H NMR of the product looked different from silyl ether **3.13**. This suggested that NBS-mediated cyclization led to the formation of bromide **3.21** exclusively. The Sohn and Rawal groups also reported that NBS-mediated cyclization led to the formation of kinetically favored tetrahydrofuran with MOM-protected alcohol even in the presence of free alcohol leading to the desired tetrahydropyran.²⁹⁴



Scheme 44. Reduction of bromide.

The 1D NOE experiment was used to determine three-dimensional conformation via the through space relations of protons for the major product of NBS-mediated cyclization, bromide **3.21** (Figure 42). When the peak at 1.52 ppm was irradiated, which corresponds to the methyl group, an interaction was observed with a peak at 3.97 ppm, which corresponds to H5. No correlation was observed between the peak at 3.97 ppm and the doublets at 3.49 and 3.59 ppm corresponding to H9.

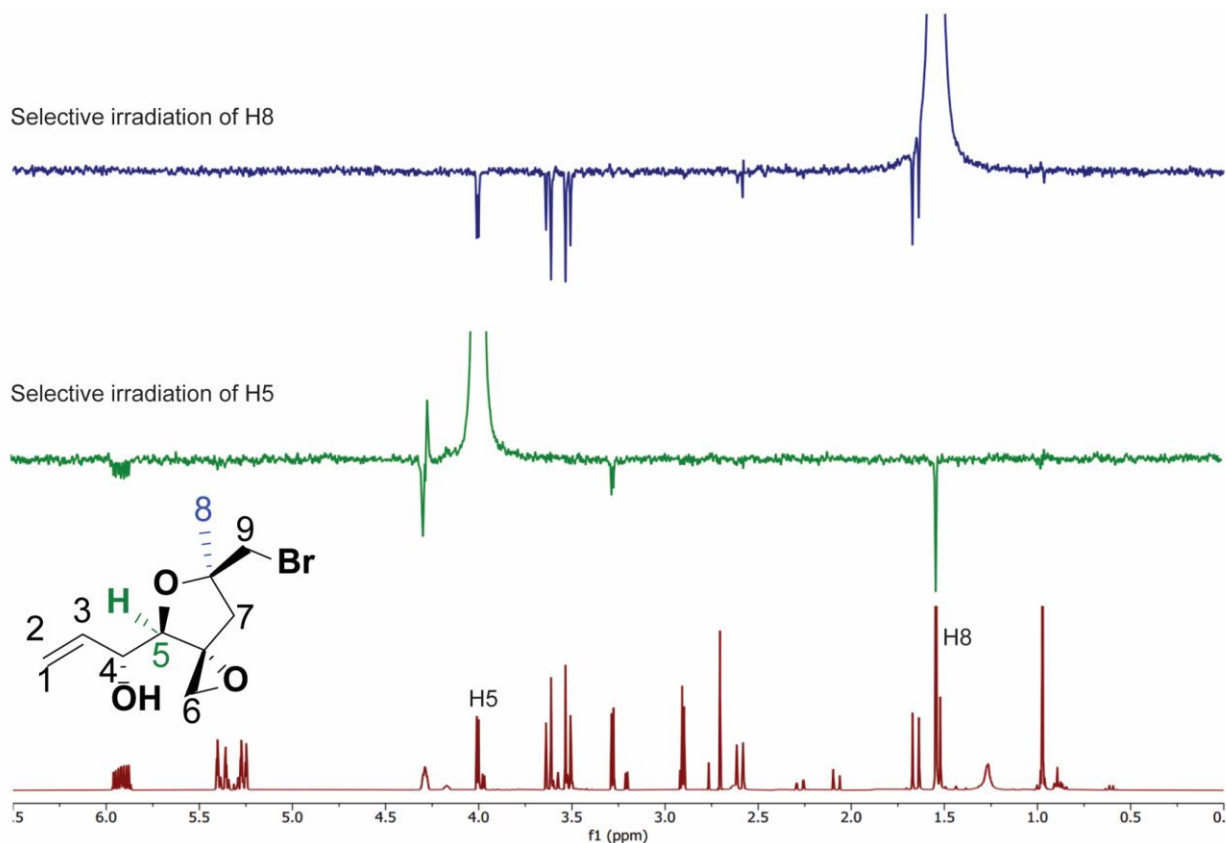


Figure 42. NOESY of tetrahydrofuran 3.21.

The outcome of this electrophilic cyclization is expected to depend on the kinetic selectivity for the bromonium ion formation.²⁹⁵ For NBS-mediated cyclization, the formation of the bromonium ion is generally believed to be reversible.²⁹⁶⁻²⁹⁸ Thus, diastereoselectivity usually reflects the greater kinetic preference of the cyclized intermediate. Generally, *trans*-2,5-tetrahydrofuranes are formed because *trans* isomers are thermodynamically more stable than *cis* isomers.²⁹⁹⁻³⁰⁰ The Fujioka group reported that γ,δ -unsaturated silyl ethers produce *cis*-2,5-disubstituted tetrahydrofurans in the presence of N-iodosuccinimide.³⁰¹ The minor *trans* product can be generated through the high energy transition states due to 1,2-steric interactions (Figure 43). Therefore, more sterically favored *cis* product is observed.

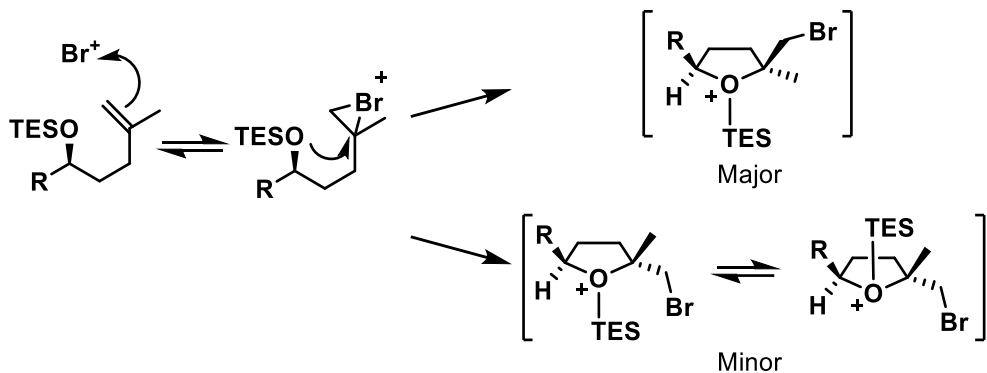
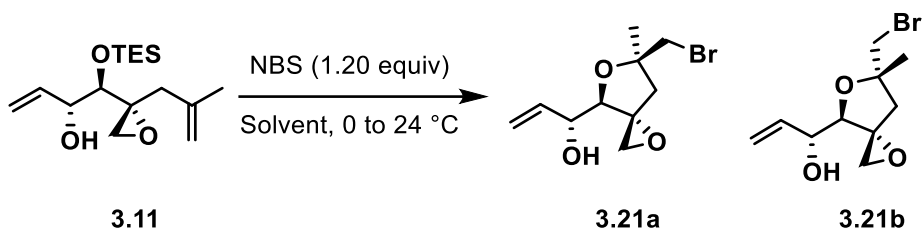


Figure 43. Plausible reaction mechanism for the NBS-mediated cyclization to form tetrahydrofuran 3.21.

Bromide **3.21** was isolated as an inseparable mixture of *cis* and *trans* (5:1) diastereomers; we attempted to control the diastereoselectivity. Lowering the temperature led to minor improvements in diastereoselectivity but lower yields were observed (Table 4, entries 1–3). Because the reaction proceeds through an ionic mechanism, polarity of the solvent may affect the outcome of the reaction. However, addition of polar solvents had no effect on the selectivity of this electrophilic cyclization (Table 4, entries 4–7).

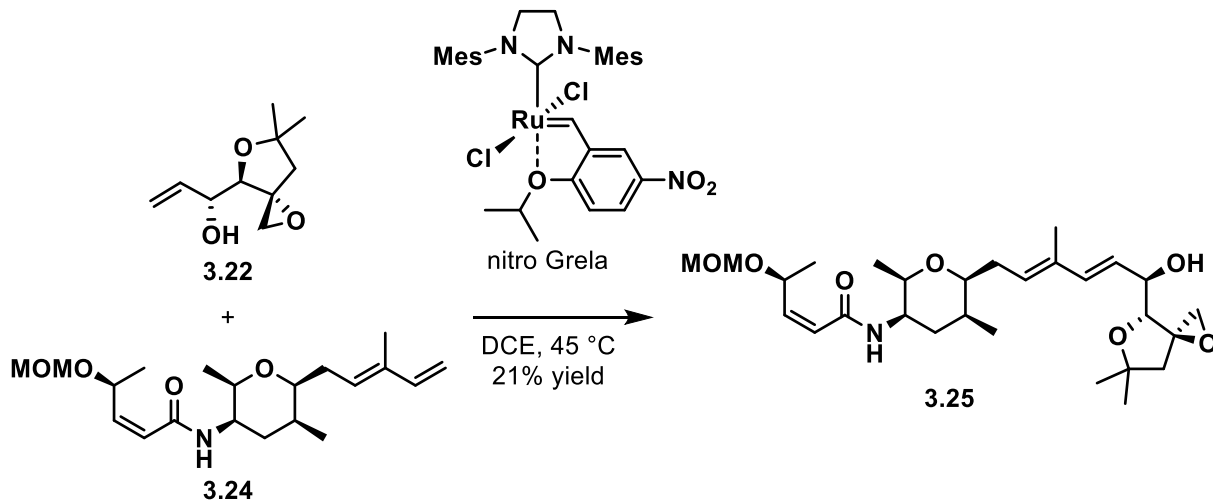
Table 4. Optimization of NBS-mediated cyclization.



Entry	Temperature (°C)	Solvent	d.r. (3.21a : 3.21b)
1	-34	CH ₂ Cl ₂	5.0 : 1.0
2	-78	CH ₂ Cl ₂	6.0 : 1.0
3	-78 to 25	CH ₂ Cl ₂	5.0 : 1.0
4	0	CH ₂ Cl ₂ /H ₂ O (9:1)	5.0 : 1.0
5	0	acetone/H ₂ O (9:1)	4.0 : 1.0
6	0	CH ₂ Cl ₂ /MeOH (7:3)	4.5 : 1.0
7	0	MeCN/MeOH (5:1)	4.0 : 1.0

3.2.4 Synthesis of a tetrahydrofuran analog of FR901464

With the new epoxide **3.22** in hand, final cross coupling between diene **3.24** was performed at 45 °C using nitro Grela catalyst to give an inseparable mixture of **3.25** and the left fragment homodimer (Scheme 45). The material was purified by HPLC and used for subsequent biological testing.



Scheme 45. Cross coupling of tetrahydrofuran analog of FR901464.

3.3 Biological Assay

(Acknowledgement to Professor John Schmitz at UPMC Hillman Cancer Center for performing cell work with HCT116 and LS174T cancer cell lines.)

The ability of tetrahydrofuran analog of FR901464 **3.25** to inhibit the growth of human cancer cells was assessed in a cell-based proliferation assay. The GI₅₀ values were determined using the WST1 assay. Wells were initially seeded with 1,500 cells per well for HTC116 cells and 10,000 cells per well for LS174T cells; 3.33X dilution of compounds was performed with 30 nM or 10 µM as the highest concentration (Figure 44). HCT116 and LS174T are human colon cancer cell lines.

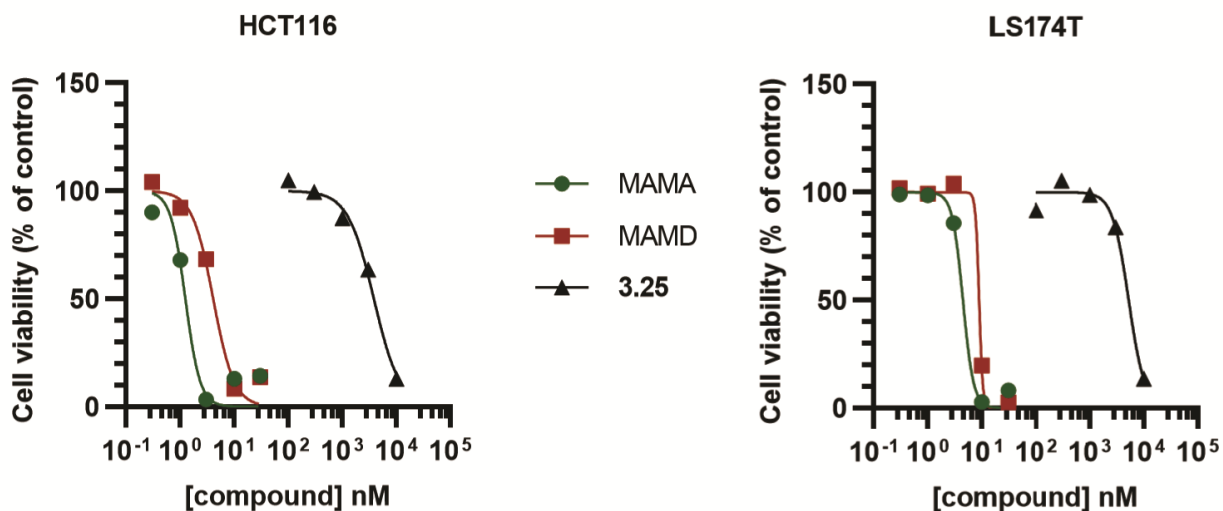


Figure 44. Antiproliferation assay.

(Acknowledgement to Professor John Schmitz at UPMC Hillman Cancer Center)

The results of the antiproliferation assay for **3.25**, meayamycin, and MAMD are summarized in Table 5. The GI₅₀ values are reported as best fits of a 95% confidence interval.

Table 5. Antiproliferative activity of MAMD and meayamycin.

(Acknowledgement to Professor John Schmitz at UPMC Hillman Cancer Center)

Cell line	GI ₅₀ (nM)		
	3.25	meayamycin	MAMD
HTC116	3312	1.11	3.16
LS174T	5434	5.98	9.38

3 day assay, 3.3X dilution, 0-30 nM meayamycin/MAMD, 0-10 μ M IP5134

*values are reported as best fit of a 95% confidence interval range

The tetrahydrofuran analog **3.25** was much less potent than meayamycin, in the low μ M range. The crystal structure of SF3B in complex with spliceostatin A demonstrates that the side chain and the left fragment are required for molecular recognition, while the right fragment epoxy-

tetrahydropyran is necessary for the irreversible, covalent binding to the SF3B complex.²⁰⁹ Furthermore, analogs lacking the epoxide moiety are less potent due to the lack of covalent binding. The tetrahydrofuran analog **3.25** is likely recognized in the binding site, but the epoxide moiety is not positioned close enough to the zinc-coordinated reactive cysteine (Figure 33) to form a covalent bond indicative of high potency.

We further looked at the structural differences between the right fragment of potent MAMD and **3.25** (Figure 45). Overlaying the structures of the two analogs suggests that the dimethyl of **3.25** may be clashing with the residues in the binding pocket.

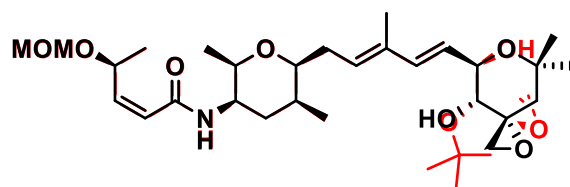


Figure 45. MAMD (black) and 3.25 (red) overlayed.

3.4 Conclusions

Overall, this effort has yielded a novel analog of the natural product FR901464. Initial growth inhibition assays show that tetrahydrofuran analog **3.25** is less potent than meayamycin but still retains low μM growth inhibition. Further work could be aimed at optimizing the position of the epoxide moiety within the right fragment tetrahydrofuran analog to allow for the covalent binding to the zinc-coordinated reactive cysteine and subsequent increased potency.

Appendix A. Supporting Information

Appendix A.1 Kinetics and inverse temperature dependence of a Tsuji–Trost reaction in aqueous buffer

Appendix A.1.1 Instrumentation and reagents

Instrumentation. All fluorescence measurements (excitation 490 nm, emission 510-570 nm) were carried out using a Promega Biosystems Modulus II Microplate Reader. Temperature increments were set using an Eppendorf Mastercycler Gradient PCR thermocycler. A temperature increment was applied, with median autocycler temperatures of 30, 45, 60, and 75 °C to span 20-85 °C (for example, 20, 23, 26, 29, 32, 35, and 38 °C for one experiment, and 35, 38, 41, 44, 47, 50, and 53 °C for another experiment).

Stock solutions. Solutions of APE in DMSO were prepared and stored in amber bottles at 25 °C for up to 6 months. All the TFP solutions in DMSO used in this study were stabilized by 500 or 250 ppm butylated hydroxytoluene (BHT) and stored in amber bottles at 25 °C for >6 months without decomposition. Palladium solutions were prepared by diluting a high purity palladium standard for atomic absorption spectroscopy (9.4 mM in 10% nitric acid) with 5% TraceMetal nitric acid in ultrapure water immediately prior to use (within 6 h).

Reagents. Water in this study was purified by a Barnstead Nanopure Diamond Lab Water System and distilled. Nitric acid was TraceMetal grade. DMSO was used without purification.

Appendix A.1.2 Experimental Procedures

Calculating concentration of APE. After the indicated time for each experiment, the PCR tubes were removed from the thermocycler, cooled to 0 °C on ice, and each solution (180 µL) was transferred to a black 96-well plate to measure fluorescence. Moles of Pittsburgh Green were calculated according to our previous work ($y = 124886x + 511$, where x = Pittsburgh Green concentration in µM and y = fluorescence intensity in arbitrary unit from the instrument³⁰²) and used to measure the product formation. The amount of remaining APE was calculated by subtracting the amount of Pittsburgh Green produced from the initial concentration of APE.

TFP concentration dependence. A solution of 1.23 M phosphate pH 7 buffer (15644 µL), 800 µM APE in DMSO (250 µL), 9.4 µM Pd(NO₃)₂ (16 µL), 2.5 M NaBH₄ in 10 N NaOH (64 µL), and DMSO (26.2 µL) were added to a scintillation vial. Aliquots (969 µL per vial) of the resulting solution were transferred to 2-mL vials and cooled on ice. These aliquots were treated with 0, 0.322, 0.643, 0.965, 1.286, 1.608, 1.929, 2.251, 2.572, 2.894, 3.215, 3.537, 3.859, 4.180, or 4.502 mM TFP in DMSO (31 µL). The resulting solutions were transferred to PCR tubes (200 µL) and incubated at 45, 66, or 80 °C for 30 min. The resulting reaction solutions were analyzed according to *Calculating concentration of APE* ($n = 3$).

Phosphate concentrations dependence. A solution of 1.23 M phosphate pH 7 buffer (4.08 mL), 500 µM APE in DMSO (120 µL), 3.2 mM TFP in DMSO (120 µL), and 50 or 0 nM Pd(NO₃)₂ in 5% TraceMetal HNO₃ (480 µL) were mixed in a scintillation vial (solution **A** with palladium or solution **B** without palladium). Water (18.764 mL), 235 µM APE in DMSO (1.148 mL), 3.2 mM TFP in DMSO (540 µL), and 94 nM Pd(NO₃)₂ in water (1148 µL) were mixed in a scintillation

vial (solution **C**). Water (19.912 mL), 235 μ M APE in DMSO (1.148 mL), and 3.2 mM TFP in DMSO (540 μ L) were mixed in a scintillation vial (solution **D**). All resulting solutions were cooled to 0 °C on ice. Solution **C** (200 μ L) was added to wells rows A–D columns 2–7, and solution **D** (200 μ L) was added to wells rows E–H columns 2–7. Solution **A** (340 μ L) was added to wells rows A–D column1, and solution **B** (340 μ L) added to wells rows E-H column1 in a 96-well plate (1 mL per well). Serial dilutions (1.4 fold) were performed by mixing an aliquot (140 μ L) from wells in column 1 to wells in column 2, mixing and continuing until wells in column 7 were mixed. Discard the last 140 μ L from wells in column 7. Each solution in these well was treated with 100 mM NaBH₄ in 10 N NaOH (20 μ L) to prepare solutions with 10 mM NaBH₄. The resulting solutions were transferred to PCR tubes (200 μ L) and incubated at 45, 66, or 80 °C for 30 min. The resulting reaction solutions were analyzed according to *Calculating concentration of APE (n = 3)*.

NaBH₄ concentration dependence. A solution of 1.2 M phosphate pH 7 buffer (2.04 mL), 500 μ M APE in DMSO (60 μ L), 3.2 mM TFP in DMSO (60 μ L), and 85 or 0 nM Pd(NO₃)₂ in 5% TraceMetal HNO₃ (240 μ L) were mixed in a scintillation vial (solution **E** with palladium or solution **F** without palladium). 1.23 M phosphate pH 7 buffer (9.382 mL), 235 μ M APE in DMSO (574 μ L), 3.2 mM TFP in DMSO (270 μ L), and 188 or 0 nM Pd(NO₃)₂ in 5% TraceMetal HNO₃ (574 μ L) were mixed in a scintillation vial (solution **G** with palladium or solution **H** without palladium). All solutions were cooled to 0 °C on ice. Solution **G** (200 μ L) was added to wells rows A–D columns 2–12 of a black 96-well plate, and solution **H** (200 μ L) was added to wells rows E–H columns 2–12. Solution **E** (360 μ L) and 640 μ M NaBH₄ (40 μ L) in 10 N NaOH were added to wells rows A-D column 1. Solution **F** (360 μ L) and 640 μ M NaBH₄ (40 μ L) were added to wells

rows E–H column 1. Two-fold serial dilutions were performed by taking an aliquot (200 µL) from wells in column 1, adding to wells in column 2, mixing and continuing until wells in column 12 are mixed. Discard the last 200 µL from wells in column 12. The resulting solutions (200 µL) were transferred to PCR tubes and incubated at 45, 66, or 80 °C for 60 min. The resulting reaction solutions were analyzed according to *Calculating concentration of APE* ($n = 3$).

Pd concentration dependence. A solution of 1.23 M phosphate pH 7 buffer (18.8 mL), 800 µM APE in DMSO (348 µL), 32 mM TFP in DMSO (83 µL), 2.5 M NaBH₄ in 10 N NaOH (89 µL) and DMSO (680 µL) were mixed in a scintillation vial. An aliquot of the resulting solution (900 µL) was treated with 0, 7, 9, 11, 13, 15, 18, 22, 26, 31, 38, 45, 54, 65, 78, or 94 nM Pd(NO₃)₂ in 5% TraceMetal HNO₃ (100 µL). The resulting solutions were transferred to PCR tubes (230 µL) and incubated at 45, 66, or 80 °C for 30 min. The resulting reaction solutions (230 µL) were analyzed according to *Calculating concentration of APE* ($n = 3$).

APE concentration dependence. A solution of 1.23 M phosphate pH 7 buffer (2.04 mL), 2.56 mM APE in DMSO (60 µL), 3.2 mM TFP in DMSO (60 µL), and 85 or 0 nM Pd(NO₃)₂ in 5% TraceMetal HNO₃ (240 µL) were mixed in a scintillation vial (solution **I** with palladium or solution **J** without palladium). 1.23 M phosphate pH 7 buffer (9.956 mL), 3.2 mM TFP in DMSO (270 µL), and 188 or 0 nM Pd(NO₃)₂ in 5% TraceMetal HNO₃ (573.6 µL) were mixed in a scintillation vial (solution **K** with palladium or solution **L** without palladium). All solutions were cooled to 0 °C on ice. Solution **K** (180 µL) was added to wells rows A–D columns 2–8 and solution **L** (180 µL) was added to wells rows E–H columns 2–8. Solution **I** (300 µL) was added to wells rows A–D column 1, and solution **J** (300 µL) was added to wells rows E–H column 1. 1.5-fold

serial dilutions were performed by taking an aliquot (120 µL) from wells in column 1, adding to wells in column 2, mixing and continuing until wells in column 8 were mixed. Discard the last 120 µL from wells column 8. Each well was treated with 100 mM NaBH₄ in 10 N NaOH (20 µL). The resulting solutions (200 µL) were transferred to PCR tubes and incubated at 45, 66, or 80 °C for 30 min. The resulting reaction solution was analyzed according to *Calculating concentration of APE (n = 3)*.

Effect of DMSO concentration. A solution of 1.23 M phosphate pH 7 buffer (1.64 mL), 3.3 mM APE in DMSO (7.5 µL), 16, 9.6, 5.3, 3.7, 2.3, 1.7, 1.1, 0.787, 0.516, or 0.384 mM TFP in DMSO (312.5, 232.5, 152.5, 112.5, 72.5, 52.5, 32.5, 22.5, 12.5, or 7.5 µL), and water (0, 80, 160, 200, 240, 260, 280, 290, 300, or 305 µL) were added to scintillation vials to prepare solutions (1.96 mL). These solutions (1.96 mL) were treated with 1.0 M NaBH₄ in 10 N NaOH (20 µL) and 1.0 µM Pd(NO₃)₂ in 5% TraceMetal HNO₃ (20 µL). The reaction mixtures (200 µL) were transferred to PCR tubes and incubated at 45, 60, or 80 °C for 60 min. The resulting reaction solution was analyzed according to *Calculating concentration of APE (n = 4)*.

Effect of DMSO on TFP-palladium binding. A solution of 1.10, 1.13, or 1.20 M phosphate pH 7 buffer (6.615, 6.440, or 6.090 mL), DMSO (35, 210, 560 µL), and 1 mM APE in DMSO (70 µL) were combined in a scintillation vial. The resulting solutions (960 µL) were treated with 500 mM NaBH₄ in 10 N NaOH (20 µL) and 1 µM Pd(NO₃)₂ in 5% TraceMetal HNO₃ (10 µL) followed by 20, 13.3, 8.89, 5.93, or 3.95 mM TFP in DMSO (10 µL). The resulting solutions were transferred to PCR tubes (230 µL) and incubated at 45, 66, or 80 °C for 30 min. The resulting reaction solutions (200 µL) were analyzed according to *Calculating concentration of APE (n = 3)*.

Competition experiment. In two separate scintillation vials, 1.23 M phosphate pH 7 buffer (945.1 μ L), 800 μ M APE in DMSO (15.6 μ L), 32 mM TFP in DMSO (3.75 μ L), and 2.5 M NaBH₄ in 10 N NaOH (4 μ L) were combined. The solution in vial 1 was diluted with DMSO (30.7 μ L). The solution in vial 2 was treated with 3.25 mM phenyl allyl ether in DMSO (3.9 μ L) and DMSO (26.8 μ L). The two solutions were treated with 10 μ M Pd(NO₃)₂ (0.94 μ L). The resulting solutions were transferred to PCR tubes (230 μ L) and incubated at 45, 66, or 80 °C for 30 min. The resulting reaction solutions (230 μ L) were analyzed according to *Calculating concentration of APE* ($n = 3$).

Effect of phosphate ions on TFP-palladium binding. A solution of 1.23 M phosphate pH 7 buffer (18 mL) or 1.23 M phosphate pH 7 buffer (7.32 mL) and water (10.68 mL) and 800 μ M APE in DMSO (459 μ L) were combined in a scintillation vial. Each solution (975 μ L) was transferred to 2-mL Eppendorf tubes and treated with 0, 0.5, 1.0, 2.0, 4.0, or 8.0 mM TFP solutions in DMSO (25 μ L). The resulting solutions were treated with 23.5 μ M Pd(NO₃)₂ in 5% TraceMetal HNO₃ (20 μ L;) and 500 mM NaBH₄ in 10 N NaOH (20 μ L). The resulting reaction solution (200 μ L) was transferred to a black 96-well fluorescence plate, and fluorescence was recorded initially and after incubation at 25 °C for 60 min. The resulting solutions (200 μ L) were incubated at 45 °C for 60 min and analyzed according to *Calculating concentration of APE*.

Appendix A.1.2 Computational Details

All calculations were performed with Gaussian 09.1. The B3LYP density functional and a mixed basis set of LANL2DZ for Pd and 6-31G(d) for other atoms were used in geometry optimizations. All minima have zero imaginary frequency and all transition states have only one imaginary frequency. Single-point energies were calculated with M062 and a mixed basis set of SDD for Pd and 6-311+G(d,p) for other atoms. Solvation energy corrections were calculated using the SMD3 model. Water was used as solvent in the calculations. Raw Data can be found in the SI of Pohorilets, I.; Tracey, M. P.; LeClaire, M. J.; Moore, E. M.; Lu, G.; Liu, P.; Koide, K., *ACS Catal.* **2019**, 9, 11720–11733.²⁰²

Appendix A.2 Development of Ligand-Accelerated Click Reactions

Appendix A.2.1 Experimental Procedures

Deallylation and depropargylation with and without serum. A solution of 50 µM RAE or RPE in 1% DMSO/25 mM phosphate pH 7 buffer (0 or 10% FBS) (92 µL) was treated with 0 or 80 µM ligand solutions in 1% DMSO/50 mM phosphate pH 7 buffer (115 µL), and 0 or 100 µM Pd(OAc)₂ solution in 1% DMSO/H₂O (23 µL). The reaction mixtures were incubated at 37 °C for 1 h. The fluorescence (excitation 525 nm; emission 580–640 nm) was measured.

The rate of deallylation and depropargylation in the presence of hydroxymethyl-TFP analogs in phosphate buffer. To A solution of 50 µM RAE or RPE in 1% DMSO/50 mM phosphate pH 7 buffer (80 µL) was treated with 80 µM ligand solutions in 1% DMSO/50 mM phosphate pH 7 buffer (100 µL), and 0 or 100 µM Pd(OAc)₂ solution in 1% DMSO/H₂O (20 µL). The fluorescence (excitation 525 nm; emission 580-640 nm) was measured every 10 min for 2 h.

Deallylation and depropargylation without Pd and phosphine premixing. A solution of 50 µM RAE or RPE in 1% DMSO/DMEM with 25 mM phosphate pH 7 buffer (10% BCS) (92 µL) was treated with 120 µM ligand solutions in 1% DMSO/DMEM with 25 mM phosphate pH 7 buffer (10% BCS) (115 µL), and 0 or 100 µM Pd(OAc)₂ solution in 1% DMSO/H₂O (23 µL). The reaction mixtures were incubated at 37 °C for 1 h. The fluorescence (excitation 525 nm; emission 580–640 nm) was measured..

Deallylation and depropargylation with palladium and TFP premixing. A solution of 22.3 μ M RAE or RPE (206 μ L) in 1% DMSO/DMEM with 25 mM phosphate buffer (10% BCS) was treated with premixed 12 or 0 mM phosphine and 0 or 100 μ M Pd(OAc)₂ solution (24 μ L). Solutions were incubated at 37 °C for 1 h. Aliquots (200 μ L) were transferred to black 96-well plate and fluorescence was measured (excitation 525 nm, emission 540–610 nm).

The optimal concentration of TFP and mono-hydroxyethyl-TFP at 37 °C in DMEM with 10% BCS. A solution of 20.2 μ M RAE (693 μ L) in 1% DMSO/DMEM with 25 mM phosphate buffer (10% BCS) was treated with premixed 20, 14.3, 10.2, 7.29, 5.21, or 0 mM phosphine and 0 or 2 mM Pd(OAc)₂ solution (7 μ L) in 14% DMSO/H₂O. Solutions were incubated at 37 °C for 1 h. Aliquots (200 μ L) were transferred to a black 96-well plate, and fluorescence was measured (excitation 525 nm, emission 540–610 nm).

Deallylation and depropargylation in the presence of second generation of phosphines in DMEM with serum. A solution of 22.3 μ M RAE or RPE (179 μ L) in 1% DMSO/DMEM with 25 mM phosphate buffer (10% FBS) was treated with premixed 12 or 0 mM phosphine and 0 or 100 μ M Pd(OAc)₂ solution (21 μ L). The fluorescence was measured (excitation 525 nm, emission 540–610 nm) every 10 min for 1 h.

Decaging reactions with second-generation phosphines without premixing. A solution of 22.3 μ M RAE or RPE (206 μ L) in 1% DMSO/DMEM with 25 mM phosphate buffer (10% FBS) was treated with premixed 12 or 0 mM phosphine and 0 or 100 μ M Pd(OAc)₂ solution (24

μL). Solutions were incubated at 37 °C for 1 h. Aliquots (200 μL) were transferred to a black 96-well plate, and fluorescence was measured (excitation 525 nm, emission 540–610 nm).

Reactivation of palladium-phosphine complexes with additional phosphine. A solution of 50 μM RAE or RPE (80 μL) in 1% DMSO/DMEM with 25 mM phosphate pH 7 buffer (10% FBS) was treated with 100 μM $\text{PdCl}_2(\text{iPhos1})_2$ or 100 μM $\text{PdCl}_2(3\text{-iPhos1})_2$ solution (20 μL) in 1% DMSO/water. The fluorescence was measured (excitation 525 nm, emission 540–610 nm) every 5 min for 60 min. After 60 min, 660 μM iPhos1 or 3-Phos1 in 1% DMSO/DMEM with 25 mM phosphate pH 7 buffer (10% FBS) were added (20 μL). The fluorescence was measured (excitation 525 nm, emission 540–610 nm) every 5 min for 60 min.

Deallylation with premixed palladium-phosphine complexes and additional phosphines. A solution of 100 μM $\text{Pd}(\text{OAc})_2$ (460 μM) in 1% DMSO in H_2O was premixed with 12 mM iPhos1 or 3iPhos1 in DMSO (23 μM) for 45 min. A solution of 100 μM $\text{Pd}(\text{iPhos1})_2$ or $\text{Pd}(3\text{iPhos1})_2$ was premixed with 4 mM iPhos1 or 3iPhos1 in DMSO for 45 min. A solution of 22.3 μM RAE in 1% DMSO/DMEM/25 mM phosphate pH 7 buffer (10% FBS) (179 μL) was treated with premixed 0 or 195 μM Pd and 571 or 190 μM iPhos1 or 3iPhos1 in 5% DMSO/ H_2O . Fluorescence was measured (excitation 525 nm, emission 540–610 nm) every 5 min for 1 h.

The correlation between palladium concentrations and optimal 3iPhos1 concentrations. In separate vials, 60, 40, 26.7, 17.8, 11.9, 7.90, 5.27, 3.51, 2.34, 1.56, 1.04, or 0 mM phosphine (46 μL) in DMSO were premixed with 200, 100, 50, 25, 12.5, 6.25, or 0 μM $\text{Pd}(\text{OAc})_2$ in 1% DMSO DMEM/25 mM phosphate pH 7 buffer (920 μL) for 60 min. A solution

of 22.3 μM RAE (179 μL) in 1% DMSO/DMEM/25 mM phosphate pH 7 buffer (10% FBS) was treated with premixed $\text{Pd}(\text{OAc})_2$ and 3iPhos1 solutions (21 μL). Fluorescence was measured (excitation 525 nm, emission 540–610 nm) every 10 seconds for 16 min.

Kinetics of palladium catalyzed deallylation. A solution of 2.23 μM RAE (179 μL) in 1% DMSO/DMEM/25 mM phosphate pH 7 buffer (10% FBS) was treated with premixed 190 μM $\text{Pd}(\text{OAc})_2$ and 1.142 mM phosphine, 95 μM $\text{Pd}(\text{OAc})_2$ and 571 μM phosphine, 47.5 μM $\text{Pd}(\text{OAc})_2$ and 285.5 μM phosphine, 23.8 μM $\text{Pd}(\text{OAc})_2$ and 142.8 μM phosphine, or 0 μM $\text{Pd}(\text{OAc})_2$ and 1142, 571, 285.5, or 142.8 μM phosphine. Fluorescence was measured (excitation 525 nm, emission 540–610 nm) every 10 seconds for 16 min.

Copper interference with lead phosphines. A solution of 25.2 μM RAE or RPE in DMSO (159 μL) was treated with 0 or 10 μM CuSO_4 (20 μL) in 1% DMSO/DMEM with 25 mM phosphate pH 7 buffer and 571 μM phosphine and 0 or 95 μM $\text{Pd}(\text{OAc})_2$ (21 μL) (Note: Pd and the ligand were premixed for 45 min). Fluorescence was measured (excitation 525 nm, emission 540–610 nm) every 10 min for 2 h.

Substrate scope of deallylation based on the pKa of the leaving group. A solution of 11.1 μM probe in 1% DMSO/DMEM/25 mM phosphate pH 7 buffer (10% FBS) (207 μL) was treated with premixed 190 μM $\text{Pd}(\text{OAc})_2$ and 24 mM phosphine (premixed for 50 min) (23 μL). The reaction mixtures were incubated for 1 h at 37 °C. Fluorescence was measured (excitation 525 nm, emission 540–610 nm).

Substrate scope of deallylation based on the sterics of the alkene. A solution of 11.1 μM probe in 1% DMSO/DMEM/25 mM phosphate pH 7 buffer (10 % FBS) (207 μL) was treated with premixed 190 μM $\text{Pd}(\text{OAc})_2$ and 24 mM phosphine (premixed for 50 min) (23 μL). The reaction mixtures were incubated for 1 h at 37 °C. Fluorescence was measured (excitation 525 nm, emission 540–610 nm).

Appendix A.2.2 Raw Data Tables

Table 6. Raw data for Figure 20 (deallylation and depropargylation with and without serum).

Fluorescence (a.u.)						
	DMEM			DMEM 10% FBS		
RAE/TFP/Pd	60971	68240	63600	36434	32858	23969
RAE/TFP	3453	3507	3527	3495	3742	2271
RAE/Pd	3500	3670	3491	3966	4352	3319
RAE	3476	3541	3456	3911	4229	2583
RPE/TFP/Pd	5341	5716	5591	3895	4613	2667
RPE/TFP	4729	4876	4842	3797	3952	2221
RPE/Pd	4702	4900	4671	4979	4838	2464
RPE	4676	4809	4637	4882	5061	3820

Table 7. Calculated %yield for Figure 20 (deallylation and depropargylation with and without serum).

	RAE/DMEM			RAE/DMEM (10% FBS)			RPE/DMEM			RPE/DMEM (10% FBS)		
0 mM TFP	0.00	0.00	0.00	0.00	0.00	0.00	0.00	0.00	0.00	0.00	0.00	0.00
40 mM TFP	5.70	6.49	5.98	4.60	4.06	2.99	0.00	0.00	0.00	0.00	0.00	0.00

Table 8. Raw data for Figure 21 (the rate of deallylation in phosphate buffer).

Time (min)	Fluorescence (a.u.)								
	TFP			TFP-(CH ₂ OH) ₁			TFP-(CH ₂ OH) ₂		
0	2252	2738	2724	7447	7812	7651	30016	27887	30033
10	11026	13191	12778	33818	33404	31451	87240	84427	84212
20	17626	22779	20688	53848	54716	52651	102025	101147	99474
30	24076	31979	30509	69040	69333	66698	109262	109849	105895
40	32257	40403	39823	79601	79647	76403	111679	112883	107076
50	40348	49355	49054	87848	87875	84061	113220	115015	109406
60	48539	58104	58164	94543	94634	89798	113256	115907	109985
70	56169	66814	66726	99655	100880	95299	113276	116402	110149
80	63583	74650	74588	103312	105198	99251	113386	117068	110227
90	70422	82523	82597	106591	108703	102124	113707	117140	110209
100	77298	90113	89817	107550	111132	103677	114033	117046	110101
110	84035	96864	96381	107660	112618	104211	114372	117222	109682
120	90382	103533	102724	107382	113495	104119	114688	117134	109409

Table 9. Raw data for Figure 21 (the rate of deallylation in phosphate buffer) continued.

Time (min)	Fluorescence (a.u.)			No ligand		
	TFP-(CH ₂ OH) ₃			No ligand		
0	13791	14150	15209	50	44	67
10	70019	73343	74297	163	93	119
20	97207	99266	98260	248	175	153
30	108413	110265	107958	332	237	204
40	113292	114833	111378	409	305	247
50	115058	116753	110177	489	354	290
60	115884	114131	115373	571	406	340
70	118824	119784	116391	648	478	384
80	119531	121168	116413	723	548	424
90	119793	121452	116454	795	623	475
100	119775	121241	116357	853	665	520
110	119650	121636	116159	909	711	558
120	119594	121649	115756	949	754	605

Table 10. Calculated %yield for Figure 21 (the rate of deallylation in phosphate buffer).

Time (min)	TFP			TFP-(CH ₂ OH) ₁			TFP-(CH ₂ OH) ₂		
	0	0	0	1.18	1.27	1.23	7.02	6.47	7.03
0	0	0	0	1.18	1.27	1.23	7.02	6.47	7.03
10	2.10	2.66	2.56	8.01	7.90	7.39	21.84	21.11	21.05
20	3.81	5.15	4.61	13.19	13.42	12.88	25.67	25.44	25.01
30	5.48	7.53	7.15	17.13	17.20	16.52	27.54	27.69	26.67
40	7.60	9.71	9.56	19.86	19.87	19.03	28.17	28.48	26.97
50	9.70	12.03	11.95	22.00	22.00	21.02	28.57	29.03	27.58
60	11.82	14.29	14.31	23.73	23.75	22.50	28.57	29.26	27.73
70	13.79	16.55	16.53	25.05	25.37	23.93	28.58	29.39	27.77
80	15.71	18.58	18.56	26.00	26.49	24.95	28.61	29.56	27.79
90	17.48	20.62	20.64	26.85	27.40	25.69	28.69	29.58	27.79
100	19.26	22.58	22.51	27.10	28.02	26.09	28.78	29.56	27.76
110	21.01	24.33	24.21	27.13	28.41	26.23	28.86	29.60	27.65
120	22.65	26.06	25.85	27.05	28.64	26.21	28.95	29.58	27.58

Table 11. Calculated %yield for Figure 21 (the rate of deallylation in phosphate buffer) continued.

Time (min)	TFP-(CH ₂ OH) ₃			No ligand		
0	2.82	2.91	3.19	0.00	0.00	0.00
10	17.38	18.24	18.49	0.00	0.00	0.00
20	24.42	24.95	24.69	0.00	0.00	0.00
30	27.32	27.80	27.20	0.00	0.00	0.00
40	28.58	28.98	28.09	0.00	0.00	0.00
50	29.04	29.48	27.78	0.00	0.00	0.00
60	29.26	28.80	29.12	0.00	0.00	0.00
70	30.02	30.27	29.39	0.00	0.00	0.00
80	30.20	30.62	29.39	0.00	0.00	0.00
90	30.27	30.70	29.40	0.00	0.00	0.00
100	30.26	30.64	29.38	0.00	0.00	0.00
110	30.23	30.74	29.33	0.00	0.00	0.00
120	30.22	30.75	29.22	0.00	0.00	0.00

Table 12. Raw data for Figure 21 (the rate of depropargylation in phosphate buffer).

Time (min)	Fluorescence (a.u.)								
	TFP		TFP-(CH ₂ OH) ₁			TFP-(CH ₂ OH) ₂			
0	54	63	0	189	162	57	1746	1734	1581
10	1048	995	610	1978	1827	2234	36137	37240	35303
20	4672	4560	3262	4675	5513	5169	59454	58064	57388
30	10633	9926	7421	9466	10875	11950	65657	64842	64458
40	16104	16093	13938	16792	17874	18999	69134	68619	68057
50	21253	21610	19640	25659	27999	26453	70911	70433	69551
60	25557	25818	24031	32629	36520	34815	71851	71348	70476
70	29219	29671	27815	41314	44404	43279	72425	71776	70987
80	32056	32749	31409	48406	51006	50282	72426	72166	71472
90	34308	35209	34251	53788	56382	55284	72410	72211	71725
100	36465	37451	36801	57568	60695	58950	72386	72323	71857
110	38554	39379	38991	60852	63469	61833	72290	72155	71904
120	40120	40966	41090	62822	65592	63891	72219	72130	71934

Table 13. Raw data for Figure 21 (the rate of depropargylation in phosphate buffer) continued.

Time (min)	Fluorescence (a.u.)			No ligand		
	TFP-(CH ₂ OH) ₃			No ligand		
0	857	636	607	153	201	87
10	12534	12256	12172	714	896	896
20	50387	49698	48256	1733	2257	2302
30	66617	65473	65774	3084	3874	3950
40	71636	71037	71331	4525	5556	5894
50	75164	75108	75406	5986	7198	7939
60	77598	77584	78131	7325	8847	9478
70	78706	78908	79570	8632	10432	11258
80	79329	79670	80418	9885	11872	12359
90	79813	80124	81146	11095	13238	13770
100	80053	80549	81472	12204	14477	14927
110	80277	80742	81723	13274	15615	16168
120	80424	80870	81874	14220	16638	17068

Table 14. Calculated %yield for Figure 21 (the rate of depropargylation in phosphate buffer).

Time (min)	TFP			TFP-(CH ₂ OH) ₁			TFP-(CH ₂ OH) ₂		
	TFP	TFP-(CH ₂ OH) ₁	TFP-(CH ₂ OH) ₂	TFP	TFP-(CH ₂ OH) ₁	TFP-(CH ₂ OH) ₂	TFP	TFP-(CH ₂ OH) ₁	TFP-(CH ₂ OH) ₂
0	0.00	0.00	0.00	0.00	0.00	0.00	0.00	0.00	0.00
10	0.00	0.00	0.00	0.00	0.00	0.00	8.61	8.89	8.39
20	0.46	0.43	0.09	0.46	0.68	0.59	14.64	14.28	14.11
30	2.00	1.82	1.17	1.70	2.06	2.34	16.25	16.04	15.94
40	3.42	3.42	2.86	3.60	3.88	4.17	17.15	17.02	16.87
50	4.75	4.84	4.33	5.89	6.50	6.10	17.61	17.49	17.26
60	5.87	5.93	5.47	7.70	8.71	8.26	17.85	17.72	17.50
70	6.81	6.93	6.45	9.95	10.75	10.46	18.00	17.83	17.63
80	7.55	7.73	7.38	11.78	12.46	12.27	18.00	17.94	17.76
90	8.13	8.37	8.12	13.18	13.85	13.56	18.00	17.95	17.82
100	8.69	8.95	8.78	14.16	14.96	14.51	17.99	17.98	17.86
110	9.23	9.45	9.35	15.01	15.68	15.26	17.97	17.93	17.87
120	9.64	9.86	9.89	15.52	16.23	15.79	17.95	17.93	17.88

Table 15. Calculated %yield for Figure 21 (the rate of depropargylation in phosphate buffer) continued.

Time (min)	TFP-(CH ₂ OH) ₃			No ligand		
0	0.00	0.00	0.00	0.00	0.00	0.00
10	2.49	2.42	2.40	0.00	0.00	0.00
20	12.30	12.12	11.74	0.00	0.00	0.00
30	16.50	16.20	16.28	0.05	0.25	0.27
40	17.80	17.64	17.72	0.42	0.69	0.78
50	18.71	18.70	18.77	0.80	1.11	1.30
60	19.34	19.34	19.48	1.15	1.54	1.70
70	19.63	19.68	19.85	1.48	1.95	2.16
80	19.79	19.88	20.07	1.81	2.32	2.45
90	19.92	20.00	20.26	2.12	2.68	2.81
100	19.98	20.11	20.34	2.41	3.00	3.11
110	20.04	20.16	20.41	2.69	3.29	3.44
120	20.07	20.19	20.45	2.93	3.56	3.67

Table 16. Raw data for Figure 22 (deallylation and depropargylation without Pd and phosphine premixing).

	Fluorescence (a.u.)											
	Pd						No Pd					
	RAE			RPE			RAE			RPE		
TFP	17000	14926	19013	286 5	225 4	280 4	241 7	244 8	218 7	237 8	294 8	283 4
TFP-(CH ₂ OH)	9745	8462	5863	211 5	240 4	228 5	323 3	289 3	265 6	262 7	271 7	234 3
¹ TFP-(CH ₂ OH)	4672	7103	7308	256 0	226 4	296 9	254 2	289 7	249 9	262 8	293 1	283 3
² TFP-(CH ₂ OH)	4531	3938	5153	299 1	274 8	175 9	182 1	203 3	179 0	251 0	195 3	179 2
³ No ligand	2843	2534	3135	348 7	185 5	183 5	250 1	157 4	175 0	253 6	291 9	225 7

Table 17. Calculated %yield for Figure 22 (deallylation and depropargylation without Pd and phosphine premixing).

	RAE			RPE		
TFP	9.86	8.35	11.47	0	0	0
TFP-(CH ₂ OH) ₁	4.07	3.40	1.70*	0	0	0
TFP-(CH ₂ OH) ₂	0.93*	2.42	2.85	0	0	0
TFP-(CH ₂ OH) ₃	1.35	0.77	1.81	0	0	0
No ligand	0.00	0.09	0.40	0	0	0

Table 18. Raw data for Figure 22 (deallylation and depropargylation with Pd and TFP premixing).

Fluorescence (a.u.)						
	RAE			RPE		
TFP	2310	4007	7167	1284	1028	0
TFP-(CH ₂ OH) ₁	84474	52031*	75790	3001	3412	2970
TFP-(CH ₂ OH) ₂	25625	20406	21297	0	587	0
TFP-(CH ₂ OH) ₃	10981	10247	10392	590	397	451
No ligand	0	0	332	2179	2401	0

Table 19. Calculated %yield for Figure 22 (deallylation and depropargylation with Pd and TFP premixing).

	RAE			RPE		
TFP	2.12	4.55	9.08	0.65	0.28	0.00
TFP-(CH ₂ OH) ₁	100.00	73.40	100.00	3.11	3.70	3.07
TFP-(CH ₂ OH) ₂	35.55	28.06	29.34	0.00	0.00	0.00
TFP-(CH ₂ OH) ₃	14.55	13.50	13.71	0.00	0.00	0.00
No ligand	0.00	0.00	0.00	1.93	2.25	0.00

Table 20. Raw data for Figure 22 (the optimal concentration of TFP and mono-hydroxyethyl-TFP at 37 °C in DMEM with 10% BCS).

[phosphine] μM	Fluorescence (a.u.)			
	TFP		TFP-(CH ₂ OH) ₁	
200	1612	2838	1460	66034
142	589	3595*	4481	58112
102	1786	323	1697*	76013
72	13242	7070	7186	126052
52	5207	4838	2845	62744*
0	0	176	204	102894
				43099
				11814
				7699
				16161
				3445
				4094
				5782
				0
				318
				0

Table 21. Raw data for Figure 23 (deallylation in the presence of second generation of phosphines in DMEM with serum).

Time (min)	Fluorescence (a.u.)											
	RAE											
TFP	iPhos1			Me-iPhos1			3-iPhos1					
0	170	157	182	1686	1522	1886	1764	1733	1700	1494	1712	1756
	4	2	3									
2	179	181	253	4141	3601	6232	2322	2564	2815	1174	8970	2079
	3	7	1							7	0	
12	199	209	272	1025	8209	1186	5279	5384	9134	2219	2477	3116
	3	4	3	2		0				2	8	6
22	214	222	301	1573	1225	1669	8310	1042	1192	2740	3165	3398
	1	5	7	1	7	9		4	2	6	5	5
32	228	240	323	1993	1551	2088	1081	1351	1564	3053	4057	3822
	1	6	9	8	9	7	5	3	6	6	0	8
42	238	253	339	2740	1995	2435	1506	1660	1846	3858	4546	4246
	7	9	8	6	8	4	1	5	5	2	3	4
52	250	286	351	3484	2397	2760	1883	1962	1954	4370	4913	4648
	6	1	5	1	7	1	4	0	9	6	4	9
62	262	312	364	4026	3173	3085	2319	2234	2284	5356	5268	5029
	9	8	5	1	3	8	3	6	7	8	3	2
72	279	346	378	4523	3798	4058	2920	2524	2615	5760	5569	4401
	3	3	8	7	1	7	8	1	3	9	2	2
82	290	374	394	5009	4302	4408	3353	2820	2945	6110	5872	6199
	6	8	7	5	0	5	4	9	2	3	9	5
92	300	396	382	5439	4796	4732	3772	3123	3271	6441	6149	6613
	6	6	3	0	8	5	4	5	9	1	4	3
102	319	410	396	5879	5355	5037	4168	3455	3597	6724	6374	6898
	7	5	3	9	7	2	2	0	7	7	9	5
112	340	426	407	6187	5686	5335	4549	3758	3915	6990	6616	7162
	4	5	2	0	8	0	5	3	3	0	6	2
122	341	438	419	6433	6061	5624	4900	4056	4233	7239	6550	7408
	6	2	6	9	1	6	3	4	8	2	9	0

Table 22. Raw data for Figure 23 (deallylation in the presence of second generation of phosphines in DMEM with serum) continued.

Time (min)	Fluorescence (a.u.)											
	Me-3-iPhos1			iPhos2			iPhos3			None		
0	1704	1644	1723	1591	1624	1573	1745	1504	1745	208	181	189
										9	6	5
2	5336	5296	9866	7183	8151	1106	4263	3324	4393	164	165	177
						7				8	2	8
12	1054	1033	1651	1004	1382	1444	7639	5471	1266	176	180	188
	2	0	5	3	5	8			2	4	0	7
22	1409	1409	2054	1133	1602	1561	1055	5957	1566	208	198	199
	7	3	7	0	9	2	2		9	4	3	5
32	1707	1685	2403	1272	1664	1662	1149	7431	1584	288	205	203
	6	5	6	8	1	6	4		5	1	1	8
42	1931	1942	2690	1505	1738	1757	1235	1243	1652	288	216	214
	5	1	0	7	7	1	1	8	4	8	9	3
52	2234	2158	2923	1731	1827	1844	1290	1379	1444	253	218	222
	9	2	9	0	5	5	5	2	8	9	3	7
62	2331	2343	3125	1846	1910	1930	1299	1431	1487	253	227	226
	5	6	6	8	5	1	2	1	7	7	2	0
72	2562	2603	3298	1932	1991	1979	1340	1594	1525	252	233	222
	5	2	9	2	9	3	9	4	6	4	4	2
82	2766	2761	3450	2012	2063	2056	1378	1660	1561	250	235	224
	0	7	6	9	4	7	2	1	0	9	9	0
92	2902	2927	3580	2149	2130	2133	1415	1505	1595	249	242	304
	8	0	5	0	3	9	8	9	0	1	6	0
102	3053	3127	3703	2288	2206	2207	1441	1540	1625	247	246	307
	6	5	7	5	8	3	8	0	5	2	9	1
112	3220	3233	3809	2392	2271	2280	1469	1575	1654	245	251	310
	8	8	6	7	1	2	4	9	7	3	5	1
122	3360	3546	3905	2488	2333	2348	1498	1608	1681	243	255	312
	8	9	2	8	9	5	7	4	6	0	3	6

Table 23. Calculated %yield for Figure 23 (deallylation in the presence of second generation of phosphines in DMEM with serum).

Time (min)	TFP			iPhos1			Me-iPhos1			3-iPhos1		
0	0.0	0.0	0.0	0.00	0.00	0.00	0.00	0.00	0.00	0.00	0.00	0.00
	0	0	0									
2	0.0	0.0	0.0	4.75	3.97	7.74	0.00	2.48	2.84	15.65	11.6	28.61
	0	0	0							7		
12	0.0	0.0	2.7	13.5	10.5	15.8	6.38	6.53	11.9	30.62	34.3	43.49
	0	0	1	1	8	1			0		3	
22	0.0	0.0	3.1	21.3	16.3	22.7	10.7	13.7	15.9	38.10	44.1	47.53
	0	0	3	6	8	5	2	5	0		9	
32	0.0	0.0	3.4	27.3	21.0	28.7	14.3	18.1	21.2	42.59	56.9	53.62
	0	0	5	9	6	5	1	8	4		7	
42	0.0	0.0	3.6	38.1	27.4	33.7	20.4	22.6	25.2	54.12	63.9	59.69
	0	0	8	0	2	2	0	1	8		9	
52	0.0	2.9	3.8	48.7	33.1	38.3	25.8	26.9	26.8	61.47	69.2	65.46
	0	1	5	6	8	8	1	4	4		5	
62	2.5	3.2	4.0	56.5	44.3	43.0	32.0	30.8	31.5	75.61	74.3	70.91
	8	9	3	3	0	5	6	5	6		4	
72	2.8	3.7	4.2	63.6	53.2	57.0	40.6	35.0	36.3	81.40	78.6	
	1	7	4	6	6	0	8	0	0		5	
82	2.9	4.1	4.4	70.6	60.4	62.0	46.8	39.2	41.0	86.41	83.0	87.69
	7	8	7	3	9	1	9	5	3		1	
92	3.1	4.4	4.2	76.7	67.5	66.6	52.8	43.5	45.7	91.15	86.9	93.62
	2	9	9	9	8	6	9	9	2		7	
102	3.3	4.6	4.4	83.1	75.5	71.0	58.5	48.3	50.3	95.22	90.2	97.71
	9	9	9	1	9	3	7	4	9		0	
112	3.6	4.9	4.6	87.5	80.3	75.3	64.0	52.6	54.9	99.02	93.6	101.4
	9	2	5	1	4	0	3	9	4		7	9
122	3.7	5.0	4.8	91.0	85.7	79.4	69.0	56.9	59.5	102.6	92.7	105.0
	1	9	2	5	1	5	6	6	1	0	3	2

Table 24. Calculated %yield for Figure 23 (deallylation in the presence of second generation of phosphines in DMEM with serum) continued.

Time (min)	Me-3-iPhos1			iPhos2			iPhos3			None		
0	0.00	0.00	0.00	0.00	0.00	0.00	0.00	0.00	0.00	0	0	0
2	6.46	6.40	12.95	9.11	10.49	14.67	4.92	3.57	5.11	0	0	0
12	13.92	13.62	22.49	13.21	18.63	19.52	9.76	6.65	16.96	0	0	0
22	19.02	19.01	28.27	15.05	21.79	21.19	13.94	7.35	21.27	0	0	0
32	23.29	22.97	33.27	17.06	22.67	22.64	15.29	9.46	21.53	0	0	0
42	26.50	26.65	37.37	20.40	23.74	24.00	16.52	16.64	22.50	0	0	0
52	30.85	29.75	40.73	23.63	25.01	25.25	17.31	18.58	19.52	0	0	0
62	32.23	32.41	43.62	25.29	26.20	26.48	17.43	19.33	20.14	0	0	0
72	35.55	36.13	46.10	26.51	27.37	27.19	18.03	21.67	20.68	0	0	0
82	38.46	38.40	48.28	27.67	28.39	28.30	18.57	22.61	21.19	0	0	0
92	40.43	40.77	50.14	29.62	29.35	29.40	19.11	20.40	21.68	0	0	0
102	42.59	43.65	51.91	31.62	30.45	30.45	19.48	20.89	22.11	0	0	0
112	44.98	45.17	53.43	33.11	31.37	31.50	19.87	21.40	22.53	0	0	0
122	46.99	49.66	54.80	34.49	32.27	32.48	20.30	21.87	22.92	0	0	0

Table 25. Raw data for Figure 23 (depropargylation in the presence of second generation of phosphines in DMEM with serum).

Time (min)	Fluorescence (a.u.)											
	TFP			iPhos1			Me-iPhos1			3-iPhos1		
0	1417	1362	2722	1407	1660	2669	2477	2785	2476	1421	1569	1539
2	1399	1479	1367	1519	1405	1555	1663	1441	1559	2323	2429	2439
12	1560	1583	1616	2094	2054	1700	2944	1982	1729	5784	3856	3588
22	1638	1843	1578	2170	2160	1768	3025	2766	1875	7541	4774	4591
32	2663	1859	1575	2964	3191	2099	3082	3113	2228	9296	5317	5094
42	2781	2389	1607	3444	3819	2132	2908	3214	2221	8910	6179	5248
52	2776	2536	1607	3706	4059	2294	2982	3297	2276	9318	6535	5338
62	2730	2711	1715	3970	4359	2314	3052	3372	2576	9616	6943	5774
72	2764	2838	1775	4162	4595	2532	3119	3447	2994	9805	7302	5978
82	2748	2965	1911	4334	4765	2655	3183	3517	3401	10004	12232	6118
92	2748	3045	2054	4486	4825	2669	3241	3578	3679	10179	12575	6295
102	2753	3052	2144	4606	4925	3103	3300	3640	3851	10347	12714	6578
112	2755	3072	2229	4715	4992	4119	3354	3698	3968	10456	12812	6670
122	2758	3071	2427	4821	5079	4244	3406	3754	4103	10553	12903	6784

Table 26. Raw data for Figure 23 (depropargylation in the presence of second generation of phosphines in DMEM with serum) continued.

Time (min)	Fluorescence (a.u.)											
	Me-3-iPhos1			iPhos2			iPhos3			None		
0	1431	1346	1669	1386	1655	1289	1699	1773	1714	1851	1776	1831
2	1485	1449	1414	1548	1890	1752	1514	1512	1608	1847	1860	1673
12	2381	2019	2063	2106	2075	2032	2686	1761	1693	1863	1954	1758
22	4299	3481	2761	3257	2104	2133	3027	1805	1945	1884	1855	1727
32	5221	5322	3302	3386	2068	2208	3166	1919	2317	1953	1786	1757
42	5879	6346	3694	3609	3507	2352	3214	1996	2884	1921	1877	1860
52	6395	7496	4169	3387	3315	2521	3244	2152	3199	1920	1916	1957
62	6803	7761	4477	3416	3450	2662	3229	2500	3345	1928	1950	2011
72	7160	8235	4900	3238	3564	2794	3198	3308	3472	1931	1918	2135
82	7486	8544	5078	3262	3601	3082	3186	3328	3519	1957	1575	2353
92	7771	8855	5163	3288	3622	3321	3105	3337	3548	2010	1652	2577
102	8027	9101	5380	3309	3627	3439	3100	3342	3560	2008	1674	2754
112	8261	9153	5579	3313	3624	3575	3097	3346	3630	2030	2623	2902
122	8469	9296	5978	3312	3622	3843	3093	3332	3671	2052	2990	2994

Table 27. Calculated %yield for Figure 23 (depropargylation in the presence of second generation of phosphines in DMEM with serum).

Time (min)	TFP			iPhos1			Me-iPhos1			3-iPhos1		
	0.00	0.00	0.00	0.00	0.00	0.00	0.00	0.00	0.00	0.00	0.00	0*
0	0.00	0.00	0.00	0.00	0.00	0.00	0.00	0.00	0.00	0.00	0.00	0*
2	0.00	0.00	0.00	0.00	0.00	0.00	0.00	0.00	0.00	0.00	0.00	0*
12	0.00	0.00	0.00	0.00	0.00	0.00	0.31	0.00	0.00	2.62	1.05	0.83*
22	0.00	0.00	0.00	0.00	0.00	0.00	0.38	0.16	-0.56*	4.05	1.80	1.65*
32	0.08	0.00	0.00	0.33	0.51	0.00	0.42	0.45	-0.27*	5.48	2.24	2.06*
42	0.18	0.00	0.00	0.72	1.02	0.00	0.28	0.53	-0.28*	5.17	2.94	2.18*
52	0.17	0.00	0.00	0.93	1.22	0.00	0.34	0.60	-0.23*	5.50	3.23	2.26*
62	0.14	0.12	0.00	1.14	1.46	0.00	0.40	0.66	0.01	5.74	3.56	2.61*
72	0.16	0.22	0.00	1.30	1.65	0.00	0.45	0.72	0.35	5.89	3.86	2.78*
82	0.15	0.33	0.00	1.44	1.79	0.07	0.50	0.78	0.68	6.06	7.87	2.89*
92	0.15	0.39	0.00	1.56	1.84	0.09	0.55	0.83	0.91	6.20	8.15	3.04*
102	0.15	0.40	0.00	1.66	1.92	0.44	0.60	0.88	1.05	6.34	8.26	3.27*
112	0.16	0.41	0.00	1.75	1.98	1.27	0.64	0.92	1.14	6.42	8.34	3.34*
122	0.16	0.41	0.00	1.84	2.05	1.37	0.69	0.97	1.25	6.50	8.42	3.44*

Table 28. Calculated %yield for Figure 23 (depropargylation in the presence of second generation of phosphines in DMEM with serum) continued.

Time (min)	Me-3-iPhos1			iPhos2			iPhos3			None		
0	0.00	0.00	0*	0.00	0.00	0.00	0.00	0.00	0.00	0.00	0.00	0.00
2	0.00	0.00	0*	0.00	0.00	0.00	0.00	0.00	0.00	0.00	0.00	0.00
12	0.00	0.00	0*	0.00	0.00	0.00	0.10	0.00	0.00	0.00	0.00	0.00
22	1.41	0.75	0.16*	0.56	0.00	0.00	0.38	0.00	0.00	0.00	0.00	0.00
32	2.16	2.25	0.60*	0.67	0.00	0.00	0.49	0.00	0.00	0.00	0.00	0.00
42	2.70	3.08	0.92*	0.85	0.77	0.00	0.53	0.00	0.26	0.00	0.00	0.00
52	3.12	4.01	1.31*	0.67	0.61	0.00	0.55	0.00	0.52	0.00	0.00	0.00
62	3.45	4.23	1.56*	0.69	0.72	0.08	0.54	0.00	0.64	0.00	0.00	0.00
72	3.74	4.62	1.90*	0.55	0.81	0.19	0.52	0.61	0.74	0.00	0.00	0.00
82	4.01	4.87	2.05*	0.57	0.84	0.42	0.51	0.62	0.78	0.00	0.00	0.00
92	4.24	5.12	2.12*	0.59	0.86	0.62	0.44	0.63	0.80	0.00	0.00	0.00
102	4.45	5.32	2.29*	0.61	0.87	0.71	0.44	0.63	0.81	0.00	0.00	0.00
112	4.64	5.36	2.45*	0.61	0.86	0.82	0.43	0.64	0.87	0.00	0.00	0.00
122	4.81	5.48	2.78*	0.61	0.86	1.04	0.43	0.63	0.90	0.00	0.00	0.00

Table 29. Raw data for Figure 24 (decaging reactions with second-generation phosphines without premixing).

Phosphine	Fluorescence (a.u.)											
	Pd			No Pd			Pd			No Pd		
	RAE	RPE	RAE	RPE	RAE	RPE	RAE	RPE	RAE	RPE	RAE	RPE
iPhos1	1696 3	17995 8	8957 6	175 9	184 4	172 2	1809 9	2326 7	3085 6	2585 9	2440 8	1702 7
Me-iPhos1	2400 1	23723 6	2518 9	337 4	299 2	363 2	3070 1	2151 7	1734 9	1676 1	2381 8	1615 7
3iPhos1	1853 8	19864 1	2001 3	414 3	427 7	250 9	1651 7	1719 0	1691 8	1544 1	1332 8	1477 7
Me-3iPhos1	1399 0	14983 3	1134 7	175 0	174 8	260 8	2941 4	2166 9	1582 3	1352 1	1478 8	1461 7
No ligand	2484	3074	3176	219 4	207 9	239 3	1687 4	1536 4	1699 4	2255 3	1866 2	3047 3
TFP	1700 0	14926 3	1901 5	286 4	225 4	280 4	2417 4	2448 4	2187 4	2378 3	2948 2	2834 3

Table 30. Calculated %yield for Figure 24 (decaging reactions with second-generation phosphines without premixing).

Phosphine	RAE			RPE		
iPhos1	11.56	12.30	5.83	0.66	0.73	0.64
Me-iPhos1	16.61	16.41	17.46	1.83	1.55	2.01
3iPhos1	12.69	13.64	13.75	2.37	2.47	1.20
Me-3iPhos1	9.43	10.14	7.54	0.66	0.65	1.27
No ligand	1.19	1.61	1.68	0.98	0.89	1.12
TFP	11.59	10.10	13.03	1.46	1.02	1.41

Table 31. Raw data for Figure 25 (reactivation of palladium-phosphine complexes with additional phosphine).

Time (min)	Fluorescence (a.u.)					
	Cl ₂ Pd(iPhos1) ₂		Cl ₂ Pd(3-iPhos1) ₂			
0	1545	1566	2251	1484	2108	2288
2	2645	2474	2601	2473	2693	2536
7	3062	2873	3016	2635	2858	2707
12	3312	3102	3274	2725	2928	2791
17	3491	3261	3446	2724	2966	2845
22	3629	3379	3572	2773	3004	2886
27	3734	3466	3671	2818	3031	2924
32	3821	3535	3743	2855	3061	2958
37	3893	3589	3801	2887	3083	2991
42	3951	3634	3844	2921	3038	3019
47	4002	3672	3886	2949	3056	3046
52	4047	3705	3918	2977	3076	3073
57	4086	3729	3948	3005	3093	3099
62	4122	3754	3974	3031	3111	3122
65	4122	3754	3974	3031	3111	3122
70	4155	3852	4006	3084	3146	3163
75	4171	3881	3999	3118	3162	3185
80	4179	3699	3999	3135	3182	3203
85	4189	3691	3998	3152	3196	3217
90	4201	3758	3986	3166	3206	3233
95	4209	3743	3982	3177	3215	3245
100	4220	3719	3981	3186	3223	3293
105	4227	3721	3981	3192	3226	3303
110	4235	3726	3979	3197	3230	3311
115	4242	3727	3978	3201	3234	3319
120	4246	3729	3978	3205	3238	3329
125	4256	3732	3981	3211	3241	3468

Table 32. Raw data for Figure 25 (deallylation with premixed palladium-phosphine complexes and additional phosphines).

Time (min)	Fluorescence (a.u.)					
	Premixed Pd(OAc) ₂ and iPhos1		Premixed Pd(OAc) ₂ and 3iPhos1		Premixed Pd(iPhos1) ₂ Cl ₂ and iPhos1	
0	0	0	0	0	0	0
2	3439	3117	3371	15530	16301	16167
7	7731	6937	7468	36750	38394	37524
12	11910	10560	11483	44950	46748	45537
17	16080	14220	15463	50833	52976	51479
22	20046	17862	19338	55863	58450	56514
27	23851	21384	23101	60307	63416	61010
32	27529	24810	26717	64247	67799	64949
37	31188	28195	30260	67696	71695	68328
42	34700	31470	33706	70581	74975	71197
47	38072	34634	37068	72936	77679	73521
52	41252	37628	40234	74816	79897	75455
57	44154	40182	43155	76310	81699	76952
62	46446	42064	45416	77490	83067	78138
					7799	5807
						7407

Table 33. Raw data for Figure 25 (deallylation with premixed palladium-phosphine complexes and additional phosphines) continued.

Time (min)	Fluorescence (a.u.)					
	Premixed Pd(3iPhos1) ₂ Cl ₂ and 3iPhos1		Pd(iPhos1) ₂ Cl ₂		Pd(3iPhos1) ₂ Cl ₂	
0	0	0	0	0	0	0
2	6020	6784	7005	3177	3389	3176
7	9583	10600	11228	3740	3978	3724
12	11695	12864	13582	4134	4381	4114
17	13492	14740	15721	4413	4387	4413
22	15198	16525	17623	4636	4505	4635
27	16840	18328	19284	4817	4677	4819
32	18432	19992	20554	4963	4812	4968
37	20012	21592	21427	5084	4928	5087
42	21534	23139	22227	5190	5022	5189
47	23000	24649	23030	5279	5099	5278
52	24416	26080	23680	5364	5168	5353
57	25662	27342	24113	5437	5231	5420
62	26728	28338	24381	5503	5284	5477
					5453	5947
						5532

Table 34. Raw data for Figure 26 (the correlation between palladium concentrations and optimal 3iPhos1 concentrations).

[3Phos1] uM	[Pd(OAc) ₂] uM	Fluorescence (a.u.)											
		300	214	153	109	78.1	55.8	39.8	28.5	20.3	14.5	10.4	0
	20	768 8	1065 0	1923 8	2106 2	1195 9	378 0	234 2	154 2	144 5	962 117	831 884	54 44
	10	624 2	6839 5	9111 1	1018 1	9782 1	726 1	289 1	149 3	229 3	117 8	884 2	44 2
	5	242 5	3081 5	3411 2	4921 4	5482 4	496 4	415 4	152 5	214 1	111 1	795 4	59 4
	2.5	166 1	1766 1	1987 6	2556 5	2577 5	292 2	262 2	219 2	192 2	177 5	108 9	50 4
	0	536	521	563	551	564	542	567	568	568	568	571	55 1

Table 35. Raw data for Figure 27 (kinetics of palladium catalyzed deallylation).

Time (s)	Fluorescence (a.u.)											
	10 uM Pd			5 uM Pd			2.5 uM Pd			1.25 uM Pd		
0	177	187	169	177	187	169	177	187	169	177	187	169
10	1937	1953	1700	1116	1168	1113	799	763	739	429	572	570
20	2148	2167	1891	1231	1278	1219	843	817	787	452	598	596
30	2351	2338	2055	1328	1370	1309	882	861	828	470	616	616
40	2514	2489	2199	1411	1450	1391	916	897	861	484	631	632
50	2653	2630	2328	1481	1523	1463	944	927	890	496	644	646
60	2783	2755	2446	1545	1587	1530	971	955	917	507	656	657
70	2905	2867	2558	1601	1645	1590	996	978	940	516	665	667
80	3020	2971	2658	1655	1699	1644	1019	1000	964	524	675	676
90	3125	3065	2756	1708	1750	1696	1041	1023	985	532	683	685
100	3223	3153	2846	1757	1795	1744	1063	1045	1008	540	691	693
110	3310	3237	2933	1805	1843	1789	1083	1065	1028	546	698	701
120	3395	3313	3017	1851	1886	1833	1103	1086	1048	553	705	709
130	3479	3390	3098	1897	1933	1877	1122	1107	1067	560	712	717
140	3552	3461	3174	1940	1975	1916	1140	1124	1084	566	718	724
150	3628	3529	3250	1984	2016	1957	1157	1144	1104	573	725	731
160	3697	3595	3322	2024	2059	1996	1174	1163	1121	579	731	738
170	3765	3660	3392	2064	2099	2034	1191	1180	1137	585	737	744
180	3831	3723	3462	2104	2139	2072	1208	1198	1156	590	743	751
190	3895	3784	3532	2144	2180	2109	1225	1216	1172	596	750	757
200	3958	3844	3599	2182	2218	2145	1241	1233	1188	602	755	763
210	4023	3903	3666	2221	2257	2181	1257	1250	1205	607	760	769
220	4085	3961	3731	2258	2295	2217	1273	1268	1220	613	765	775
230	4146	4018	3792	2296	2334	2253	1288	1285	1238	618	770	781
240	4205	4073	3853	2332	2371	2287	1304	1301	1253	623	775	786
250	4265	4129	3913	2370	2410	2323	1320	1320	1270	629	780	792
260	4322	4183	3969	2406	2445	2357	1334	1336	1286	634	785	797
270	4377	4235	4024	2442	2481	2391	1349	1353	1301	639	789	802
280	4430	4286	4075	2476	2516	2424	1363	1369	1315	644	794	808
290	4486	4338	4128	2511	2552	2458	1377	1385	1332	649	799	813
300	4538	4386	4176	2544	2587	2492	1391	1401	1347	653	804	818

Table 36. Calculated [resorufin] μ M for Figure 27 (kinetics of palladium catalyzed deallylation).

Time (s)	10 μ M Pd			5 μ M Pd		
0	0.0343	0.0372	0.0319	0.0343	0.0372	0.0319
10	0.5403	0.5449	0.4722	0.3042	0.3192	0.3033
20	0.6010	0.6064	0.5271	0.3374	0.3508	0.3338
30	0.6593	0.6556	0.5743	0.3653	0.3773	0.3599
40	0.7061	0.6991	0.6157	0.3889	0.4003	0.3833
50	0.7461	0.7395	0.6527	0.4091	0.4212	0.4040
60	0.7835	0.7756	0.6868	0.4276	0.4397	0.4234
70	0.8186	0.8077	0.7190	0.4438	0.4563	0.4404
80	0.8517	0.8377	0.7478	0.4592	0.4720	0.4561
90	0.8818	0.8645	0.7757	0.4744	0.4864	0.4710
100	0.9099	0.8898	0.8017	0.4887	0.4995	0.4848
110	0.9351	0.9142	0.8267	0.5023	0.5132	0.4976
120	0.9597	0.9359	0.8509	0.5155	0.5258	0.5103
130	0.9838	0.9580	0.8742	0.5289	0.5391	0.5230
140	1.0047	0.9784	0.8959	0.5412	0.5511	0.5344
150	1.0264	0.9981	0.9179	0.5537	0.5631	0.5462
160	1.0462	1.0171	0.9384	0.5652	0.5755	0.5573
170	1.0659	1.0357	0.9587	0.5770	0.5868	0.5683
180	1.0849	1.0539	0.9789	0.5884	0.5985	0.5791
190	1.1033	1.0714	0.9989	0.5998	0.6102	0.5898
200	1.1214	1.0888	1.0181	0.6107	0.6211	0.6001
210	1.1401	1.1055	1.0373	0.6219	0.6324	0.6104
220	1.1580	1.1223	1.0563	0.6327	0.6432	0.6208
230	1.1754	1.1385	1.0738	0.6436	0.6543	0.6310
240	1.1925	1.1544	1.0911	0.6539	0.6650	0.6409
250	1.2096	1.1704	1.1084	0.6647	0.6762	0.6513
260	1.2261	1.1861	1.1245	0.6751	0.6864	0.6612
270	1.2420	1.2011	1.1404	0.6854	0.6967	0.6709
280	1.2572	1.2158	1.1551	0.6954	0.7068	0.6804
290	1.2732	1.2307	1.1702	0.7053	0.7173	0.6901
300	1.2883	1.2446	1.1841	0.7149	0.7271	0.6999
Time (s)	2.5 μ M Pd			1.25 μ M Pd		
0	0.0343	0.0372	0.0319	0.0343	0.0372	0.0319
10	0.2132	0.2028	0.1958	0.1068	0.1479	0.1472
20	0.2258	0.2184	0.2098	0.1133	0.1553	0.1546
30	0.2370	0.2310	0.2214	0.1184	0.1605	0.1604
40	0.2466	0.2414	0.2310	0.1226	0.1649	0.1650
50	0.2549	0.2500	0.2393	0.1261	0.1686	0.1690
60	0.2627	0.2581	0.2470	0.1291	0.1719	0.1723
70	0.2699	0.2645	0.2537	0.1317	0.1747	0.1751
80	0.2763	0.2710	0.2605	0.1341	0.1774	0.1778
90	0.2828	0.2775	0.2665	0.1364	0.1799	0.1802
100	0.2889	0.2839	0.2733	0.1386	0.1821	0.1827
110	0.2948	0.2897	0.2788	0.1405	0.1841	0.1850
120	0.3004	0.2956	0.2846	0.1425	0.1860	0.1872
130	0.3060	0.3016	0.2902	0.1443	0.1882	0.1895

140	0.3111	0.3066	0.2950	0.1462	0.1897	0.1915
150	0.3160	0.3123	0.3009	0.1480	0.1918	0.1937
160	0.3211	0.3177	0.3057	0.1497	0.1936	0.1956
170	0.3259	0.3225	0.3104	0.1514	0.1954	0.1974
180	0.3307	0.3278	0.3156	0.1531	0.1971	0.1994
190	0.3355	0.3329	0.3205	0.1547	0.1989	0.2011
200	0.3402	0.3379	0.3250	0.1563	0.2003	0.2027
210	0.3448	0.3429	0.3298	0.1580	0.2020	0.2045
220	0.3495	0.3478	0.3342	0.1596	0.2035	0.2064
230	0.3538	0.3528	0.3394	0.1612	0.2049	0.2080
240	0.3584	0.3575	0.3435	0.1626	0.2062	0.2095
250	0.3628	0.3628	0.3484	0.1642	0.2077	0.2112
260	0.3670	0.3674	0.3530	0.1657	0.2091	0.2126
270	0.3711	0.3723	0.3574	0.1671	0.2104	0.2141
280	0.3754	0.3769	0.3614	0.1685	0.2117	0.2157
290	0.3794	0.3816	0.3663	0.1698	0.2133	0.2171
300	0.3832	0.3862	0.3707	0.1712	0.2146	0.2187

Table 37. Calculated [RAE] μ M for Figure 27 (kinetics of palladium catalyzed deallylation).

Time (s)	10 uM Pd			5 uM Pd		
0	1.9657	1.9628	1.9681	1.9657	1.9628	1.9681
10	1.4597	1.4551	1.5278	1.6958	1.6808	1.6967
20	1.3990	1.3936	1.4729	1.6626	1.6492	1.6662
30	1.3407	1.3444	1.4257	1.6347	1.6227	1.6401
40	1.2939	1.3009	1.3843	1.6111	1.5997	1.6167
50	1.2539	1.2605	1.3473	1.5909	1.5788	1.5960
60	1.2165	1.2244	1.3132	1.5724	1.5603	1.5766
70	1.1814	1.1923	1.2810	1.5562	1.5437	1.5596
80	1.1483	1.1623	1.2522	1.5408	1.5280	1.5439
90	1.1182	1.1355	1.2243	1.5256	1.5136	1.5290
100	1.0901	1.1102	1.1983	1.5113	1.5005	1.5152
110	1.0649	1.0858	1.1733	1.4977	1.4868	1.5024
120	1.0403	1.0641	1.1491	1.4845	1.4742	1.4897
130	1.0162	1.0420	1.1258	1.4711	1.4609	1.4770
140	0.9953	1.0216	1.1041	1.4588	1.4489	1.4656
150	0.9736	1.0019	1.0821	1.4463	1.4369	1.4538
160	0.9538	0.9829	1.0616	1.4348	1.4245	1.4427
170	0.9341	0.9643	1.0413	1.4230	1.4132	1.4317
180	0.9151	0.9461	1.0211	1.4116	1.4015	1.4209
190	0.8967	0.9286	1.0011	1.4002	1.3898	1.4102
200	0.8786	0.9112	0.9819	1.3893	1.3789	1.3999
210	0.8599	0.8945	0.9627	1.3781	1.3676	1.3896
220	0.8420	0.8777	0.9437	1.3673	1.3568	1.3792
230	0.8246	0.8615	0.9262	1.3564	1.3457	1.3690
240	0.8075	0.8456	0.9089	1.3461	1.3350	1.3591
250	0.7904	0.8296	0.8916	1.3353	1.3238	1.3487
260	0.7739	0.8139	0.8755	1.3249	1.3136	1.3388
270	0.7580	0.7989	0.8596	1.3146	1.3033	1.3291
280	0.7428	0.7842	0.8449	1.3046	1.2932	1.3196
290	0.7268	0.7693	0.8298	1.2947	1.2827	1.3099
300	0.7117	0.7554	0.8159	1.2851	1.2729	1.3001

Time (s)	2.5 uM Pd			1.25 uM Pd		
0	1.9657	1.9628	1.9681	1.9657	1.9628	1.9681
10	1.7868	1.7972	1.8042	1.8932	1.8521	1.8528
20	1.7742	1.7816	1.7902	1.8867	1.8447	1.8454
30	1.7630	1.7690	1.7786	1.8816	1.8395	1.8396
40	1.7534	1.7586	1.7690	1.8774	1.8351	1.8350
50	1.7451	1.7500	1.7607	1.8739	1.8314	1.8310
60	1.7373	1.7419	1.7530	1.8709	1.8281	1.8277
70	1.7301	1.7355	1.7463	1.8683	1.8253	1.8249
80	1.7237	1.7290	1.7395	1.8659	1.8226	1.8222
90	1.7172	1.7225	1.7335	1.8636	1.8201	1.8198
100	1.7111	1.7161	1.7267	1.8614	1.8179	1.8173
110	1.7052	1.7103	1.7212	1.8595	1.8159	1.8150
120	1.6996	1.7044	1.7154	1.8575	1.8140	1.8128
130	1.6940	1.6984	1.7098	1.8557	1.8118	1.8105

140	1.6889	1.6934	1.7050	1.8538	1.8103	1.8085
150	1.6840	1.6877	1.6991	1.8520	1.8082	1.8063
160	1.6789	1.6823	1.6943	1.8503	1.8064	1.8044
170	1.6741	1.6775	1.6896	1.8486	1.8046	1.8026
180	1.6693	1.6722	1.6844	1.8469	1.8029	1.8006
190	1.6645	1.6671	1.6795	1.8453	1.8011	1.7989
200	1.6598	1.6621	1.6750	1.8437	1.7997	1.7973
210	1.6552	1.6571	1.6702	1.8420	1.7980	1.7955
220	1.6505	1.6522	1.6658	1.8404	1.7965	1.7936
230	1.6462	1.6472	1.6606	1.8388	1.7951	1.7920
240	1.6416	1.6425	1.6565	1.8374	1.7938	1.7905
250	1.6372	1.6372	1.6516	1.8358	1.7923	1.7888
260	1.6330	1.6326	1.6470	1.8343	1.7909	1.7874
270	1.6289	1.6277	1.6426	1.8329	1.7896	1.7859
280	1.6246	1.6231	1.6386	1.8315	1.7883	1.7843
290	1.6206	1.6184	1.6337	1.8302	1.7868	1.7829
300	1.6168	1.6138	1.6293	1.8288	1.7854	1.7813

Table 38. Raw data for Figure 28 (copper does not interfere in the presence of iPhos1).

Time (min)	Fluorescence (a.u.)											
	RAE and iPhos1											
	10 uM Pd(OAc) ₂			10 uM Pd(OAc) ₂ + 1 uM CuSO ₄			1 uM CuSO ₄			0 uM Pd(OAc) ₂ + 0 uM CuSO ₄		
0	2849	1618	3326	2849	1618	3326	2849	1618	3326	2849	1618	3326
2	4347	5130	5093	4585	4641	3345	3667	2838	3121	2849	1618	3326
22	8608	8215	9795	9222	9589	6786	3672	2855	3102	2850	1667	3168
42	1097	1008	1264	1180	1200	8577	3339	2847	2958	2518	1695	3153
	1	4	4	4	0							
62	1210	1117	1209	1303	1186	9461	3310	2830	2942	2453	1629	3146
	0	3	9	6	8							
82	1270	1169	1252	1187	1263	1005	3288	2431	2925	2450	1631	3136
	1	6	9	9	4	7						
102	1312	1196	1282	1221	1313	1051	3266	2420	2903	2446	1634	3121
	3	8	5	6	9	4						
122	1341	1216	1306	1250	1354	1092	3249	2410	2884	2441	1636	3107
	2	2	2	0	0	3						
RPE and iPhos1												
Time (min)	10 uM Pd(OAc) ₂			10 uM Pd(OAc) ₂ + 1 uM CuSO ₄			1 uM CuSO ₄			0 uM Pd(OAc) ₂ + 0 uM CuSO ₄		
0	117	1522	1412	1179	1522	1412	1179	1522	1412	1179	1522	1412
	9											
2	236	1493	1577	2303	2244	2344	1344	1574	1511	1179	1522	1412
	6											
22	260	1609	2250	2172	2485	2513	1407	1437	1586	1238	1588	1483
	6											
42	282	1749	2449	2315	2705	2684	1435	1436	1636	1278	1628	1501
	7											
62	290	1872	2448	2427	2888	2821	1460	1718	1674	1869	1657	1529
	7											
82	278	2273	2542	2505	2999	2913	1481	2105	1704	1938	1678	1553
	0											
102	263	2335	2597	2551	3058	2962	1499	2110	1866	1950	1693	1574
	6											
122	266	2359	2627	2572	3077	2974	1513	2116	1830	1961	1704	1586
	5											

Table 39. Raw data for Figure 28 (copper does not interfere in the presence of 3iPhos1).

Time (min)	RAE and 3iPhos1											
	10 uM Pd(OAc) ₂			10 uM Pd(OAc) ₂ + 1 uM CuSO ₄			1 uM CuSO ₄			0 uM Pd(OAc) ₂ + 0 uM CuSO ₄		
0	1687	1818	1500	1687	1818	1500	1687	1818	1500	1687	1818	1500
2	2282	2394	2021	1856	1622	1687	2961	2286	2815	1687	1818	1500
	2	1	9	5	6	1						
22	3620	3690	3126	3279	3908	2830	2942	2327	2843	1927	1818	1482
	2	6	8	1	0	6						
42	3909	3872	3346	3625	4194	3100	2808	2342	2848	2278	1689	1453
	7	3	6	4	0	2						
62	4003	3886	3416	3757	4294	3214	2523	2339	2849	2313	2604	1442
	9	9	5	7	1	7						
82	4026	3847	3423	3809	4315	3271	2506	2275	2836	2322	2601	1448
	2	4	6	2	8	9						
102	4014	3791	3401	3826	4301	3299	2492	2280	2822	2250	2595	1451
	2	1	7	5	7	1						
122	3990	3734	3372	3821	4013	3306	2479	2281	2806	2241	2590	1453
	1	6	7	5	3	4						
RPE and 3iPhos1												
Time (min)	10 uM Pd(OAc) ₂			10 uM Pd(OAc) ₂ + 1 uM CuSO ₄			1 uM CuSO ₄			0 uM Pd(OAc) ₂ + 0 uM CuSO ₄		
0	1197	1125	1199	1197	1125	1199	1197	1125	1199	1197	1125	1199
2	3247	3072	2938	2978	2831	3062	1353	1596	1282	1197	1125	1199
22	5019	4611	4168	4662	4405	4529	1413	1638	1325	1244	1170	1241
42	5255	4843	4408	4922	4683	4801	1451	1670	1361	1818	1175	1262
62	5293	4839	4428	4974	4750	4867	1482	1692	1406	1696	1206	1275
82	5284	4777	4405	4977	4769	4880	1508	1707	1429	1526	1223	1297
102	5263	4713	4378	4963	4774	4878	1528	1719	1445	1742	1295	1277
122	5234	4652	4352	4946	4767	4867	1548	1727	1458	1746	1478	1289

Table 40. Raw data for Figure 29 (substrate scope of deallylation based on the pK_a of the leaving group).

Probe	Fluorescence (a.u.)											
	iPhos1			3iPhos1			No Pd					
alloc-N-4-methylcoumarin	6262	6635	6662	6005	6095	6449	614	683	700			
Alloc-resorufin	12359	11650	12817	10761	13616	12152	13385	12116	12402			
	7	0	2	8	1	8	1	2	3			
APE	67078	62375	62964	39708	38267	54036	8776	4544	4146			
	7	0	5	2	4	4						
RAE	13539	13121	11863	11758	11768	10526	2379	2296	2079			
	8	3	6	2	2	7						
ATE	47664	47097	42446	2E+33	2E+33	2E+33	24366	24059	40631			
	5	7	5	*	*	*						
O-allylcoumarin	3020	3140	2908	6410	6657	6716	595	615	619			
N-allyl-4-methylcoumarin	9656	9979	10056	7889	9606	9587	9921	9005	9927			

Table 41. Calculated %yield for Figure 29 (substrate scope of deallylation based on the pKa of the leaving group).

Probe	iPhos1			3iPhos1		
alloc-N-4-methylcoumarin	104	111	111	99	100	107
Alloc-resorufin	0	0	0	0	0	0
APE	82	76	77	47	46	66
RAE	123	119	107	106	106	95
ATE	23	23	20	100	100	100
O-allylcoumarin	41	43	38	115	120	121
N-allyl-4-methylcoumarin	0	0	0	0	0	0

Table 42. Raw data for Figure 30 (substrate scope of deallylation based on the sterics of the alkene).

Probe	Fluorescence (a.u.)						No Pd		
	iPhos1			3iPhos1					
RAE	30417	35873	38002	108556	112319	110000	2536	2450	2295
2.71	7481	6871	7463	9802	8532	11667	3453	3650	3397
2.72	17586	18080	18625	52217	45905	52312	1485	1550	1596
2.73	19032	20705	19588	57957	55466	55717	1475	1471	1457
2.74	29161	20693	26898	57989	69132	41589	2179	2114	2099
2.75	15571	16908	16146	51152	50798	48867	1586	1603	1608

Table 43. Calculated %yield for Figure 30 (substrate scope of deallylation based on the sterics of the alkene).

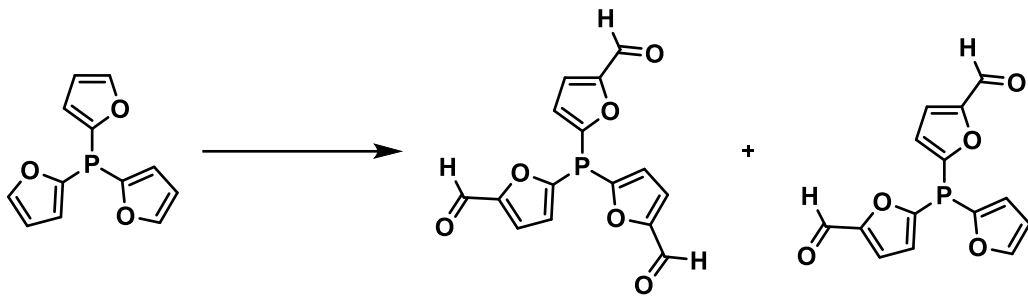
Probe	iPhos1			3iPhos1		
RAE	22.9	28.1	30.3	97.3	100.9	98.9
2.71	0.1	0.0	0.2	2.3	1.0	4.2
2.72	11.6	12.0	12.5	44.6	38.5	44.6
2.73	13.0	14.6	13.6	50.1	47.7	48.0
2.74	22.0	14.0	19.9	49.4	60.1	33.9
2.75	9.6	10.9	10.1	43.5	43.1	41.3

Appendix A.2.3 Chemistry General Procedures

All of the flasks used for carrying out reactions were dried in an oven at 80 °C prior to use. Unless specifically stated, the temperature of a water bath during the evaporation of organic solvents using a rotary evaporator was about 35±5 °C. All of the syringes in this study were dried in an oven at 80 °C and stored in a desiccator over Drierite®. Tetrahydrofuran (THF) was distilled over Na metal and benzophenone. Dichloromethane, acetonitrile, methanol, and toluene were stored over 3Å molecular sieves. Yields refer to chromatographically and spectroscopically (¹H NMR) homogenous materials, unless otherwise stated. All reactions were monitored by thin layer chromatography (TLC) carried out on 0.25-mm Merck silica gel plates (60F-254) using UV light (254 nm) for visualization or anisaldehyde in ethanol or 0.2% ninhydrin in ethanol as a developing agents and heat for visualization. Silica gel (230–400 mesh) was used for flash column chromatography. A rotary evaporator was connected to a PIAB Lab Vac LVH40 that produced a vacuum pressure of approximately 60 mmHg when it was connected to the evaporator. NMR spectra were recorded on a Bruker Advance spectrometer at 300, 400, 500, or 600 MHz. The chemical shifts are given in parts per million (ppm) on a delta (δ) scale. The solvent peak was used as a reference value, for ¹H NMR: CHCl₃ = 7.26 ppm, CH₃OH = 3.31 ppm, DMSO = 2.50 ppm, acetone = 2.05 ppm, for ¹³C NMR: CDCl₃ = 77.16 ppm, CD₃OD = 49.00 ppm, DMSO-d₆ = 39.52 ppm, and acetone-d₆ = 29.84 ppm. The following abbreviations are used to indicate the multiplicities: s = singlet; d = doublet; t = triplet; q = quartet; m = multiplet; br = broad; app = apparent. High-resolution mass spectra were recorded on a VG 7070 spectrometer. Infrared (IR) spectra were collected on a Mattson Cygnus 100

spectrometer or a PerkinElmer FT-IR Spectrum Two UATR. Samples for acquiring IR spectra were prepared as a thin film on a NaCl plate by dissolving the compound in CH₂Cl₂ and then evaporating the CH₂Cl₂ or from neat samples.

Appendix A.2.4 Chemistry Experimental Procedures

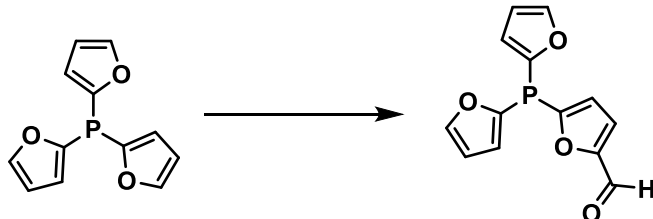


Preparation of 5,5',5"-phosphanetriyltris(furan-2-carbaldehyde) and 5,5'-(furan-2-ylphosphanediyi)bis(furan-2-carbaldehyde): A 100-mL round-bottomed flask equipped with a Teflon-coated magnetic stir bar containing tri(2-furyl)phosphine (469 mg, 2.01 mmol) was vacated and filled with nitrogen three times. The flask was treated with THF (24 mL) and TMEDA (0.86 mL, 6.00 mmol) consecutively. The mixture was cooled to -78 °C, and 2.5 M *n*-BuLi in hexanes (2.66 mL, 6.60 mmol) was added to the flask. The mixture was stirred at the same temperature for 1 h. Then, the mixture was warmed to -10 °C over 2 h. The mixture was cooled again to -78 °C, and DMF (1.14 mL, 12.0 mmol) was added to the flask. The mixture stirred for 1.5 h and was allowed to warm to -20 °C. It was quenched with sat. NH₄Cl. The quenched mixture was extracted with EtOAc (3 × 20 mL). The combined organic layers were dried over Na₂SO₄, filtered, and concentrated *in vacuo*. The crude residue was purified by flash chromatography (15 to 60% EtOAc in hexanes) on silica gel (50 mL) to afford 5,5',5"-phosphanetriyltris(furan-2-carbaldehyde) (162 mg, 26%) as a yellow oil and 5,5'-(furan-2-ylphosphanediyi)bis(furan-2-carbaldehyde) (127 mg, 27 %) as a yellow solid.

Data for 5,5',5"-phosphanetriyltris(furan-2-carbaldehyde): R_f = 0.33 (60% EtOAc in hexanes); IR (neat) ν_{max} = 3346, 3134, 2824, 2714, 2582, 1723, 1670 (C=O), 1559, 1455, 1381, 1338, 1259, 1193, 1116, 1020 cm⁻¹; ¹H NMR (300 MHz, CDCl₃, 293 K): δ 9.70 (s, 3H), 7.26 (s,

3H), 7.01 (d, J = 3.6 Hz, 3H); ^{13}C NMR (100 MHz, CDCl_3 , 293 K): δ 178.0, 156.9 (d, J = 3.0 Hz), 152.9 (d, J = 9.0 Hz), 123.8 (d, J = 19.0), 120.5 (d, J = 5.0 Hz); ^{31}P NMR (120 MHz, CDCl_3 , 293 K) δ -70.18; HRMS (ESI-TOF) m/z : calcd. for $\text{C}_{15}\text{H}_{10}\text{O}_6\text{P}$ [M + H] $^+$ = 317.0210, found 317.0213.

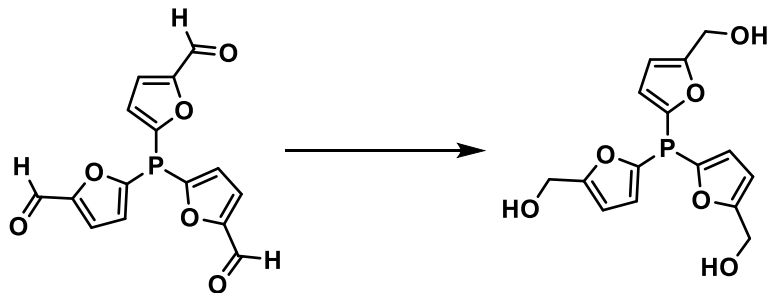
Data for 5,5'-(furan-2-ylphosphanediyyl)bis(furan-2-carbaldehyde): m.p. = 91-92 °C; R_f = 0.48 (60% EtOAc in hexanes); IR (neat) ν_{max} = 1681 (C=O), 1666, 1560, 1552, 1463, 1453, 1388, 1370, 1342, 1259, 1217, 1192, 1123, 1107, 1059 cm $^{-1}$; ^1H NMR (300 MHz, CDCl_3 , 293 K): δ 9.67 (s, 2H), 7.73 (s, 1H), 7.23 (d, J = 3.6 Hz, 2H), 7.03 (appt. t, J = 3.6 Hz, 1H), 6.87 (d, J = 3.6 Hz, 2H), 6.50–6.47 (m, 1H); ^{13}C NMR (100 MHz, CDCl_3 , 293 K): δ 178.0, 156.5 (d, J = 4.0 Hz), 155.4 (d, J = 6.0 Hz), 148.9 (d, J = 2.0 Hz), 144.5 (d, J = 9.0 Hz), 124.6 (d, J = 3.2 Hz), 122.3 (d, J = 16.0 Hz), 120.6, 111.3 (d, J = 8.0 Hz); ^{31}P NMR (120 MHz, CDCl_3 , 293 K) δ -72.34; HRMS (ESI-TOF) m/z : calcd. for $\text{C}_{14}\text{H}_{10}\text{O}_5\text{P}$ [M + H] $^+$ = 289.0260, found 289.0263.



Preparation of 5-(di(furan-2-yl)phosphaneyl)furan-2-carbaldehyde: A 100-mL round-bottomed flask equipped with a Teflon-coated magnetic stir bar containing tri(2-furyl)phosphine (471 mg, 2.02 mmol) was vacated and filled with nitrogen three times. The flask was treated with THF (24 mL) and TMEDA (0.29 mL, 2.00 mmol) consecutively. The mixture was cooled to -78 °C, and 2.5 M *n*-BuLi in hexanes (0.97 mL, 2.40 mmol) was added to the flask. The mixture was stirred at the same temperature for 1 h. Then, the mixture was warmed to -20 °C over 2 h. The mixture was cooled again to -78 °C, and DMF (0.38 mL, 4.00 mmol) was added to the flask. The mixture stirred for 1.5 h and was allowed to warm to -20 °C. It was quenched with sat. NH_4Cl .

The quenched mixture was extracted with EtOAc (3×20 mL). The combined organic layers were dried over Na₂SO₄, filtered, and concentrated *in vacuo*. The crude residue was purified by flash chromatography (10 to 40% EtOAc in hexanes) on silica gel (500 mL) to afford 5-(di(furan-2-yl)phosphaneyl)furan-2-carbaldehyde (338 mg, 65%) as a yellow solid.

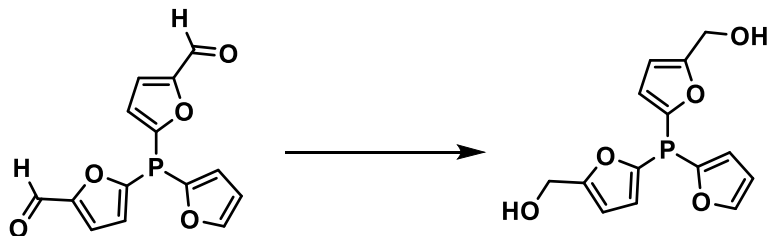
Data for 5-(di(furan-2-yl)phosphaneyl)furan-2-carbaldehyde: m.p. = 77–79 °C; R_f = 0.30 (20% EtOAc in hexanes); IR (neat) ν_{max} = 3119, 1662 (C=O), 1552, 1458, 1451, 1377, 1337, 1263, 1218, 1198, 1122, 1030, 1006 cm⁻¹; ¹H NMR (300 MHz, CDCl₃, 293 K): δ 9.64 (s, 1H), 7.69 (d, J = 1.2 Hz, 2H), 7.21 (dd, J = 3.6, 0.6 Hz, 1H), 6.91 (appt. t, J = 2.7 Hz, 2H), 6.71 (d, J = 3.6 Hz, 1H), 6.45–6.43 (m, 2H); ¹³C NMR (75 MHz, CDCl₃, 293 K): δ 178.0, 157.9 (d, J = 2.0 Hz), 156.2 (d, J = 4.0 Hz), 148.2 (d, J = 2.0 Hz), 146.6 (d, J = 6.0 Hz), 123.1, 122.7, 120.8 (d, J = 12.0 Hz), 111.0 (d, J = 7.5 Hz); ³¹P NMR (120 MHz, CDCl₃, 293 K) δ -74.44; HRMS (ESI-TOF) *m/z*: calcd. for C₁₃H₁₀O₄P [M +H]⁺ = 261.0311, found 261.0315.



Preparation of (phosphanetriyltris(furan-5,2-diyl))trimethanol: A 50-mL round-bottomed flask equipped with a Teflon-coated magnetic stir bar containing 5,5',5"-phosphanetriyltris(furan-2-carbaldehyde) (162 mg, 0.51 mmol) was treated with THF (13.6 mL) and MeOH (6.9 mL). The mixture was cooled to 0 °C, and NaBH₄ (31.5 mg, 0.83 mmol) was added. The mixture was stirred at the same temperature for 30 min and was quenched with 1M NaOH (17.0 mL) and allowed to warm to room temperature. The organic solvents were evaporated from the reaction solution *in*

vacuo. The mixture was extracted with EtOAc (4×70 mL). The combined organic layers were dried over Na₂SO₄, filtered, and concentrated *in vacuo* to obtain (phosphanetriyltris(furan-5,2-diyl))trimethanol (129 mg, 78%) as white solid. The resulting crude was used without further purification.

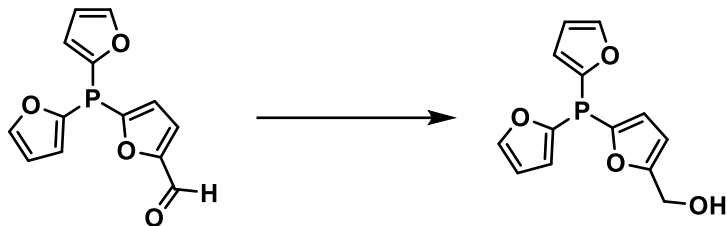
Data for (phosphanetriyltris(furan-5,2-diyl))trimethanol: m.p. = 180–183 °C; R_f = 0.46 (90% EtOAc in hexanes); IR (neat) ν_{max} = 3338 (br, O-H), 3120, 2931, 2869, 1729, 1405, 1366, 1193, 1176, 1011, 1003 cm⁻¹; ¹H NMR (400 MHz, CD₃OD, 293 K): δ 6.74 (dd, *J* = 3.4, 1.2 Hz, 3H), 6.34 (dt, *J* = 4.4, 1.2 Hz, 3H), 4.52 (s, 6H). ¹³C NMR (100 MHz, DMSO-*d*₆, 293 K): δ 160.9 (d, *J* = 3.0 Hz), 147.2, 122.1 (d, *J* = 21.0 Hz), 108.3 (d, *J* = 5.0 Hz), 55.8; ³¹P NMR (160 MHz, CD₃OD, 293 K) δ -74.88; HRMS (ESI-TOF) *m/z*: calcd. for C₁₅H₁₆O₆P [M +H]⁺ = 323.0679, found 323.0677.



Preparation of ((furan-2-ylphosphanediyyl)bis(furan-5,2-diyl))dimethanol: A 50-mL round-bottomed flask equipped with a Teflon-coated magnetic stir bar containing 5,5'-(furan-2-ylphosphanediyyl)bis(furan-2-carbaldehyde) (127 mg, 0.44 mmol) was treated with THF (11.7 mL) and MeOH (6.0 mL). The mixture was cooled to 0 °C, and NaBH₄ (32.4 mg, 0.86 mmol) was added. The mixture was stirred at the same temperature for 30 min and was quenched with 1M NaOH (15.0 mL) and allowed to warm to room temperature. The organic solvents were evaporated from the reaction solution *in vacuo*. The mixture was extracted with EtOAc (4×60 mL). The combined organic layers were dried over Na₂SO₄, filtered, and concentrated *in vacuo* to obtain

((furan-2-ylphosphanediyi)bis(furan-5,2-diyl))dimethanol (125 mg, 97%) as a clear oil. The resulting crude was used without further purification.

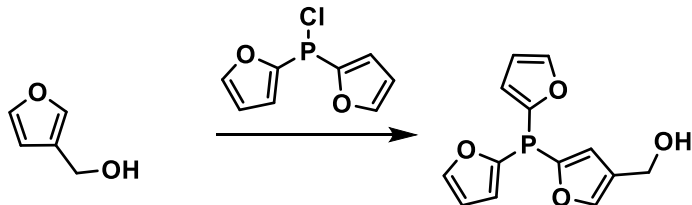
Data for ((furan-2-ylphosphanediyi)bis(furan-5,2-diyl))dimethanol: R_f = 0.31 (40% EtOAc in hexanes); IR (neat) ν_{max} = 3551, 3319 (br, OH), 3124, 2919, 1498, 1453, 1403, 1367, 1237, 1198, 1154, 1181, 1119, 1062, 1006 cm⁻¹; ¹H NMR (400 MHz, CD₃OD, 293 K): δ 7.72 (d, J = 1.6 Hz, 1H), 6.80–6.78 (m, 1H), 6.72 (dd, J = 3.2, 1.6 Hz, 2H), 6.47–6.45 (m, 1H), 6.35–6.33 (m, 2H), 4.52 (s, 4H); ¹³C NMR (100 MHz, CDCl₃, 293 K): δ 159.3 (d, J = 2.5 Hz), 148.6 (d, J = 3.8 Hz), 147.4 (d, J = 2.5 Hz), 122.1 (d, J = 26.2 Hz), 121.2 (d, J = 26.2 Hz), 110.8 (d, J = 6.2 Hz), 108.7 (d, J = 6.2), 57.3; ³¹P NMR (161 MHz, CD₃OD, 293 K) δ -75.44; HRMS (ESI-TOF) *m/z*: calcd. for C₁₄H₁₄O₅P [M + H]⁺ = 293.0573, found 293.0570.



Preparation of (5-(di(furan-2-yl)phosphaneyl)furan-2-yl)methanol: A 100-mL round-bottomed flask equipped with a Teflon-coated magnetic stir bar containing 5-(di(furan-2-yl)phosphaneyl)furan-2-carbaldehyde (233 mg, 0.90 mmol) was treated with THF (23.7 mL) and MeOH (12.0 mL). The mixture was cooled to 0 °C, and NaBH₄ (51.9 mg, 1.37 mmol) was added. After stirring for 30 min at the same temperature, the reaction mixture was quenched with 1M NaOH (30 mL) and allowed to warm to room temperature. The organic solvents were evaporated from the reaction solution *in vacuo*. The mixture was extracted with EtOAc (4 × 120 mL). The combined organic layers were dried over Na₂SO₄, filtered, and concentrated *in vacuo* to obtain (5-

(di(furan-2-yl)phosphaneyl)furan-2-yl)methanol (223 mg, 95%) as a clear oil. The resulting crude was used without further purification.

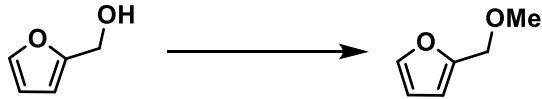
Data for (5-(di(furan-2-yl)phosphaneyl)furan-2-yl)methanol: $R_f = 0.31$ (40% EtOAc in hexanes); IR (neat) $\nu_{max} = 3318$ (br, OH), 3124, 2924, 2868, 1589, 1550, 1454, 1366, 1319, 1211, 1153, 1005 cm^{-1} ; 1H NMR (400 MHz, CD₃OD, 293 K): δ 7.72 (t, $J = 1.6$ Hz, 2H), 6.78–6.76 (m, 2H), 6.70 (dd, $J = 3.2, 1.6$ Hz, 1H), 6.46 (quint, $J = 6.4, 3.2, 1.6$ Hz, 2H), 6.34 (d, $J = 2.4$ Hz, 1H), 4.52 (s, 2H); ^{13}C NMR (160 MHz, CDCl₃, 293 K): δ 159.2 (d, $J = 4.8$ Hz), 148.8, 148.6 (d, $J = 6.4$ Hz), 147.4 (d, $J = 3.2$ Hz), 121.8 (d, $J = 35.2$ Hz), 121.2 (d, $J = 41.6$ Hz), 110.7 (d, $J = 11.2$ Hz), 108.7 (d, $J = 9.6$ Hz), 57.4; ^{31}P NMR (161 MHz, CD₃OD, 293 K) δ -76.04; HRMS (ESI-TOF) m/z : calcd. for C₁₃H₁₂O₄P [M + H]⁺ = 263.0468, found 263.0470.



Preparation of (5-(di(furan-2-yl)phosphaneyl)furan-3-yl)methanol: A 25-mL round-bottomed flask equipped with a Teflon-coated magnetic stir bar was purged with nitrogen three times. The flask was treated with furane-3-methanol (202 mg, 2.06 mmol) and THF (4.0 mL). The mixture was cooled to -78 °C, and 2.5 M n-BuLi in hexanes (1.60 mL, 4.00 mmol) was added to the flask. The mixture was stirred at the same temperature for 1 h. Then, the mixture was warmed to 0 °C and stirred for 2 h. The mixture was cooled again to -78 °C and bis(2-furyl)phosphine chloride (0.18 mL, 1.00 mmol) was added to the flask. The mixture stirred overnight and was allowed to warm to 25 °C. It was quenched with sat. NH₄Cl. The quenched mixture was extracted with EtOAc (2 × 10 mL). The combined organic layers were dried over Na₂SO₄, filtered, and

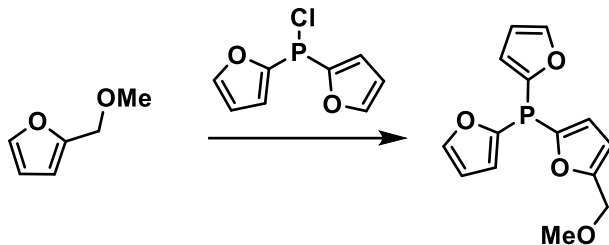
concentrated *in vacuo*. The crude residue was purified by flash chromatography (10 to 40% EtOAc in hexanes) on silica gel (30 mL) to afford (5-(di(furan-2-yl)phosphaneyl)furan-3-yl)methanol (80 mg, 36%) as a white solid.

Data for (5-(di(furan-2-yl)phosphaneyl)furan-3-yl)methanol: m.p. = 154–157; R_f = 0.38 (40% EtOAc in hexanes); IR (neat) ν_{max} = 3334 (br, OH), 3127, 2876, 1754, 1151, 1476, 1454, 1390, 1368, 1212, 1155, 1135, 1120, 1044, 1006 cm⁻¹; ¹H NMR (300 MHz, CDCl₃, 293 K): δ 7.65–7.62 (m, 3H), 6.79–6.77 (m, 2H), 6.52 (dd, J = 3.0, 1.4 Hz, 1H), 6.40 (quint, J = 6.9, 3.0, 1.4 Hz, 2H), 4.67 (d, J = 1.4 Hz, 2H). ¹³C NMR (125 MHz, CDCl₃, 293 K): δ 148.4, 147.7, 147.5 (d, J = 2.5 Hz), 144.9 (d, J = 15.0 Hz), 136.1 (d, J = 27.5 Hz), 121.1 (d, J = 23.8 Hz), 111.4 (d, J = 5.0 Hz), 110.8 (d, J = 6.3 Hz), 56.6 (d, J = 10.0 Hz); ³¹P NMR (120 MHz, CDCl₃, 293 K) δ -85.56; HRMS (ESI-TOF) *m/z*: calcd. for C₁₃H₁₂O₄P [M +H]⁺ = 263.0468, found 263.0467.



Preparation of 2-(methoxymethyl)furan: A 50-mL round-bottomed flask equipped with a Teflon-coated magnetic stir bar containing KOH (10.5 g, 262.9 mmol) was vacated and filled with nitrogen three times. The flask was treated with THF (10 mL) and cooled to 0 °C. Furfuryl alcohol (10.0 mL, 115.6 mmol) and MeI (11.6 mL, 302.8 mmol) were added to the flask. The mixture was warmed to 25 °C, and stirred at the same temperature for 21 h. After removal of THF, ultrapure water was added (20 mL) and the mixture was extracted with Et₂O (2 × 60 mL). The combined organic layers were dried over anhydrous Na₂SO₄, filtered through a cotton plug, and concentrated *in vacuo* to obtain 2-(methoxymethyl)furan (8.06 g, 62% yield) as a clear oil. The resulting crude was used without further purification.

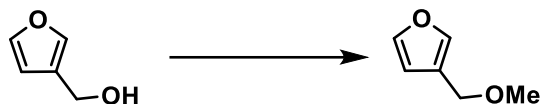
Data for 2-(methoxymethyl)furan: ^1H NMR (400 MHz, CDCl_3 , 293 K): δ 7.41(dd, $J = 3.0, 0.8$ Hz 1H), 6.34–6.31 (m, 2H), 4.39 (s, 2H), 3.36 (s, 3H). Spectroscopic data matched the known literature (*J. Chem. Soc., Perkin Trans.*, **1986**, 545–550)



Preparation of di(furan-2-yl)(5-(methoxymethyl)furan-2-yl)phosphane: A 50-mL round-bottomed flask equipped with a Teflon-coated magnetic stir bar containing 2-furylmethyl methyl ether (361 mg, 3.33 mmol) was vacated and filled with nitrogen three times. The flask was treated with THF (11.0 mL) and cooled to 0 °C. To the reaction mixture was added 2.5 M *n*-BuLi in hexanes (1.30 mL, 3.33 mmol). The mixture was stirred at the same temperature for 50 min and then warmed to 0 °C. After 30 min the mixture was cooled to -78 °C, and bis(2-furyl)phosphine chloride (0.33 mL, 2.12 mmol) was added dropwise. The mixture was stirred overnight and was allowed to warm to 25 °C. It was quenched with sat. NH_4Cl (22 mL), extracted with EtOAc (3 × 50 mL). The combined organic layers were dried over Na_2SO_4 , filtered, and concentrated *in vacuo*. The crude residue was purified by flash chromatography (5 to 15% EtOAc in hexanes) on silica gel (30 mL) to afford di(furan-2-yl)(5-(methoxymethyl)furan-2-yl)phosphane (340 mg, 68%) as a yellow oil.

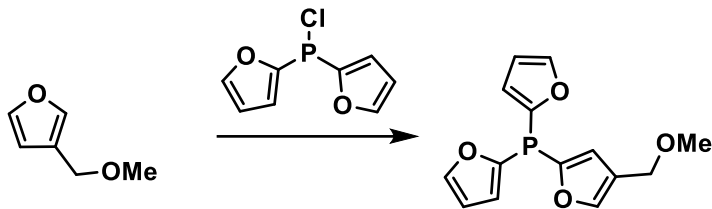
Data for di(furan-2-yl)(5-(methoxymethyl)furan-2-yl)phosphane: $R_f = 0.44$ (20% EtOAc in hexanes); IR (neat) $\nu_{\text{max}} = 3119, 2930, 2893, 2822, 1780, 1551, 1496, 1454, 1368, 1280, 1226, 1212, 1194, 1153, 1135, 1120, 1089, 1007 \text{ cm}^{-1}$; ^1H NMR (500 MHz, CDCl_3 , 293 K): δ 7.64 (d, $J = 1.5$ Hz, 2H), 6.80–6.78 (m, 2H), 6.71 (dd, $J = 3.0, 1.5$ Hz, 1H), 6.39 (quint, $J = 7.0, 3.0, 1.5$ Hz,

2H), 6.33 (dd, J = 3.0, 1.5 Hz, 1H), 4.40 (s, 2H), 3.34 (s, 3H); ^{13}C NMR (100 MHz, CDCl_3 , 293 K): δ 156.7 (d, J = 4.0 Hz), 149.2, 148.6 (d, J = 3.0 Hz), 147.4 (d, J = 3.0 Hz), 121.6, 121.4 (d, J = 9.0 Hz), 121.1, 110.7 (d, J = 6.0 Hz), 110.3 (d, J = 5.0 Hz), 66.4, 57.9; ^{31}P NMR (200 MHz, CDCl_3 , 293 K) δ -76.53; HRMS (ESI-TOF) m/z : calcd. for $\text{C}_{14}\text{H}_{14}\text{O}_4\text{P}$ [$\text{M} + \text{H}]^+$ = 277.0624, found 277.0626.



Preparation of 3-(methoxymethyl)furan: A 10-mL round-bottomed flask equipped with a Teflon-coated magnetic stir bar containing KOH (1.08 g, 18.8 mmol) was vacated and filled with nitrogen three times. The flask was treated with THF (3.00 mL) and cooled to 0 °C. Furane-3-methanol (1.00 mL, 11.8 mmol) and MeI (1.20 mL, 18.8 mmol) were added to the flask. The mixture was warmed to 25 °C, and stirred at the same temperature for 21 h. After removal of THF, ultrapure water was added (10.0 mL) and the mixture was extracted with Et_2O (2×50 mL). The combined organic layers were dried over anhydrous Na_2SO_4 , filtered through a cotton plug, and concentrated *in vacuo* to obtain 3-(methoxymethyl)furan (410 mg, 58% yield) as a clear oil. The resulting crude was used without further purification.

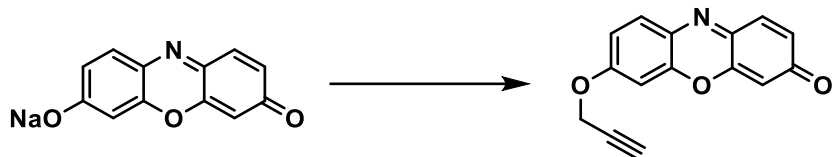
Data for 3-(methoxymethyl)furan: ^1H NMR (300 MHz, CDCl_3 , 293 K): δ = 7.40 (d, J = 3.0 Hz, 2H), 6.40 (s, 1H), 4.32 (s, 2H), 3.34 (s, 3H). Spectroscopic data matched the known literature (*Org. Lett.*, **2014**, 16, 2732–2735.)



Preparation of di(furan-2-yl)(4-(methoxymethyl)furan-2-yl)phosphane: A 50-mL round-bottomed flask equipped with a Teflon-coated magnetic stir bar containing 3-furylmethyl methyl ether (367 mg, 3.33 mmol) was vacated and filled with nitrogen three times. The flask was treated with THF (11.0 mL) and cooled to 0 °C. To the reaction mixture was added 2.5 M *n*-BuLi in hexanes (1.33 mL, 3.33 mmol) was added to the flask. The mixture was stirred at the same temperature for 50 min and then warmed to 0 °C. After 30 min the mixture was cooled to -78 °C, and bis(2-furyl)phosphine chloride (0.40 mL, 2.57 mmol) was added dropwise. The mixture was stirred overnight and was allowed to warm to 25 °C. It was quenched with sat. NH₄Cl (22 mL), extracted with EtOAc (3 × 50 mL). The combined organic layers were dried over Na₂SO₄, filtered, and concentrated *in vacuo*. The crude residue was purified by flash chromatography (5 to 15% EtOAc in hexanes) on silica gel (40 mL) to afford di(furan-2-yl)(4-(methoxymethyl)furan-2-yl)phosphane (410 mg, 58%) as a clear oil.

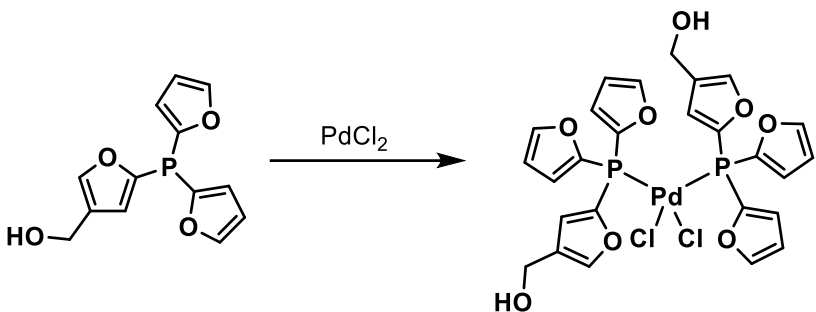
Data for di(furan-2-yl)(4-(methoxymethyl)furan-2-yl)phosphane: R_f = 0.38 (20% EtOAc in hexanes); IR (neat) ν_{max} = 2929, 2820, 1779, 1573, 1551, 1479, 1455, 1390, 1368, 1284, 1214, 1192, 1156, 1134, 1121, 1100, 1058, 1038, 1007 cm⁻¹; ¹H NMR (500 MHz, CDCl₃, 293 K): δ 7.64 (d, *J* = 2.0 Hz, 3H), 6.78–6.77 (m, 2H), 6.48 (dd, *J* = 3.5, 2.0 Hz, 1H), 6.39 (quint, *J* = 7.0, 3.5, 2.0 Hz, 2H), 4.49 (d, *J* = 2.0 Hz, 2H), 3.29 (s, 3H); ¹³C NMR (100 MHz, CDCl₃, 293 K): δ 148.4, 147.6, 147.3 (d, *J* = 3.0 Hz), 145.6 (d, *J* = 17.0 Hz), 133.2 (d, *J* = 29.0 Hz), 120.9 (d, *J* = 29.0 Hz), 121 (d, *J* = 24.0 Hz), 111.4 (d, *J* = 6.0 Hz), 110.7 (d, *J* = 7.0 Hz), 65.6 (d, *J* = 10.0 Hz), 57.6; ³¹P

¹NMR (200 MHz, CDCl₃, 293 K) δ -86.21; HRMS (ESI-TOF) *m/z*: calcd. for C₁₄H₁₄O₄P [M +H]⁺ = 277.0624, found 277.0623.



Preparation of 7-(prop-2-yn-1-yloxy)-3H-phenoxazin-3-one: A 10-mL round-bottomed flask equipped with a Teflon-coated magnetic stir bar containing resorufin sodium salt (307 mg, 1.28 mmol) and K₂CO₃ (529 mg, 3.83 mmol) was vacated and filled with nitrogen three times. The flask was treated with DMF (2.6 mL) and 80% by weight propargyl bromide in toluene (0.43 mL, 3.83 mmol). After 48 h the reaction mixture quenched with cold H₂O (100 mL) and filtered through a coarse fritted funnel. The resulting solid was washed with hexanes (2 × 100 mL) and cold H₂O (100 mL). The solid was recrystallized from ethyl acetate and hexanes, affording 7-(prop-2-yn-1-yloxy)-3H-phenoxazin-3-one (247 mg, 75% yield) as a red-orange solid.

Data for 7-(prop-2-yn-1-yloxy)-3H-phenoxazin-3-one: m.p. = >200 °C; R_f = 0.39 (60% ethyl acetate in hexanes); IR (neat) ν_{max} = 3434, 1646, 1612, 1506, 1366, 1271, 1214, 1106 cm⁻¹, ¹H NMR (400 MHz, CDCl₃, 293 K): δ 7.82 (d, *J* = 7.6 Hz, 1H), 7.55 (d, *J* = 7.6 Hz, 1H), 7.18 (d, *J* = 2.0 Hz, 1H), 7.11 (dd, *J* = 7.6, 2.0 Hz), 6.80 (dd, *J* = 7.6, 2.0 Hz, 1H), 6.30 (d, *J* = 2.0 Hz, 1H), 5.01 (d, *J* = 2.0 Hz, 1H), 3.70 (s, 1H); ¹³C NMR (100 MHz, DMSO-*d*₆, 293 K): 185.4, 161.0, 149.7, 145.7, 145.1, 135.0, 133.9, 131.3, 128.4, 114.1, 105.8, 101.4, 79.2, 78.3, 56.5; δ; HRMS (ESI-TOF) *m/z*: calcd for C₁₅H₁₀NO₃ [M+H]⁺ = 252.0655, found 252.0655.

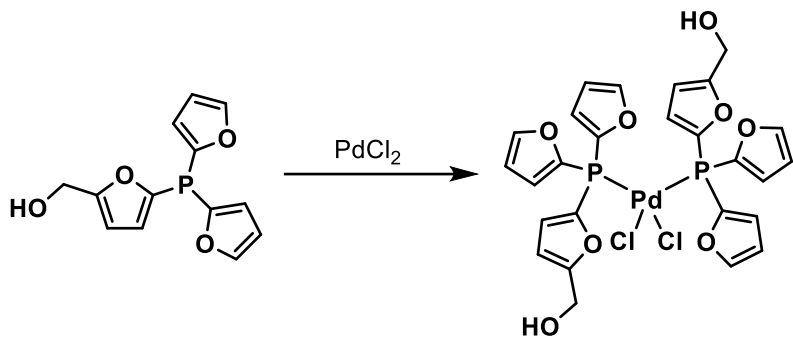


Preparation of dichlorobis((5-(di(furan-2-yl)phosphaneyl)furan-3-yl)methanol)palladium(II):

A 10-mL round-bottomed flask equipped with a Teflon-coated magnetic stir bar containing PdCl_2 (5.0 mg, 0.028 mmol) and (5-(di(furan-2-yl)phosphaneyl)furan-3-yl)methanol (15.0 mg, 0.056 mmol) was vacated and filled with argon three times. The flask was treated with MeCN (2.5 mL) and stirred for 4 h. Upon completion, the reaction mixture was concentrated *in vacuo*, affording dichlorobis((5-(di(furan-2-yl)phosphaneyl)furan-3-yl)methanol)palladium(II) (19.2 mg, 96% yield) as a yellow solid.

Data for dichlorobis((5-(di(furan-2-yl)phosphaneyl)furan-3-yl)methanol)palladium(II):

m.p = 140–143 °C; IR (neat) $\nu_{\text{max}} = 3408, 3116, 2826, 1659, 1572, 1549, 1449, 1386, 1367, 1215, 1160, 1124, 1048, 1010 \text{ cm}^{-1}$; ^1H NMR (400 MHz, DMSO- d_6 , 293 K): δ 7.92 (br. s, 2H), 7.85 (br. s, 3H), 6.77 (br. s, 2H), 6.73 (s, 1H), 6.51 (t, $J = 1.6 \text{ Hz}$, 2H), 4.60 (s, 2H); ^{13}C NMR (150 MHz, DMSO- d_6 , 293 K): δ 149.7, 149.0, 140.7 (d, $J = 19.5 \text{ Hz}$), 140.0 (d, $J = 91.5 \text{ Hz}$), 132.7 (d, $J = 91.5 \text{ Hz}$), 124.4 (d, $J = 28.0 \text{ Hz}$), 112.6, 111.8, 55.6; ^{31}P NMR (200 MHz, DMSO- d_6 , 293 K) δ -24.8.

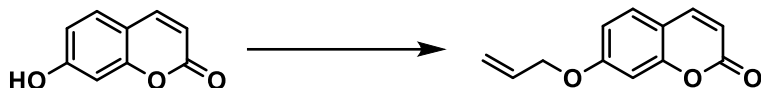


Preparation of dichlorobis((5-(di(furan-2-yl)phosphaneyl)furan-2-yl)methanol)palladium(II):

A 10-mL round-bottomed flask equipped with a Teflon-coated magnetic stir bar containing PdCl₂ (11.0 mg, 0.062 mmol) and (5-(di(furan-2-yl)phosphaneyl)furan-2-yl)methanol (32.8 mg, 0.12 mmol) was vacated and filled with argon three times. The flask was treated with MeCN (2.5 mL) and stirred for 4 h. Upon completion, the reaction mixture was concentrated *in vacuo*, affording dichlorobis((5-(di(furan-2-yl)phosphaneyl)furan-2-yl)methanol)palladium(II) (39.6 mg, 90% yield) as a yellow solid.

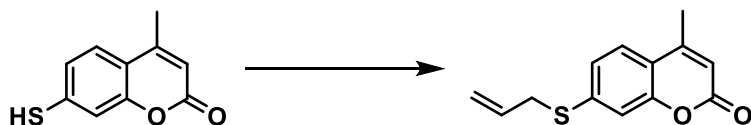
Data for dichlorobis((5-(di(furan-2-yl)phosphaneyl)furan-2-yl)methanol)palladium(II):

m.p = 182–186 °C; IR (neat) ν_{max} = 3399, 3112, 1587, 1548, 1489, 1450, 1404, 1366, 1216, 1124, 1065, 1010 cm⁻¹; ¹H NMR (400 MHz, DMSO-*d*₆, 293 K): δ 7.93 (s, 2H), 6.91 (q, *J* = 6.0, 2.8 Hz, 3H), 6.57 (t, *J* = 1.6 Hz, 2H), 6.37 (d, *J* = 2.8 Hz, 1H), 5.41 (t, *J* = 6.0 Hz, 1H), 4.28 (d, *J* = 6.0 Hz, 3H); ¹³C NMR (125 MHz, DMSO-*d*₆, 293 K): δ 162.6 (d, *J* = 6.2 Hz), 149.6 (d, *J* = 5.0 Hz), 140.4 (d, *J* = 92.5 Hz), 138.5 (d, *J* = 92.5 Hz), 125.9 (d, *J* = 18.8 Hz), 124.6 (d, *J* = 20.0 Hz), 111.6 (d, *J* = 8.8 Hz), 108.7 (d, *J* = 7.5 Hz), 55.7; ³¹P NMR (200 MHz, DMSO-*d*₆, 293 K) δ -22.00.



Preparation of 7-(allyloxy)-2H-chromen-2-one: A 10-mL round-bottomed flask equipped with a Teflon-coated magnetic stir bar containing 7-hydroxycoumarin (126 mg, 1.00 mmol) and K₂CO₃ (286 mg, 3.00 mmol) was vacated and filled with nitrogen three times. The flask was treated with DMF (1.0 mL) and allyl bromide (0.18 mL, 2.05 mmol). The reaction mixture was heated to 60 °C (external). After 4 h the mixture was allowed to warm to 25 °C. It was quenched with H₂O (10 mL), extracted with EtOAc (2 × 20 mL). The combined organic layers were dried over Na₂SO₄, filtered, and concentrated *in vacuo*. The crude residue was purified by flash chromatography (10 to 30% EtOAc in hexanes) on silica gel (10 mL) to afford 7-(allyloxy)-2H-chromen-2-one (80.5 mg, 40%) as a white solid.

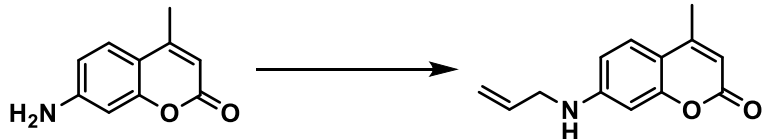
Data for 7-(allyloxy)-2H-chromen-2-one: R_f = 0.30 (20% EtOAc in hexanes); ¹H NMR (400 MHz, CDCl₃, 293 K): δ 7.63 (d, J = 9.2 Hz, 1H), 7.37 (d, J = 9.2 Hz, 1H), 6.87 (dd, J = 8.8, 2.4 Hz, 2H), 6.83 (d, J = 2.4 Hz, 1H), 6.25 (d, J = 8.8 Hz, 1H), 6.05 (ddt, J = 15.6, 10.4, 5.2 Hz, 1H), 5.44 (ddd, J = 17.2, 3.2, 1.2 Hz, 1H), 5.35 (dd, J = 10.4, 1.2 Hz, 1H), 4.60 (ddt, J = 5.2, 3.2, 1.2 Hz, 2H). Spectroscopic data matched the known literature (*Tetrahedron*, **2002**, 58, 2831–2837).



Preparation of 7-(allylthio)-4-methyl-2H-chromen-2-one: A 10-mL round-bottomed flask equipped with a Teflon-coated magnetic stir bar containing 7-mercaptop-4-methylcoumarin (101 mg, 0.52 mmol) and K₂CO₃ (127 mg, 0.80 mmol) was vacated and filled with nitrogen three times.

The flask was treated with acetone (3.0 mL) and allyl bromide (48 μ L, 0.55 mmol). After 4 h the reaction mixture was concentrated *in vacuo*. The crude residue was purified by flash chromatography (10 to 30% EtOAc in hexanes) on silica gel (10 mL) to afford 7-(allylthio)-4-methyl-2*H*-chromen-2-one (66.2 mg, 55%) as a white solid.

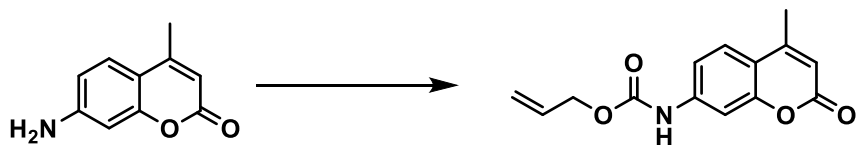
*Data for 7-(allylthio)-4-methyl-2*H*-chromen-2-one:* m.p. = 51–53 °C; R_f = 0.29 (20% EtOAc in hexanes); IR (neat) ν_{max} = 1732, 1715, 1679, 1598, 1541, 1406, 1386, 1370, 1325, 1246, 1165, 1054, 1009 cm⁻¹; ¹H NMR (400 MHz, CDCl₃, 293 K): δ 7.46 (d, J = 8.4 Hz, 1H), 7.20 (d, J = 1.6 Hz, 1H), 7.17 (dd, J = 8.4, 1.6 Hz, 1H), 6.22 (d, J = 1.6 Hz, 1H), 5.94–5.84 (m, 1H), 5.29 (ddd, J = 16.8, 2.0, 1.2 Hz, 1H), 5.18 (dd, J = 10.0, 1.2 Hz, 1H), 3.65 (ddt, J = 6.4, 2.0, 1.2 Hz, 2H), 2.41 (d, J = 1.2 Hz, 3H); ¹³C NMR (100 MHz, CDCl₃, 293 K): δ 160.6, 153.8, 152.2, 142.5, 132.4, 124.5, 123.5, 118.8, 117.4, 114.8, 114.0, 35.5, 18.6; HRMS (ESI-TOF) *m/z*: calcd. for C₁₃H₁₃O₂S [M + H]⁺ = 233.0631, found 233.0632.



*Preparation of 7-(allylamino)-4-methyl-2*H*-chromen-2-one:* A 10-mL round-bottomed flask equipped with a Teflon-coated magnetic stir bar containing 7-amino-4-methylcoumarin (49.8 mg, 0.29 mmol) and K₂CO₃ (46.8 mg, 0.34 mmol) was vacated and filled with nitrogen three times. The flask was treated with DMF (1.0 mL) and allyl bromide (26 μ L, 0.30 mmol). The reaction mixture was heated to 60 °C (external). After 4 h the mixture was allowed to warm to 25 °C and stirred overnight. It was quenched with H₂O (10 mL), extracted with EtOAc (3 \times 15 mL). The combined organic layers were dried over Na₂SO₄, filtered, and concentrated *in vacuo*. The crude

residue was purified by flash chromatography (10 to 40% EtOAc in hexanes) on silica gel (5 mL) to afford 7-(allylamino)-4-methyl-2*H*-chromen-2-one (17.1 mg, 28%) as a white solid.

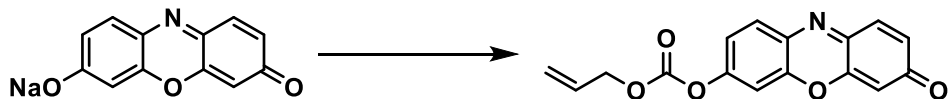
*Data for 7-(allylamino)-4-methyl-2*H*-chromen-2-one:* m.p. = 97-98 °C; R_f = 0.29 (20% EtOAc in hexanes); IR (neat) ν_{max} = 3346, 2927, 1693, 1621, 1614, 1601, 1574, 1525, 1504, 1488, 1398, 1374, 1366, 1334, 1265, 1216, 1154 cm⁻¹; ¹H NMR (400 MHz, acetone-*d*₆, 293 K): δ 7.45 (d, *J* = 8.8 Hz, 1H), 6.67 (dd, *J* = 8.8, 2.0 Hz, 1H), 6.44 (d, *J* = 2.0 Hz, 1H), 6.10 (br. s, 1H), 6.00–5.90 (m, 1H), 5.89 (d, *J* = 1.6 Hz, 1H) 5.29 (ddt, *J* = 17.2, 3.6, 1.6 Hz, 1H), 5.14 (ddd, *J* = 10.4, 3.6, 1.6 Hz, 1H), 3.89 (m, 2H), 2.35 (d, *J* = 1.6 Hz, 3H); ¹³C NMR (100 MHz, CDCl₃, 293 K): δ 161.9, 155.8, 152.9, 151.3, 133.9, 125.4, 117.0, 110.7, 110.4, 109.4, 98.4, 45.9, 18.9; HRMS (ESI-TOF) *m/z*: calcd. for C₁₃H₁₄O₂N [M + H]⁺ = 216.1019, found 216.1020.



*Preparation of allyl (4-methyl-2-oxo-2*H*-chromen-7-yl)carbamate:* A 10-mL round-bottomed flask equipped with a Teflon-coated magnetic stir bar containing 7-amino-4-methylcoumarin (51 mg, 0.29 mmol) and K₂CO₃ (42.3 mg, 0.31 mmol) was vacated and filled with nitrogen three times. The flask was treated with DMF (0.8 mL) and allyl chloroformate (104 μL, 1.31 mmol). The reaction mixture was stirred overnight. It was quenched with 1M HCl (10 mL), and extracted with EtOAc (3 × 15 mL). The combined organic layers were dried over Na₂SO₄, filtered, and concentrated *in vacuo* to obtain allyl (4-methyl-2-oxo-2*H*-chromen-7-yl)carbamate (69.0 mg, 93%) as white solid. The resulting crude was used without further purification.

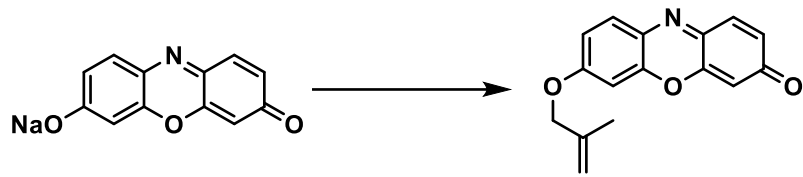
*Data for allyl (4-methyl-2-oxo-2*H*-chromen-7-yl)carbamate:* m.p. = 178-179 °C; R_f = 0.31 (20% EtOAc in hexanes); IR (neat) ν_{max} = 3275, 2982, 1724, 1684, 1617, 1582, 1536, 1512, 1423,

1397, 1232, 1210, 1172, 1162, 1052, 1020, 1012, cm^{-1} ; ^1H NMR (400 MHz, CDCl_3 , 293 K): δ 7.52 (d, $J = 8.8$ Hz, 1H), 7.44 (d, $J = 2.0$ Hz, 1H), 7.38 (d, $J = 8.8$ Hz, 1H), 6.94 (br. s, 1H), 6.19 (d, $J = 1.6$ Hz, 1H), 6.02–5.92 (m, 1H), 5.38 (dd, $J = 17.2, 1.6$ Hz, 1H), 5.29 (dd, $J = 10.4, 1.6$ Hz, 1H), 4.70 (d, $J = 5.6$ Hz, 2H), 2.41 (d, $J = 1.2$ Hz, 3H); ^{13}C NMR (100 MHz, $\text{DMSO}-d_6$, 293 K): δ 160.5, 154.3, 153.7, 153.5, 143.2, 133.4, 126.5, 118.4, 114.9, 114.7, 112.4, 104.9, 65.6, 18.5; HRMS (ESI-TOF) m/z : calcd. for $\text{C}_{14}\text{H}_{14}\text{O}_4\text{N}$ [$\text{M} + \text{H}]^+$ = 260.0917, found 260.0913.



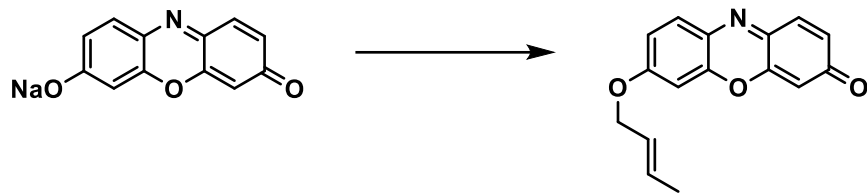
Preparation of allyl (3-oxo-3H-phenoxazin-7-yl) carbonate: A 10-mL round-bottomed flask equipped with a Teflon-coated magnetic stir bar containing resorufin sodium salt (102 mg, 0.43 mmol) and K_2CO_3 (118 mg, 0.85 mmol) was vacated and filled with nitrogen three times. The flask was treated with DMF (2.0 mL) and allyl chloroformate (0.18 μL , 1.70 mmol). The reaction mixture was stirred overnight. It was quenched with H_2O (10 mL), and the resulting mixture was filtered through a coarse fritted funnel. The resulting solid was washed with water (3 x 10 mL) and cold hexanes (3 x 10 mL) to obtain allyl (3-oxo-3H-phenoxazin-7-yl) carbonate (80.9 mg, 93%) as brown-red solid. The resulting crude was used without further purification.

Data for allyl (3-oxo-3H-phenoxazin-7-yl) carbonate: ^1H NMR (400 MHz, CDCl_3 , 293 K): δ 7.52 (d, $J = 8.8$ Hz, 1H), 7.44 (d, $J = 10.0$ Hz, 1H), 7.37 (dd, $J = 8.8, 2.8$ Hz, 1H), 6.93 (s, 1H), 6.19 (d, $J = 1.2$ Hz, 1H), 6.02–5.92 (m, 1H), 5.41 (dd, $J = 17.2, 1.2$ Hz, 1H), 5.29 (dd, $J = 10.0, 1.2$ Hz, 1H), 4.70 (d, $J = 5.6$ Hz, 2H); Spectroscopic data matched the known literature (*Dalton Trans.*, **2016**, 11682–11687).



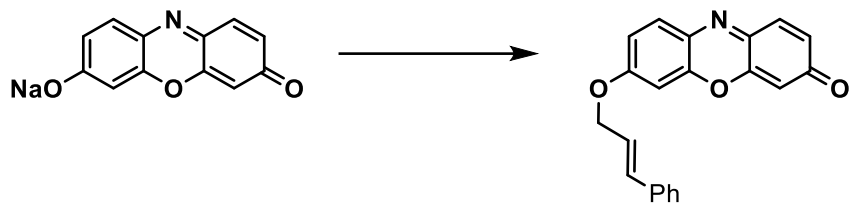
Preparation of 7-((2-methylallyl)oxy)-3H-phenoxazin-3-one: To a 10 mL round bottom flask containing a Teflon-coated magnetic stir bar and resorufin sodium salt (0.1035 g, 0.425 mmol) in dry DMF (0.5 mL) added 3-chloro-2-methyl-1-propene (0.13 mL, 1.28 mmol) in DMF (0.75 mL) under nitrogen atmosphere. To the mixture was added K_2CO_3 (0.180 g, 1.28 mmol). After 7 days, the reaction mixture was quenched with water (50 mL), and the mixture was filtered through a coarse fritted funnel. The resulting solid was washed with water (3×50 mL) and cold hexanes (50 mL) affording 7-((2-methylallyl)oxy)-3H-phenoxazin-3-one (0.118 g, quantitative yield) as a dark red-orange solid.

Data for 7-((2-methylallyl)oxy)-3H-phenoxazin-3-one: m.p. = 205-206 °C; R_f = 0.71 (50 % EtOAc in hexanes); IR (neat) ν_{max} = 1614, 1565, 1488, 858 cm^{-1} ; ^1H NMR (300 MHz, CDCl_3 , 293 K) δ 7.71 (d, J = 9.0 Hz, 1H), 7.44 (d, J = 9.0 Hz, 1H), 6.98 (dd, J = 9.0, 3.0 Hz, 1H), 6.87 (s, 1H), 6.84 (s, 1H), 6.36 (s, 1H), 5.13 (s, 1H), 5.07 (s, 1H), 4.56 (s, 2H), 1.86 (s, 3H); ^{13}C NMR (100 MHz, CDCl_3 , 293 K) δ 186.3, 162.8, 149.8, 145.6, 139.5, 134.7, 134.2, 131.6, 128.4, 114.2, 113.8, 106.7, 100.9, 72.6, 19.3; HRMS (ESI-TOF) m/z : calcd. for $\text{C}_{16}\text{H}_{13}\text{NO}_3$ $[\text{M} + \text{H}]^+$ = 268.0968, found 268.0970.



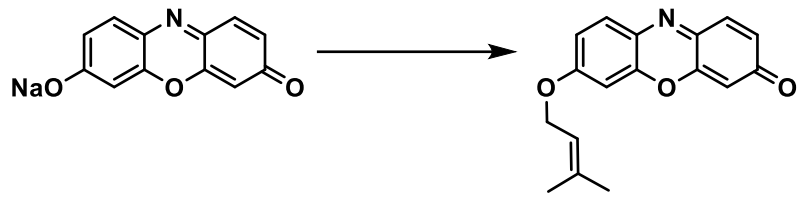
Preparation of (E)-7-(but-2-en-1-yloxy)-3H-phenoxazin-3-one: To a 10 mL round bottom flask containing a Teflon-coated magnetic stir bar and resorufin sodium salt (0.1025 g, 0.436 mmol) in dry DMF (1.25 mL) added K_2CO_3 (0.182 g, 1.31 mmol) and 1-chloro-2-butene (0.125 mL, 1.27 mmol) under nitrogen atmosphere. After 5 days, the reaction mixture was quenched with water (50 mL), and the mixture was filtered through a coarse fritted funnel. The resulting solid was washed with water (3×50 mL) and cold hexanes (50 mL) affording (E)-7-(but-2-en-1-yloxy)-3H-phenoxazin-3-one (0.114 g, quantitative yield) as a dark red-orange solid.

Data for (E)-7-(but-2-en-1-yloxy)-3H-phenoxazin-3-one: m.p. = 199–201 °C; R_f = 0.60 (50 % EtOAc in hexanes); IR (neat) ν_{max} = 3056, 2950, 1515, 1564, 1504, 1363, 1272, 1212, 1116, 1099, 972, 956 cm¹. ¹H NMR (300 MHz, CDCl_3 , 293 K) δ 7.72 (d, J = 9.0 Hz, 1H), 7.45 (d, J = 9.0 Hz, 1H), 6.96 (dd, J = 2.4, 9.0 Hz, 1H), 6.88 (d, J = 1.8 Hz, 1H), 6.85 (d, J = 1.8 Hz, 1H), 6.83 (d, J = 2.4 Hz, 1H), 6.38 (s, 1H, Ar), 5.97–5.90 (m, 1H), 5.76–5.69 (m, 1H), 4.58 (d, J = 6.0 Hz, 2H), 1.80 (d, J = 6.0 Hz, 3H); ¹³C NMR (100 MHz, CDCl_3 , 293 K) δ 186.3, 162.8, 149.9, 145.7, 145.5, 134.7, 134.2, 132.0, 131.6, 128.3, 124.7, 114.3, 106.7, 100.8, 69.7, 17.9; HRMS (ESI-TOF) m/z : calcd. for $\text{C}_{16}\text{H}_{13}\text{NO}_3$ [M + H]⁺ = 268.0968, found 268.0971.



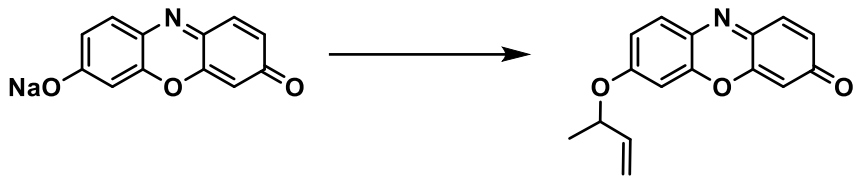
Preparation of 7-(cinnamyl)phenoxazin-3-one: To a 10 mL round bottom flask containing a Teflon-coated magnetic stir bar and resorufin sodium salt (0.101 g, 0.429 mmol) in dry DMF (1.25 mL) added K_2CO_3 (0.181 g, 1.31 mmol), (3-chloropropenyl)benzene (0.178 mL, 1.27 mmol) and NaI (0.007 g, 0.045 mmol) under nitrogen atmosphere. After 5 days the reaction mixture was quenched with water (50 mL), and the resulting mixture was filtered through a coarse fritted funnel. The resulting solid was washed with water (3×50 mL) and cold hexanes (50 mL) affording 7-(cinnamyl)phenoxazin-3-one (0.141 g, 95% yield) as a dark red-orange solid.

Data for 7-(cinnamyl)phenoxazin-3-one: m.p. = 201–203 °C; R_f = 0.39 (50 % EtOAc in hexanes); IR (neat) ν_{max} = 3434, 1665, 1645, 1614, 1564, 1492, 1449, 1388, 1364, 1341, 1316, 1271, 1214, 1098, 991, 960, 906, 857, 816, 731, 683 cm^{-1} ; ^1H NMR (300 MHz, CDCl_3 , 293 K) δ 7.72 (d, J = 6.6 Hz, 1H), 7.44 (d, J = 3.9 Hz, 1H), 7.41 (s, 2H), 7.38–7.28 (m, 3H), 7.00 (dd, J = 6.6, 2.1 Hz, 1H), 6.87 (d, J = 2.1 Hz, 1H), 6.84 (dd, J = 6.6, 1.2 Hz, 1H), 6.77 (d, J = 12.0 Hz, 1H), 6.44–6.37 (m, 1H), 6.33 (s, 1H), 4.81 (d, J = 3.9 Hz, 2H); ^{13}C NMR (100 MHz, CDCl_3 , 293 K) δ 186.3, 162.6, 149.8, 145.7, 135.9, 134.7, 134.3, 134.2, 131.6, 128.7, 128.5, 128.4, 126.7, 122.7, 114.2, 106.8, 100.9, 69.6; HRMS (ESI-TOF) m/z : calcd. for $\text{C}_{21}\text{H}_{15}\text{NO}_3$ [$\text{M} + \text{H}]^+$ = 330.1125, found 330.1138.



Preparation of 7-((3-methylbut-2-en-1-yl)oxy)-3H-phenoxyazin-3-one: To a 10 mL round bottom flask containing a Teflon-coated magnetic stir bar and resorufin sodium salt (0.1034 g, 0.439 mmol) in dry DMF (1.25 mL) was added K_2CO_3 (0.177 g, 1.28 mmol) and 1-chloro-3-methyl-2-butene (0.144 mL, 1.27 mmol) under nitrogen atmosphere. After 3 days, the reaction mixture was quenched with water (50 mL), and the resulting mixture was filtered through a coarse fritted funnel. The resulting solid was washed with water (3×50 mL) and cold hexanes (50 mL) affording 7-((3-methylbut-2-en-1-yl)oxy)-3H-phenoxyazin-3-one (0.124 g, quantitative yield) as a dark red-orange solid.

Data for 7-((3-methylbut-2-en-1-yl)oxy)-3H-phenoxyazin-3-one: m.p. = 210–213 °C; R_f = 0.38 (50 % EtOAc in hexanes); IR (neat) ν_{\max} = 2928, 1644, 1614, 1593, 1562, 1503, 1363, 1342, 1271, 1213, 1097, 987, 858 cm^{-1} ; ^1H NMR (300 MHz, CDCl_3 , 293 K) δ 7.72 (d, J = 7.2 Hz, 1H), 7.46 (d, J = 7.2 Hz, 1H), 6.95 (dd, J = 6.6, 1.8 Hz, 1H), 6.84 (dd, J = 9.8, 1.8 Hz, 1H), 6.82 (d, J = 2.6 Hz, 1H), 6.33 (d, J = 1.8 Hz, 1H), 5.51–5.48 (m, 1H), 4.64 (d, J = 5.1 Hz, 1H), 1.83 (s, 3H), 1.79 (s, 3H); ^{13}C NMR (100 MHz, CDCl_3 , 293 K) δ 186.3, 163.0, 149.9, 145.7, 145.4, 139.8, 134.7, 134.2, 131.5, 128.3, 118.3, 114.3, 106.7, 100.7, 65.9, 25.9, 18.3; HRMS (ESI-TOF) m/z : calcd. for $\text{C}_{17}\text{H}_{15}\text{NO}_3$ [$\text{M} + \text{H}]^+$ = 282.1125, found 282.1132.



Preparation of 7-((3-methylbut-2-en-1-yl)oxy)-3H-phenoxazin-3-one: To a 10 mL round bottom flask containing a Teflon-coated magnetic stir bar and resorufin sodium salt (0.106 g, 0.449 mmol) in dry DMF (1.25 mL) was added K₂CO₃ (0.176 g, 1.28 mmol) and 3-chlorobut-1-ene (0.128 mL, 1.27 mmol) under nitrogen atmosphere. The reaction mixture was heated to 50 °C (external). After 9 days, the reaction mixture was quenched with water (50 mL), and the resulting mixture was filtered through a coarse fritted funnel. The resulting solid was washed with water (3 × 50 mL) and cold hexanes (50 mL) affording 7-((3-methylbut-2-en-1-yl)oxy)-3H-phenoxazin-3-one (0.0515 g, 45 yield) as a dark brown solid.

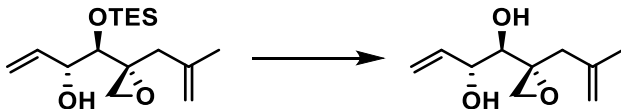
Data for 7-((3-methylbut-2-en-1-yl)oxy)-3H-phenoxazin-3-one: m. p. = 207-208 °C; R_f = 0.47 (50 % EtOAc in hexanes); IR (neat) ν_{max} = 1645, 1613, 1593, 1565, 1492, 1446, 1364, 1286, 1271, 1238, 1214, 1101, 1101 cm⁻¹; ¹H NMR (300 MHz, CDCl₃, 293 K) δ 7.68 (d, J = 9.0 Hz, 1H), 7.42 (d, J = 9.0 Hz, 1H), 6.94 (dd, J = 9.0, 2.1, 1H), 6.84 (d, J = 2.1 Hz, 1H), 6.81 (d, J = 2.1 Hz, 1H), 6.32 (d, J = 2.1 Hz, 1H), 5.91 (ddt, J = 17.1, 10.8, 6.3 Hz, 1H), 5.32 (d, J = 17.1 Hz, 1H), 5.26 (d, J = 10.8 Hz, 1H), 4.92–4.88 (m, 1H), 1.50 (d, J = 6.3 Hz, 3H); ¹³C NMR (100 MHz, CDCl₃, 293 K) δ 186.5, 162.3, 149.9, 145.6, 145.3, 137.7, 134.7, 134.0, 131.5, 128.3, 116.8, 115.1, 106.6, 101.8, 100.8, 75.9, 21.3; HRMS (ESI-TOF) *m/z*: calcd. for C₁₆H₁₃NO₃ [M + H]⁺ = 268.0968, found 268.0972.

Appendix A.3 Synthesis of a Tetrahydrofuran Analog of FR901464

Appendix A.3.1 Growth Inhibition

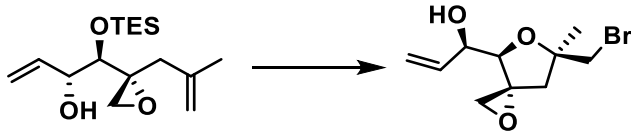
Method. 1,500 cells/well for HCT116 cell line, or 10,000 cells/well for LS174T cell line, were seeded in DMEM (10% FBS, p/s; 100 μ L) in a black, clear-bottom 96 well plate and were incubated overnight at 37 °C in a water saturated, 5% CO₂ atmosphere. Drugs were diluted with water and added to the wells. The cells were then incubated again for 72 h. Following this, WST1 reagent is added to each well (10 μ L per well) and incubated for 2 or 1 h at 37 °C. The absorbance at 450 nm is measured. Final concentrations: 0–30 nM MAMA, MAMD, 0–10 μ M **3.25**.

Appendix A.3.2 Chemistry Experimental Procedures



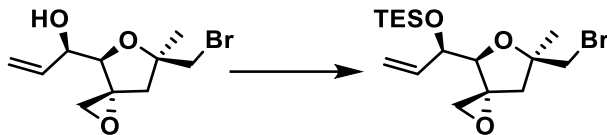
*Preparation of (1*R*,2*R*)-1-((*R*)-2-(2-methylallyl)oxiran-2-yl)but-3-ene-1,2-diol:* To a 25 mL round bottom flask containing a Teflon-coated magnetic stir bar and (1*R*,2*R*)-1-((*R*)-2-(2-methylallyl)oxiran-2-yl)-1-((triethylsilyl)oxy)but-3-en-2-ol (209 mg, 0.67 mmol) in THF (4 mL) was added TBAF (1 M in THF, 1.3 mL) at 0 °C under an open atmosphere. After 50 min at the same temperature, the reaction mixture was diluted with Et₂O (15 mL), filtered through a pad of Florisil, rinsed with Et₂O (4 × 10 mL), and concentrated under reduced pressure. The crude residue was purified by flash chromatography (15 to 50% EtOAc in hexanes) on silica gel (24 mL) to afford (1*R*,2*R*)-1-((*R*)-2-(2-methylallyl)oxiran-2-yl)but-3-ene-1,2-diol (57.1 mg, 46%) as a clear oil.

*Data for (1*R*,2*R*)-1-((*R*)-2-(2-methylallyl)oxiran-2-yl)but-3-ene-1,2-diol:* $R_f = 0.35$ (50% EtOAc in hexanes); IR (neat) $\nu_{max} = 3407$ (br, OH), 3076, 2980, 1649, 1436, 1376, 1251, 1131, 1033, 995, 959, 927, 896 cm⁻¹; ¹H NMR (400 MHz, CDCl₃, 293 K): δ 5.96 (ddd, $J = 17.4, 10.4, 5.2$ Hz, 1H), 5.40 (d, $J = 17.4$ Hz, 1H), 5.30 (d, $J = 10.4$ Hz, 1H), 4.88 (s, 1H), 4.82 (s, 1H), 4.26 (t, $J = 5.2$ Hz, 1H), 3.73 (d, $J = 5.2$ Hz, 1H), 2.97 (d, $J = 4.4$ Hz, 1H), 2.66 (d, $J = 4.4$ Hz, 1H), 2.59 (d, $J = 14.8$ Hz, 1H), 2.30 (d, $J = 14.8$ Hz, 1H), 1.77 (s, 3H); ¹³C NMR (100 MHz, CDCl₃, 293 K): δ 140.6, 136.2, 117.4, 114.5, 73.3, 72.8, 59.1, 49.6, 40.2, 23.1; HRMS (ESI-TOF) *m/z*: calcd. for C₁₀H₁₆O₃Na [M + Na]⁺ = 207.0992, found 207.0992.



*Preparation of (R)-1-((3*R*,4*R*,6*R*)-6-(bromomethyl)-6-methyl-1,5-dioxaspiro[2.4]heptan-4-yl)prop-2-en-1-ol:* A 25-mL round-bottomed flask equipped with a Teflon-coated magnetic stir bar containing (1*R*,2*R*)-1-((*R*)-2-(2-methylallyl)oxiran-2-yl)-1-((triethylsilyl)oxy)but-3-en-2-ol (401 mg, 0.940 mmol) was treated with distilled CH₂Cl₂ (6.70 mL). The mixture was cooled to 0 °C and NBS (311 mg, 1.75 mmol) was added. The mixture stirred at the same temperature for 18 hours and allowed to warm to room temperature. The organic solvents were evaporated from the reaction solution. Organic solvent was removed *in vacuo*. The crude residue was purified by flash chromatography (10 to 40% EtOAc in hexanes) on silica gel (50 mL) to afford (R)-1-((3*R*,4*R*,6*R*)-6-(bromomethyl)-6-methyl-1,5-dioxaspiro[2.4]heptan-4-yl)prop-2-en-1-ol (241 mg, 98%) as a clear oil.

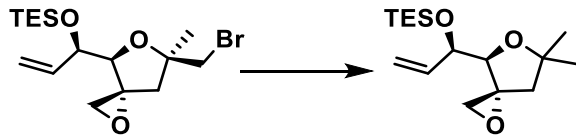
*Data for (R)-1-((3*R*,4*R*,6*R*)-6-(bromomethyl)-6-methyl-1,5-dioxaspiro[2.4]heptan-4-yl)prop-2-en-1-ol:* R_f = 0.34 (40% EtOAc in hexanes); IR (neat) ν_{max} = 3437 (br, OH), 2980, 2930, 1690, 1643, 1428, 1376, 1273, 1224, 1172, 1154, 1096, 1063, 1030, 996, 954 cm⁻¹; ¹H NMR (400 MHz, CDCl₃, 293 K): δ 5.89 (ddd, J = 17.2, 10.4, 4.4 Hz, 1H), 5.35 (d, J = 17.2 Hz, 1H), 5.24 (d, J = 10.4 Hz, 1H), 4.25 (d, J = 4.4 Hz, 1H), 3.97 (d, J = 3.6 Hz, 1H), 3.59 (d, J = 10.4 Hz, 1H), 3.49 (d, J = 10.4 Hz, 1H), 3.26 (d, J = 4.0 Hz, 1H), 2.88 (d, J = 4.0 Hz, 1H), 2.56 (d, J = 13.6 Hz, 1H), 1.63 (d, J = 13.6 Hz, 1H), 1.51 (s, 3H); ¹³C NMR (100 MHz, CDCl₃, 293 K): δ 136.0, 116.6, 83.4, 81.2, 73.3, 64.4, 47.1, 42.5, 41.0, 24.2; HRMS (ESI-TOF) m/z: calcd. for C₁₀H₁₆O₃Br [M + H]⁺ = 263.0277, found 263.0270.



*Preparation of (((R)-1-((3*R*,4*R*,6*R*)-6-(bromomethyl)-6-methyl-1,5-dioxaspiro[2.4]heptan-4-yl)allyl)oxy)triethylsilane:* To a 10 mL round bottom flask containing a Teflon-coated magnetic stir bar and imidazole (75.3 mg, 1.10 mmol) in THF (2.7 mL) was added chlorotriethylsilane (0.16 mL, 1.01 mmol), followed by the dropwise addition of alcohol (R)-1-((3*R*,4*R*,6*R*)-6-(bromomethyl)-6-methyl-1,5-dioxaspiro[2.4]heptan-4-yl)prop-2-en-1-ol (0.242 g, 0.921 mmol) in THF (1.0 mL), and then the container that initially contained (R)-1-((3*R*,4*R*,6*R*)-6-(bromomethyl)-6-methyl-1,5-dioxaspiro[2.4]heptan-4-yl)prop-2-en-1-ol was rinsed with THF (2 × 0.5 mL) and added to the reaction mixture at 0 °C under a nitrogen atmosphere. After an additional 45 min at the same temperature, H₂O (9.0 mL) was added, and most of the THF was removed under reduced pressure. The aqueous residue was extracted with Et₂O (2 × 22 mL). The combined organic layers were washed with brine (9.0 mL), dried over anhydrous Na₂SO₄, filtered,

and concentrated under reduced pressure. The resulting residue was purified by flash chromatography (1.5 to 6% EtOAc in hexanes) on silica gel (18 mL) to afford (((R)-1-((3*R*,4*R*,6*R*)-6-(bromomethyl)-6-methyl-1,5-dioxaspiro[2.4]heptan-4-yl)allyl)oxy)triethylsilane (327 mg, 94 % yield) as a colorless oil.

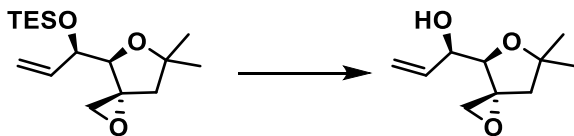
*Data for (((R)-1-((3*R*,4*R*,6*R*)-6-(bromomethyl)-6-methyl-1,5-dioxaspiro[2.4]heptan-4-yl)allyl)oxy)triethylsilane:* $R_f = 0.33$ (20% EtOAc in hexanes); IR (neat) $\nu_{max} = 2955, 2911, 2876, 1853, 1533, 1457, 1416, 1376, 1284, 1239, 1094, 1063, 1033, 1005, 958, 924 \text{ cm}^{-1}$; ^1H NMR (400 MHz, CDCl₃, 293 K): δ 5.87–5.78 (m, 1H), 5.28 (d, $J = 17.6 \text{ Hz}$, 1H), 5.18 (d, $J = 10.4 \text{ Hz}$, 1H), 4.17 (t, $J = 5.6 \text{ Hz}$, 1H), 3.80 (d, $J = 5.6 \text{ Hz}$, 1H), 3.46 (d, $J = 5.6 \text{ Hz}$, 1H), 3.24 (d, $J = 4.8 \text{ Hz}$, 1H), 2.87 (d, $J = 4.8 \text{ Hz}$, 1H), 2.46 (d, $J = 13.6 \text{ Hz}$, 1H), 1.62 (d, $J = 13.6 \text{ Hz}$, 1H), 1.51 (s, 3H), 0.93 (t, $J = 8.8 \text{ Hz}$, 9H), 0.61 (q, $J = 15.6, 7.6, 6 \text{ Hz}$); ^{13}C NMR (100 MHz, CDCl₃, 293 K): δ 138.2, 116.9, 85.0, 82.0, 75.2, 64.9, 46.9, 42.8, 41.0, 24.3, 6.9, 5.1; HRMS (ESI-TOF) m/z : calcd. for C₁₆H₃₀O₃BrSi [M + H]⁺ = 377.1142, found 377.1146.



*Preparation of (((R)-1-((3*R*,4*R*)-6,6-dimethyl-1,5-dioxaspiro[2.4]heptan-4-yl)allyl)oxy)triethylsilane:* To a 100 mL round bottom flask containing a Teflon-coated magnetic stir bar and (((R)-1-((3*R*,4*R*,6*R*)-6-(bromomethyl)-6-methyl-1,5-dioxaspiro[2.4]heptan-4-yl)allyl)oxy)triethylsilane (205 mg, 0.546 mmol) in benzene (41.0 mL) added tributylstannane (21 μL , 0.819 mmol) and AIBN (16.3 mg, 0.098 mmol). The reaction mixture was refluxed for 1 h, cooled to room temperature, and concentrated under reduced pressure. The resulting residue was purified by flash chromatography (2 to 8 % EtOAc in hexanes) on silica gel (40 mL) to afford

$((R)\text{-}1\text{-}((3R,4R)\text{-}6,6\text{-dimethyl}\text{-}1,5\text{-dioxaspiro}[2.4]\text{heptan}\text{-}4\text{-yl})\text{allyl})\text{oxy})\text{triethylsilane}$ (168 mg, 86% yield) as a colorless oil.

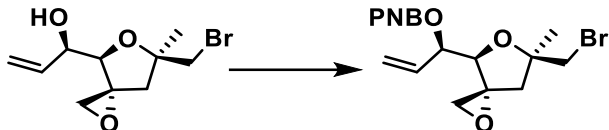
Data for $((R)\text{-}1\text{-}((3R,4R)\text{-}6,6\text{-dimethyl}\text{-}1,5\text{-dioxaspiro}[2.4]\text{heptan}\text{-}4\text{-yl})\text{allyl})\text{oxy})\text{triethylsilane}$: $R_f = 0.33$ (20% EtOAc in hexanes); IR (neat) $\nu_{\max} = 2955, 2913, 2876, 2181, 2157, 2073, 2021, 1976, 1949, 1645, 1460, 1414, 1380, 1368, 1294, 1237, 1211, 1168, 1100, 1077, 1049, 1007, 956, 920 \text{ cm}^{-1}$; $[\alpha]_D^{24} +69.8$ (c 1.0, CH_2Cl_2); ^1H NMR (500 MHz, CDCl_3 , 293 K): δ 5.81 (ddd, $J = 17.0, 10.0, 5.0 \text{ Hz}$, 1H), 5.20 (dt, $J = 17.0, 1.5 \text{ Hz}$, 1H), 5.15 (d, $J = 10.0, 1.5 \text{ Hz}$, 1H), 4.16–4.13 (m, 1H), 3.80 (d, $J = 4.0 \text{ Hz}$, 1H), 3.21 (d, $J = 4.0 \text{ Hz}$, 1H), 2.82 (d, $J = 4.0 \text{ Hz}$, 1H), 2.17 (d, $J = 13.0 \text{ Hz}$, 1H), 1.55 (d, $J = 13.0 \text{ Hz}$, 1H), 1.36 (s, 3H), 1.35 (s, 3H), 0.94 (t, $J = 4.5 \text{ Hz}$, 9H), 0.59 (q, $J = 15.5, 7.5 \text{ Hz}$, 6H); ^{13}C NMR (125 MHz, CDCl_3 , 293 K): δ 138.4, 116.3, 83.7, 80.7, 75.4, 65.4, 47.0, 45.6, 28.6, 27.0, 6.9, 5.1; HRMS (ESI-TOF) m/z : calcd. for $\text{C}_{16}\text{H}_{31}\text{O}_3\text{Si}$ [$\text{M} + \text{H}]^+ = 299.2037$, found 299.2036.



Preparation of $(R)\text{-}1\text{-}((3R,4R)\text{-}6,6\text{-dimethyl}\text{-}1,5\text{-dioxaspiro}[2.4]\text{heptan}\text{-}4\text{-yl})\text{prop-2-en-1-ol}$: To a stirred solution of $((R)\text{-}1\text{-}((3R,4R)\text{-}6,6\text{-dimethyl}\text{-}1,5\text{-dioxaspiro}[2.4]\text{heptan}\text{-}4\text{-yl})\text{allyl})\text{oxy})\text{triethylsilane}$ (260 mg, 0.870 mmol) in THF (3.50 mL) was added TBAF (1 M in THF, 1.0 mL) at 0 °C under an open atmosphere. After 20 min at the same temperature, the reaction mixture was diluted with Et_2O (15 mL) and saturated NH_4Cl (3.0 mL), filtered through a pad of Florisil, rinsed with Et_2O ($4 \times 10 \text{ mL}$), and concentrated under reduced pressure. The resulting residue was purified by flash chromatography (15 to 60% EtOAc in hexanes) on silica gel (30 mL)

to afford (*R*)-1-((3*R*,4*R*)-6,6-dimethyl-1,5-dioxaspiro[2.4]heptan-4-yl)prop-2-en-1-ol (101 mg, 63%) as an oil.

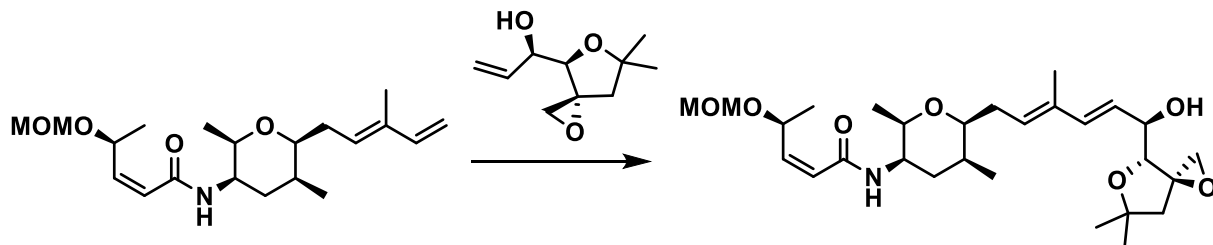
Data for (R)-1-((3R,4R)-6,6-dimethyl-1,5-dioxaspiro[2.4]heptan-4-yl)prop-2-en-1-ol: R_f = 0.30 (40% EtOAc in hexanes); IR (neat) ν_{max} = 3415 (br, OH), 2973, 2928, 2181, 2157, 2074, 2021, 2013, 1975, 1644, 1429, 1381, 1370, 1202, 1265, 1230, 1213, 1165, 1112, 1079, 1042, 997, 924 cm⁻¹; [α]_D²⁴ +102 (c 1.0, CH₂Cl₂); ¹H NMR (400 MHz, CDCl₃, 293 K): δ 5.89 (ddd, *J* = 16.8, 10.4, 5.6 Hz, 1H), 5.32 (d, *J* = 16.8 Hz, 1H), 5.22 (d, *J* = 10.4 Hz, 1H), 4.11 (s (br), 1H), 3.96 (d, *J* = 4.0 Hz, 1H), 3.17 (d, *J* = 4.0 Hz, 1H), 2.84 (d, *J* = 4.0 Hz, 1H), 2.16 (d, *J* = 13.6 Hz, 1H), 1.62 (d, *J* = 13.6 Hz, 1H), 1.37 (s, 3H), 1.36 (s, 3H); ¹³C NMR (100 MHz, CDCl₃, 293 K): δ 136.4, 116.8, 82.5, 81.0, 73.4, 65.1, 47.2, 45.7, 28.4, 26.8; HRMS (ESI-TOF) *m/z*: calcd. for C₁₀H₁₇O₃ [M + H]⁺ = 185.1172, found 185.1169.



*Preparation of (R)-1-((3*R*,4*R*,6*R*)-6-(bromomethyl)-6-methyl-1,5-dioxaspiro[2.4]heptan-4-yl)allyl 4-nitrobenzoate:* To a 10 mL round bottom flask containing a Teflon-coated magnetic stir bar, PNBCl (52.6 mg, 0.285 mmol), and crystal of DMAP in CH₂Cl₂ (1.0 mL) was added Et₃N (60 μL, 0.428 mmol), followed by the dropwise addition of alcohol (*R*)-1-((3*R*,4*R*,6*R*)-6-(bromomethyl)-6-methyl-1,5-dioxaspiro[2.4]heptan-4-yl)prop-2-en-1-ol (37.5 mg, 0.143 mmol) in CH₂Cl₂ (1.0 mL) at 0 °C under a nitrogen atmosphere. After 2 h at the same temperature, saturated NaHCO₃ (2.0 mL) was added, and the reaction mixture was extracted with CH₂Cl₂ (3 ×

4.0 mL), dried over anhydrous Na₂SO₄, filtered, and concentrated under reduced pressure. The resulting residue was purified by flash chromatography (5.0 to 40% EtOAc in hexanes) on silica gel (10 mL) to afford (*R*)-1-((3*R*,4*R*,6*R*)-6-(bromomethyl)-6-methyl-1,5-dioxaspiro[2.4]heptan-4-yl)allyl 4-nitrobenzoate (48 mg, 81 % yield) as a colorless oil.

Data for (R)-1-((3R,4R,6R)-6-(bromomethyl)-6-methyl-1,5-dioxaspiro[2.4]heptan-4-yl)allyl 4-nitrobenzoate: R_f = 0.37 (40% EtOAc in hexanes); IR (neat) ν_{max} = 3054, 2978, 2933, 2182, 2157, 2021, 2012, 1975, 1949, 1726, 1645, 1607, 1526, 1428, 1411, 1376, 1347, 1319, 1267, 1172, 1116, 1100, 1014, 982, 932 cm⁻¹; ¹H NMR (400 MHz, CDCl₃, 293 K): δ 8.30 (d, J = 9.2 Hz, 2H), 8.22 (d, J = 9.2 Hz, 2H), 5.89 (ddd, J = 17.2, 10.4, 6.0 Hz, 1H), 5.60 (dd, J = 6.0, 4.8 Hz, 1H), 5.41-5.36 (m, 2H), 4.20 (d, J = 4.4 Hz, 1H), 3.51 (d, J = 10.4 Hz, 1H), 3.44 (d, J = 10.4 Hz, 1H), 3.12 (d, J = 4.0 Hz, 1H), 2.95 (d, J = 4.0 Hz, 1H), 2.58 (d, J = 13.6 Hz, 1H), 1.70 (d, J = 13.6 Hz, 1H), 1.54 (s, 3H); ¹³C NMR (150 MHz, CDCl₃, 293 K): δ 163.6, 150.7, 135.2, 132.1, 130.8, 123.7, 119.6, 82.2, 81.7, 75.9, 64.6, 46.8, 41.9, 40.3, 24.2; HRMS (ESI-TOF) m/z: calcd. for C₁₇H₁₈BrNO₆ [M + H]⁺ = 412.03903, found 412.03814.



*Preparation of (S,Z)-N-((2*R*,3*R*,5*S*,6*S*)-6-((*R*,2*E*,4*E*)-6-((3*R*,4*R*)-6,6-dimethyl-1,5-dioxaspiro[2.4]heptan-4-yl)-6-hydroxy-3-methylhexa-2,4-dien-1-yl)-2,5-dimethyltetrahydro-2*H*-pyran-3-yl)-4-(methoxymethoxy)pent-2-enamide:* To a stirred solution of (S,Z)-N-((2*R*,3*R*,5*S*,6*S*)-2,5-dimethyl-6-((*E*)-3-methylpenta-2,4-dien-1-yl)tetrahydro-2*H*-pyran-3-yl)-4-(methoxymethoxy)pent-2-enamide (80 mg, 0.229 mmol) open to air in DCE (426 μL) were added

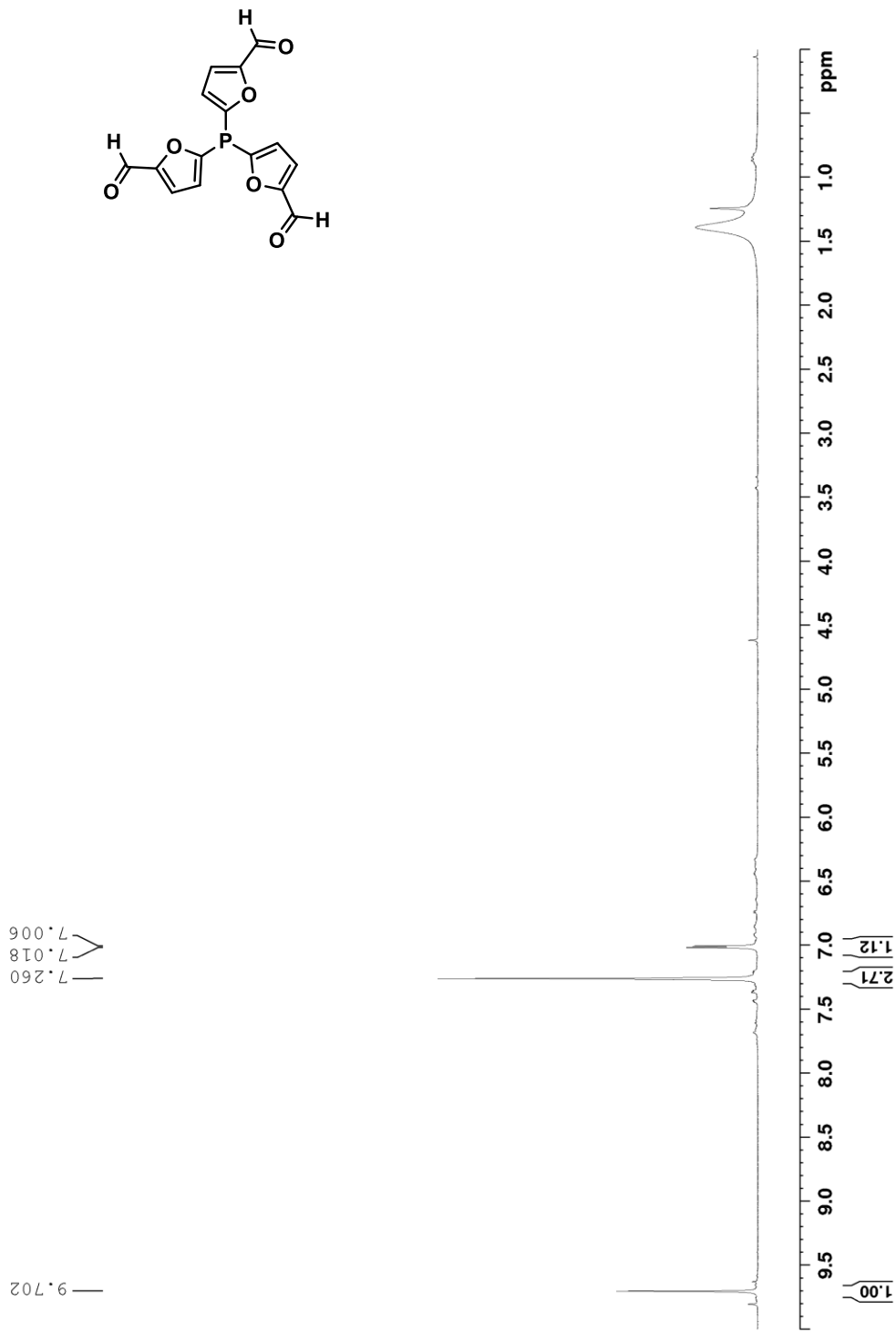
nitro Grela catalyst (10 mg, 0.015 mmol, 5 mol%), and (*R*)-1-((*3R,4R*)-6,6-dimethyl-1,5-dioxaspiro[2.4]heptan-4-yl)prop-2-en-1-ol in DCE (216 μ L, 100 mg/mL solution). After addition, the reaction was heated to 45 °C. After 2 h, (*R*)-1-((*3R,4R*)-6,6-dimethyl-1,5-dioxaspiro[2.4]heptan-4-yl)prop-2-en-1-ol in DCE (208 μ L, 100 mg/mL solution) and nitro Grela catalyst (10 mg) were added. After another 2 h, (*R*)-1-((*3R,4R*)-6,6-dimethyl-1,5-dioxaspiro[2.4]heptan-4-yl)prop-2-en-1-ol in DCE (208 μ L, 100 mg/mL solution) and nitro Grela catalyst (10 mg) were added. After a total of 8 h at 45 °C, the reaction was removed from heat and concentrated. The crude material was dissolved in CH₂Cl₂ (100 mL) and charcoal (1 g, 50x weight) was added. The reaction was stirred for 3 h, filtered, and concentrated *in vacuo*. The crude material was purified by flash chromatography (10 to 70% EtOAc in hexanes) on silica gel (20 mL) to afford and inseparable mixture of the left fragment dimer and (*S,Z*)-*N*-((*2R,3R,5S,6S*)-6-((*R,2E,4E*)-6-((*3R,4R*)-6,6-dimethyl-1,5dioxaspiro[2.4]heptan-4-yl)-6-hydroxy-3-methylhexa-2,4-dien-1-yl)-2,5-dimethyltetrahydro-2*H*-pyran-3-yl)-4-(methoxymethoxy)pent-2-enamide (24 mg, 21% yield) as a clear oil. This material was further purified by prep TLC followed by prep HPLC for characterization and used in subsequent biological experiments. (Absorption at 235 nm. Elution conditions: flow rate = 4.5 mL/min, gradient: 20→90% MeCN in water over 18 min. Column: Agilent Technologies Pursuit XR_s 5 C18 150 cm × 10 mm. *T* = 24 °C. Retention time = 11.3 min).

*Data for (*S,Z*)-*N*-((*2R,3R,5S,6S*)-6-((*R,2E,4E*)-6-((*3R,4R*)-6,6-dimethyl-1,5dioxaspiro[2.4]heptan-4-yl)-6-hydroxy-3-methylhexa-2,4-dien-1-yl)-2,5-dimethyltetrahydro-2*H*-pyran-3-yl)-4-(methoxymethoxy)pent-2-enamide:* *R*_f = 0.26 (60% EtOAc/hexanes); IR (neat): ν_{max} = 3352, 2973, 2927, 1661, 1634, 1516, 1446, 1369, 1317, 1214, 1156, 1097, 1030 cm⁻¹; ¹H NMR (600 MHz, 293 K, CD₂Cl₂) δ 6.27 (d, *J* = 15.6 Hz, 1H), 5.93 (dd, *J* = 11.4, 8.4 Hz, 1H), 5.81 (d, *J* = 8.4

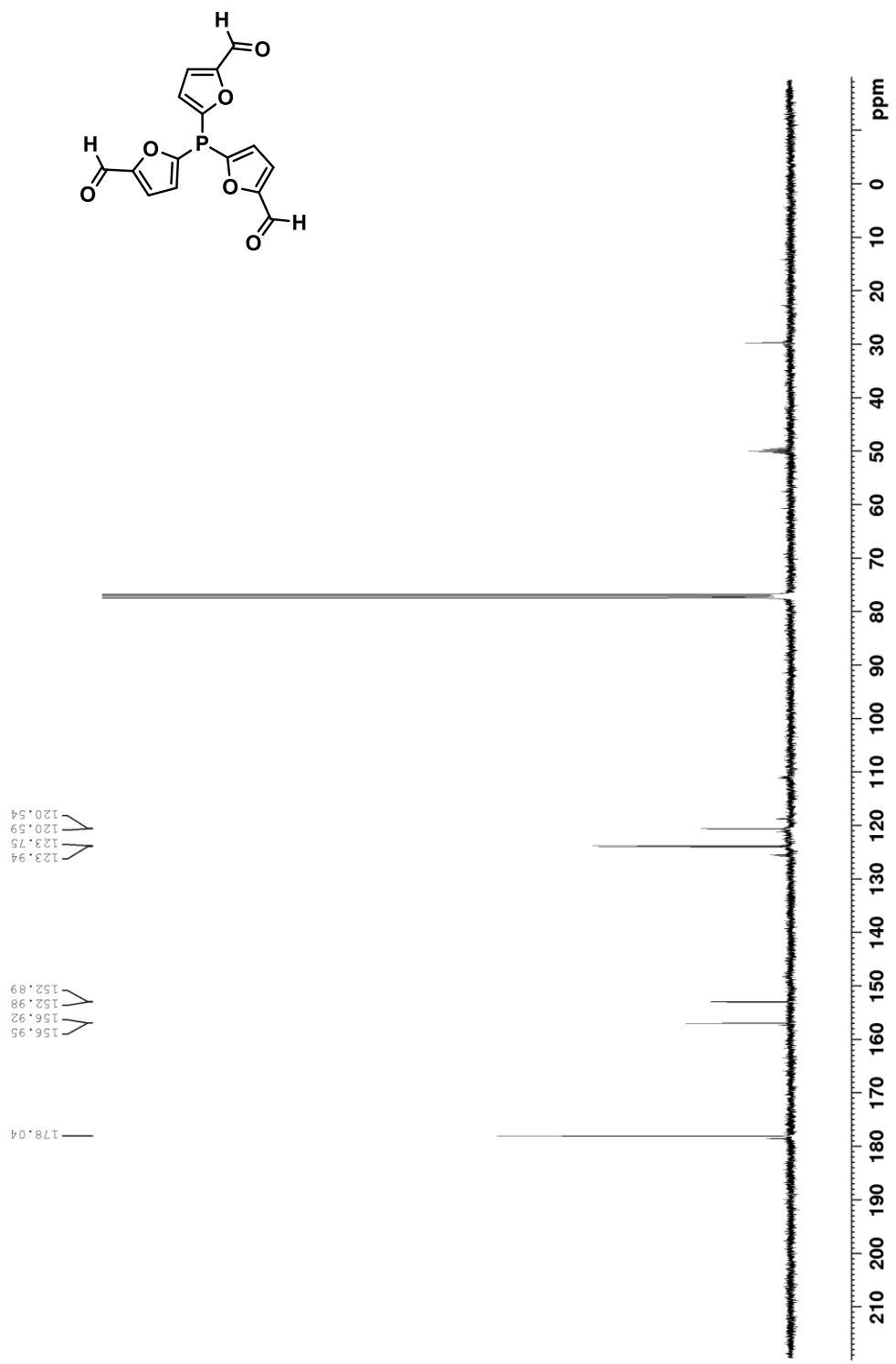
Hz, 1H), 5.72 (dd, $J = 11.4$, 1.2 Hz, 1H), 5.60 (dd, $J = 15.6$, 6.6 Hz, 1H), 5.51 (t, $J = 6.6$ Hz, 1H), 4.62 (d, $J = 7.2$ Hz, 1H), 4.56 (d, $J = 7.2$ Hz, 1H), 4.16–4.12 (m 1H), 3.91(d, $J = 3.6$ Hz, 1H), 3.89–3.86 (m, 1H), 3.67–3.63 (m, 1H), 3.55–3.53 (m, 1H), 3.33 (s, 3H), 3.09 (d, $J = 4.8$, 1H), 2.80 (d, $J = 4.8$, 1H), 2.39–2.32 (m, 1H), 2.25–2.19 (m, 1H), 2.11 (d, $J = 13.4$ Hz, 1H), 2.09 (d, $J = 5.4$ Hz, 1H), 1.93–1.91 (m, 2H), 1.75 (s, 3H), 1.59 (d, $J = 13.4$ Hz, 1H), 1.35 (s, 3H), 1.33 (d, $J = 13.4$ Hz, 1H), 1.27 (s, 3H), 1.26 (s, 3H), 1.10 (d, $J = 6.6$ Hz, 3H), 1.01 (d, $J = 6.6$ Hz, 3H); ^{13}C NMR (175 MHz, 293 K , CD_2Cl_2) δ 147.1, 136.7, 134.8, 129.6, 125.4, 122.8, 95.2, 83.3, 81.2, 81.1, 76.3, 73.8, 69.5, 65.2, 55.5, 47.4, 47.2, 45.9, 36.2, 32.4, 30.1, 29.6, 28.5, 26.9, 21.1, 17.9, 15.3, 12.8; HRMS (ESI-TOF) m/z : calcd. For $\text{C}_{28}\text{H}_{46}\text{NO}_7$ [$\text{M}+\text{H}]^+$ 508.32688, found 508.32590.

**Specific rotation was not obtained for this compound due to insufficient quantity according to 2021 JOC guidelines.*

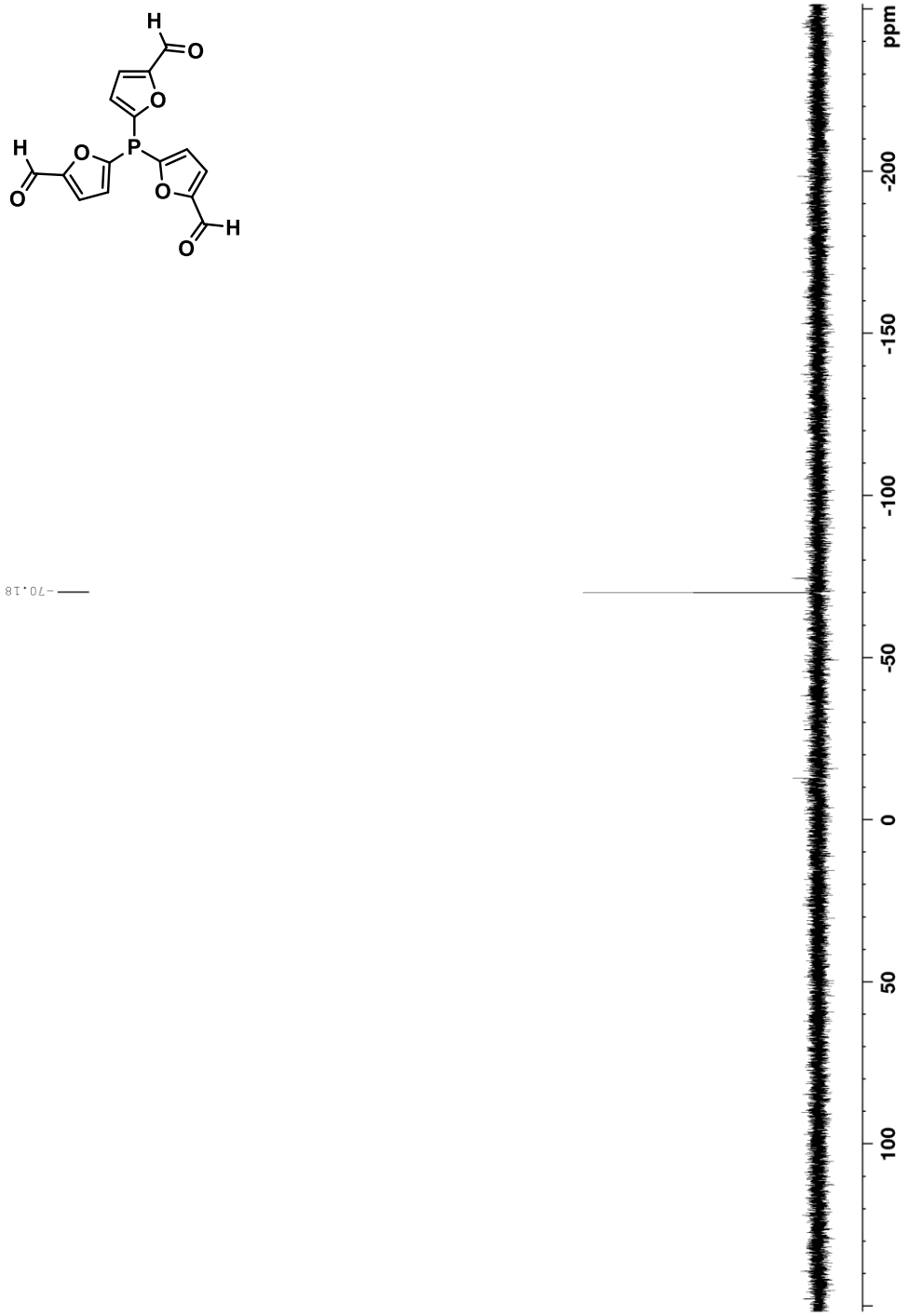
Appendix B. NMR Spectra



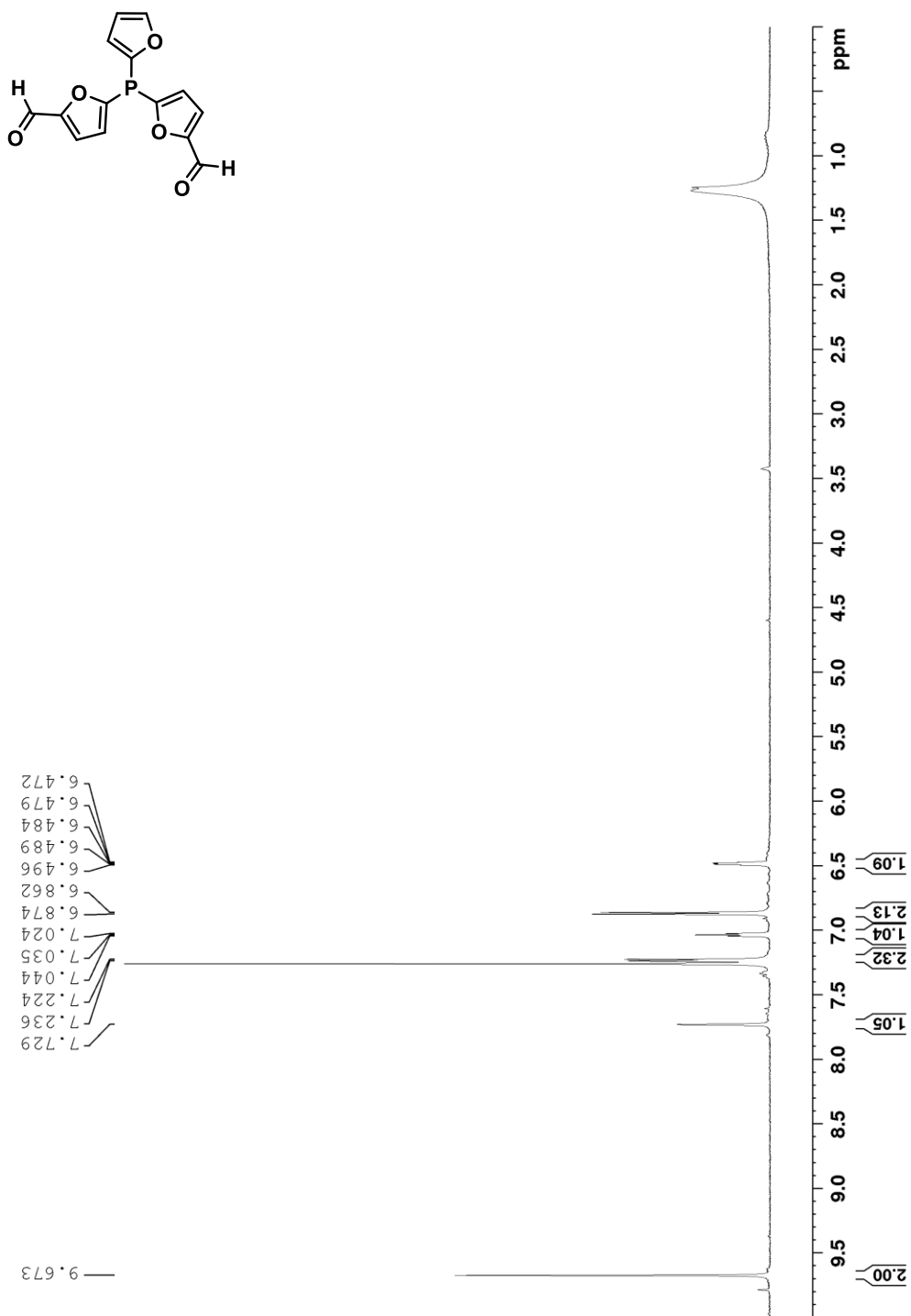
Spectrum 1. ^1H NMR spectrum of 5,5',5''-phosphanetriyltris(furan-2-carbaldehyde) (300 MHz, CDCl_3 , 293K).



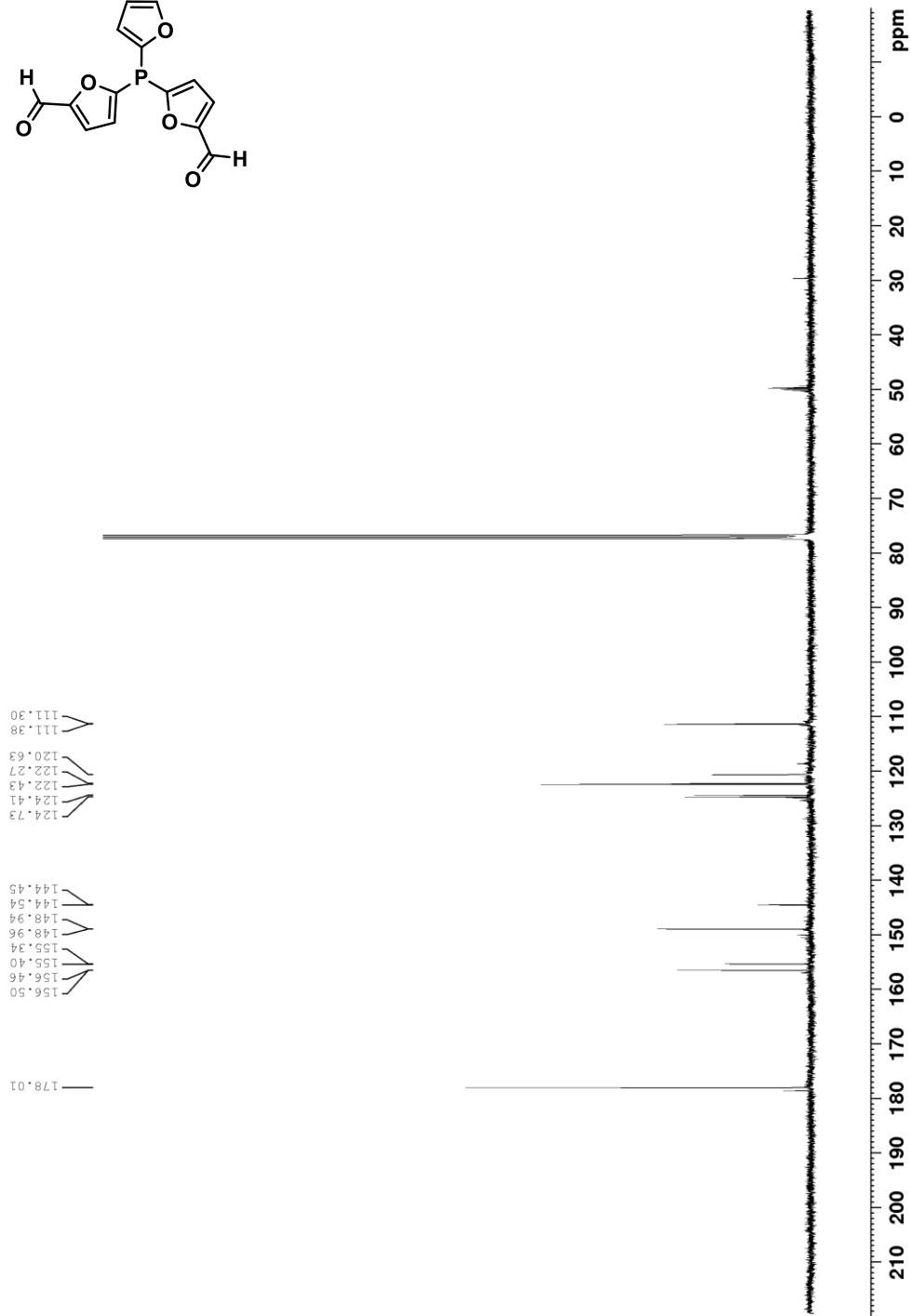
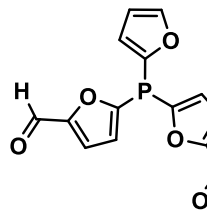
Spectrum 2. ^{13}C NMR spectrum of 5,5',5''-phosphanetriyltris(furan-2-carbaldehyde) (100 MHz, CDCl_3 , 293K).



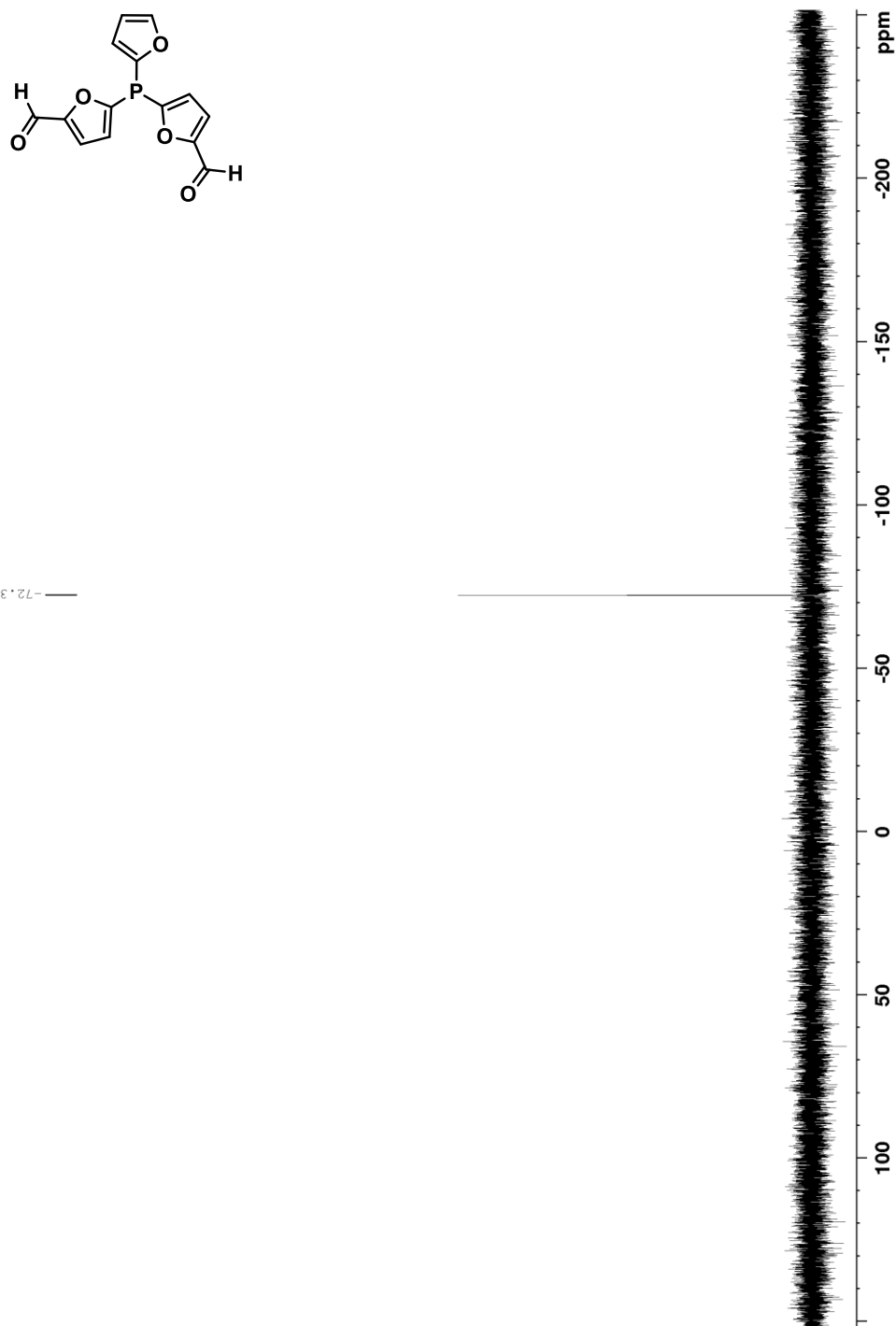
Spectrum 3. ^{31}P NMR spectrum of 5,5',5''-phosphanetriyltris(furan-2-carbaldehyde) (120 MHz, CDCl_3 , 293K).



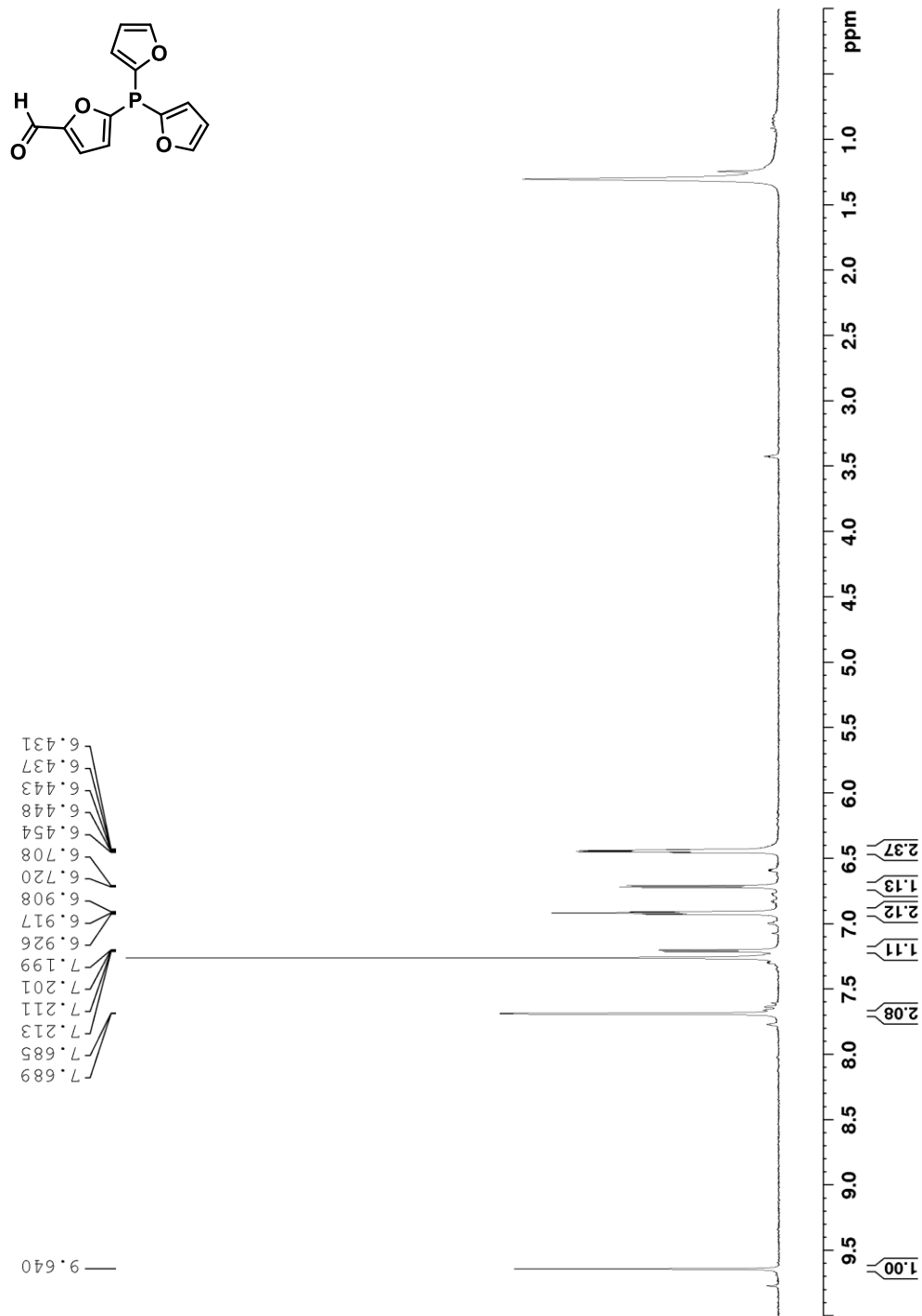
Spectrum 4. ^1H NMR spectrum of 5,5'-(furan-2-ylphosphanediy)bis(furan-2-carbaldehyde) (300 MHz, CDCl_3 , 293K).



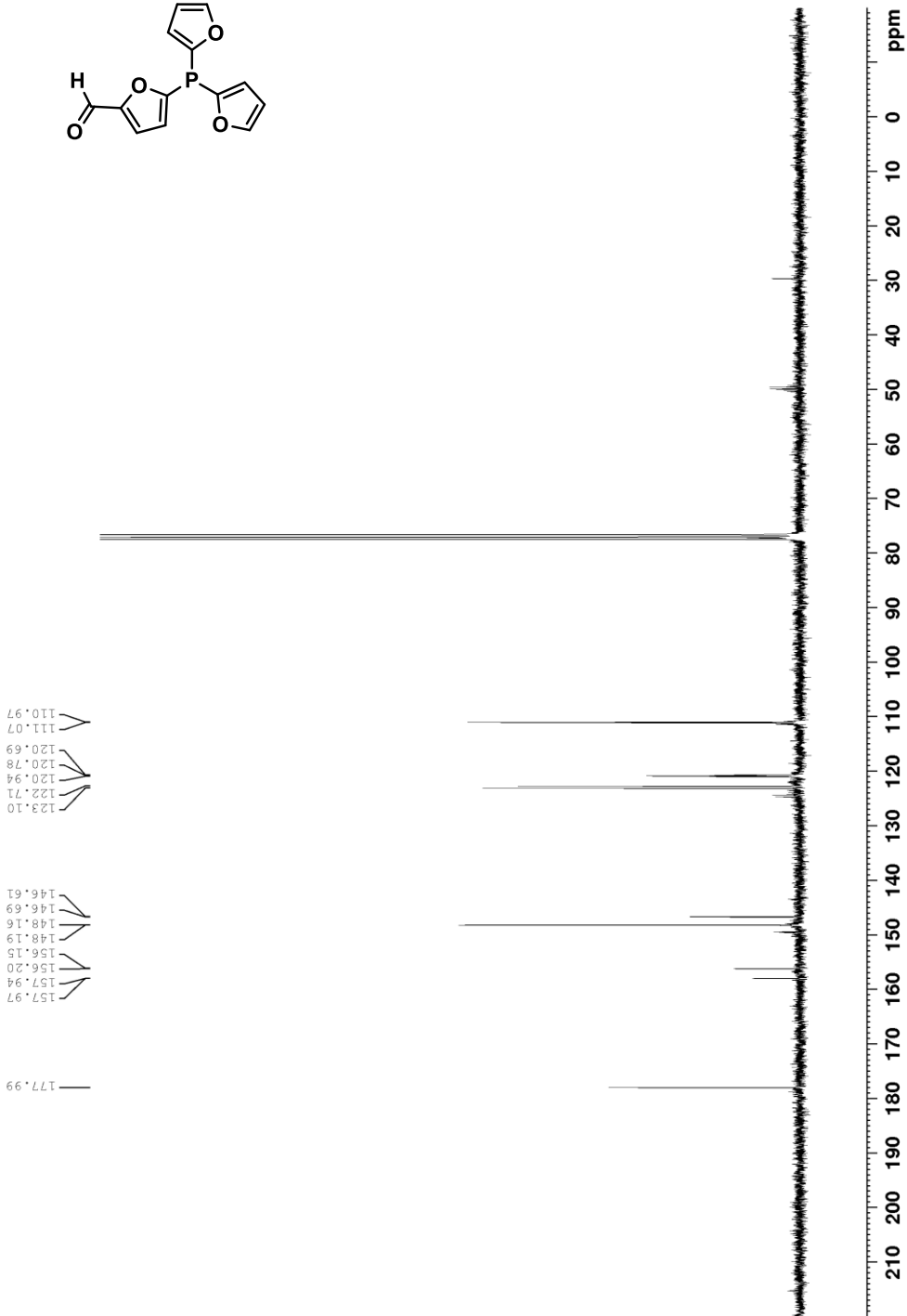
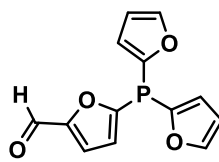
Spectrum 5. ¹³C NMR spectrum of 5,5'-(furan-2-ylphosphanediyi)bis(furan-2-carbaldehyde) (100 MHz, CDCl₃, 293K).



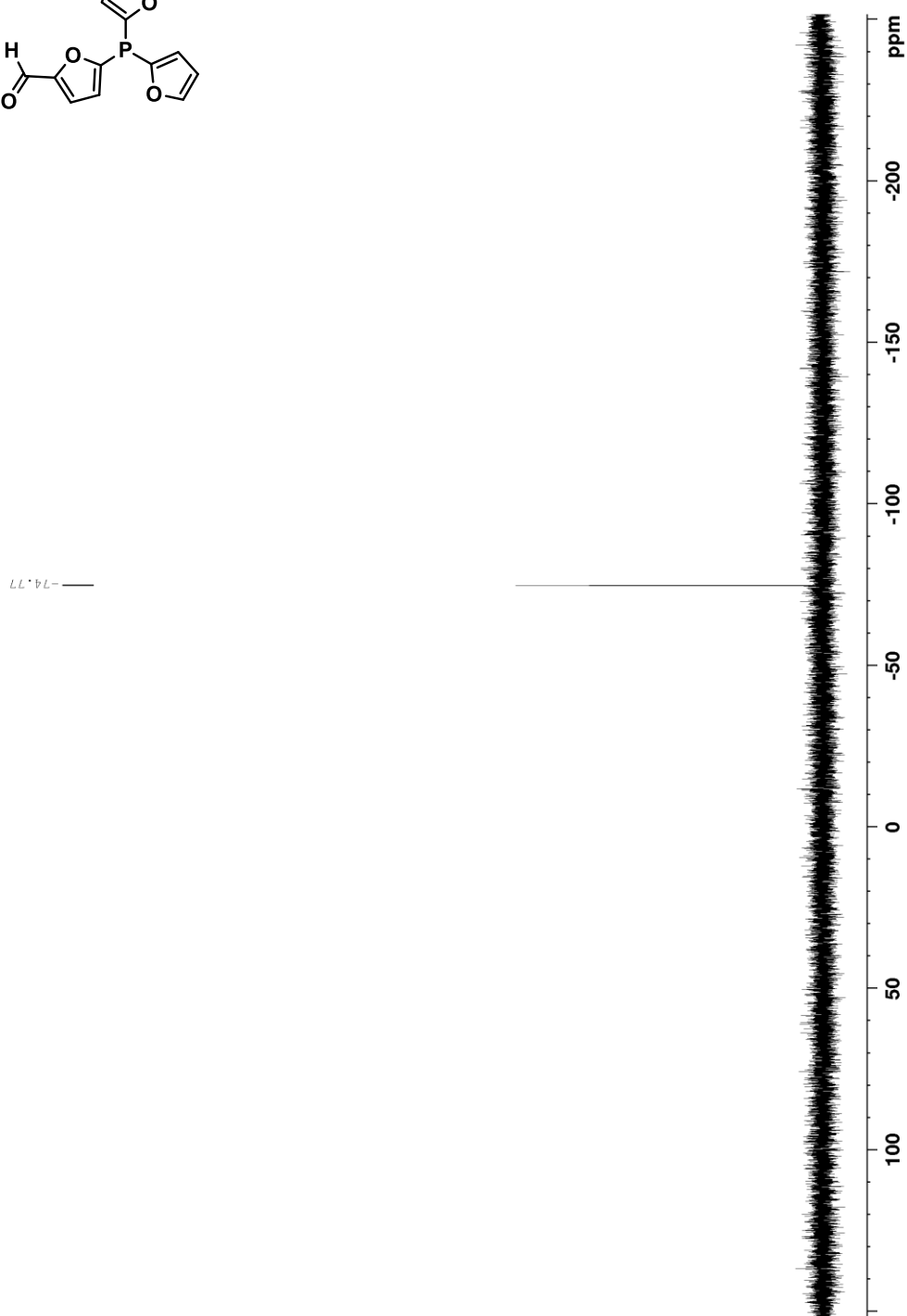
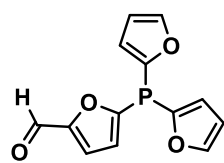
Spectrum 6. ^{31}P NMR spectrum of 5,5'-(furan-2-ylphosphanediy)bis(furan-2-carbaldehyde) (120 MHz, CDCl_3 , 293K).



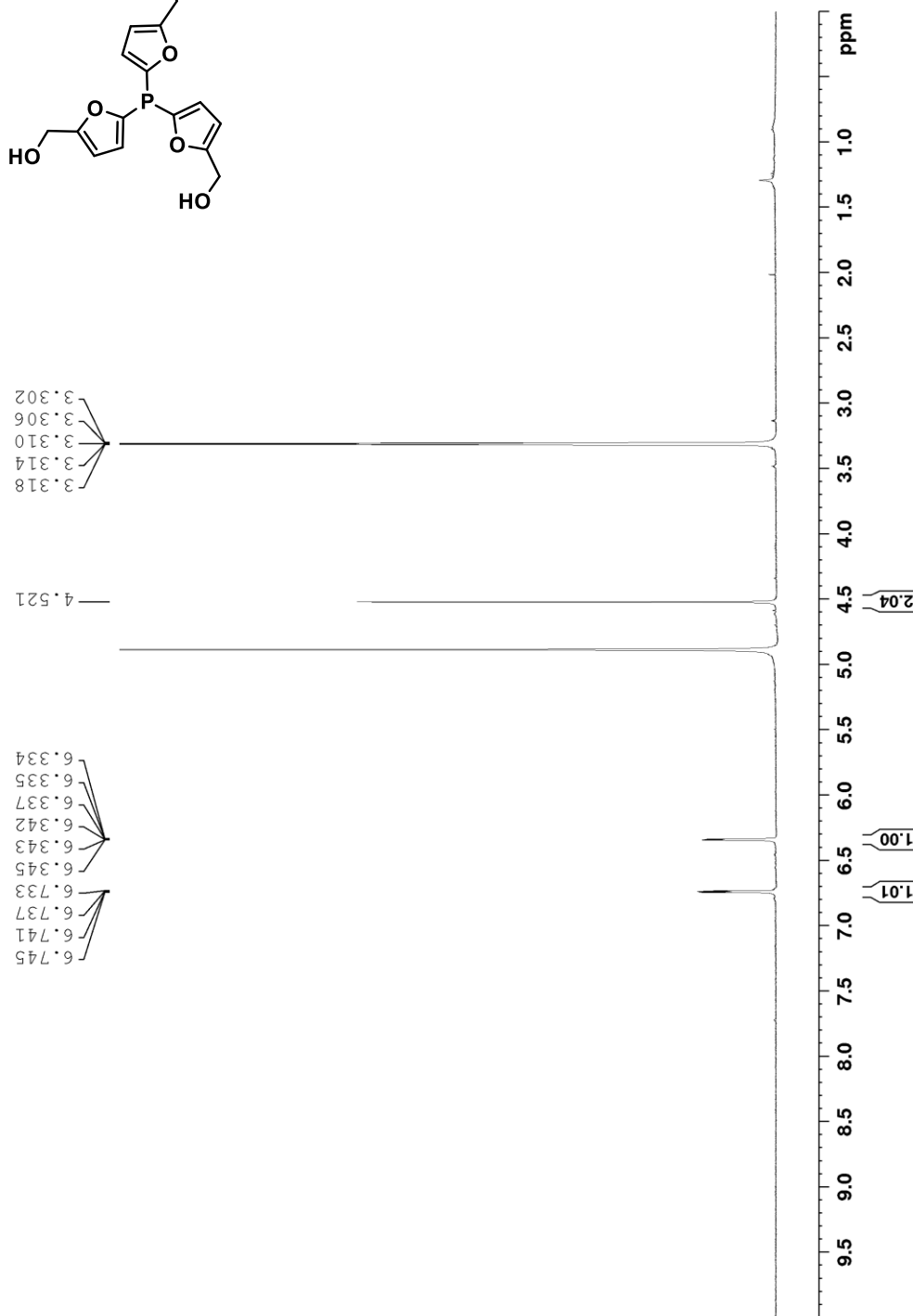
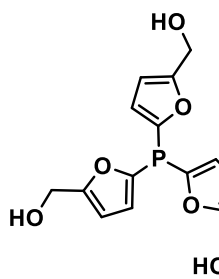
Spectrum 7. ^1H NMR spectrum of 5-(di(furan-2-yl)phosphaneyl)furan-2-carbaldehyde (300 MHz, CDCl_3 , 293K).



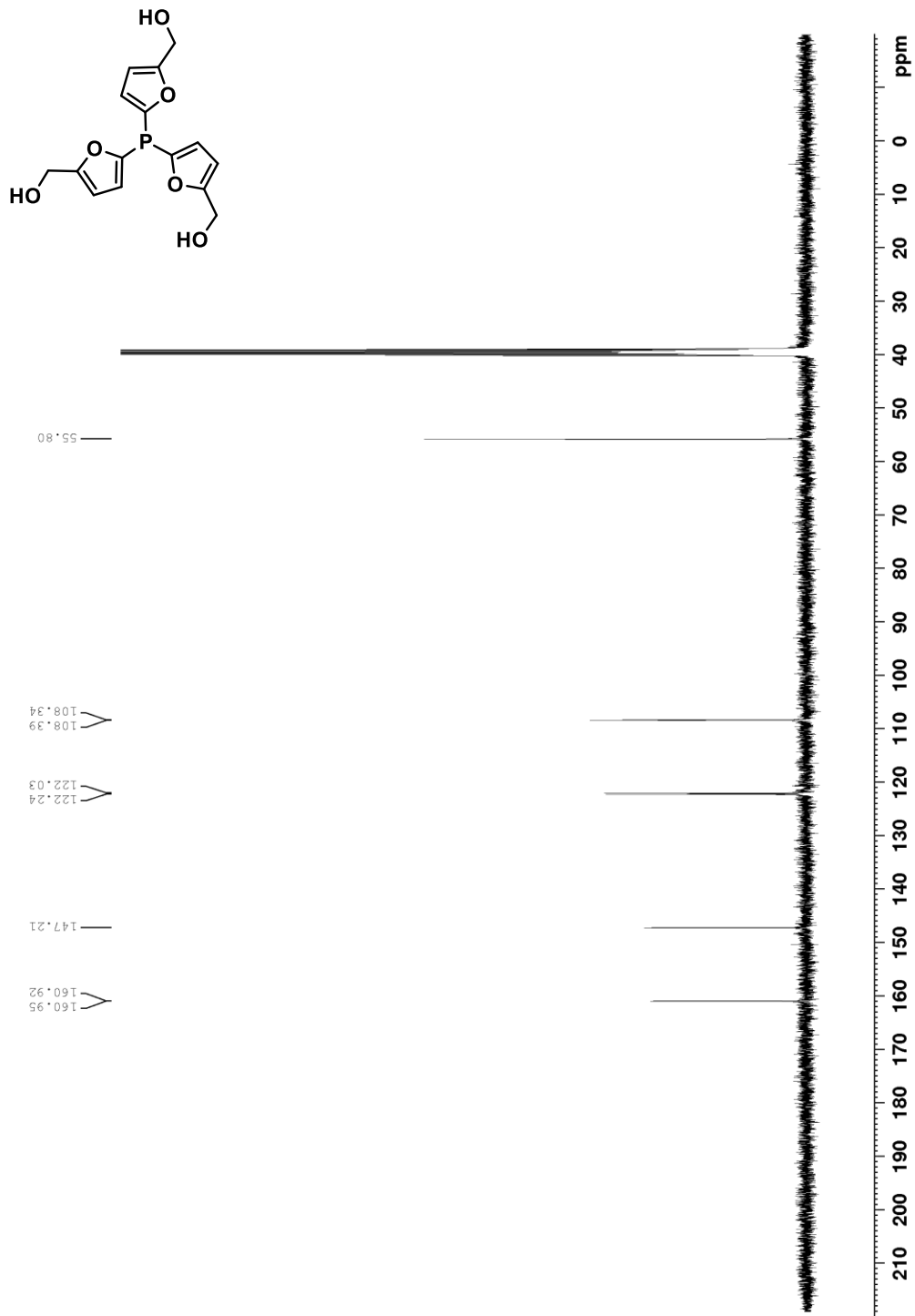
Spectrum 8. ^{13}C NMR spectrum of **5**-(di(furan-2-yl)phosphaneyl)furan-2-carbaldehyde (75 MHz, CDCl_3 , 293K).



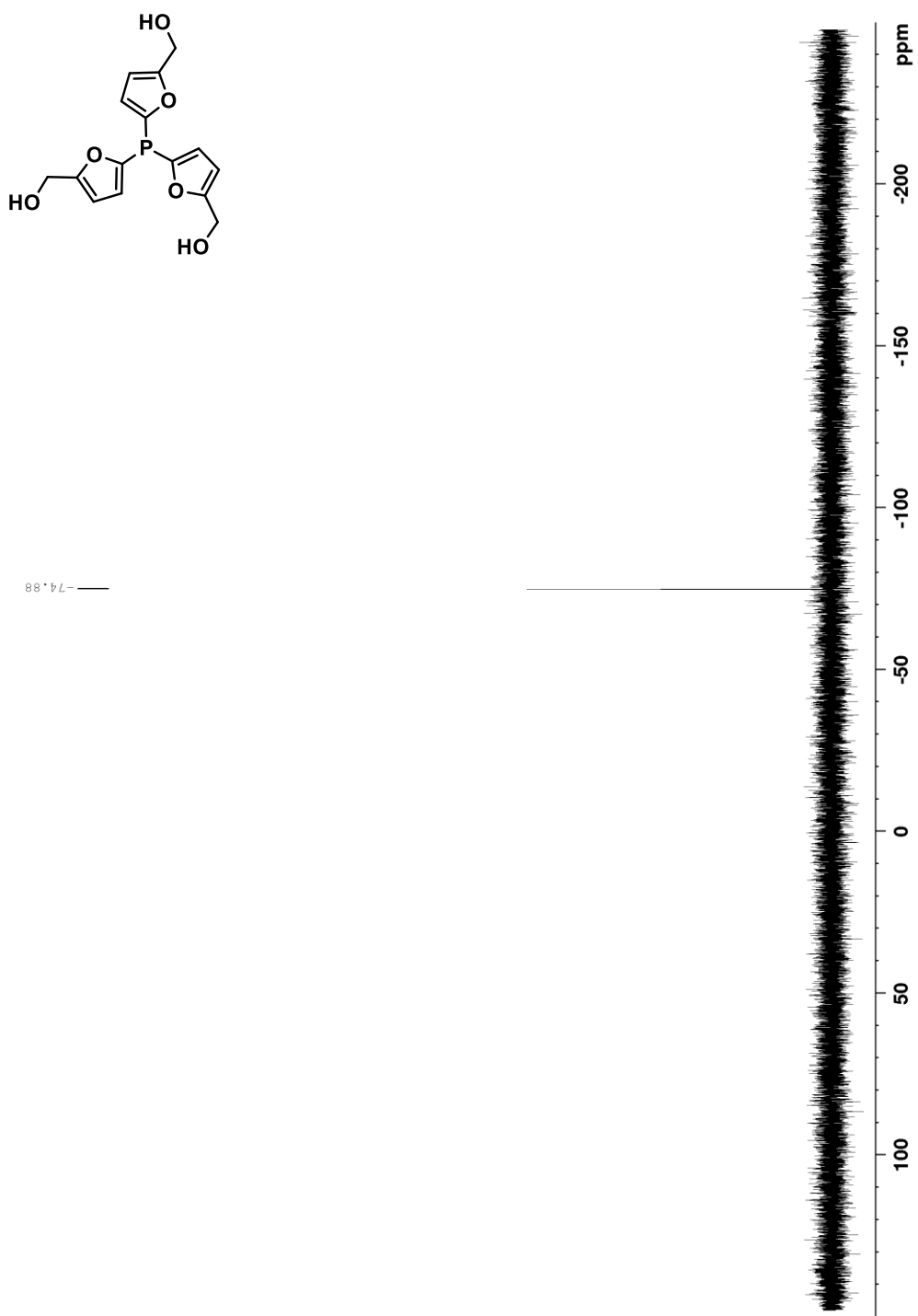
Spectrum 9. ^{31}P NMR spectrum of 5-(di(furan-2-yl)phosphaneyl)furan-2-carbaldehyde (120 MHz, CDCl_3 , 293K).



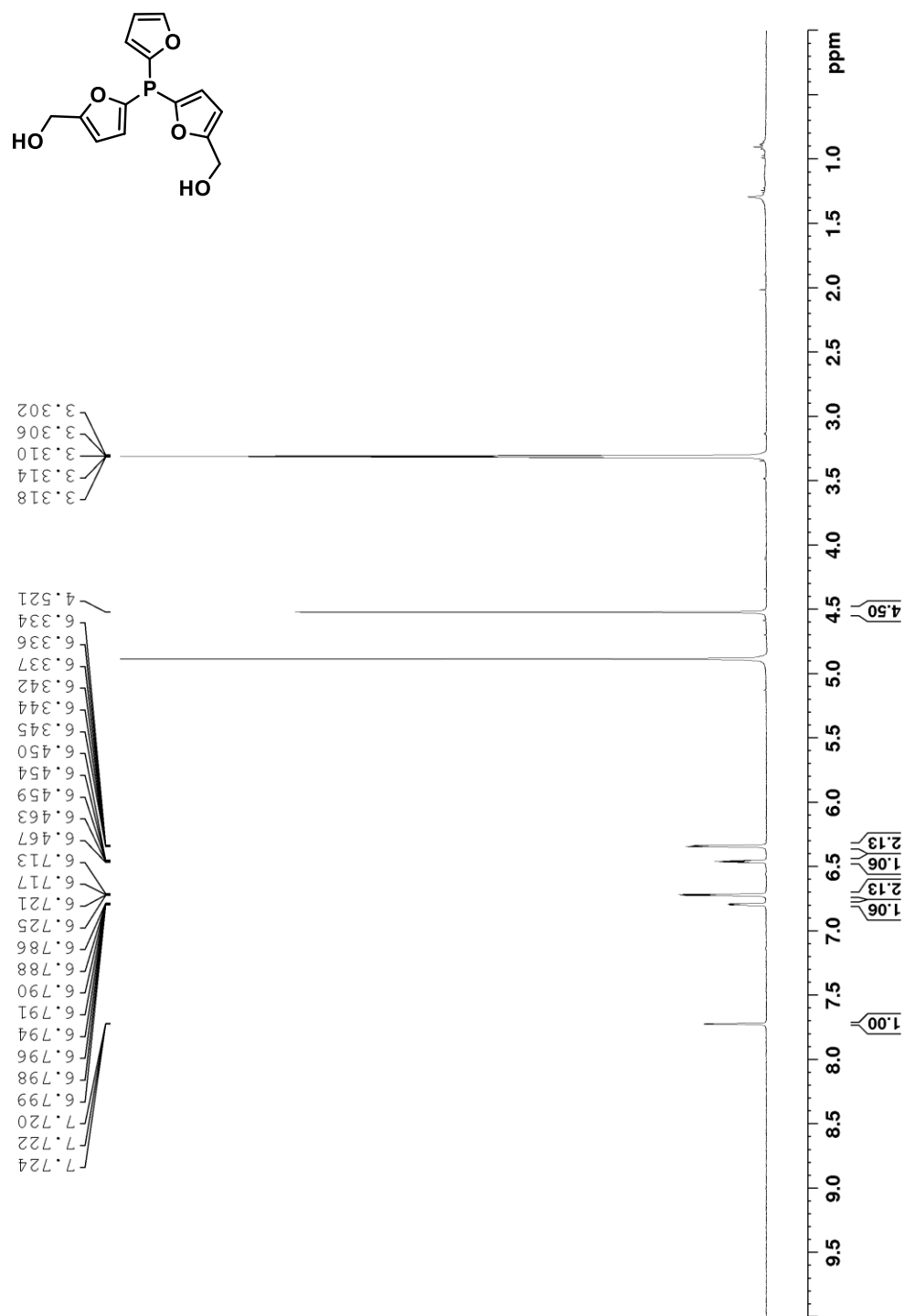
Spectrum 10. ^1H NMR spectrum of (phosphanetriyltris(furan-5,2-diyl))trimethanol (400 MHz, CD_3OD , 293K).



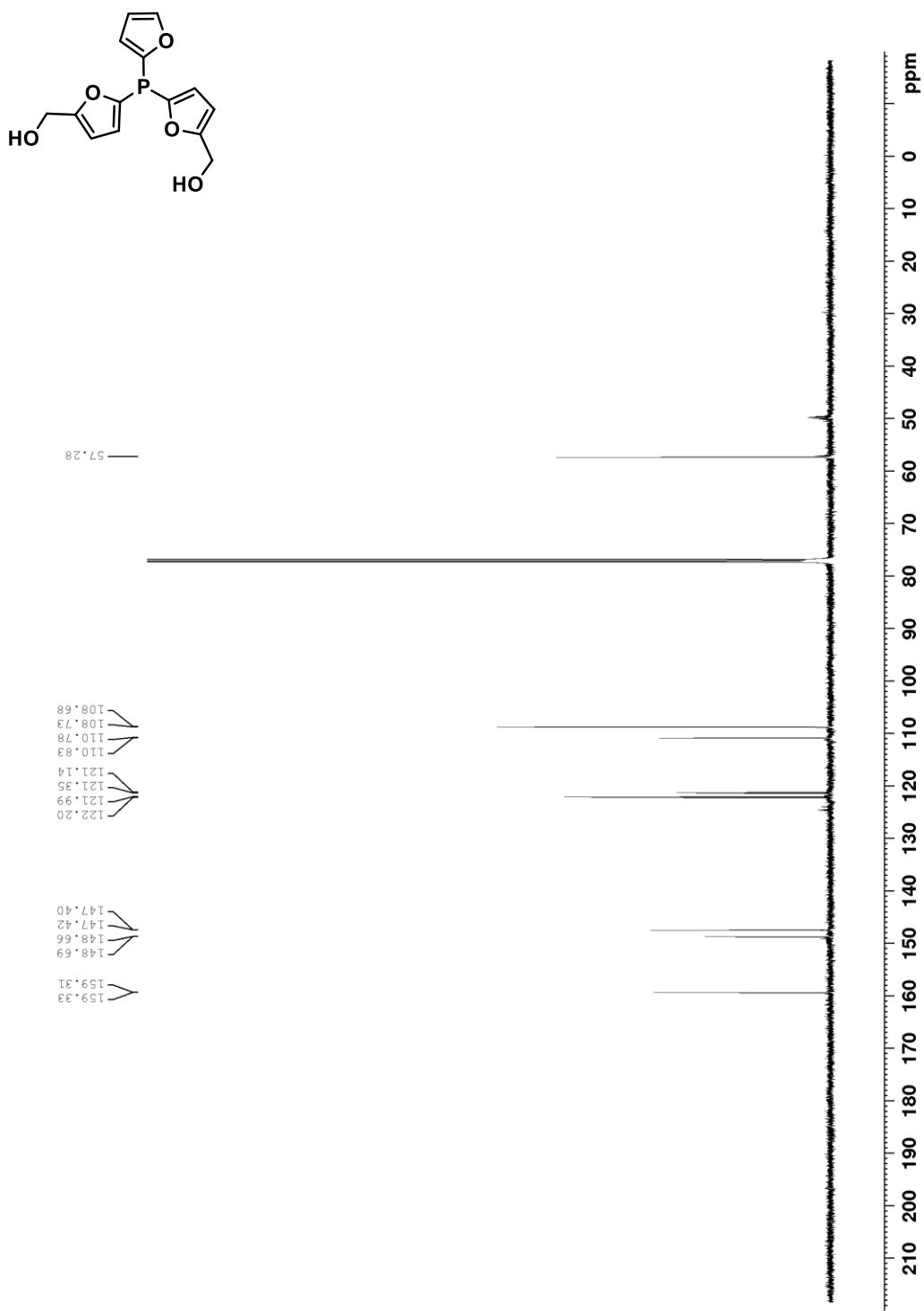
Spectrum 11. ^{13}C NMR spectrum of (phosphanetriyltris(furan-5,2-diyl))trimethanol (100 MHz, $\text{DMSO}-d_6$, 293K).



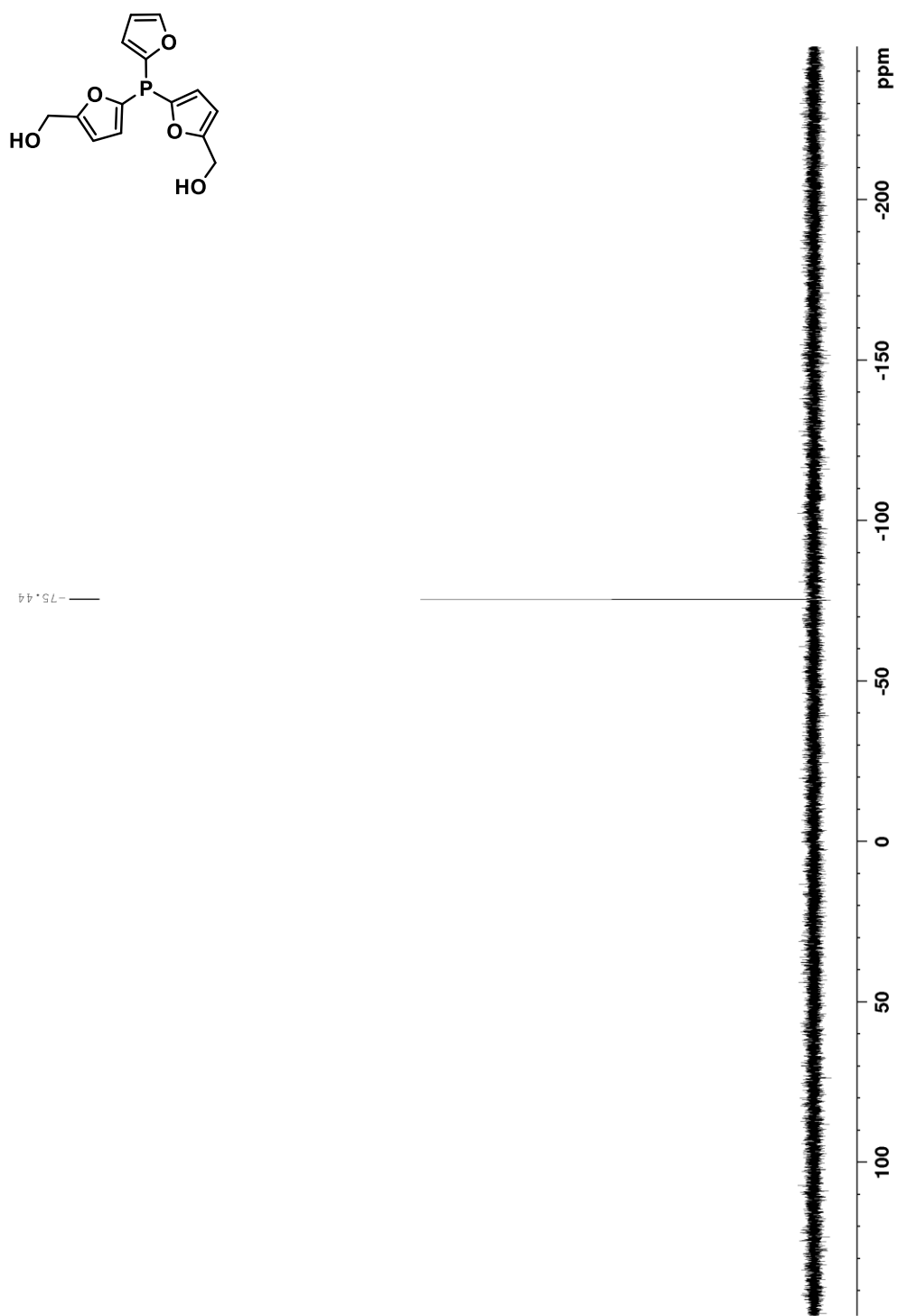
Spectrum 12. ^{31}P NMR spectrum of (phosphanetriyltris(furan-5,2-diyl))trimethanol (160 MHz, CD_3OD , 293K).



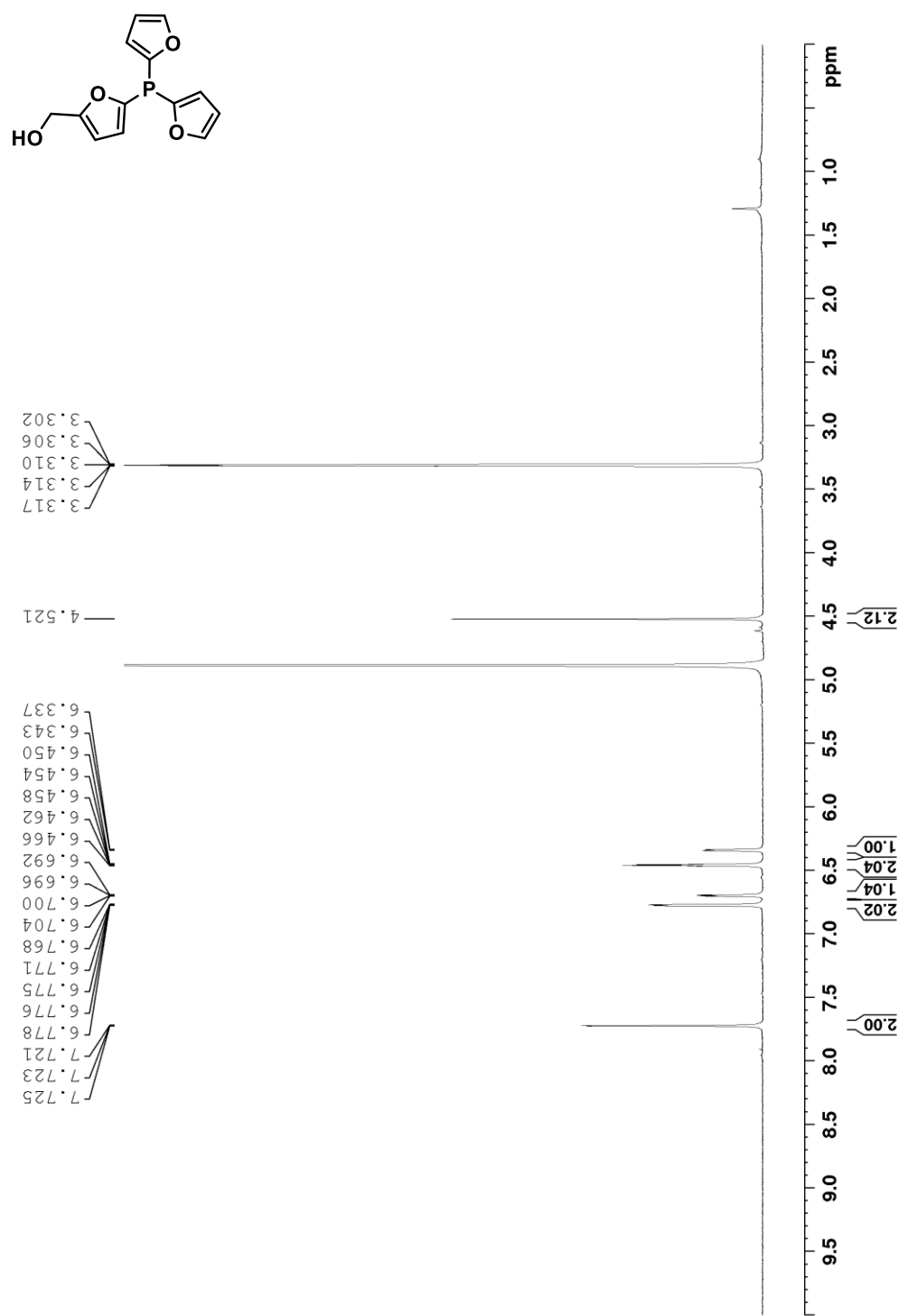
Spectrum 13. ^1H NMR spectrum of ((furan-2-ylphosphanediyi)bis(furan-5,2-diyl))dimethanol (400 MHz, CD_3OD , 293K).



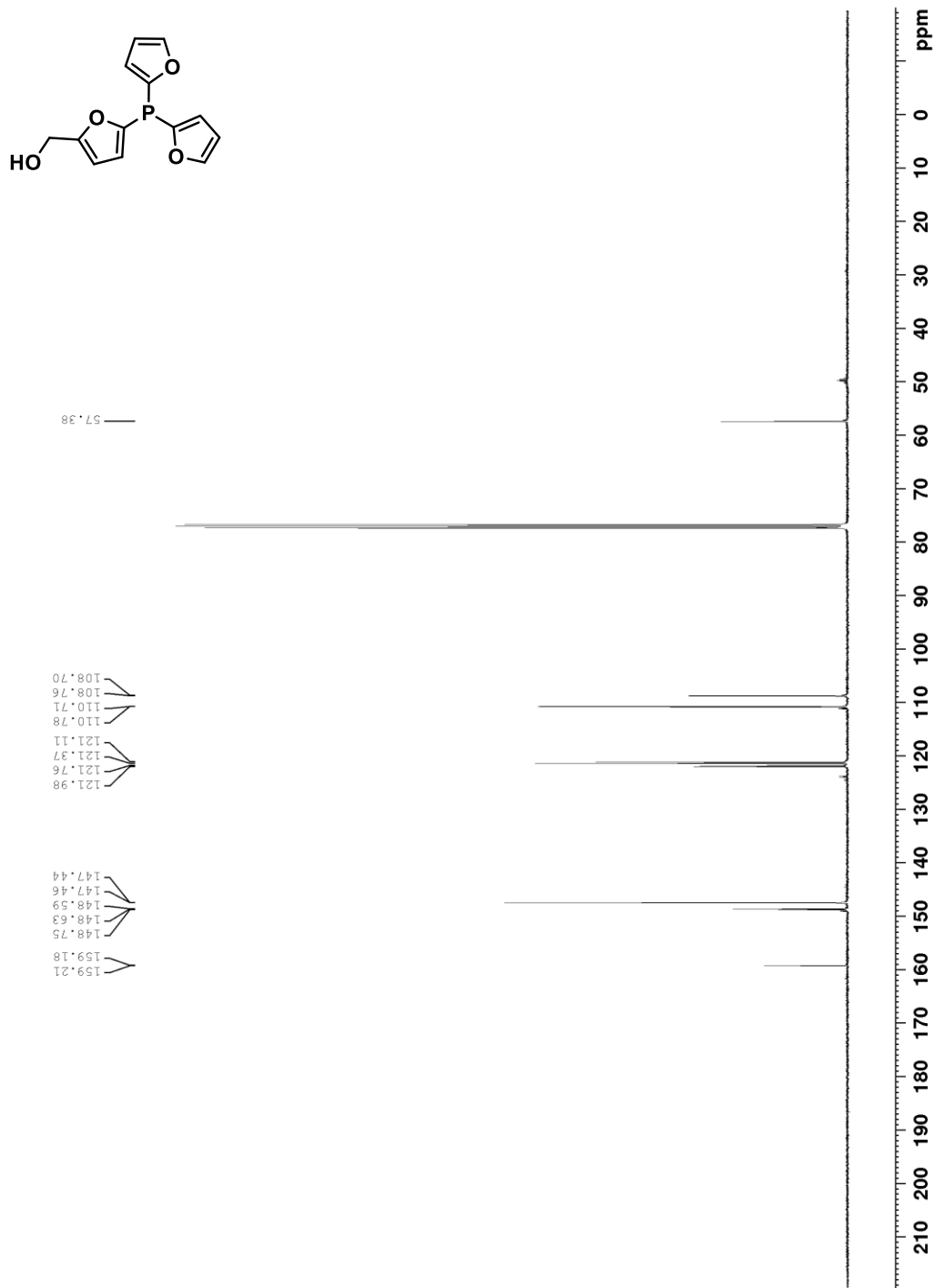
Spectrum 14. ^{13}C NMR spectrum of ((furan-2-ylphosphanediyil)bis(furan-5,2-diyl))dimethanol (125 MHz, CDCl_3 , 293K).



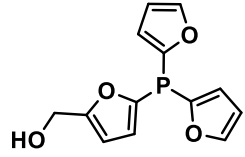
Spectrum 15. ^{31}P NMR spectrum of ((furan-2-ylphosphanediyil)bis(furan-5,2-diyl))dimethanol (160 MHz, CD_3OD , 293K).



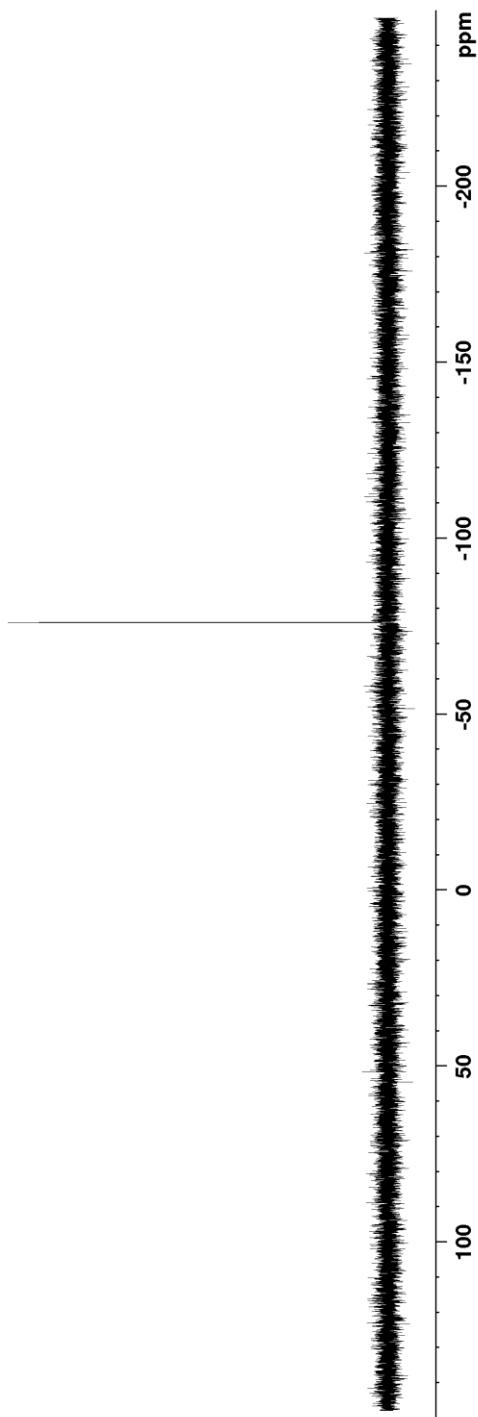
Spectrum 16. ¹H NMR spectrum of (5-(di(furan-2-yl)phosphaneyl)furan-2-yl)methanol (400 MHz, CD₃OD, 293K).



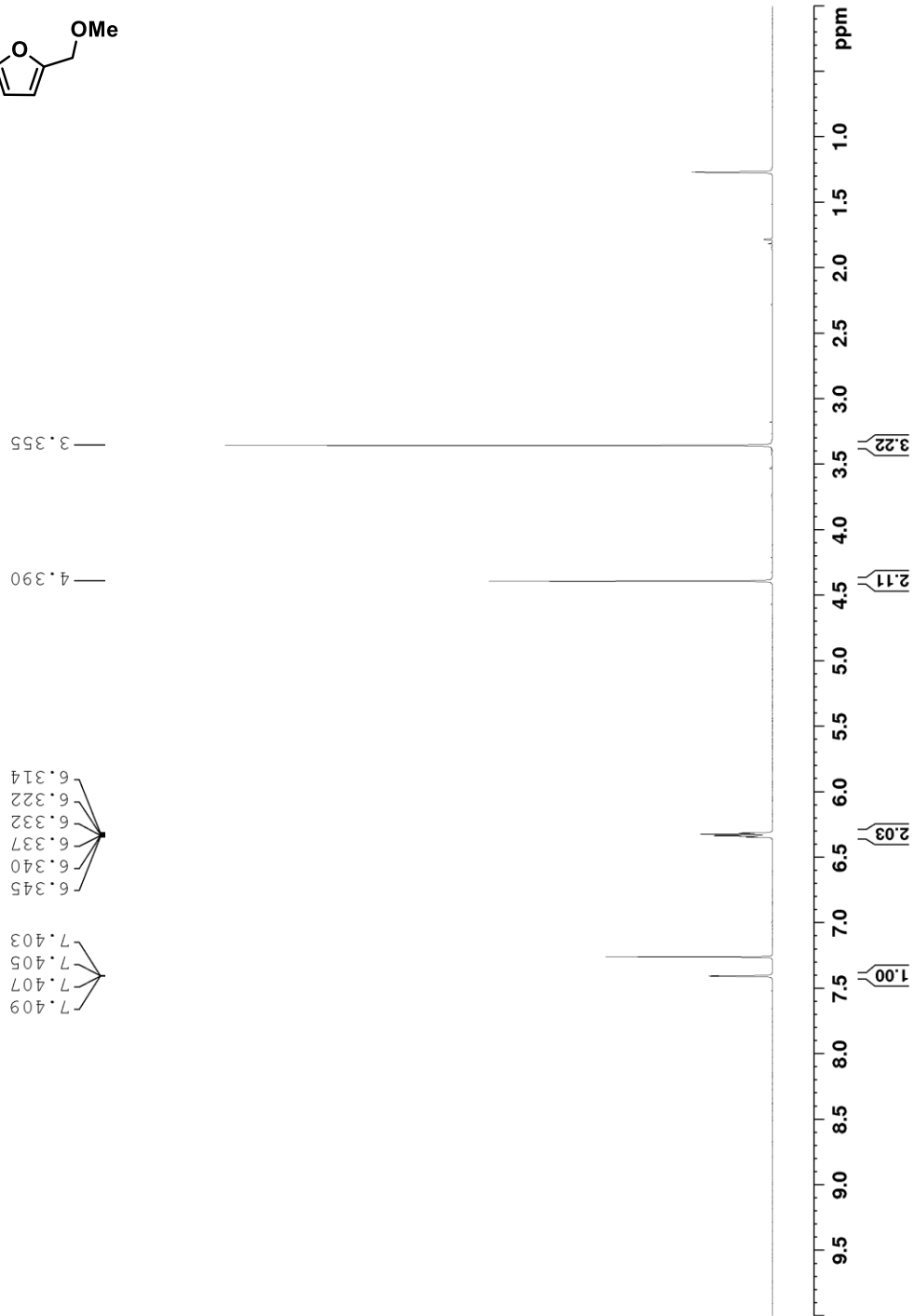
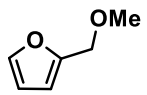
Spectrum 17. ^{13}C NMR spectrum of (5-(di(furan-2-yl)phosphaneyl)furan-2-yl)methanol (160 MHz, CDCl_3 , 293K).



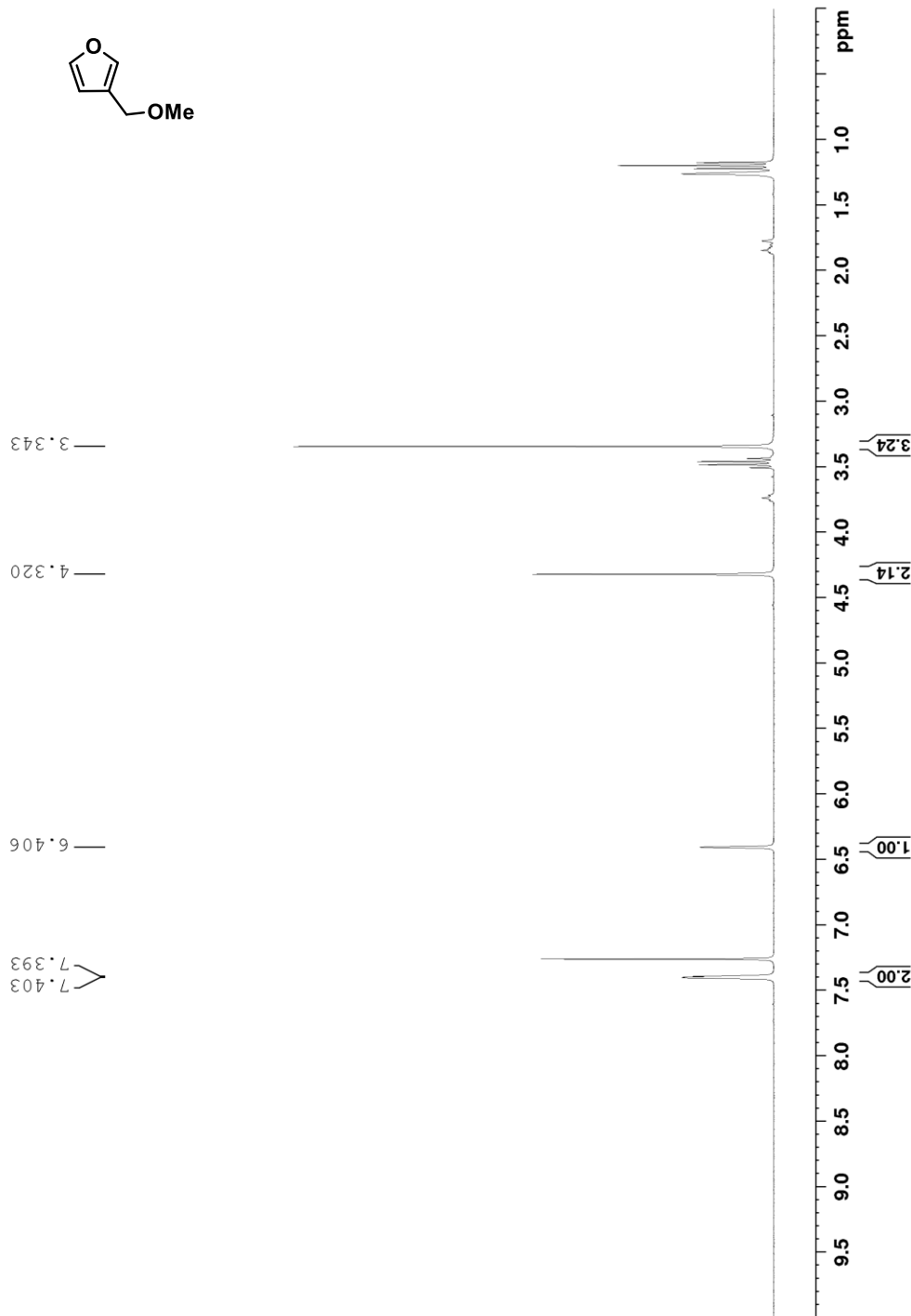
40 * 97 —



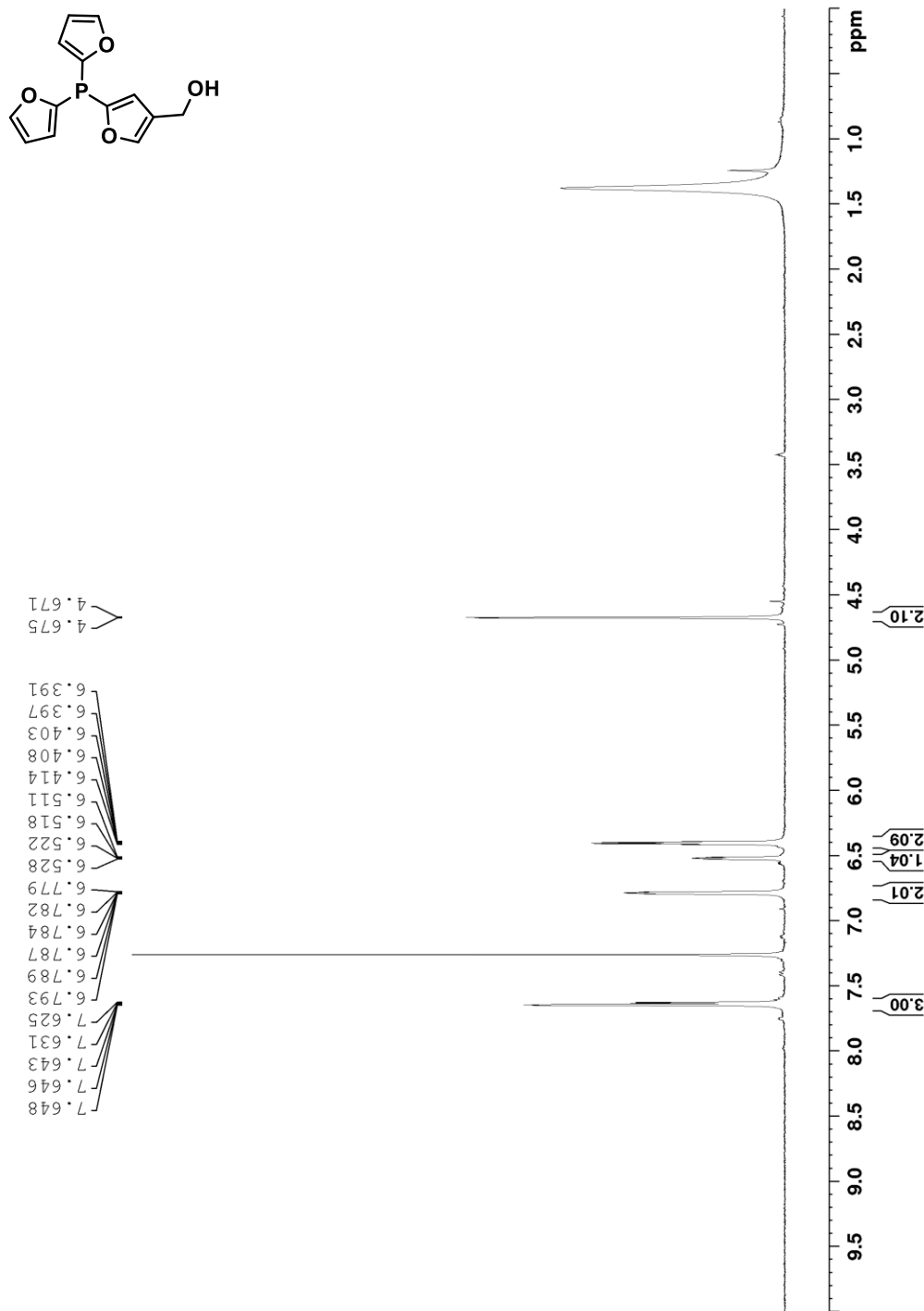
Spectrum 18. ^{31}P NMR spectrum of (5-(di(furan-2-yl)phosphaneyl)furan-2-yl)methanol (160 MHz, CD_3OD , 293K).



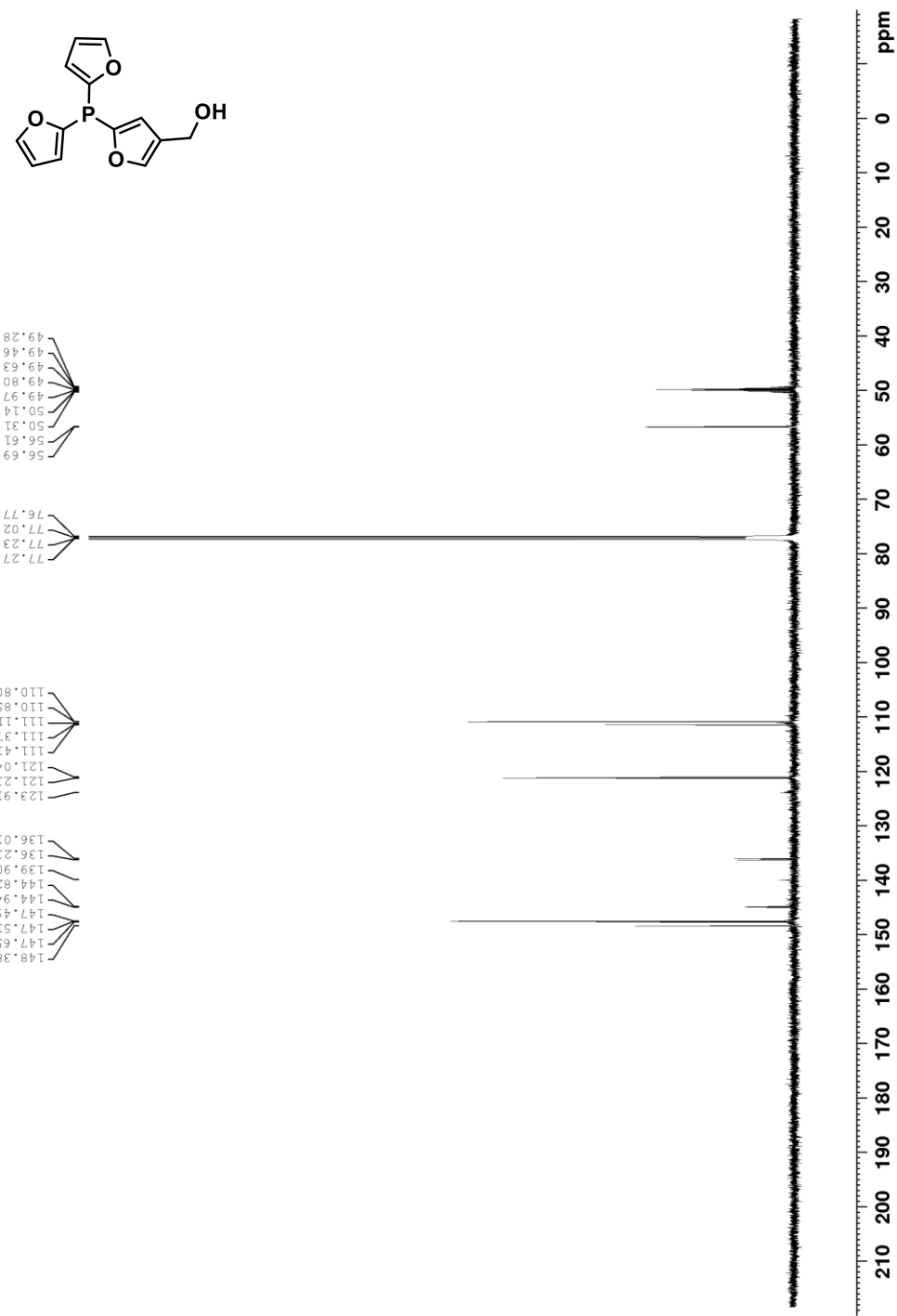
Spectrum 19. ¹H NMR spectrum of 2-(methoxymethyl)furan (400 MHz, CDCl₃, 293K).



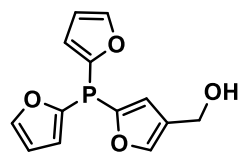
Spectrum 20. ¹H NMR spectrum of 3-(methoxymethyl)furan (300 MHz, CDCl₃, 293K).



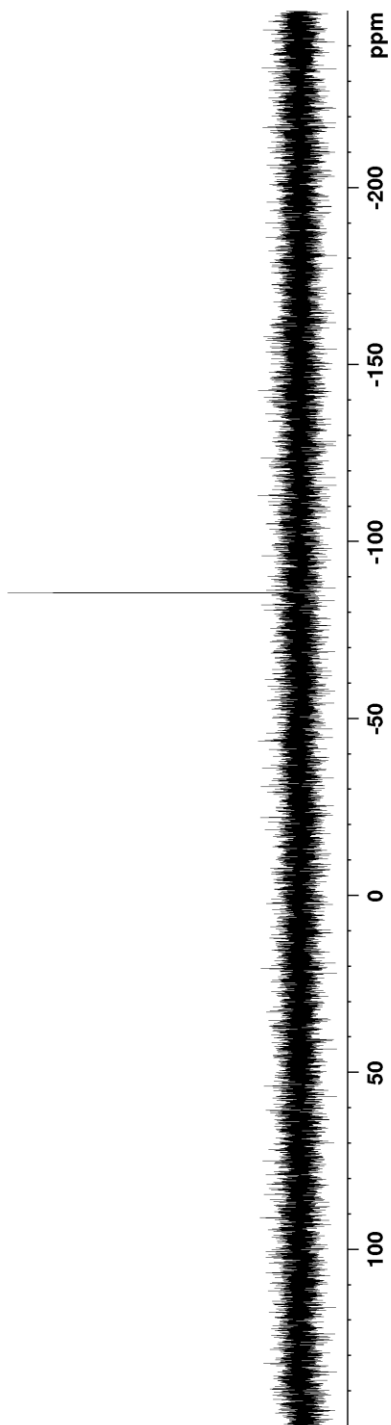
Spectrum 21. ^1H NMR spectrum of (5-(di(furan-2-yl)phosphaneyl)furan-3-yl)methanol (300 MHz, CDCl_3 , 293K).



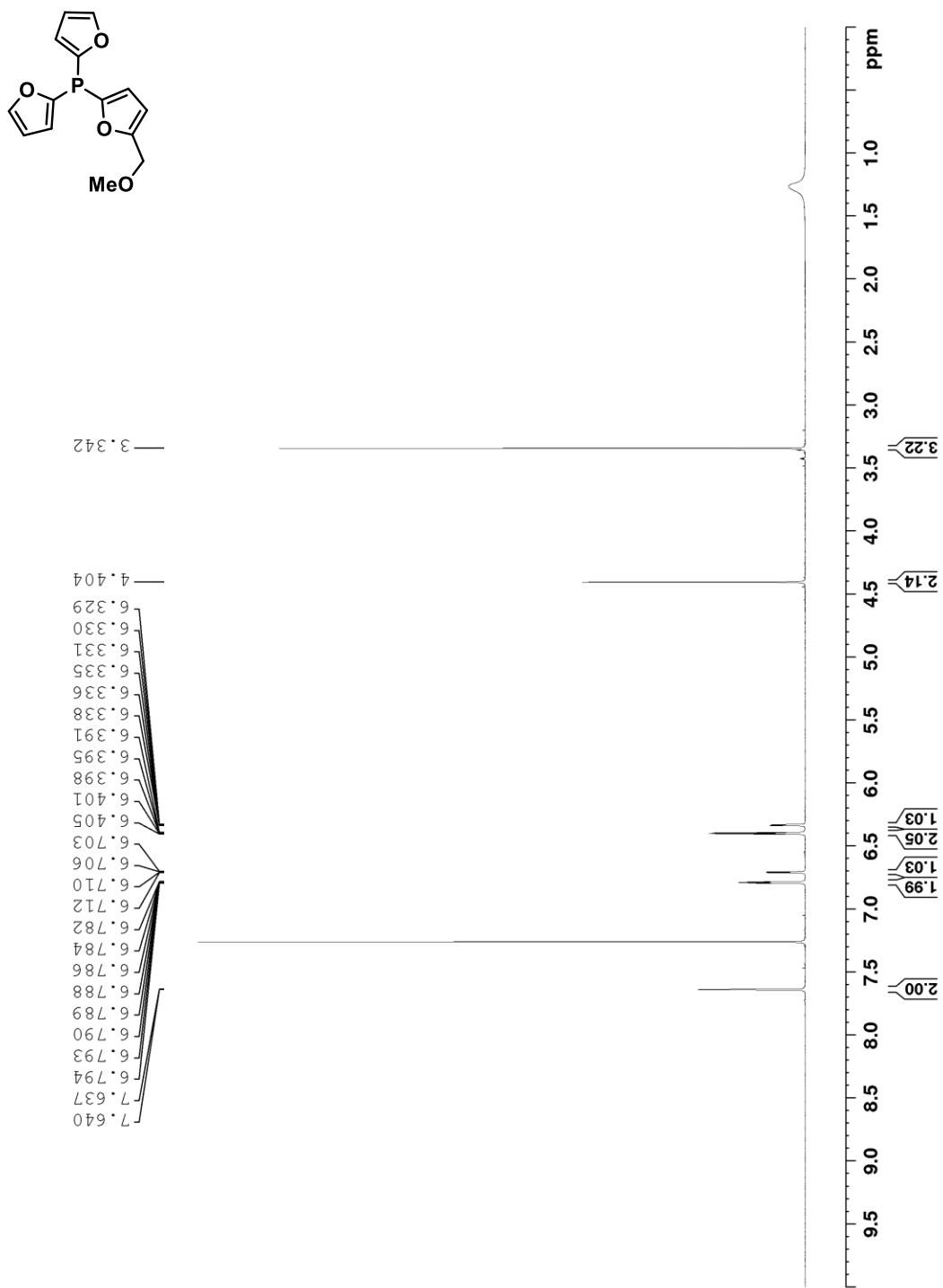
Spectrum 22. ^{13}C NMR spectrum of (5-(di(furan-2-yl)phosphaneyl)furan-3-yl)methanol (125 MHz, CDCl_3 , 293K).



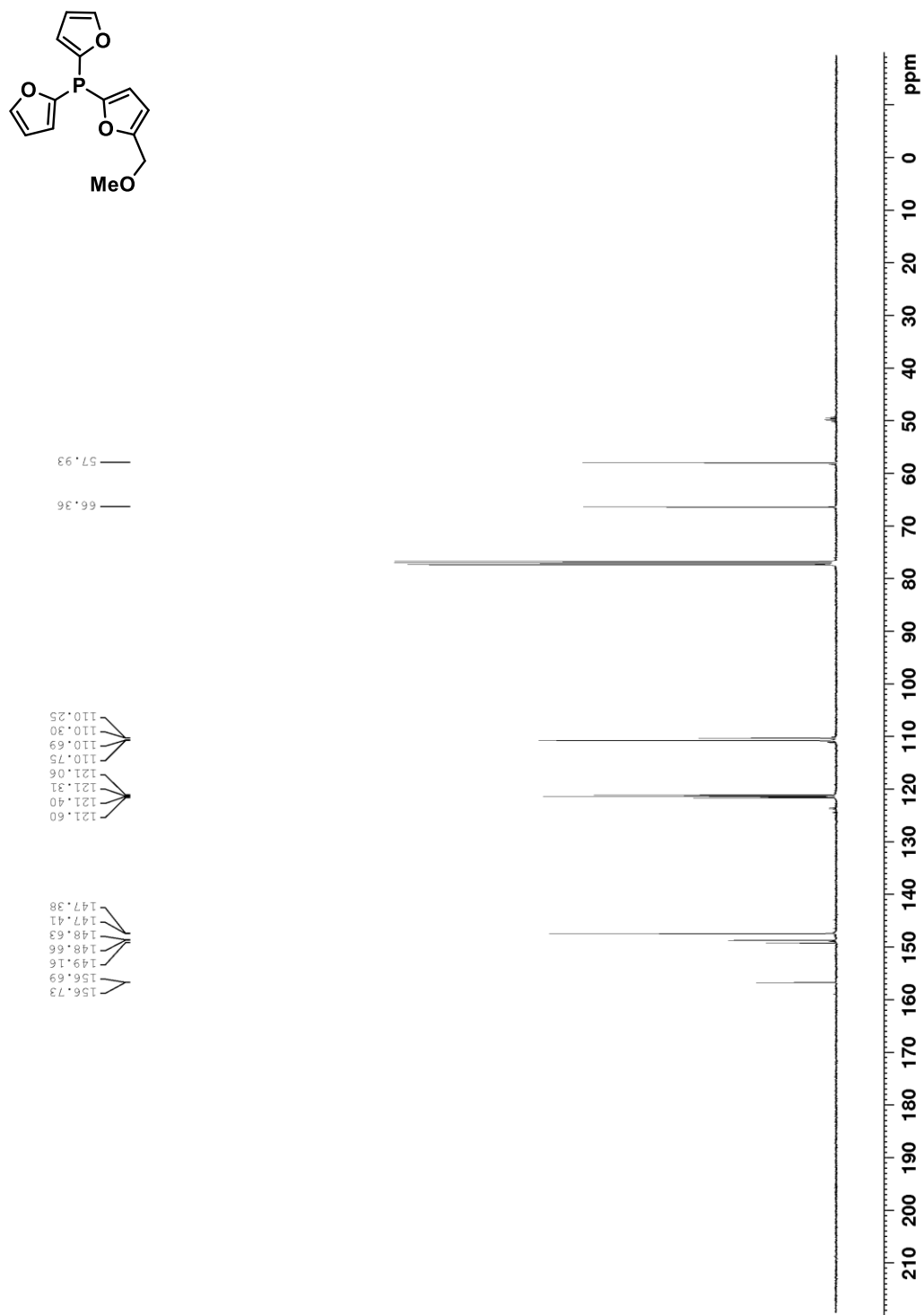
-85.56



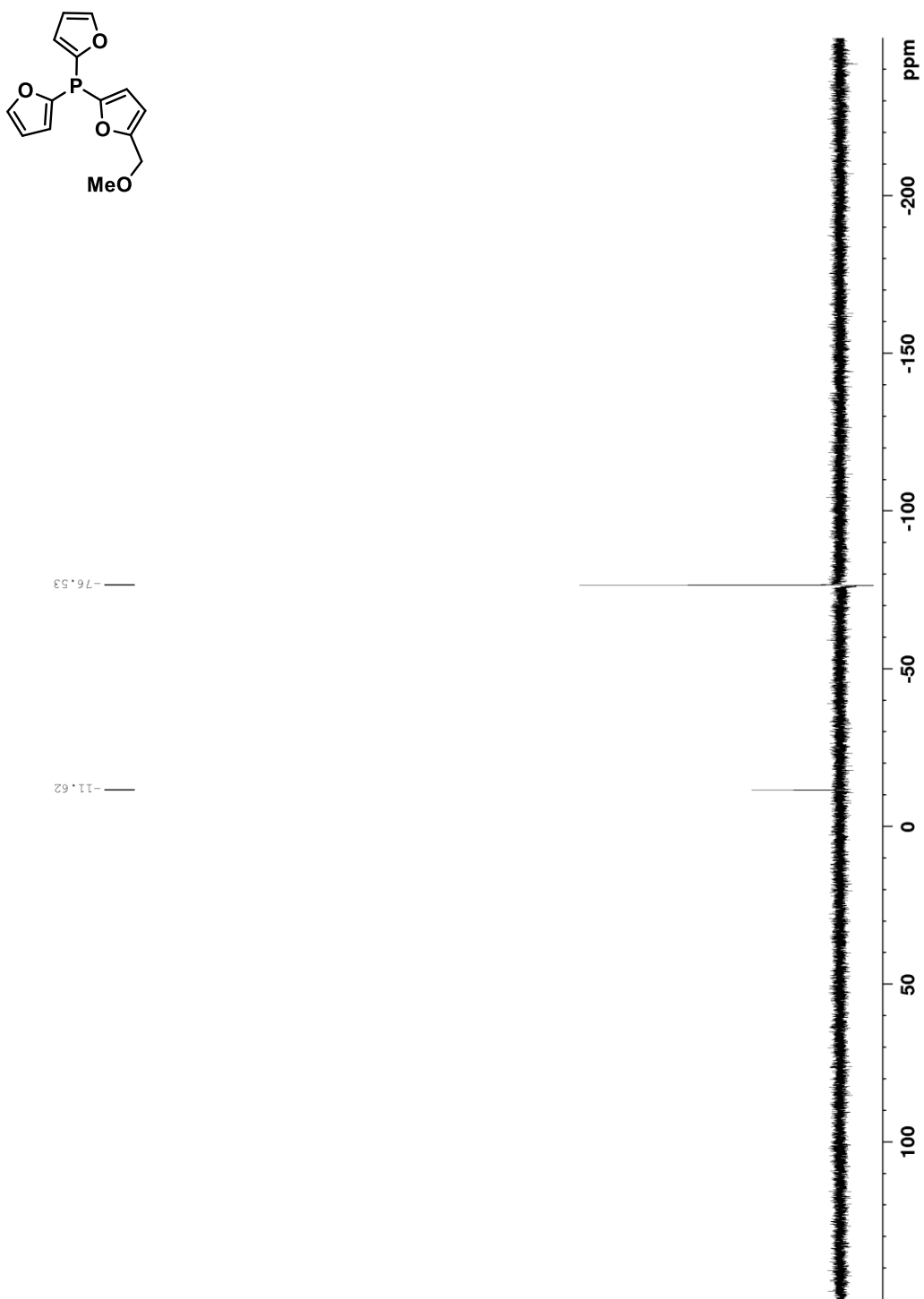
Spectrum 23. ^{31}P NMR spectrum of (5-(di(furan-2-yl)phosphaneyl)furan-3-yl)methanol (120 MHz, CDCl_3 , 293K).



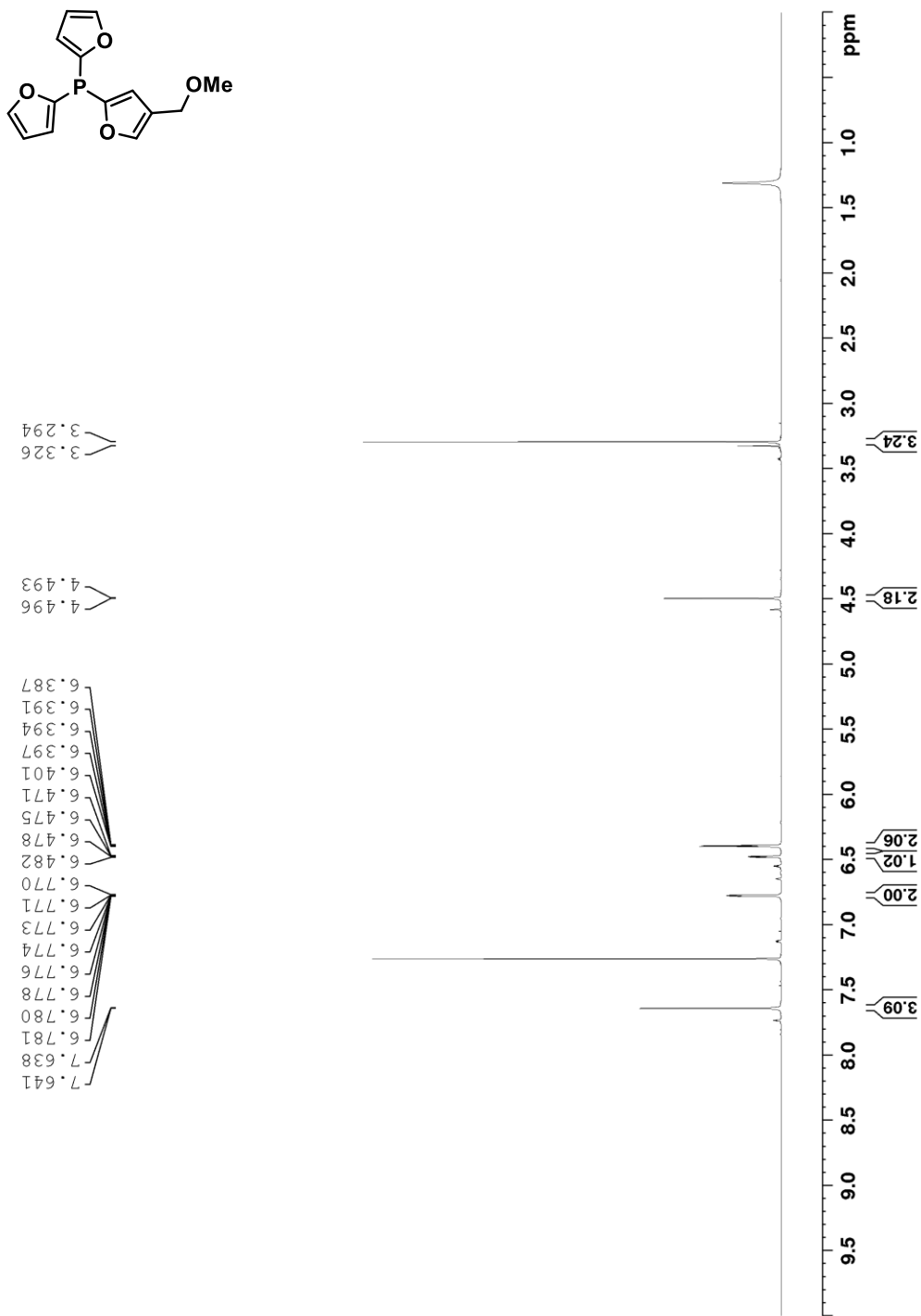
Spectrum 24. ¹H NMR spectrum of di(furan-2-yl)(5-(methoxymethyl)furan-2-yl)phosphane (500 MHz, CDCl₃, 293K).



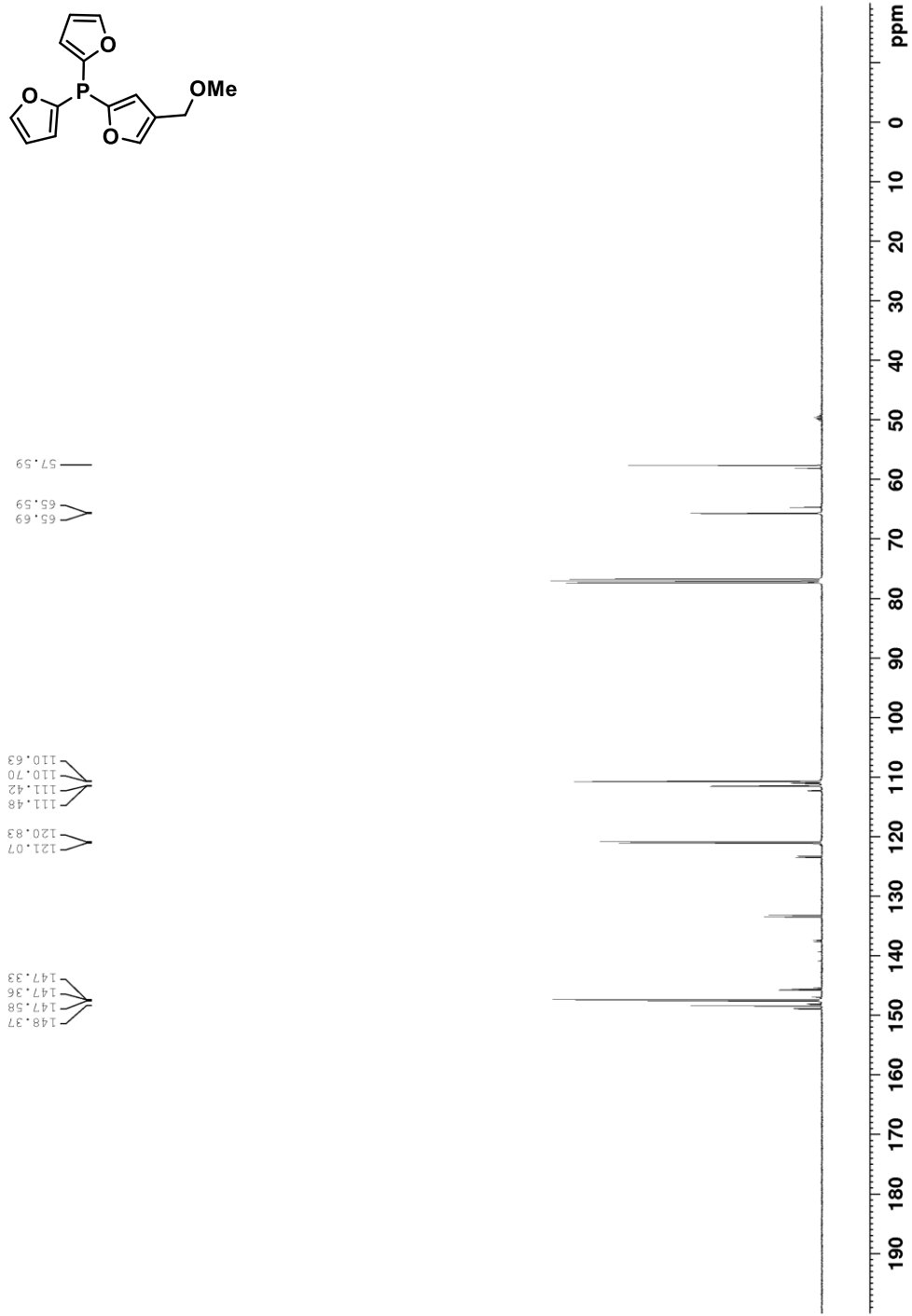
Spectrum 25. ^{13}C NMR spectrum of di(furan-2-yl)(5-(methoxymethyl)furan-2-yl)phosphane (100 MHz, CDCl_3 , 293K).



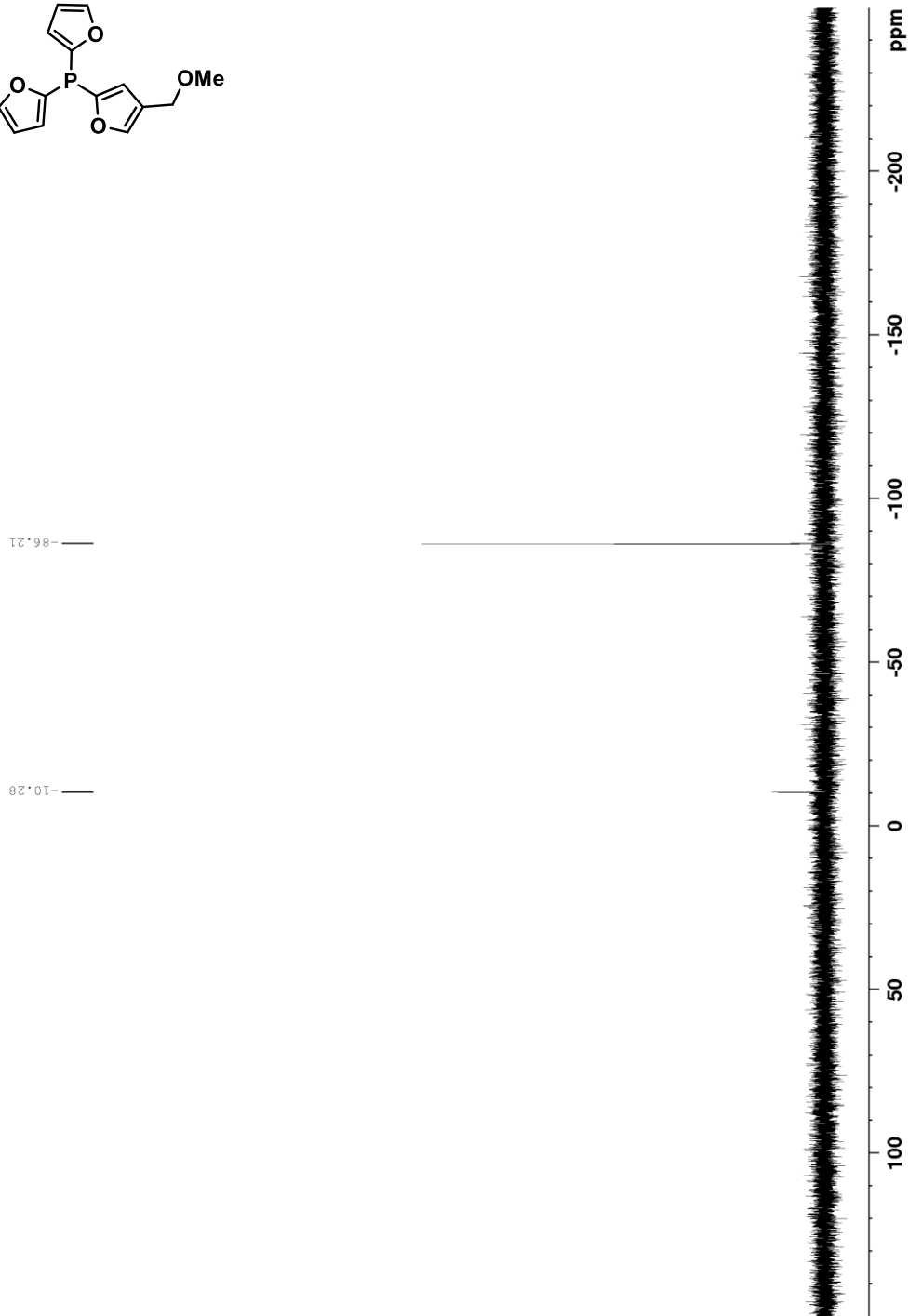
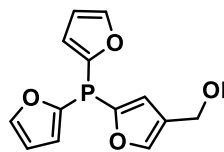
Spectrum 26. ^{31}P NMR spectrum of di(furan-2-yl)(5-(methoxymethyl)furan-2-yl)phosphane (200 MHz, CDCl_3 , 293K).



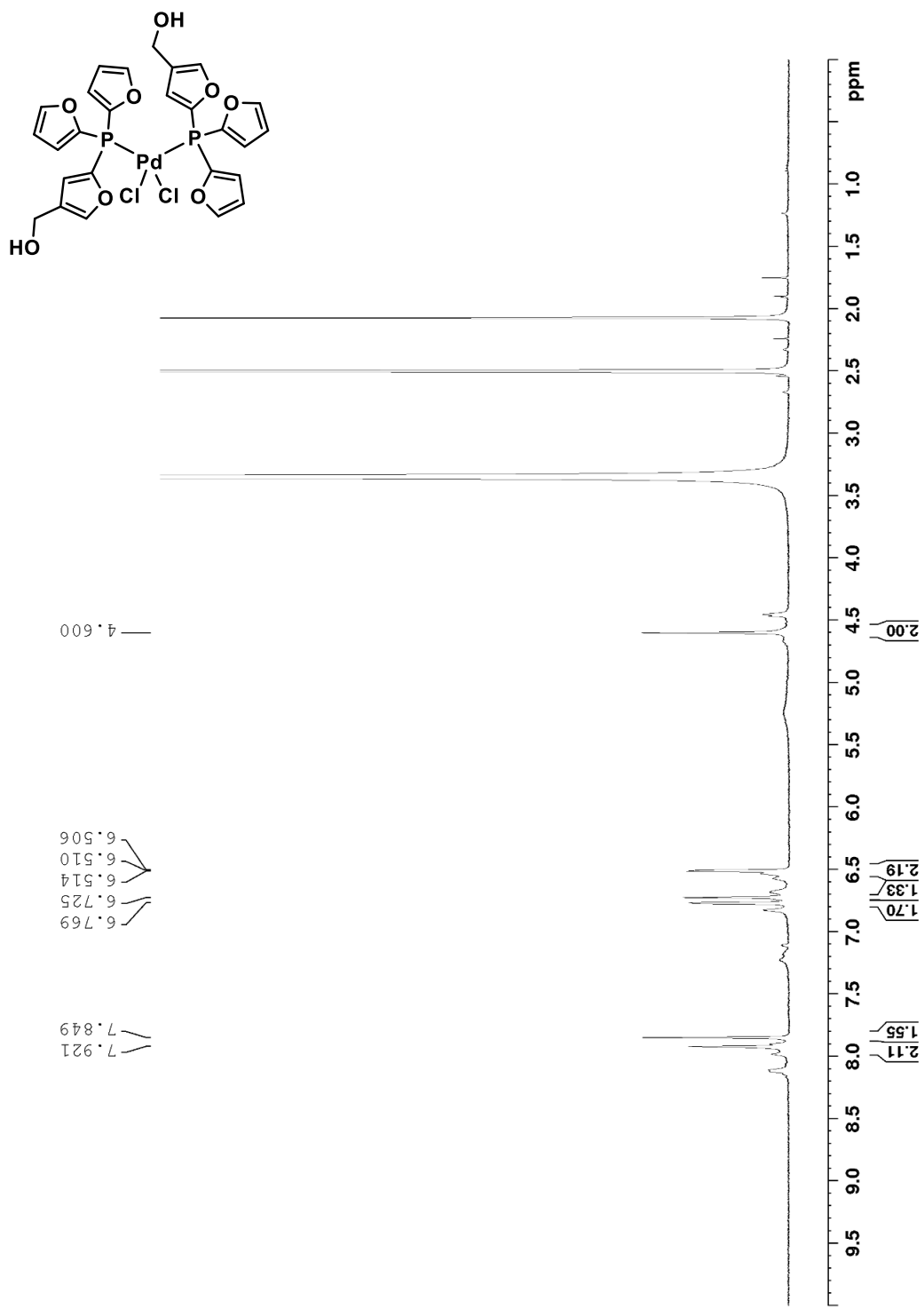
Spectrum 27. ^1H NMR spectrum of di(furan-2-yl)(4-(methoxymethyl)furan-2-yl)phosphane (500 MHz, CDCl_3 , 293K).



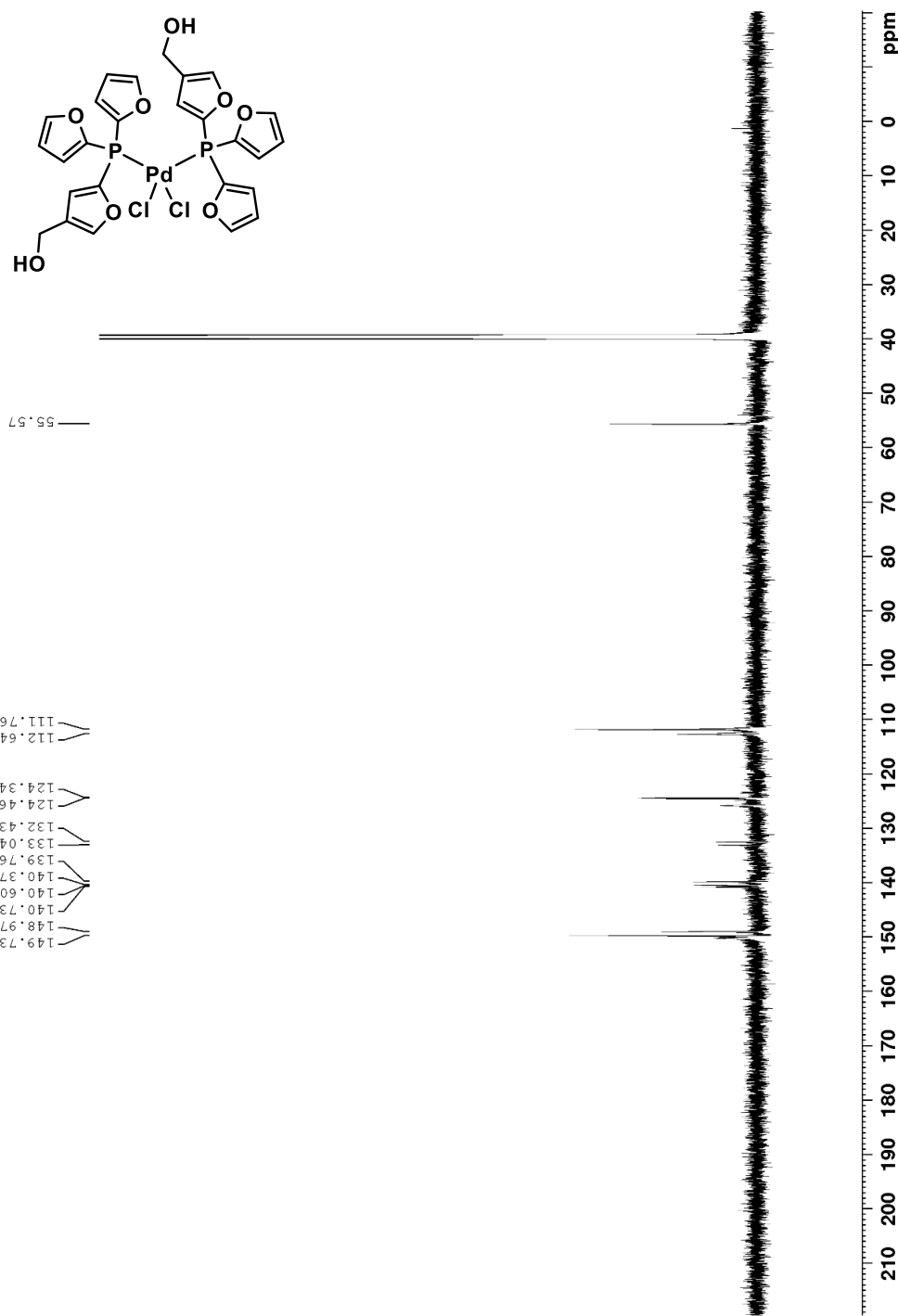
Spectrum 28. ¹³C NMR spectrum of di(furan-2-yl)(4-(methoxymethyl)furan-2-yl)phosphane (100 MHz, CDCl₃, 293K).



Spectrum 29. ^{31}P NMR spectrum of di(furan-2-yl)(4-(methoxymethyl)furan-2-yl)phosphane (200 MHz, CDCl_3 , 293K).

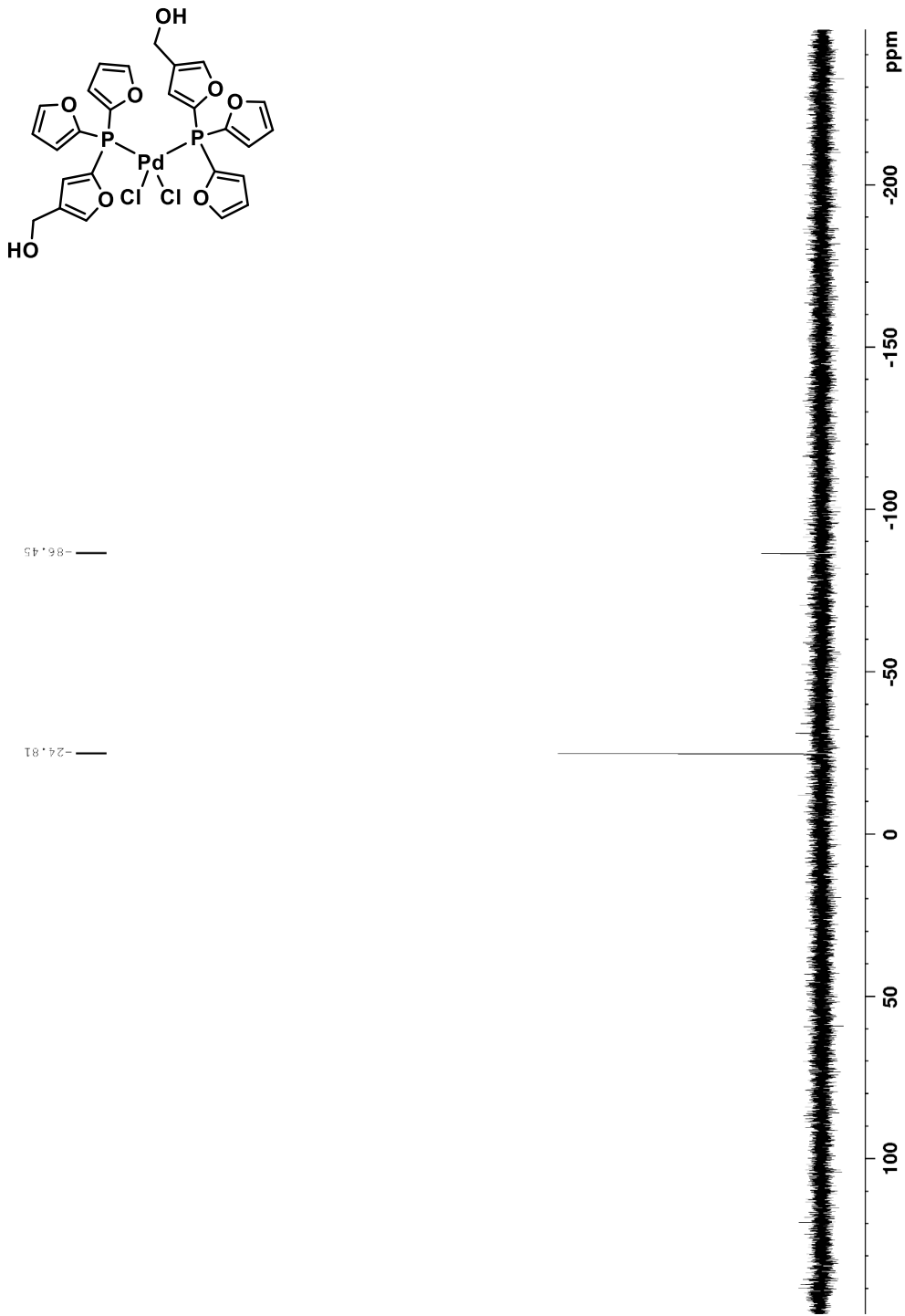


Spectrum 30. ¹H NMR spectrum of dichlorobis((5-(di(furan-2-yl)phosphaneyl)furan-3-yl)methanol)palladium(II) (400 MHz, DMSO-*d*₆, 293K).

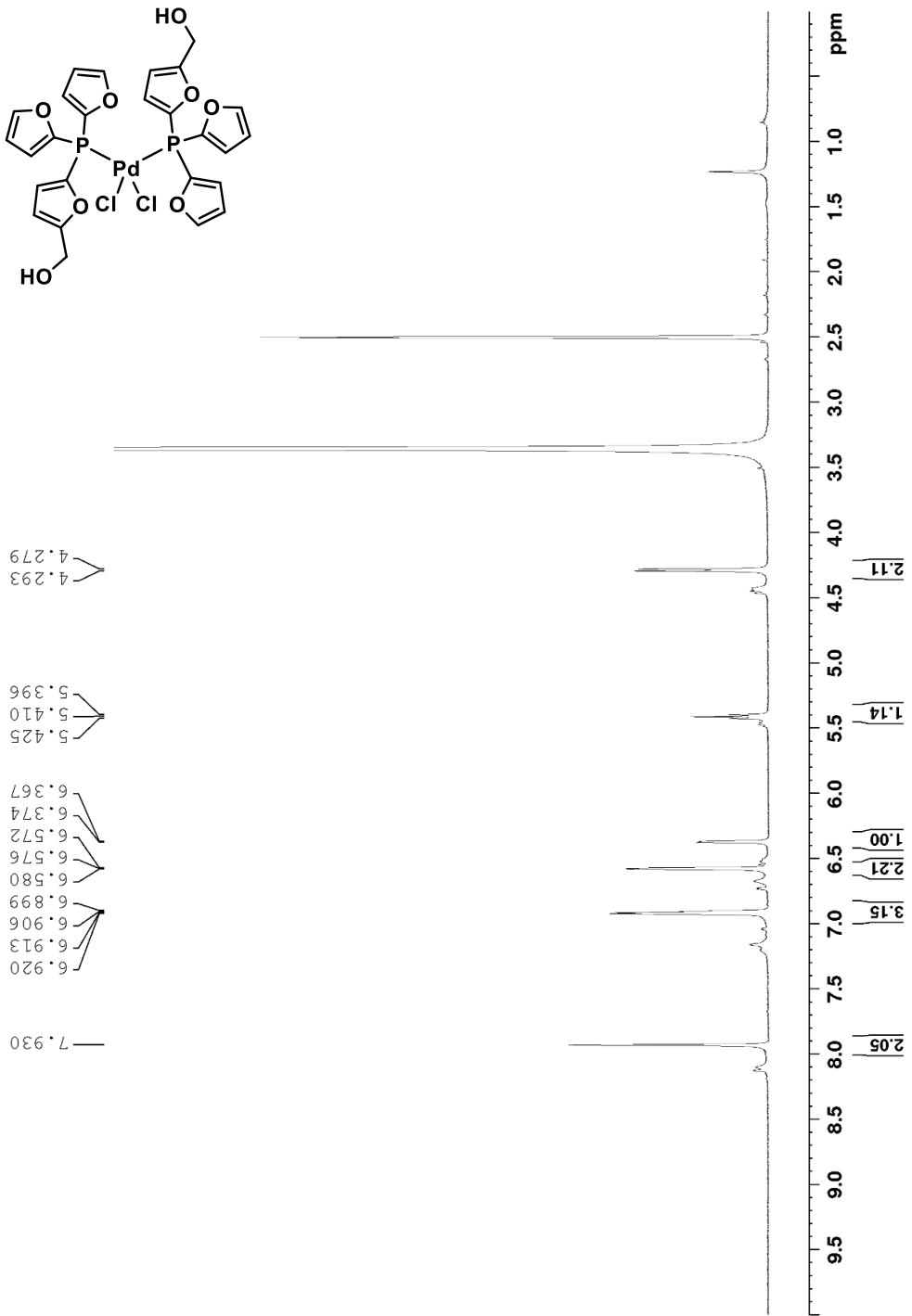


Spectrum 31. ^{13}C NMR spectrum of dichlorobis((5-(di(furan-2-yl)phosphaneyl)furan-3-

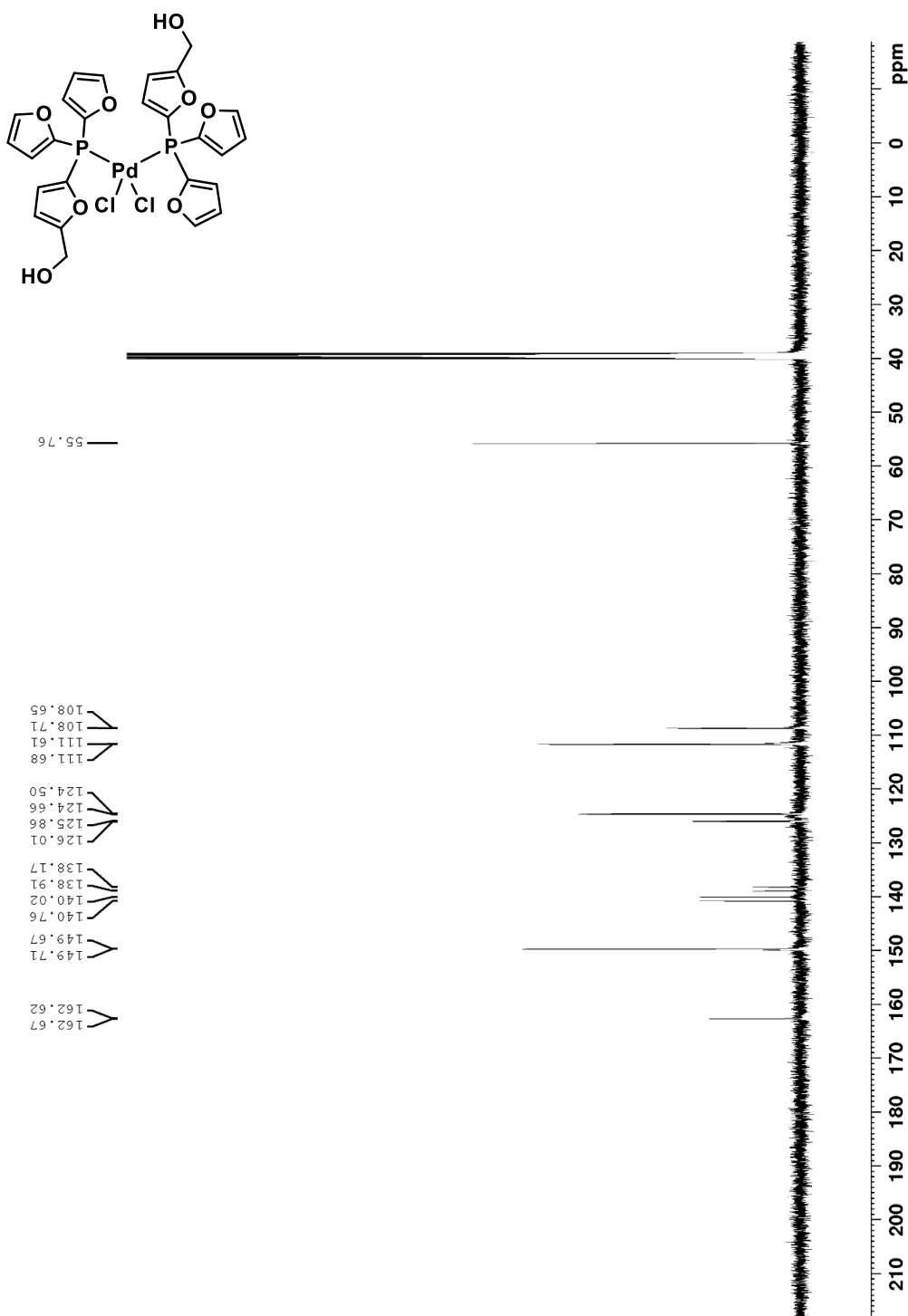
yl)methanol)palladium(II) (150 MHz, $\text{DMSO}-d_6$, 293K).



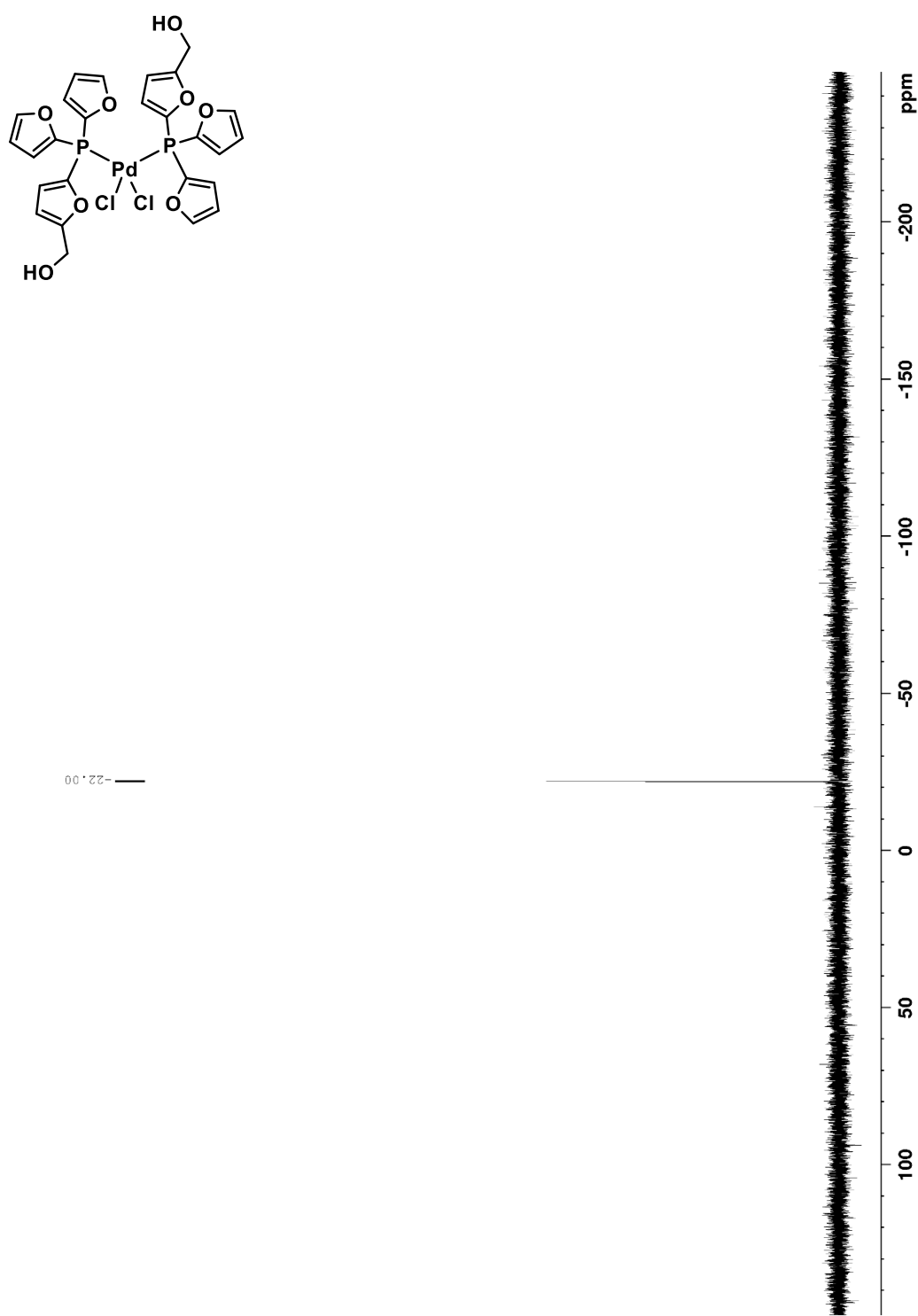
Spectrum 32. ^{31}P NMR spectrum of dichlorobis((5-(di(furan-2-yl)phosphanoyl)furan-3-yl)methanol)palladium(II) (120 MHz, $\text{DMSO}-d_6$, 293K).



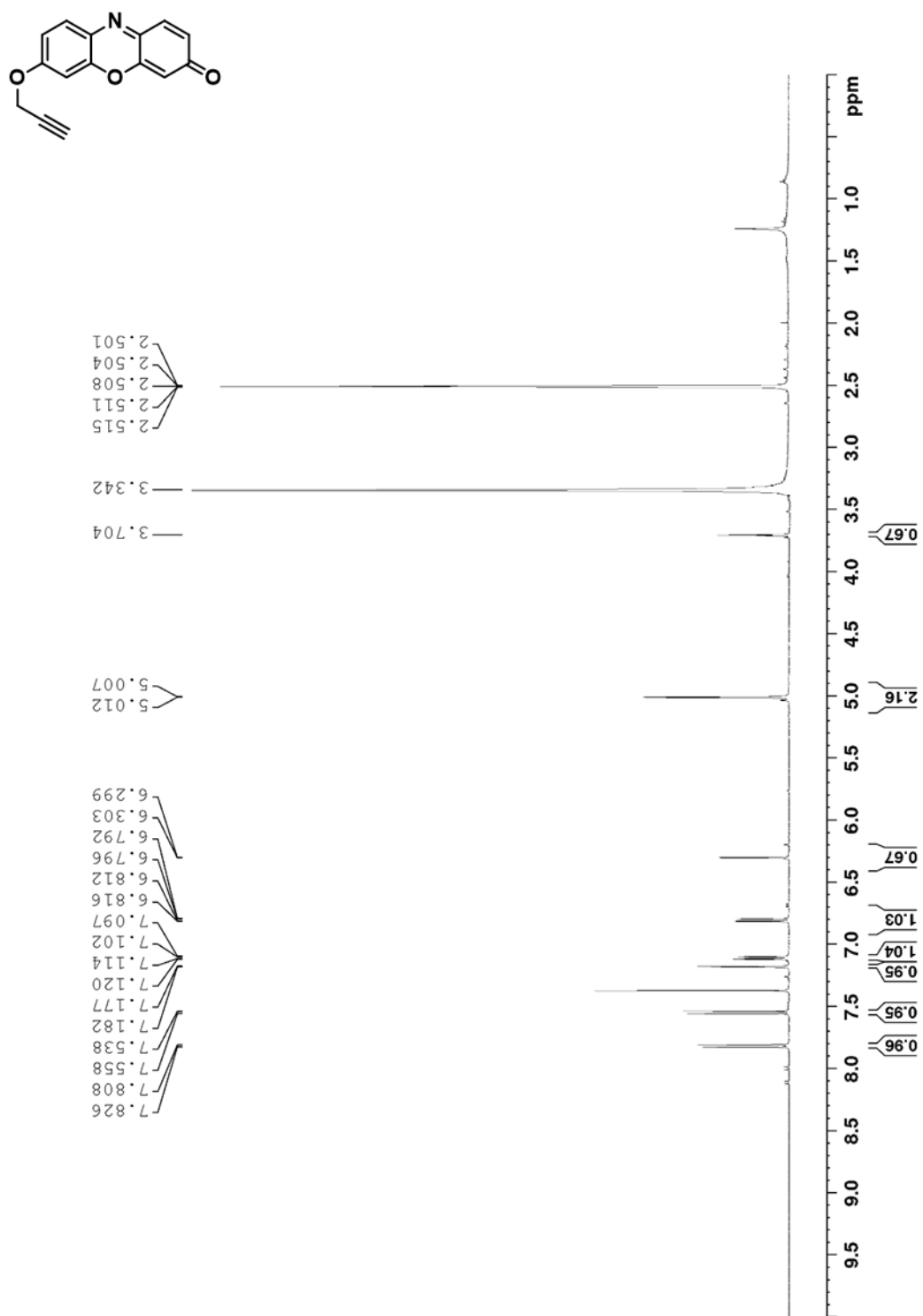
Spectrum 33. ¹H NMR spectrum of dichlorobis((5-(di(furan-2-yl)phosphaneyl)furan-2-yl)methanol)palladium(II) (400 MHz, DMSO-*d*₆, 293K).



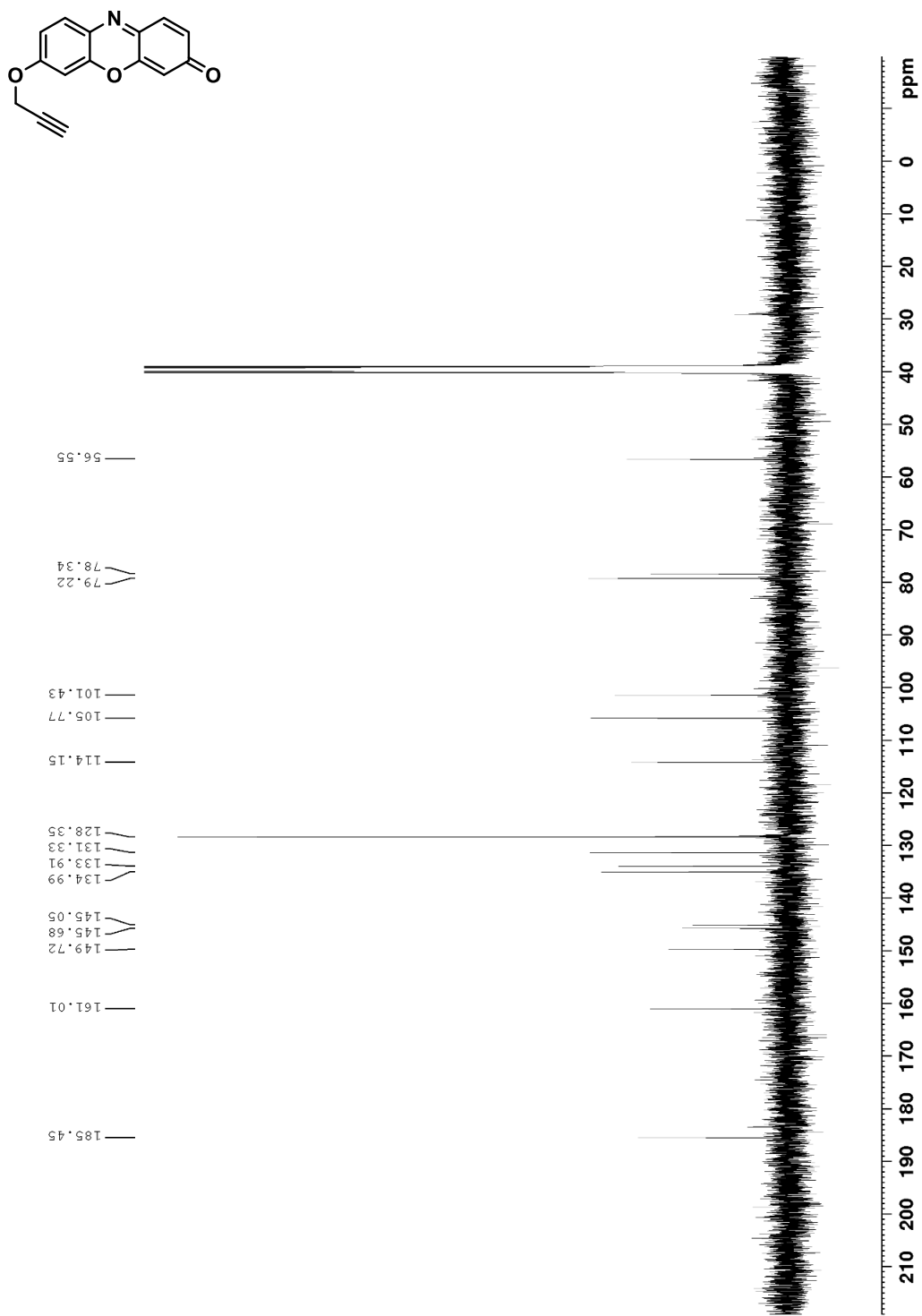
Spectrum 34. ^{13}C NMR spectrum of dichlorobis((5-(di(furan-2-yl)phosphaneyl)furan-2-yl)methanol)palladium(II) (125 MHz, $\text{DMSO}-d_6$, 293K).



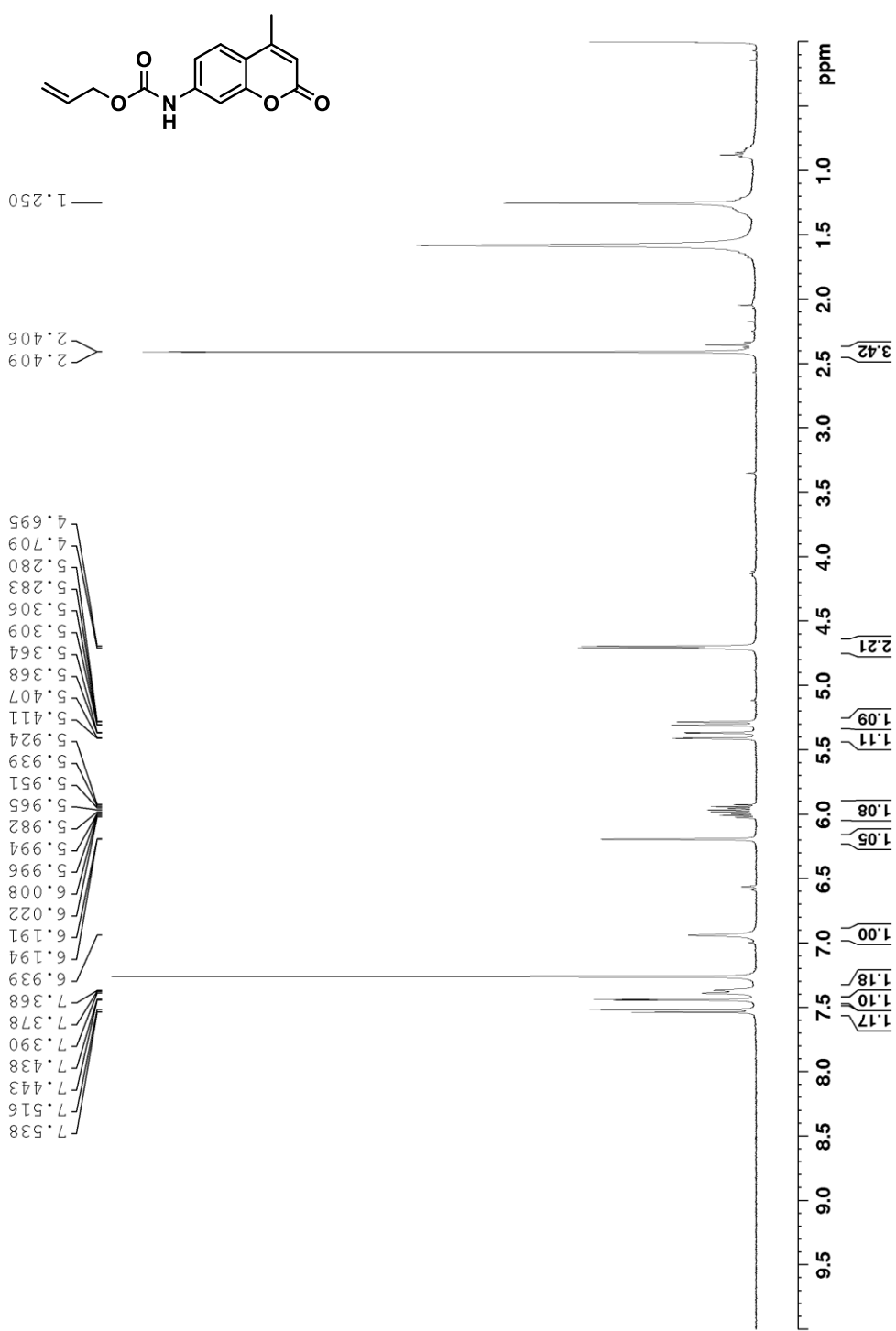
Spectrum 35. ^{31}P NMR spectrum of dichlorobis((5-(di(furan-2-yl)phosphanoyl)furan-2-yl)methanol)palladium(II) (120 MHz, DMSO-*d*₆, 293K).



Spectrum 36. ^1H NMR spectrum of 7-(prop-2-yn-1-yloxy)-3*H*-phenoxazin-3-one (500 MHz, $\text{DMSO}-d_6$, 293K).

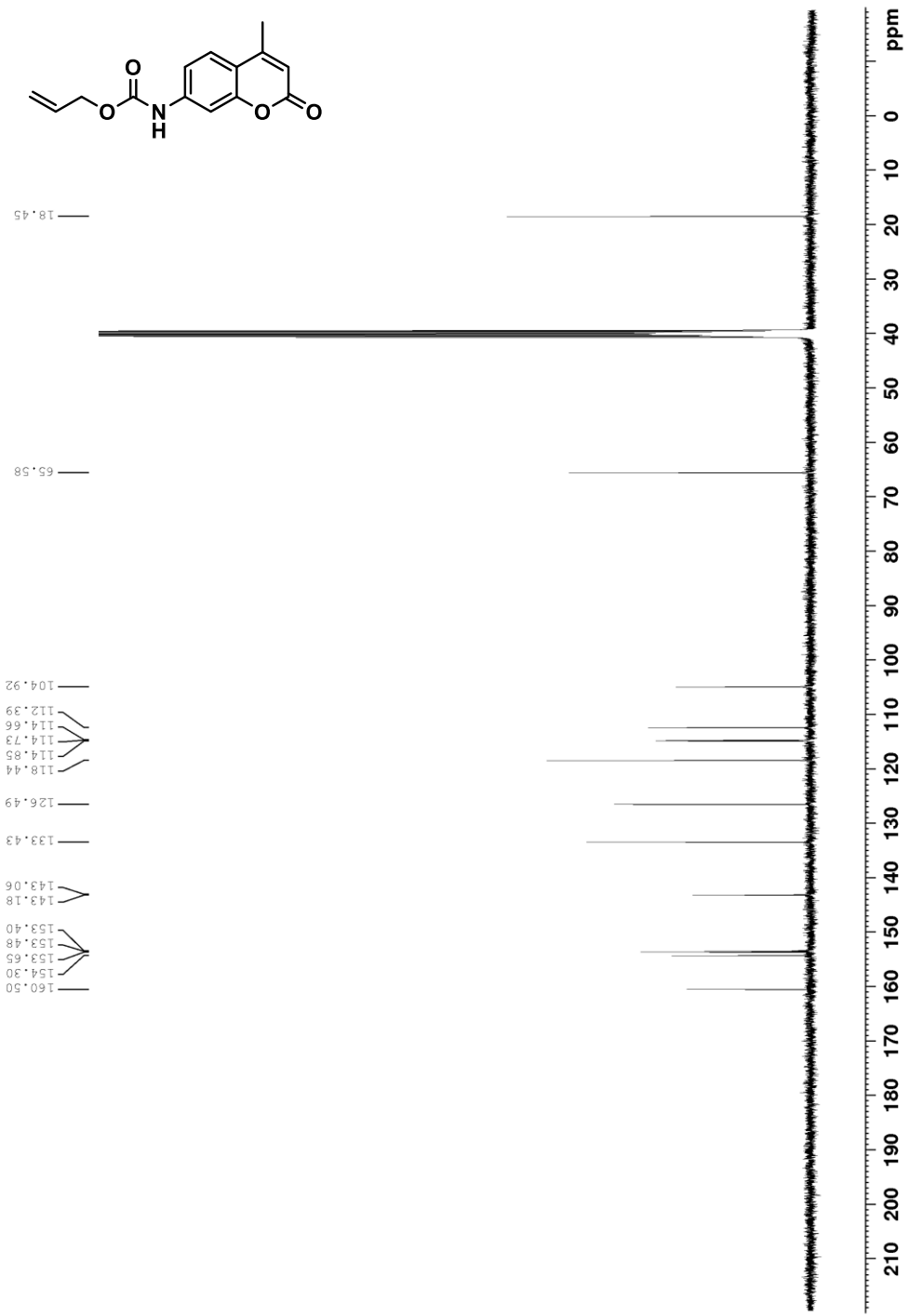


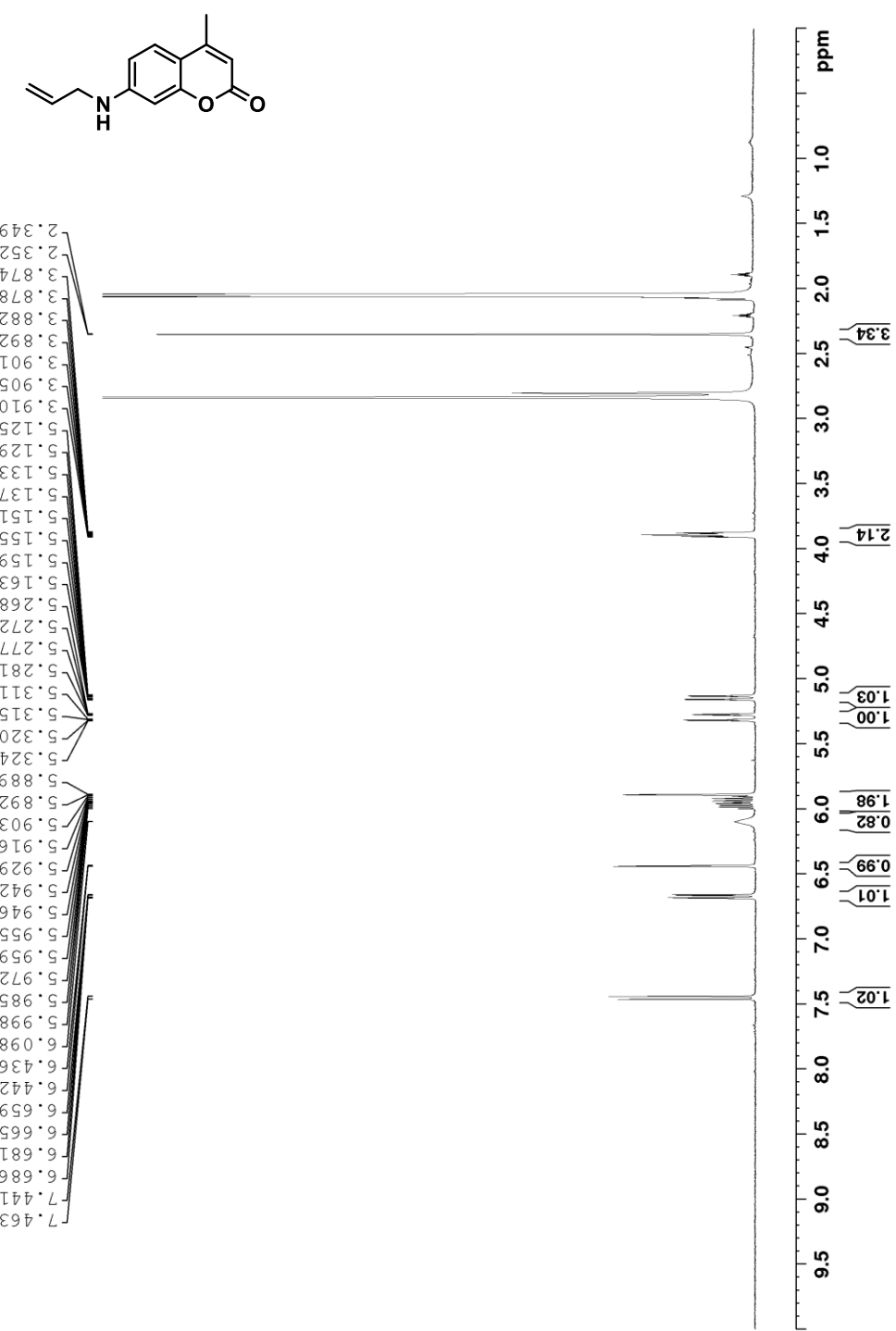
Spectrum 37. ^{13}C NMR spectrum of 7-(prop-2-yn-1-yloxy)-3*H*-phenoxazin-3-one (100 MHz, $\text{DMSO}-d_6$, 293K).



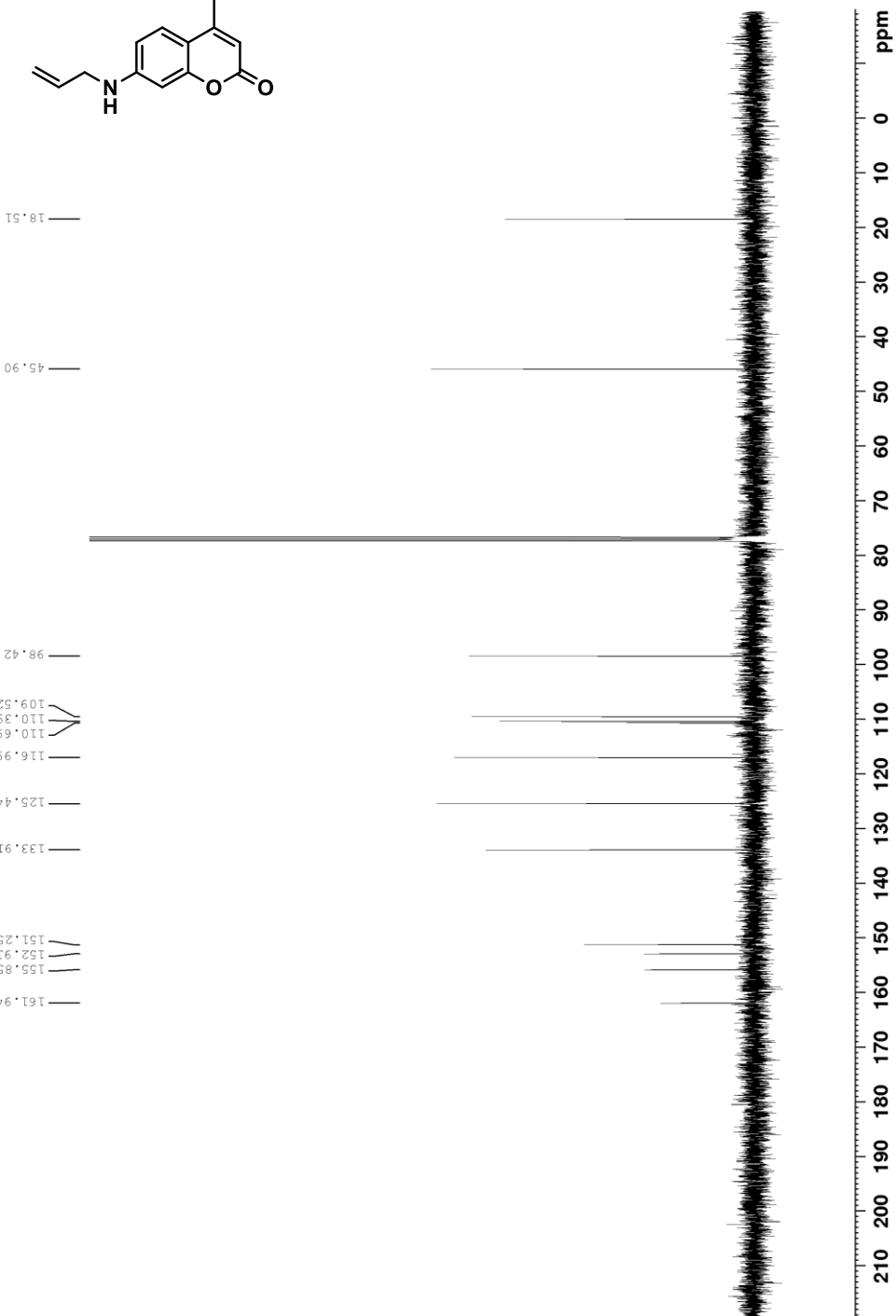
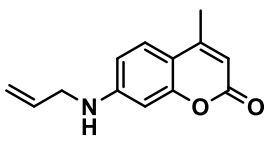
Spectrum 38. ¹H NMR spectrum of allyl (4-methyl-2-oxo-2H-chromen-7-yl)carbamate (400 MHz, CDCl₃,

293K).

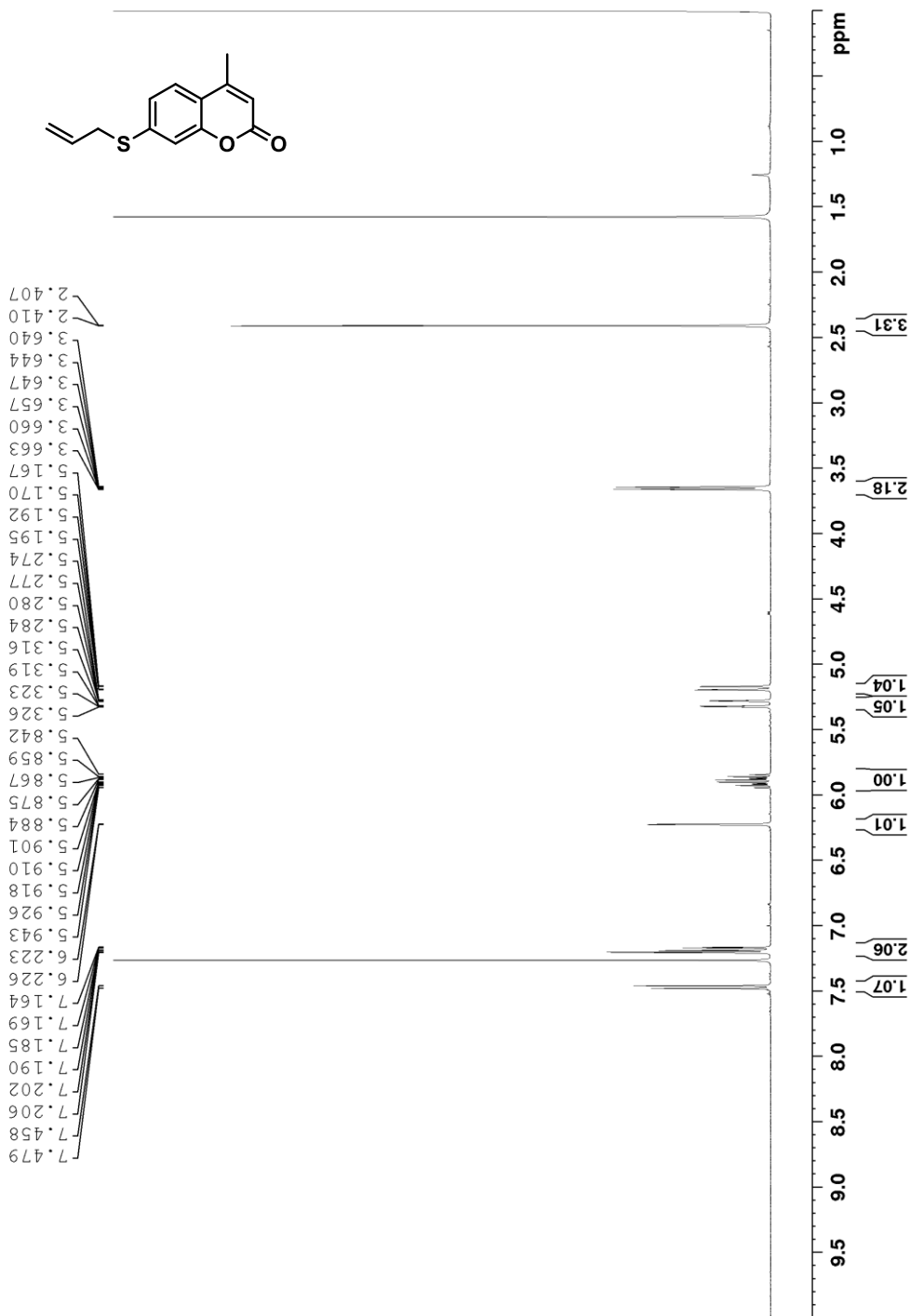




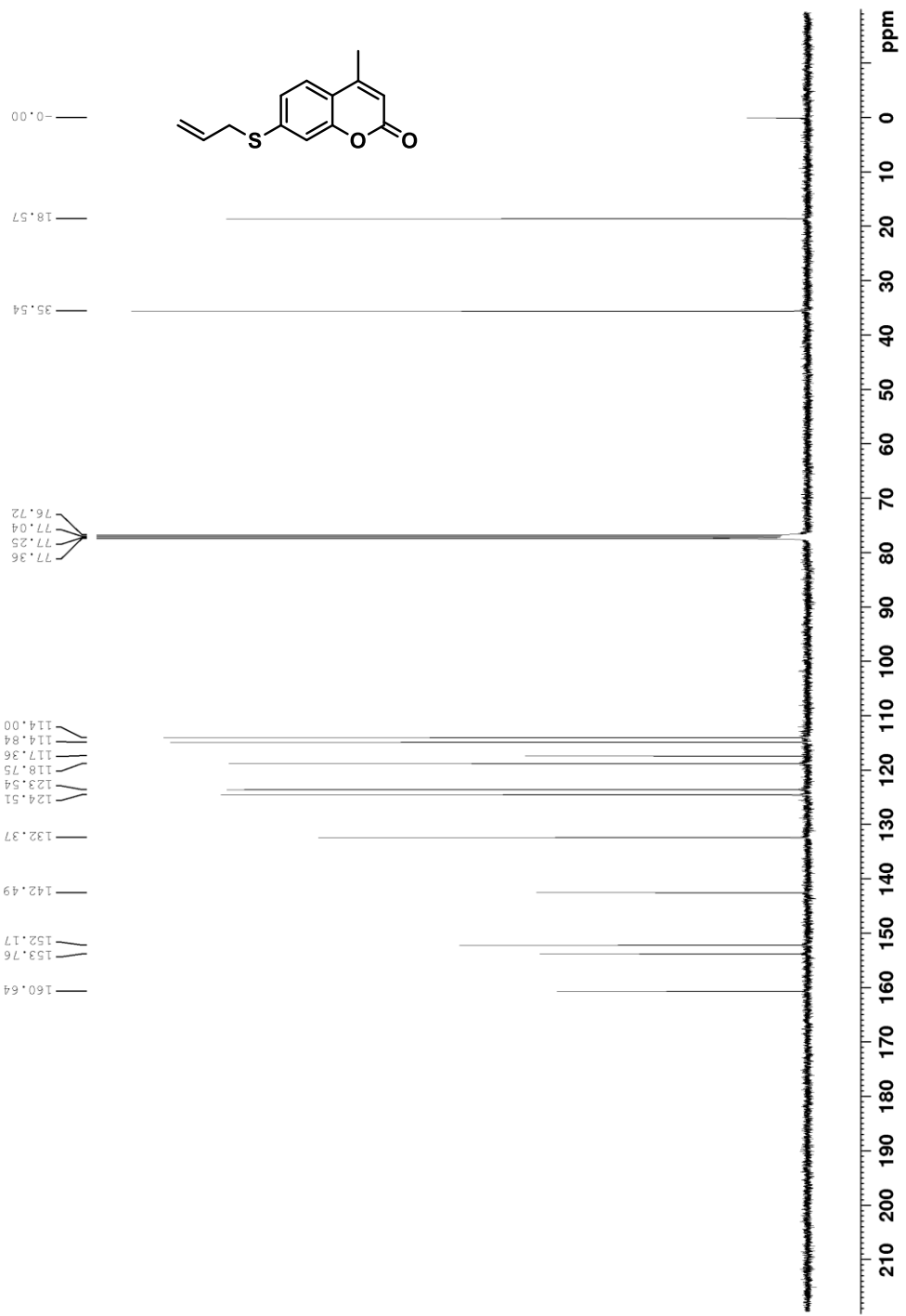
Spectrum 40. ^1H NMR spectrum of 7-(allyloxy)-2*H*-chromen-2-one (400 MHz, acetone- d_6 , 293K).



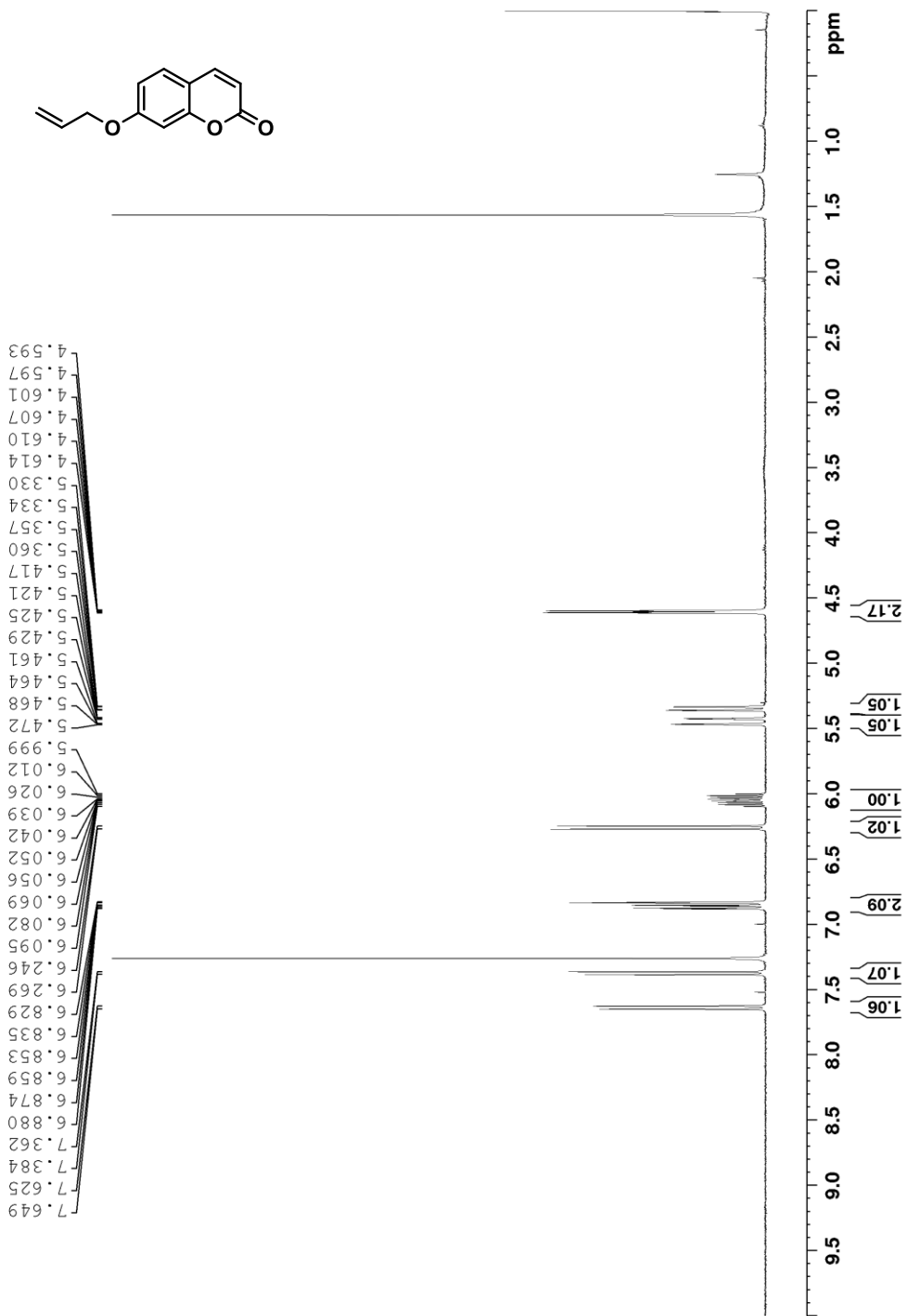
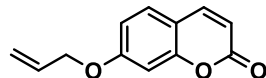
Spectrum 41. ^{13}C NMR spectrum of 7-(allyloxy)-2H-chromen-2-one (100 MHz, CDCl_3 , 293K).

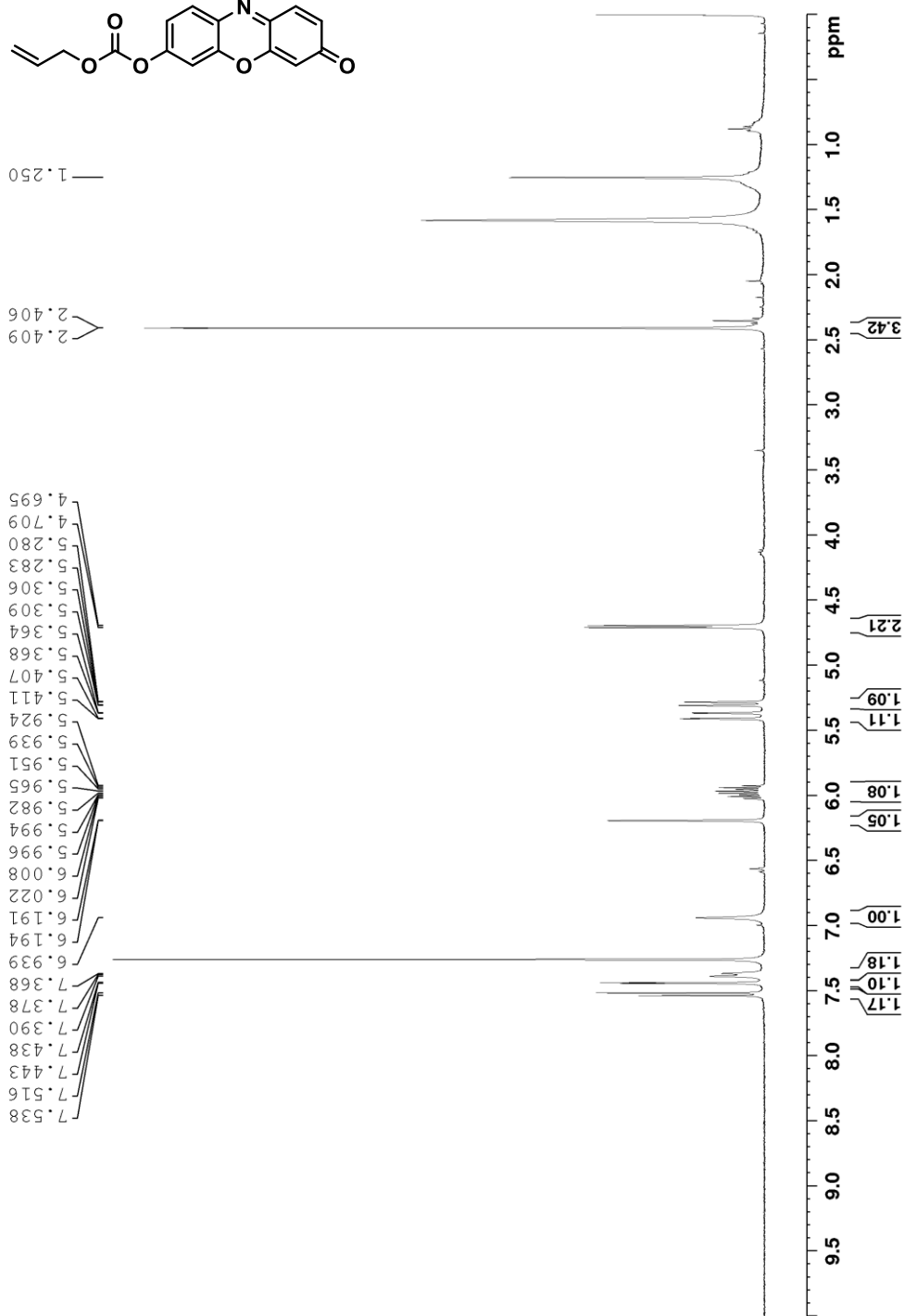
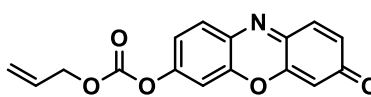


Spectrum 42. ^1H NMR spectrum of 7-(allylthio)-4-methyl-2*H*-chromen-2-one (400 MHz, CDCl_3 , 293K).

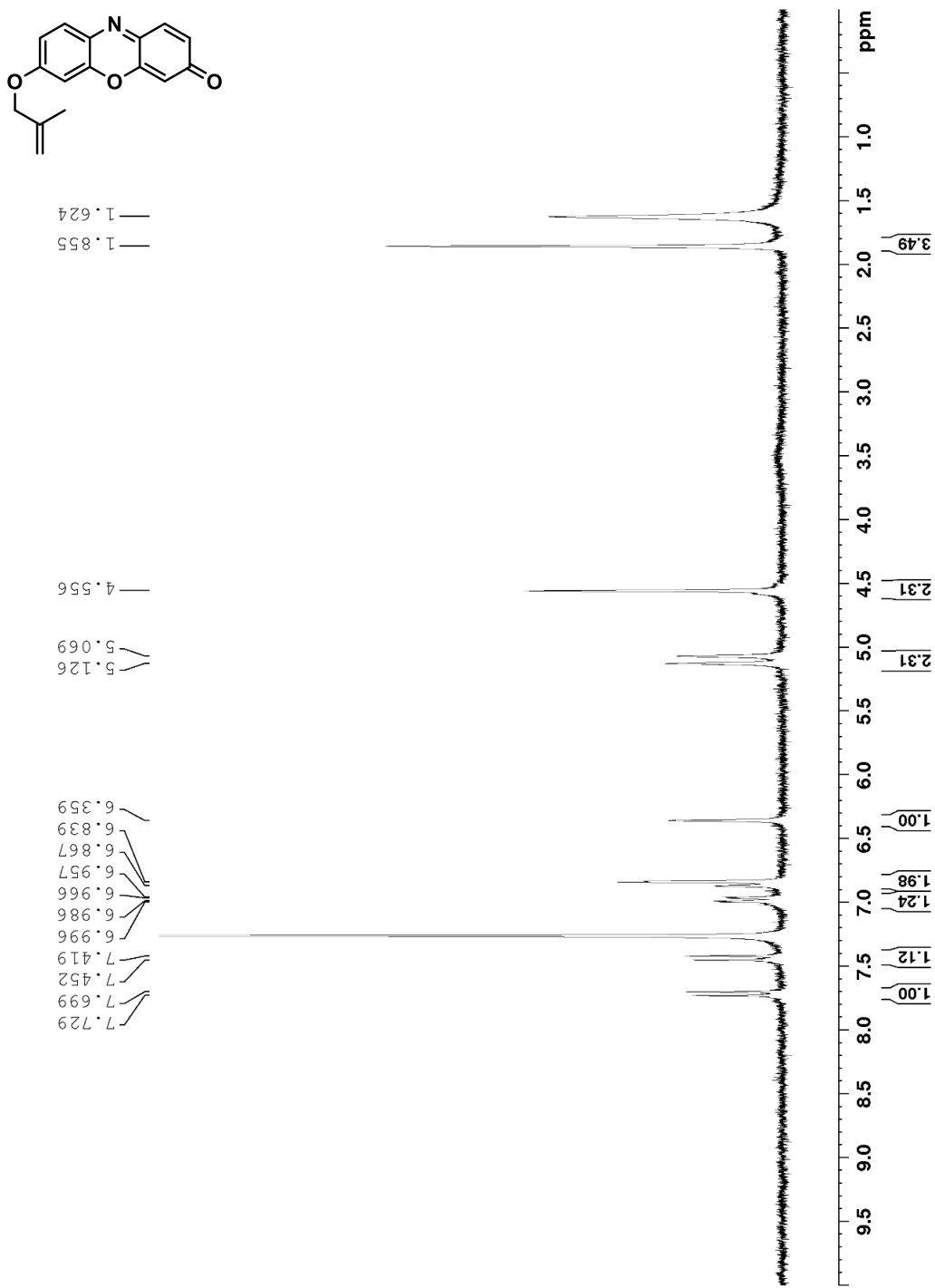


Spectrum 43. ^{13}C NMR spectrum of 7-(allylthio)-4-methyl-2H-chromen-2-one (100 MHz, CDCl_3 , 293K).

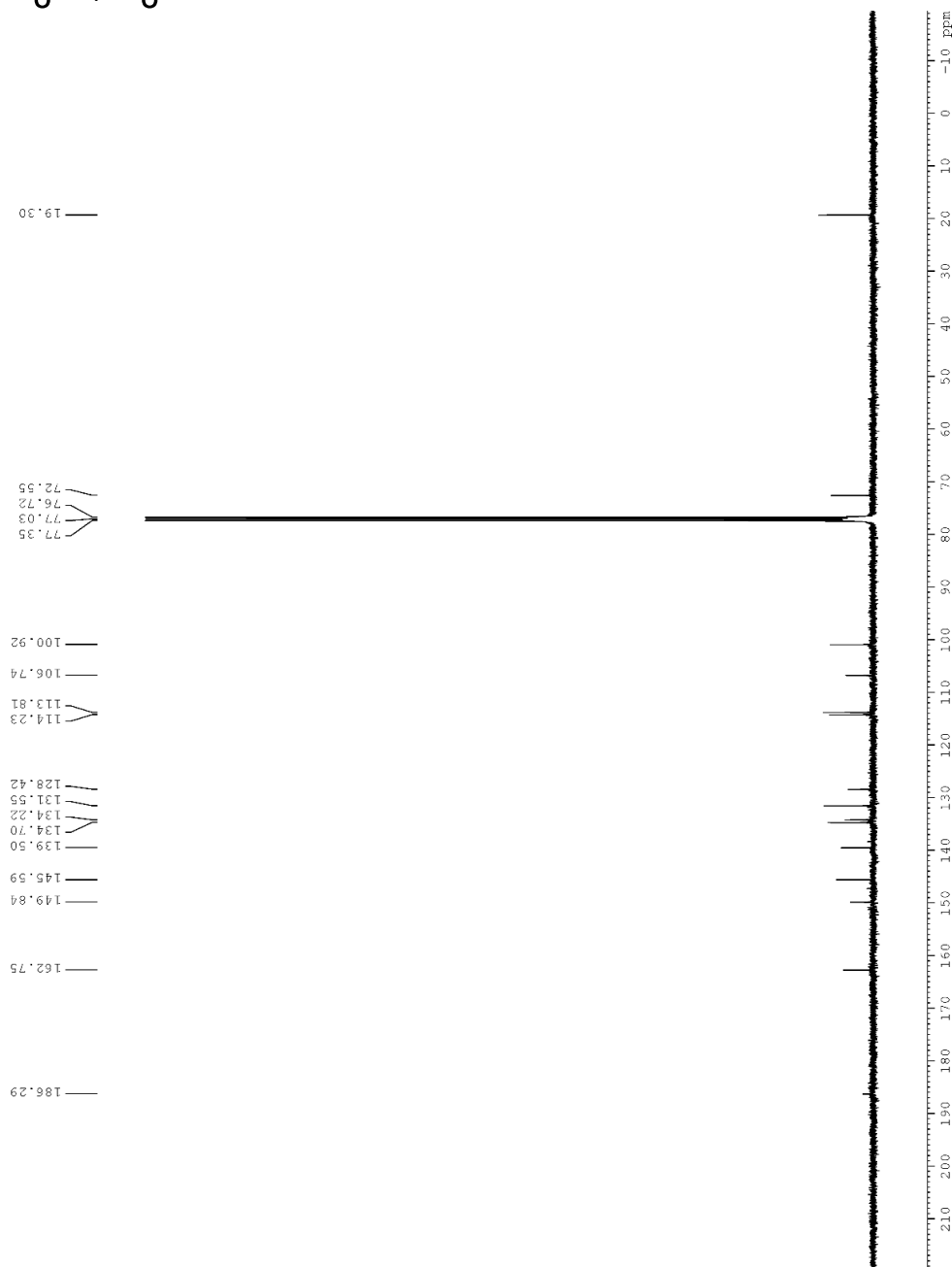
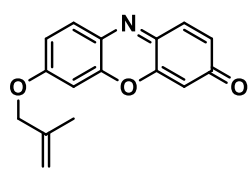




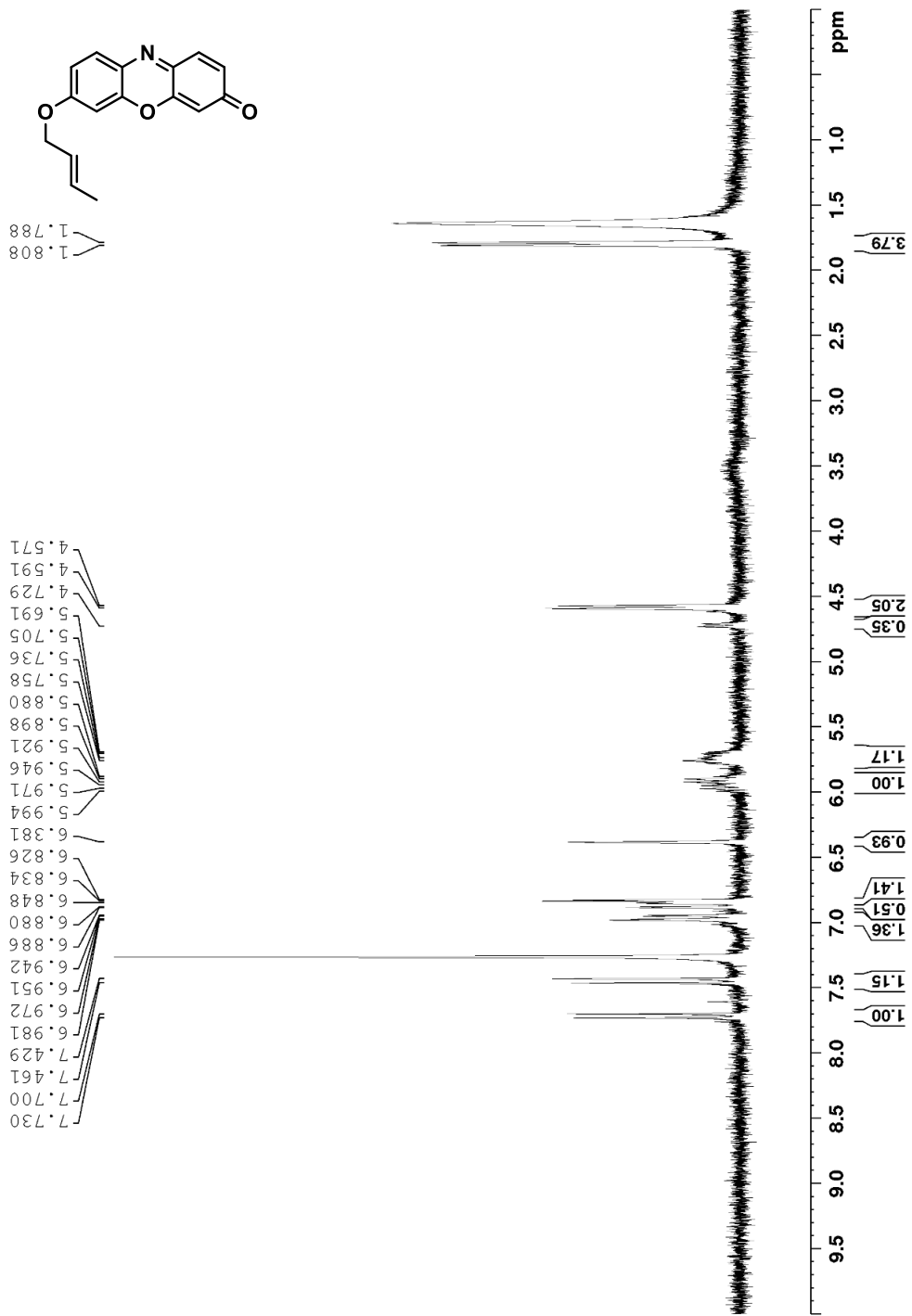
Spectrum 45. ^1H NMR spectrum of (4-methyl-2-oxo-2H-chromen-7-yl)carbamate (400 MHz, CDCl_3 , 293K).

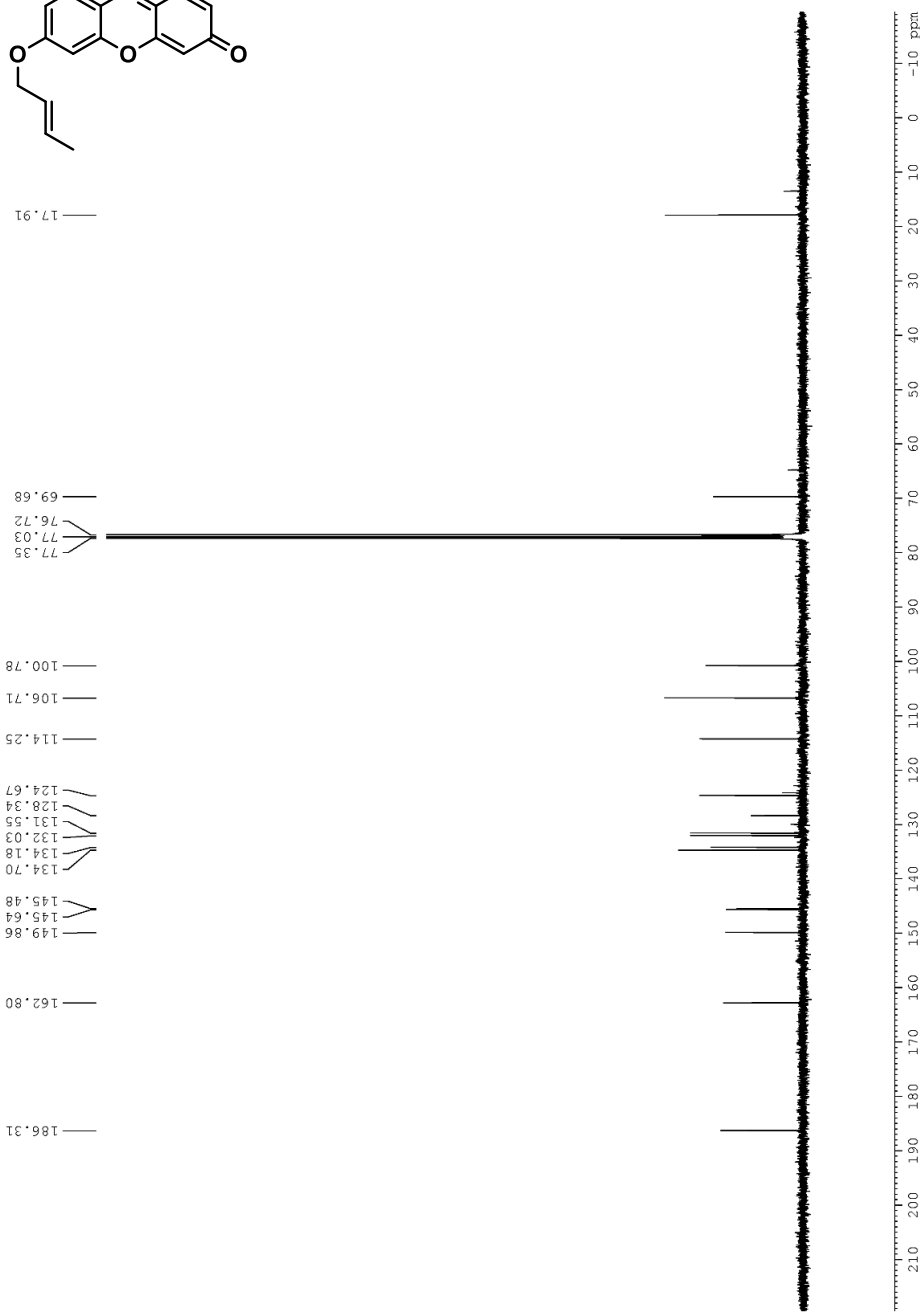
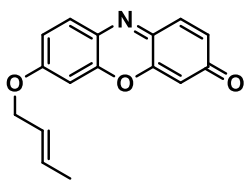


Spectrum 46. ¹H NMR spectrum of 7-((2-methylallyl)oxy)-3H-phenoxazin-3-one (300 MHz, CDCl₃, 293 K).

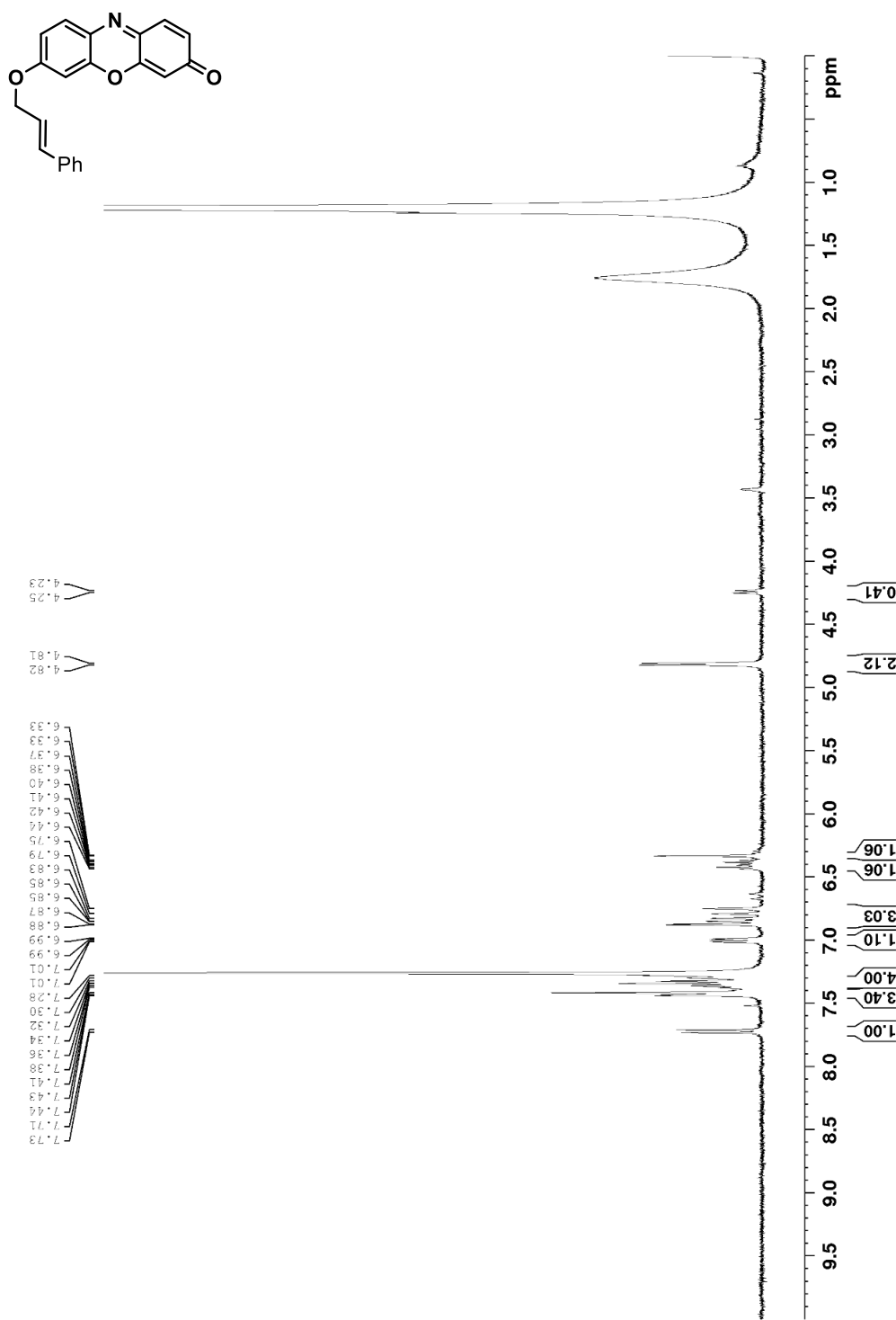


Spectrum 47. ^{13}C NMR of 7-((2-methylallyl)oxy)-3H-phenoxazin-3-one (100 MHz, CDCl_3 , 293 K).

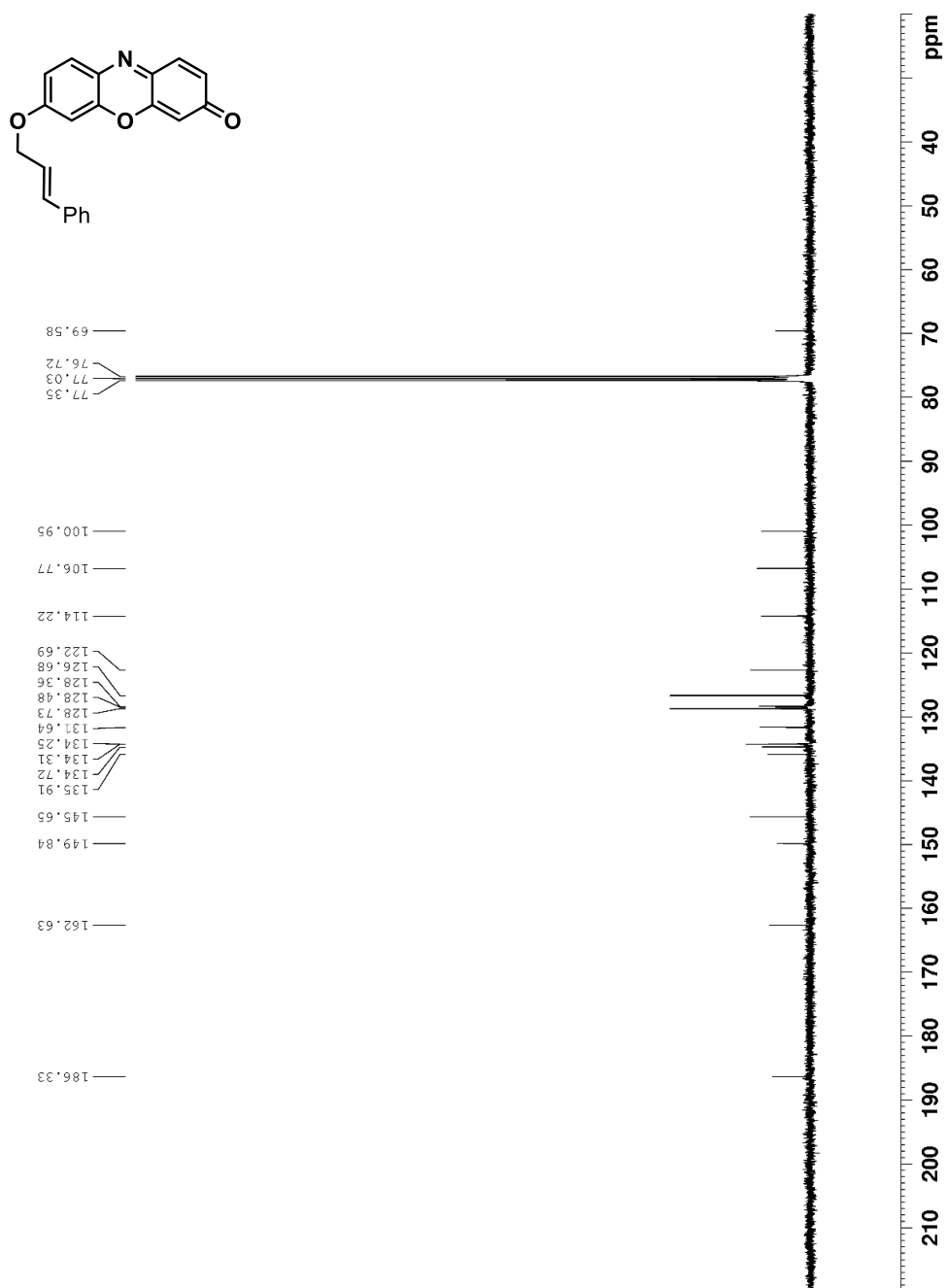




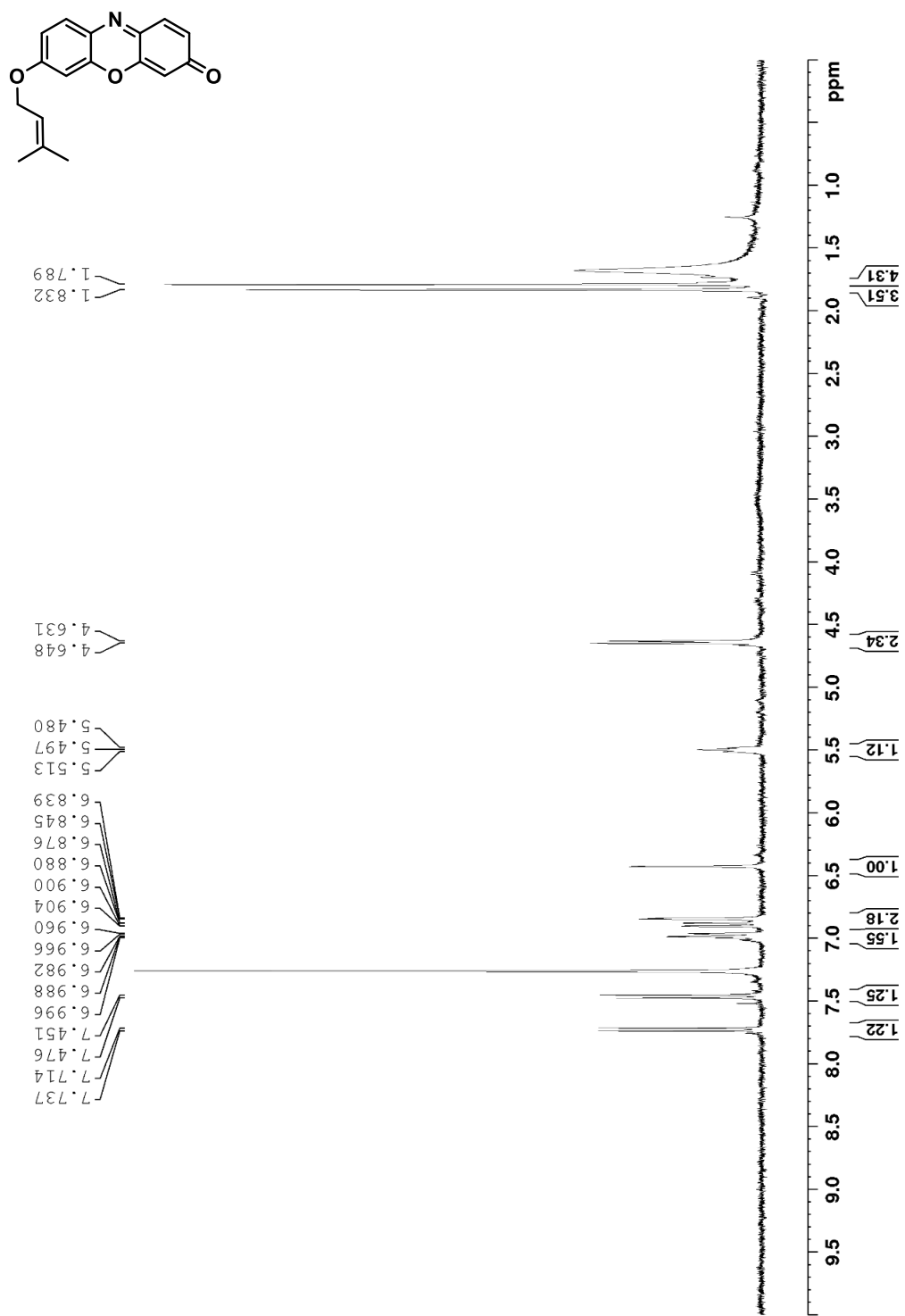
Spectrum 49. ^{13}C NMR of (E)-7-(but-2-en-1-yloxy)-3*H*-phenoxazin-3-one (100 MHz, CDCl_3 , 293 K).



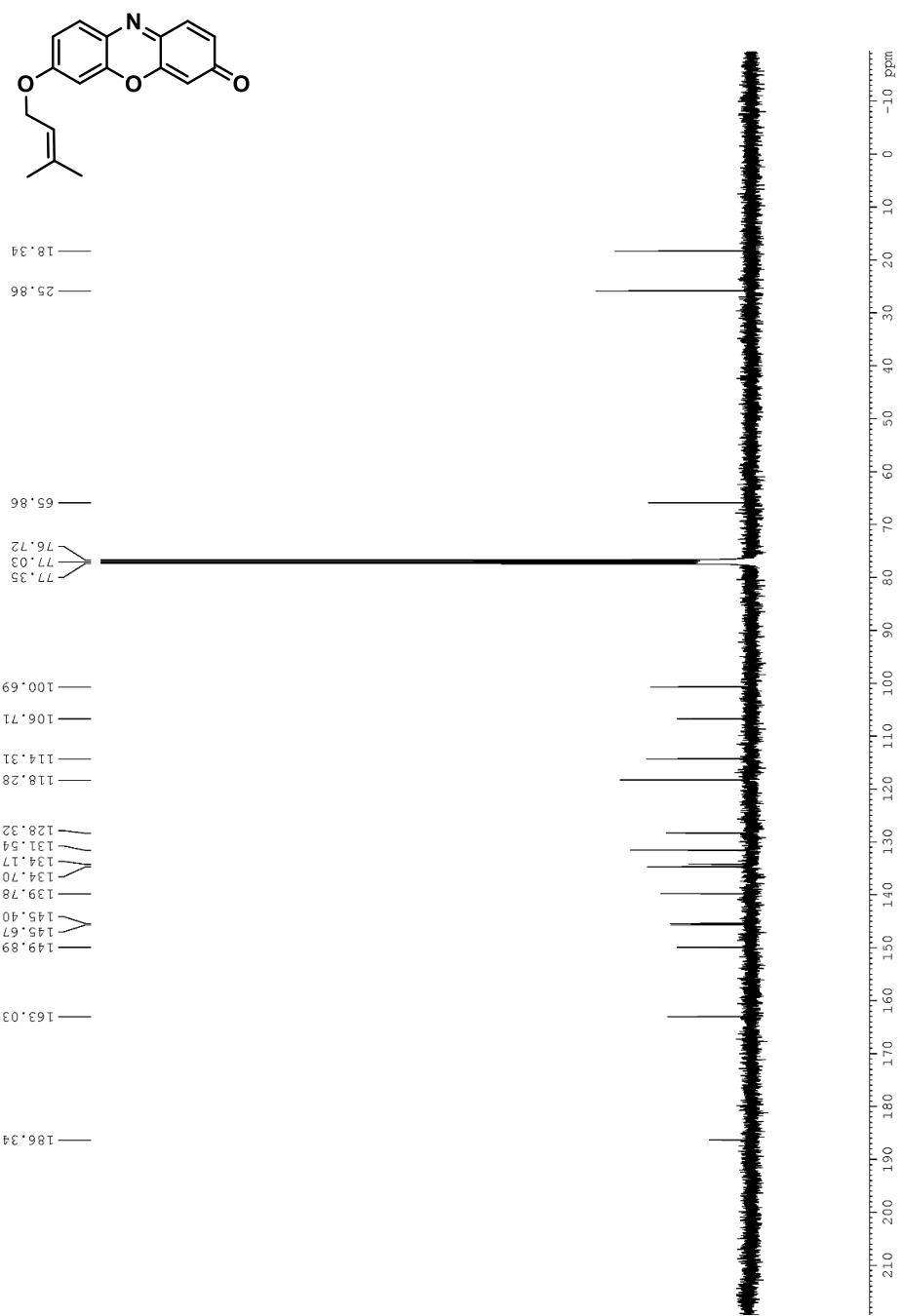
Spectrum 50. ^1H NMR of 7-(cinnamylxyloxy)-3*H*-phenoxazin-3-one (400 MHz, CDCl_3 , 293 K).



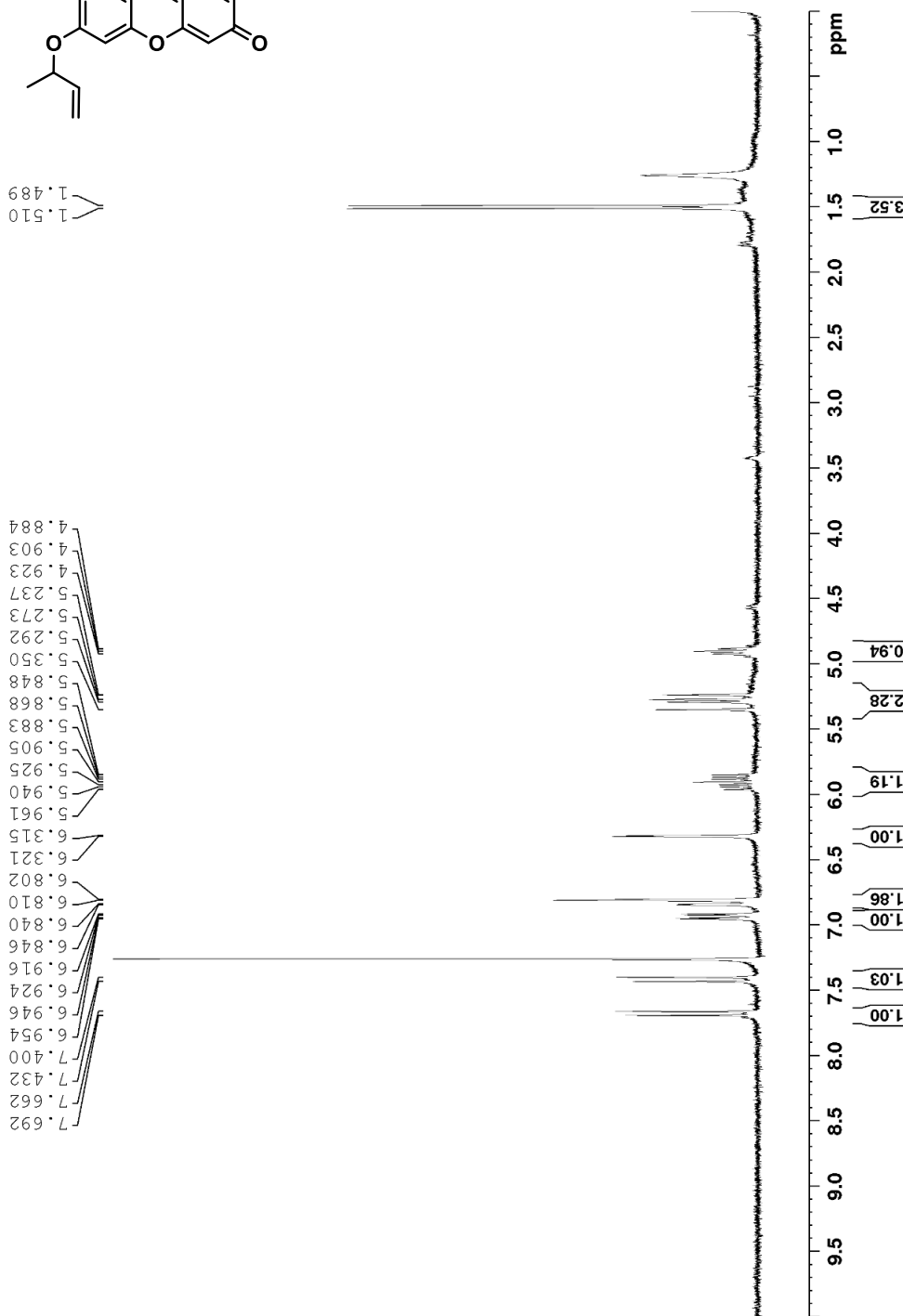
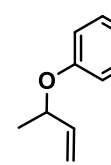
Spectrum 51. ^{13}C NMR of 7-(cinnamylxyloxy)-3*H*-phenoxazin-3-one (100 MHz, CDCl_3 , 293 K).



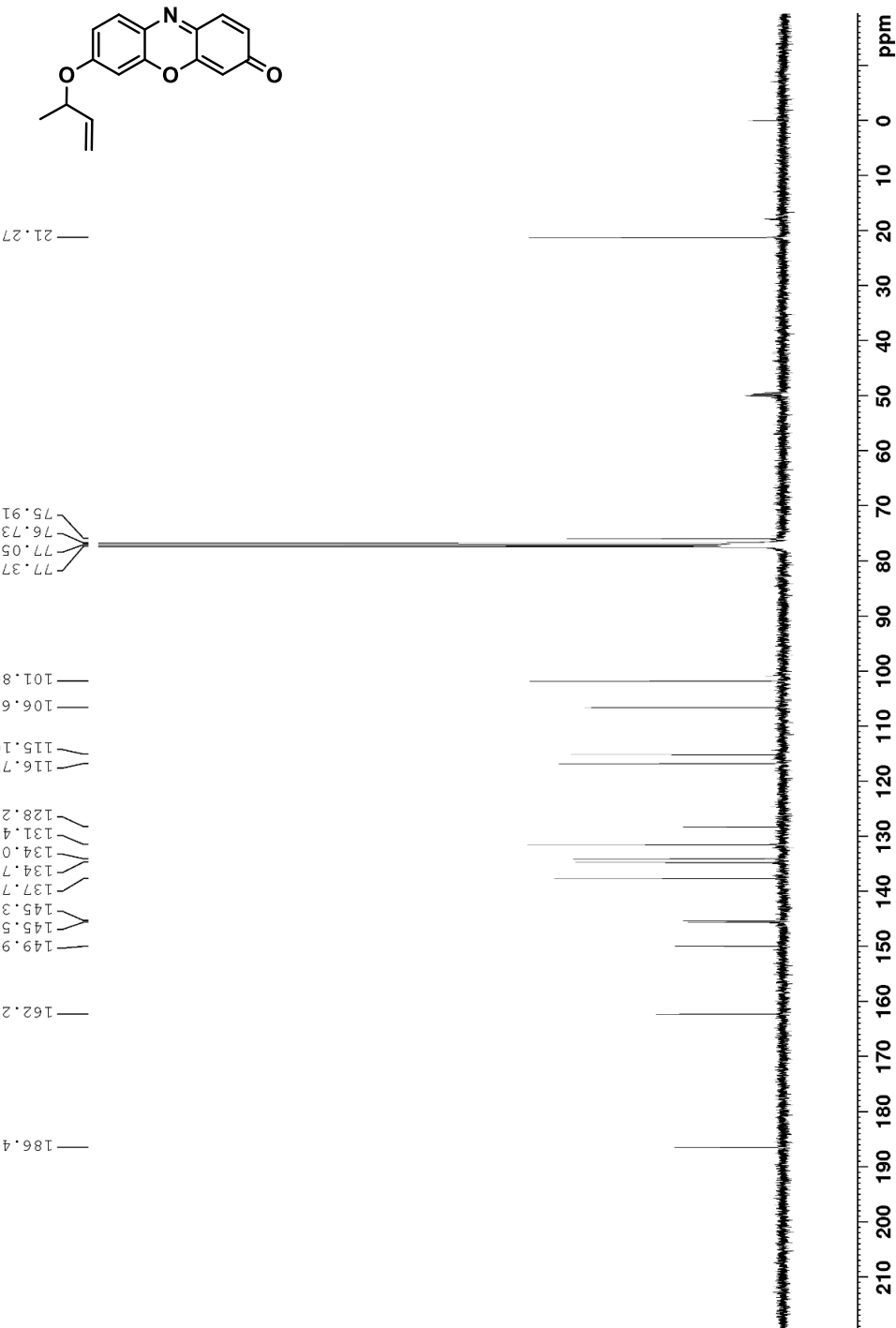
Spectrum 52. ¹H NMR of 7-((3-methylbut-2-en-1-yl)oxy)-3H-phenoxazin-3-one (400 MHz, CDCl₃, 293 K).



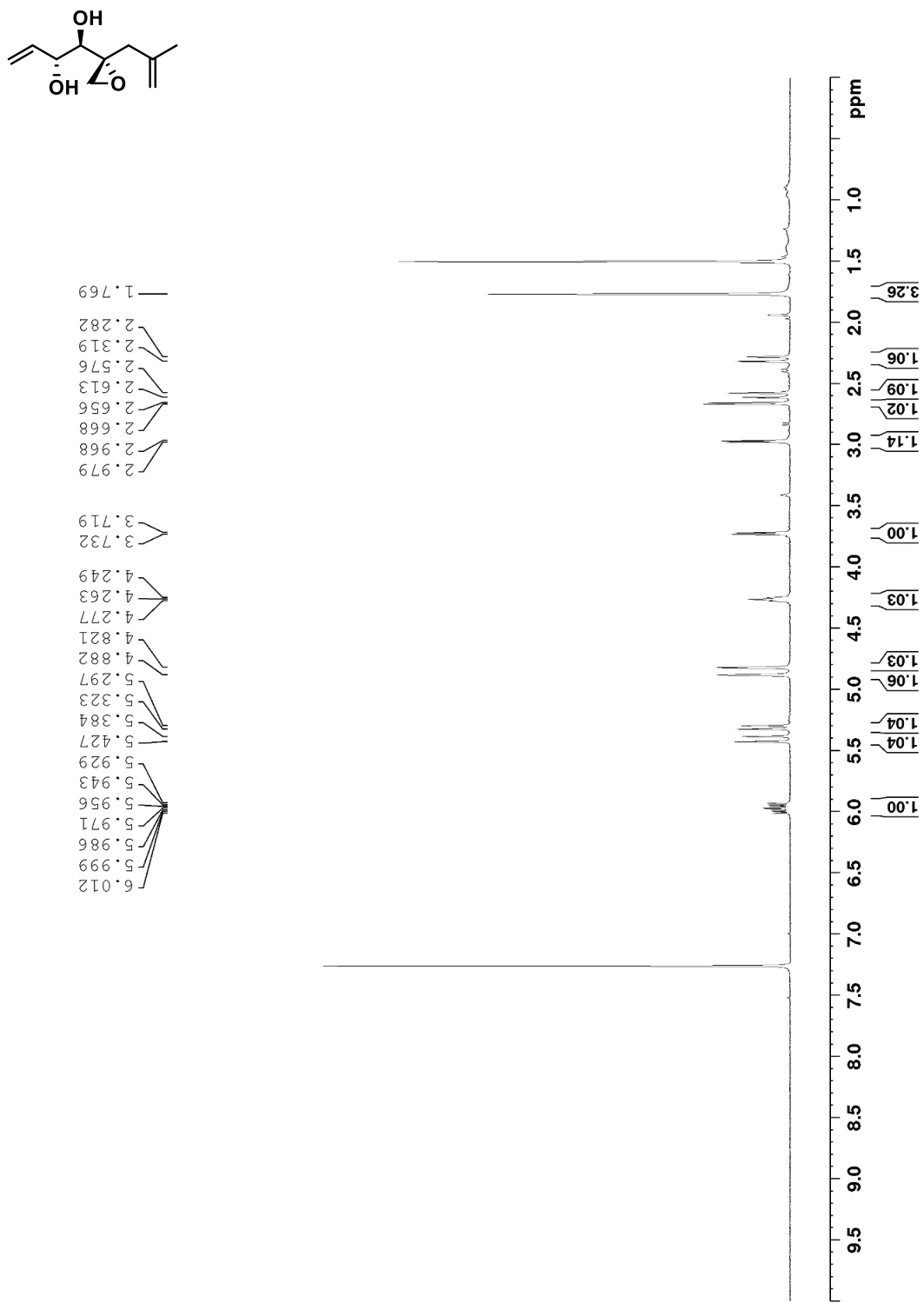
Spectrum 53. ^{13}C NMR of 7-((3-methylbut-2-en-1-yl)oxy)-3H-phenoxazin-3-one (100 MHz, CDCl_3 , 293 K).



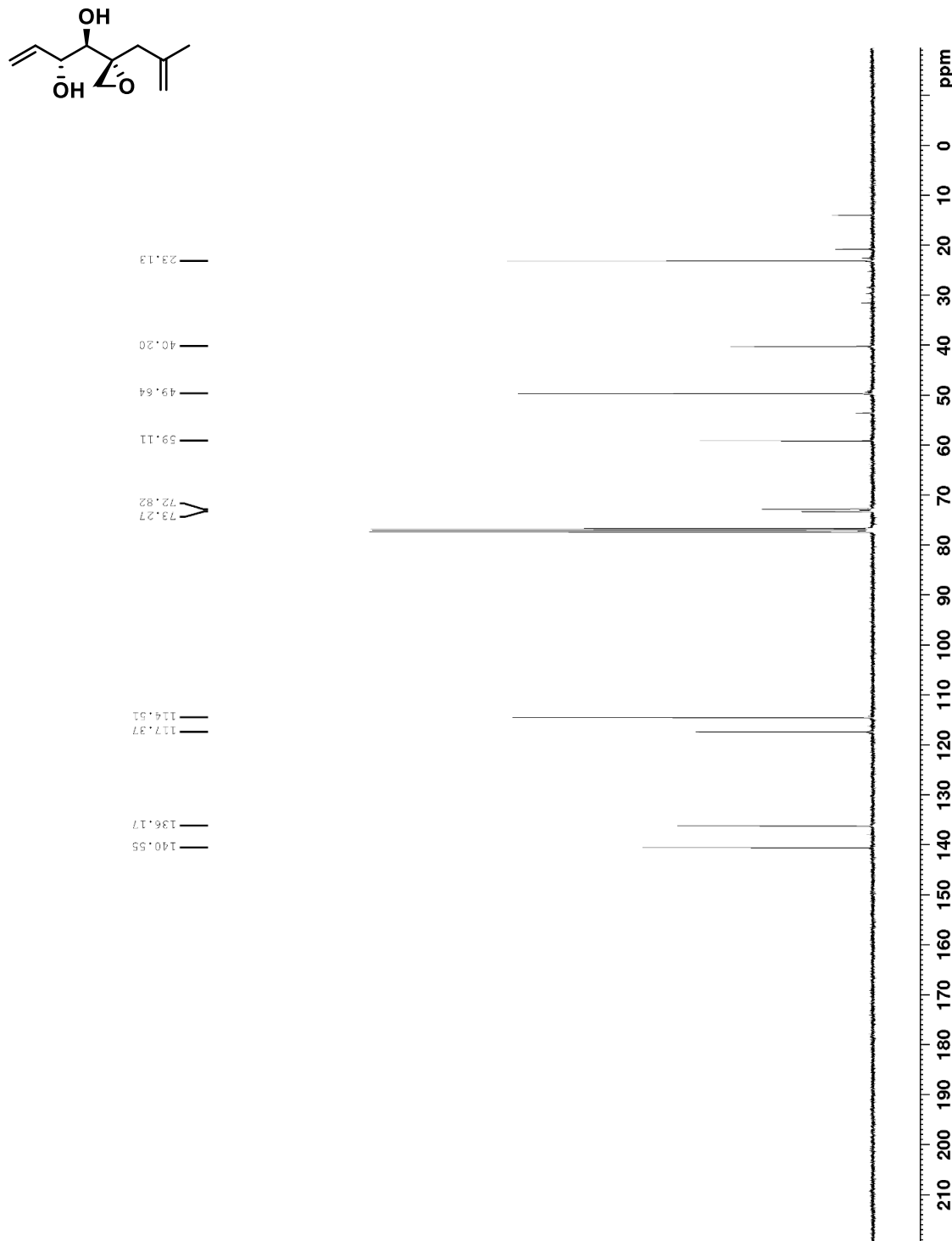
Spectrum 54. ^1H NMR of 7-(but-3-en-2-yloxy)-3*H*-phenoxazin-3-one (300 MHz, CDCl_3 , 293 K).



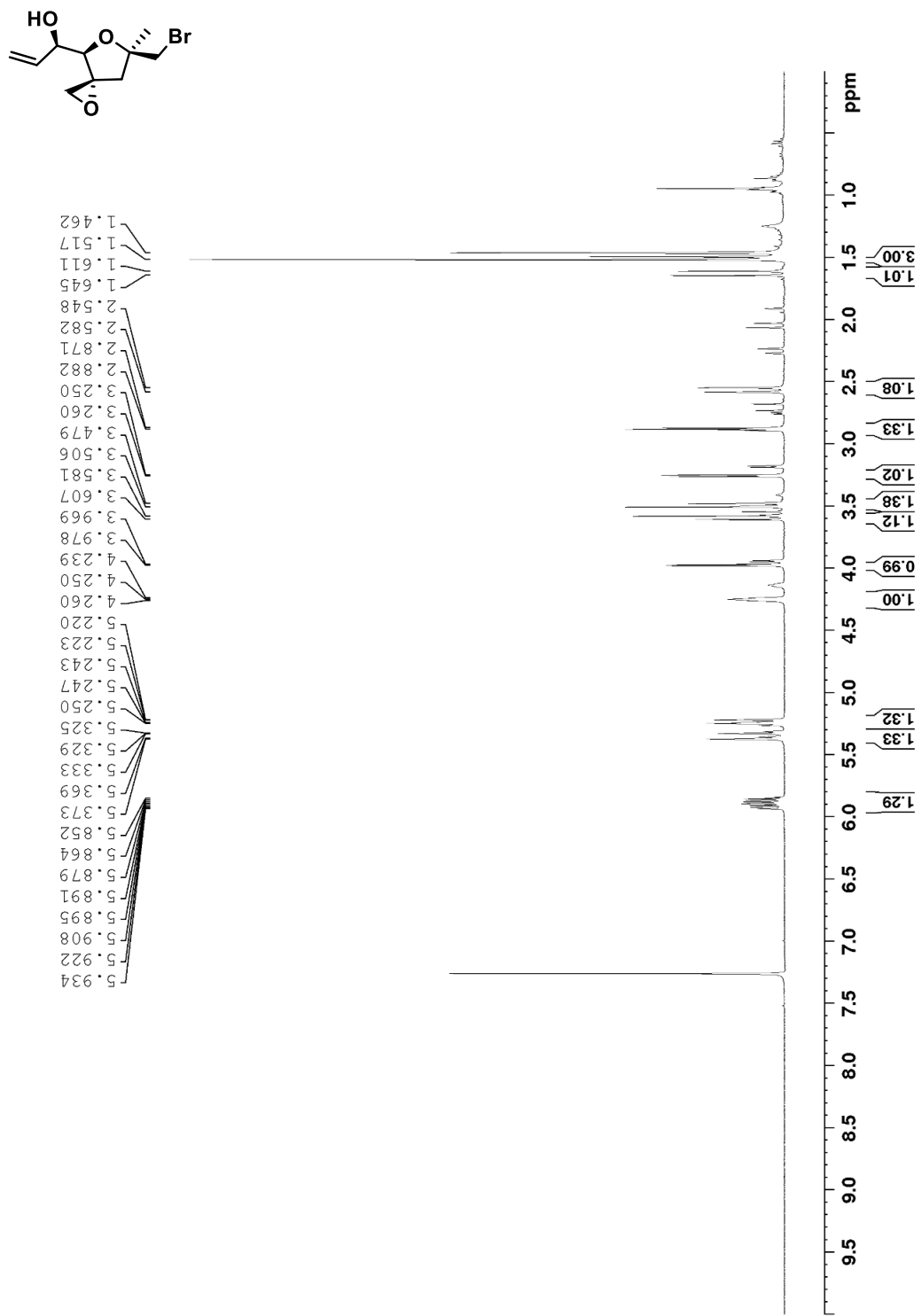
Spectrum 55. ^{13}C NMR of 7-(but-3-en-2-yloxy)-3*H*-phenoxyazin-3-one (100 MHz, CDCl_3 , 293 K).



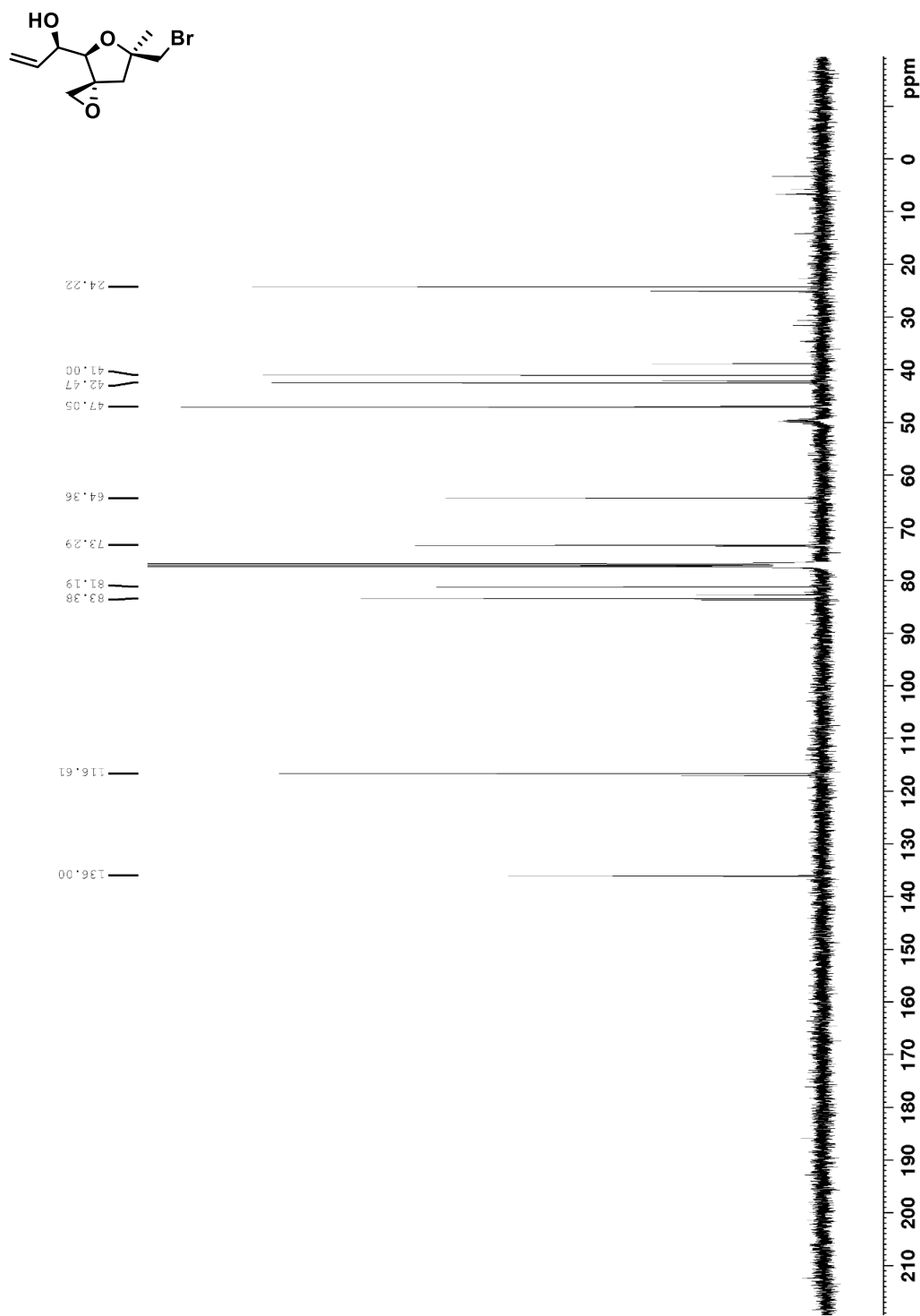
Spectrum 56. ^1H NMR spectrum of (*1R,2R*)-1-((*R*)-2-(2-methylallyl)oxiran-2-yl)but-3-ene-1,2-diol (400 MHz, CDCl_3 , 293K).



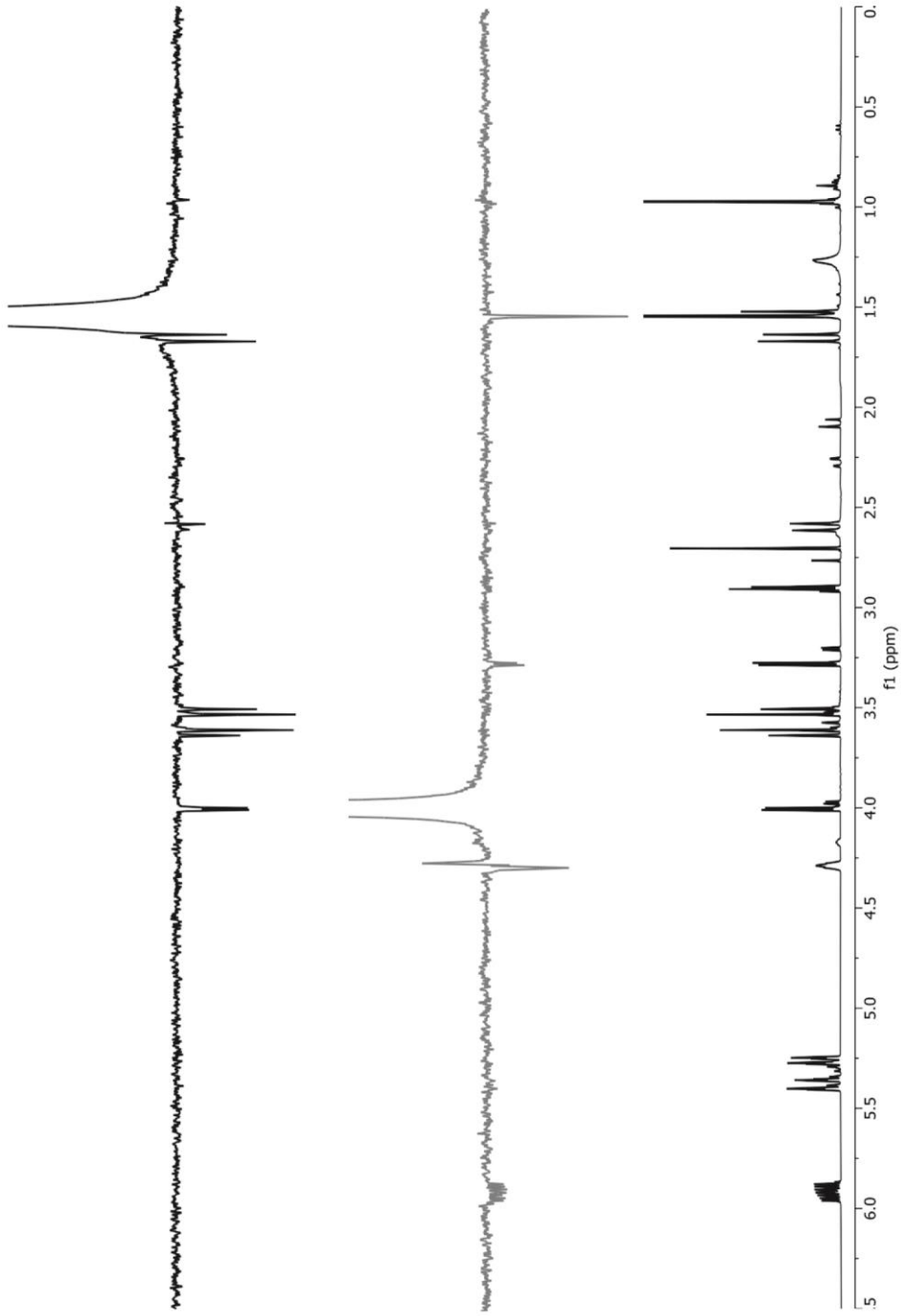
Spectrum 57. ^{13}C NMR spectrum of (*1R,2R*)-1-((*R*)-2-(2-methylallyl)oxiran-2-yl)but-3-ene-1,2-diol (100 MHz, CDCl_3 , 293K).



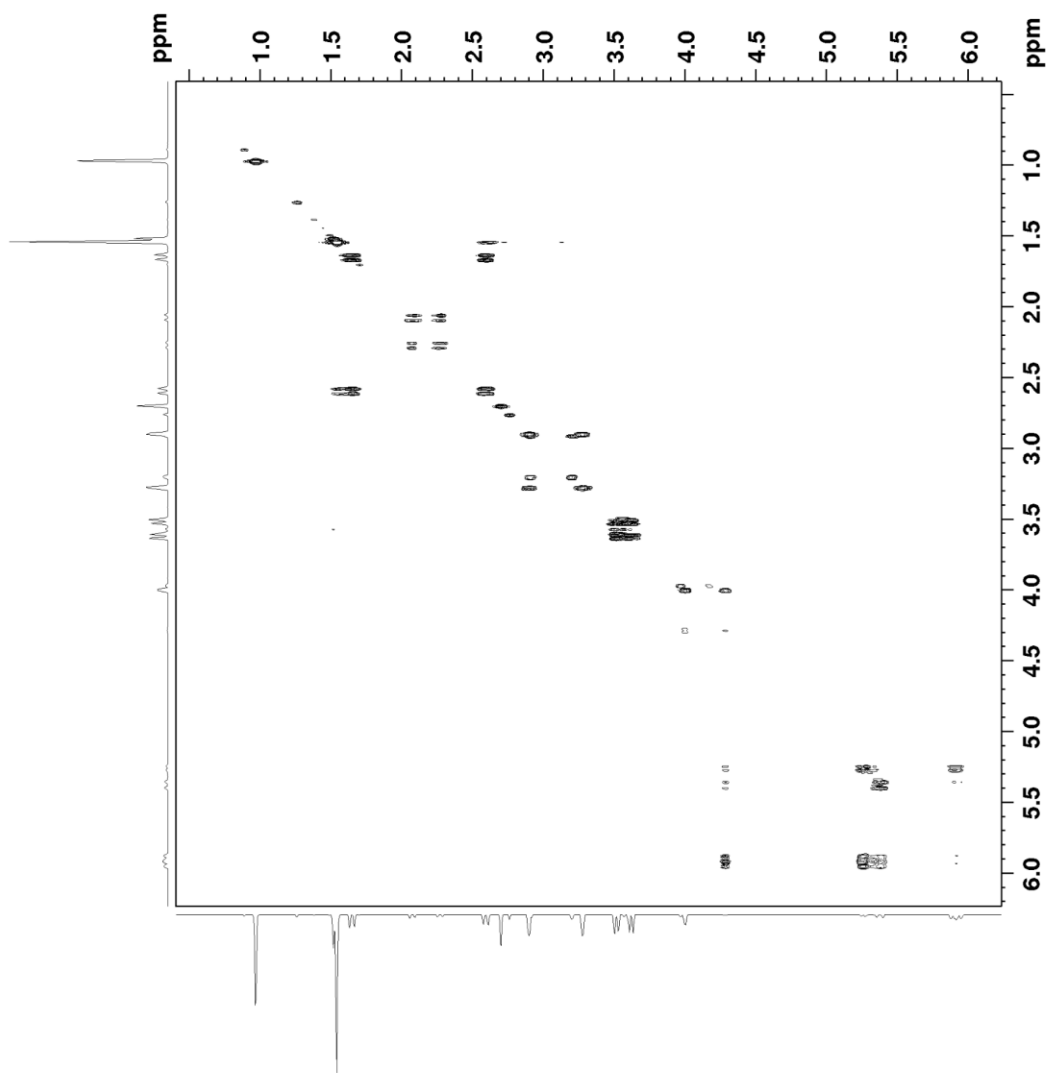
Spectrum 58. . ^1H NMR spectrum of (*R*)-1-((3*R*,4*R*,6*R*)-6-(bromomethyl)-6-methyl-1,5-dioxaspiro[2.4]heptan-4-yl)prop-2-en-1-ol (400 MHz, CDCl_3 , 293K).



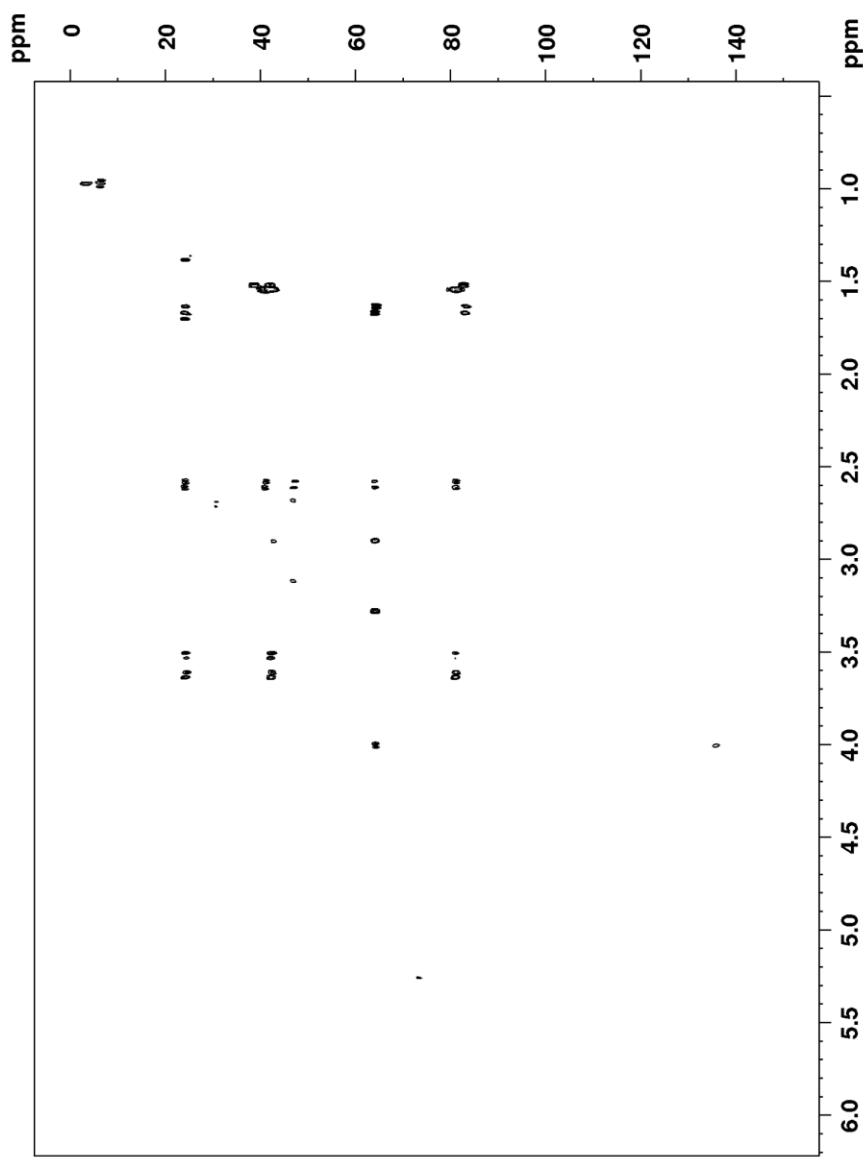
Spectrum 59. ^{13}C NMR spectrum of (*R*)-1-((3*R*,4*R*,6*R*)-6-(bromomethyl)-6-methyl-1,5-dioxaspiro[2.4]heptan-4-yl)prop-2-en-1-ol (100 MHz, CDCl_3 , 293K).



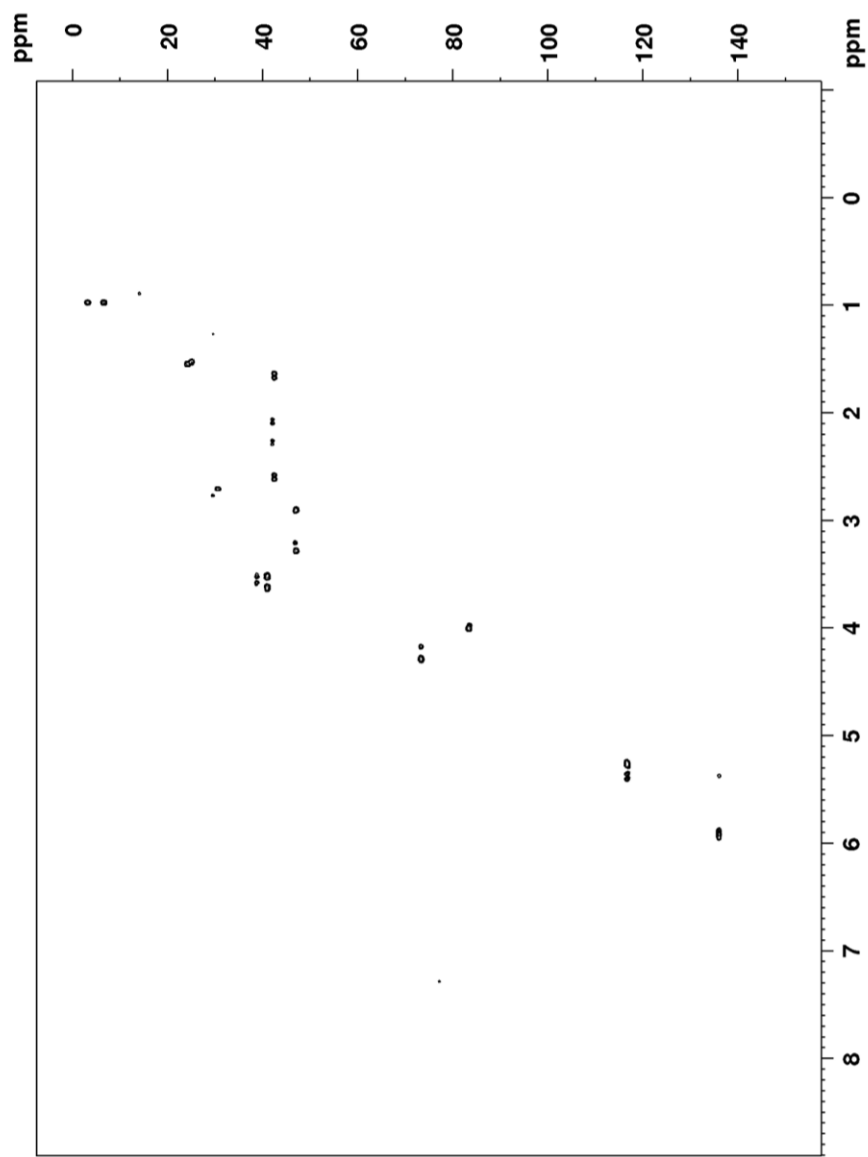
Spectrum 60. NOESY spectrum of (*R*)-1-((3*R*,4*R*,6*R*)-6-(bromomethyl)-6-methyl-1,5-dioxaspiro[2.4]heptan-4-yl)prop-2-en-1-ol (400 MHz, CDCl_3 , 293K).



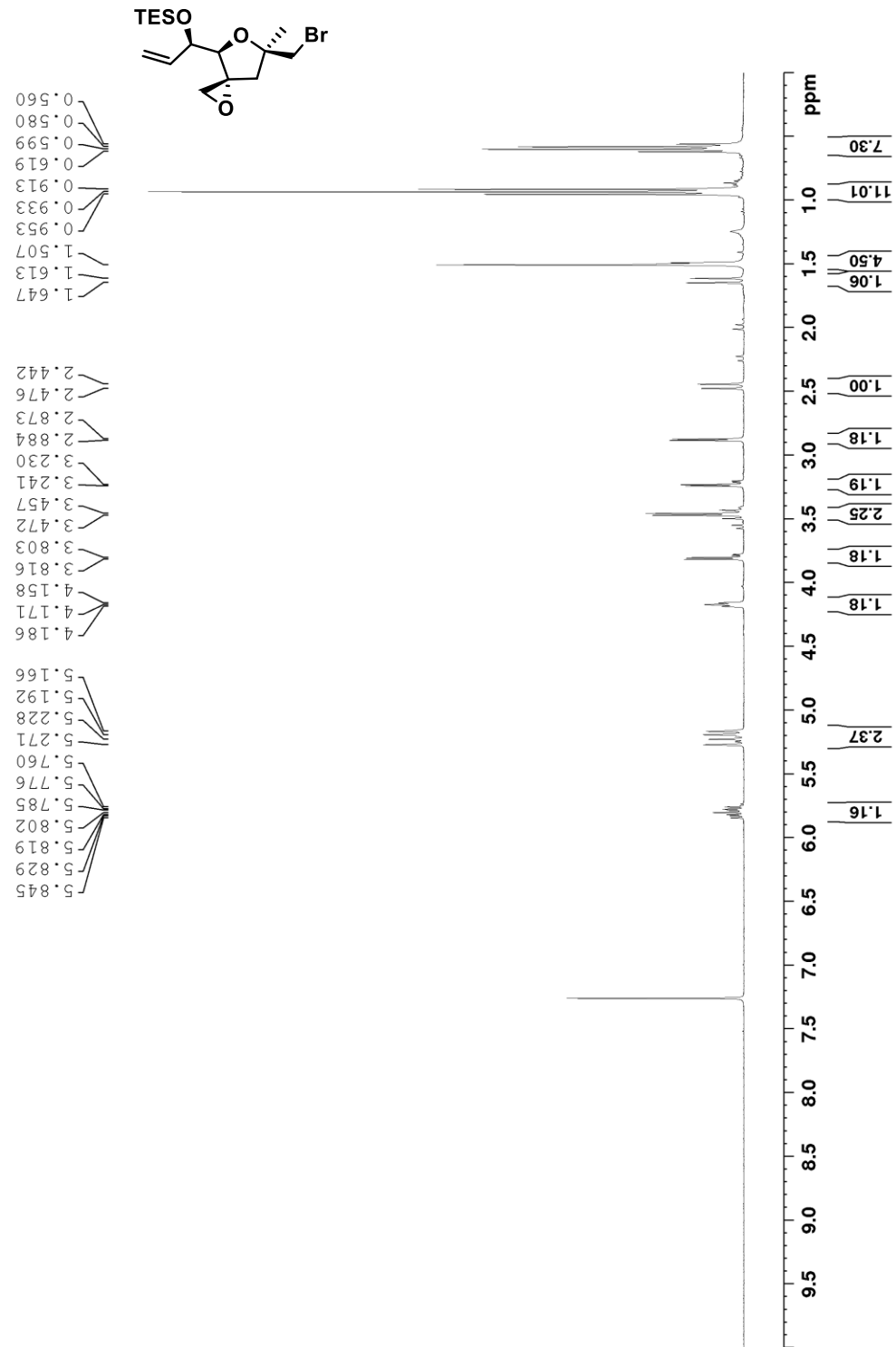
Spectrum 61. COSY spectrum of (*R*)-1-((3*R*,4*R*,6*R*)-6-(bromomethyl)-6-methyl-1,5-dioxaspiro[2.4]heptan-4-yl)prop-2-en-1-ol (400 MHz, CDCl₃, 293K).



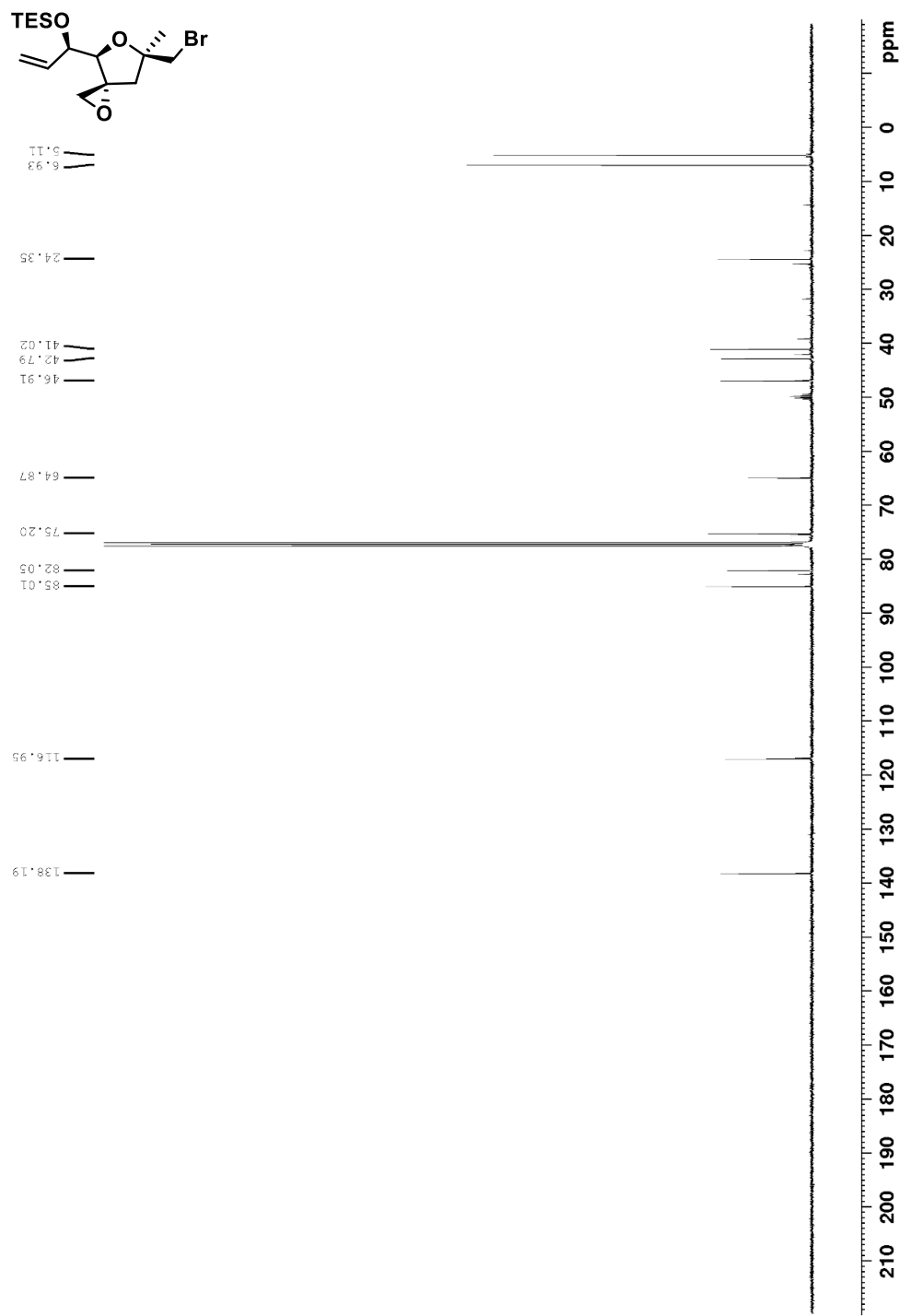
Spectrum 62. HMBC spectrum of (*R*)-1-((3*R*,4*R*,6*R*)-6-(bromomethyl)-6-methyl-1,5-dioxaspiro[2.4]heptan-4-yl)prop-2-en-1-ol (400 MHz, CDCl₃, 293K).



Spectrum 63. HSQC spectrum of (*R*)-1-((3*R*,4*R*,6*R*)-6-(bromomethyl)-6-methyl-1,5-dioxaspiro[2.4]heptan-4-yl)prop-2-en-1-ol (400 MHz, CDCl₃, 293K).

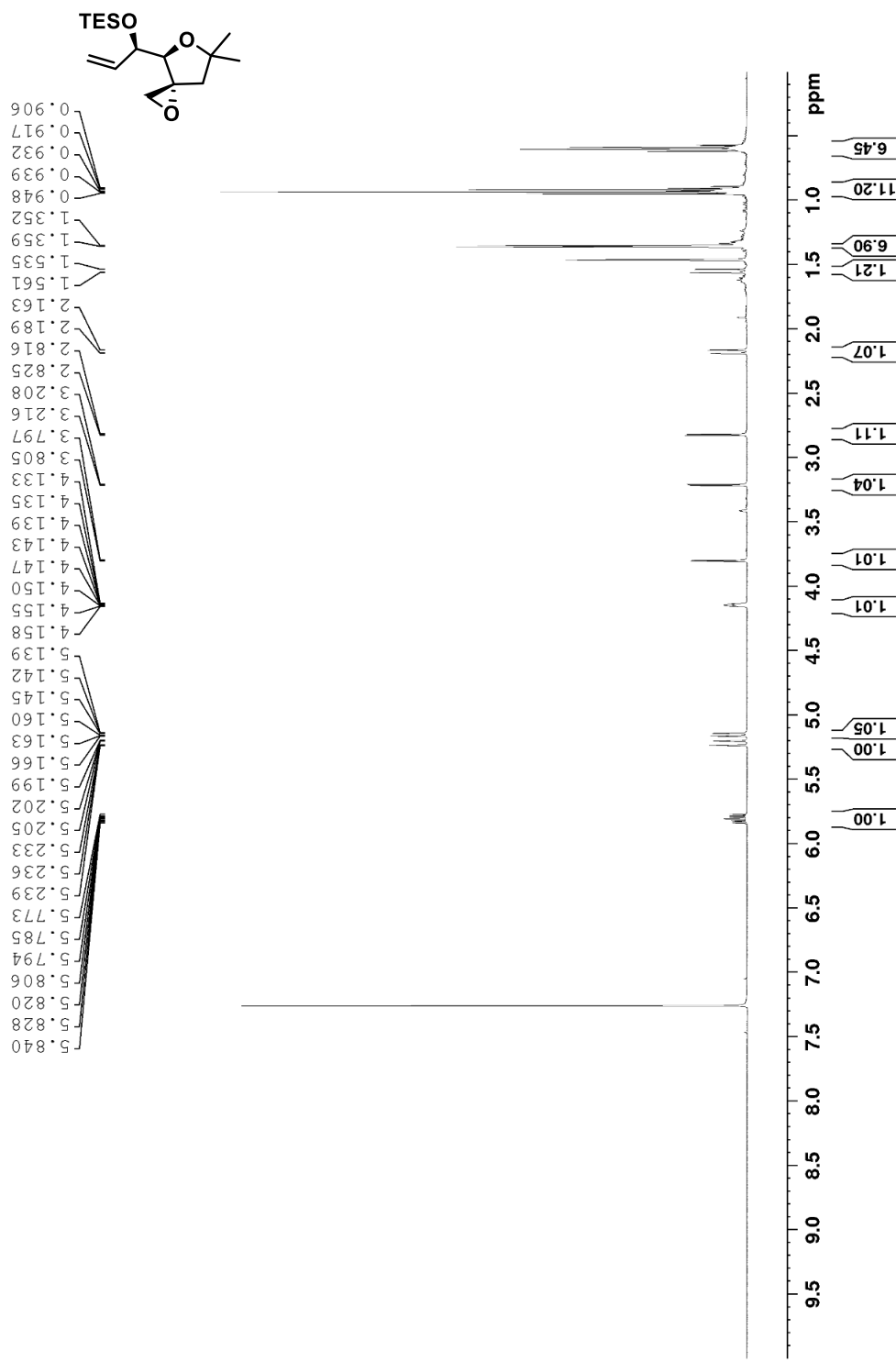


Spectrum 64. ^1H NMR spectrum of $((\text{R})\text{-}1\text{-}((3\text{R},4\text{R},6\text{R})\text{-}6\text{-}(\text{bromomethyl})\text{-}6\text{-methyl}\text{-}1,5\text{-dioxaspiro}[2.4]\text{heptan-4-yl})\text{allyl})\text{oxy})\text{triethylsilane}$ (400 MHz, CDCl_3 , 293K).

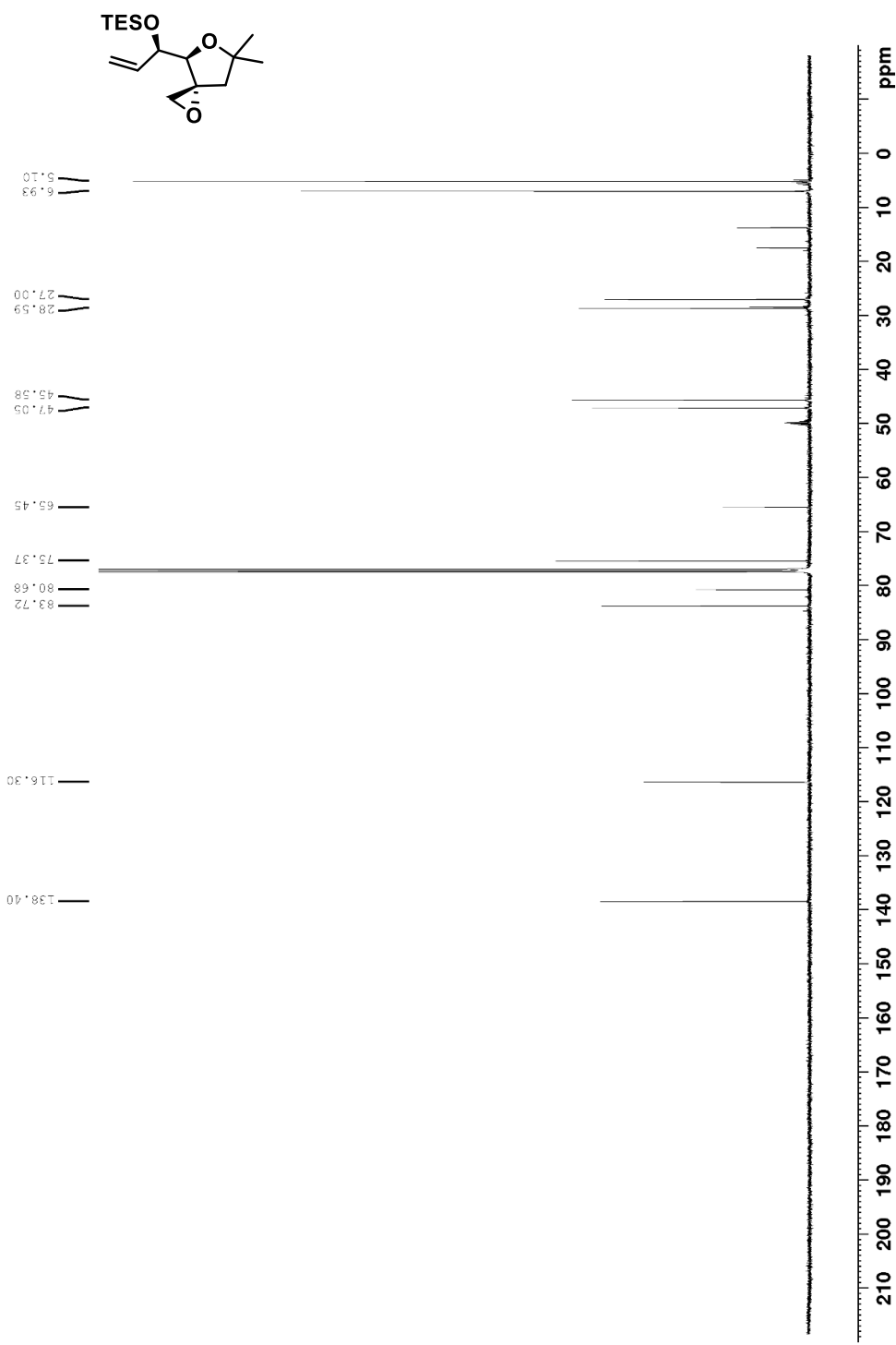


Spectrum 65. ^{13}C NMR spectrum of ((*R*)-1-((3*R*,4*R*,6*R*)-6-(bromomethyl)-6-methyl-1,5-

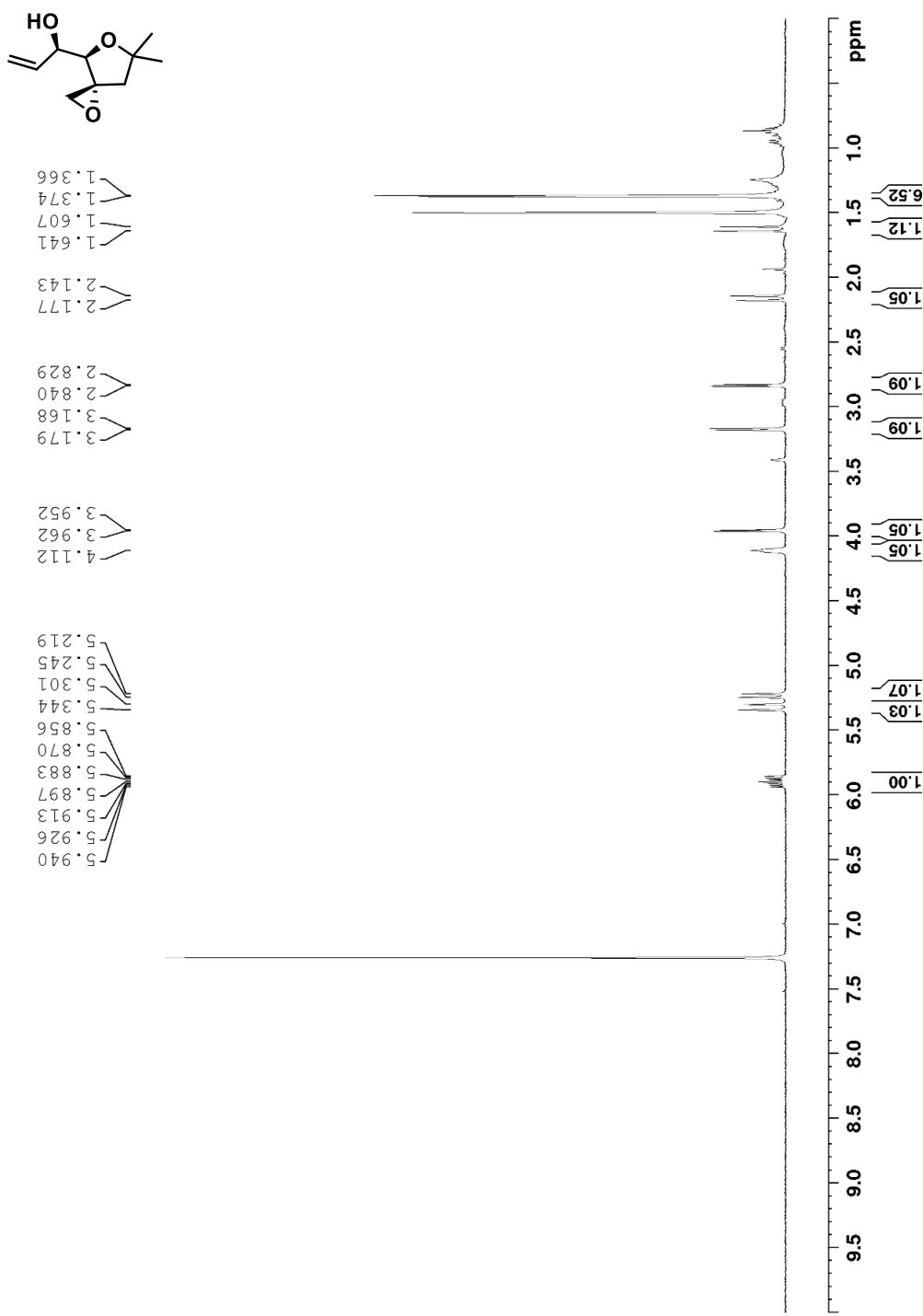
dioxaspiro[2.4]heptan-4-yl)allyl)oxytriethylsilane (100 MHz, CDCl_3 , 293K).



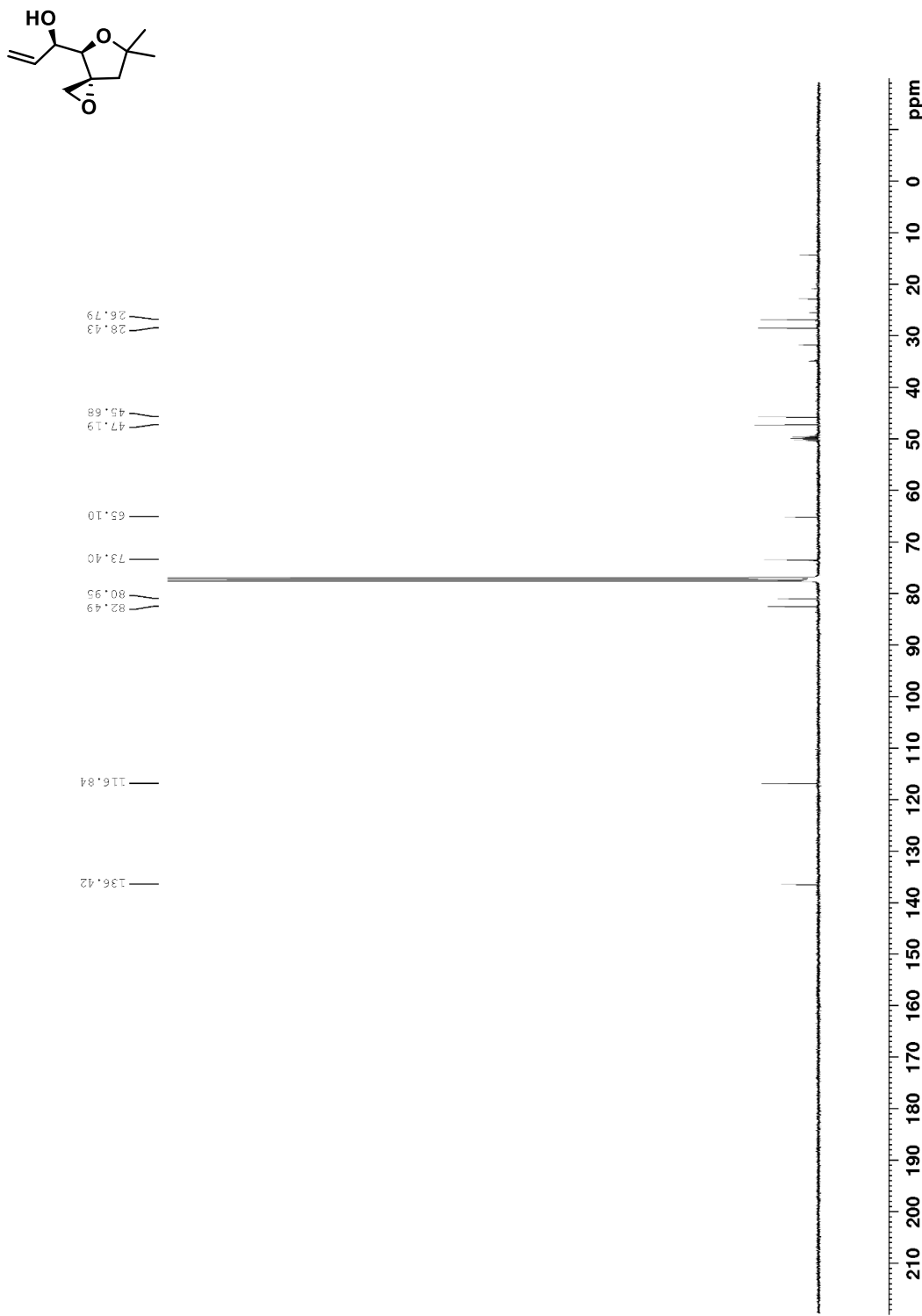
Spectrum 66. ^1H NMR spectrum of (((*R*)-1-((3*R*,4*R*)-6,6-dimethyl-1,5-dioxaspiro[2.4]heptan-4-yl)allyl)oxy)triethylsilane (400 MHz, CDCl_3 , 293K).



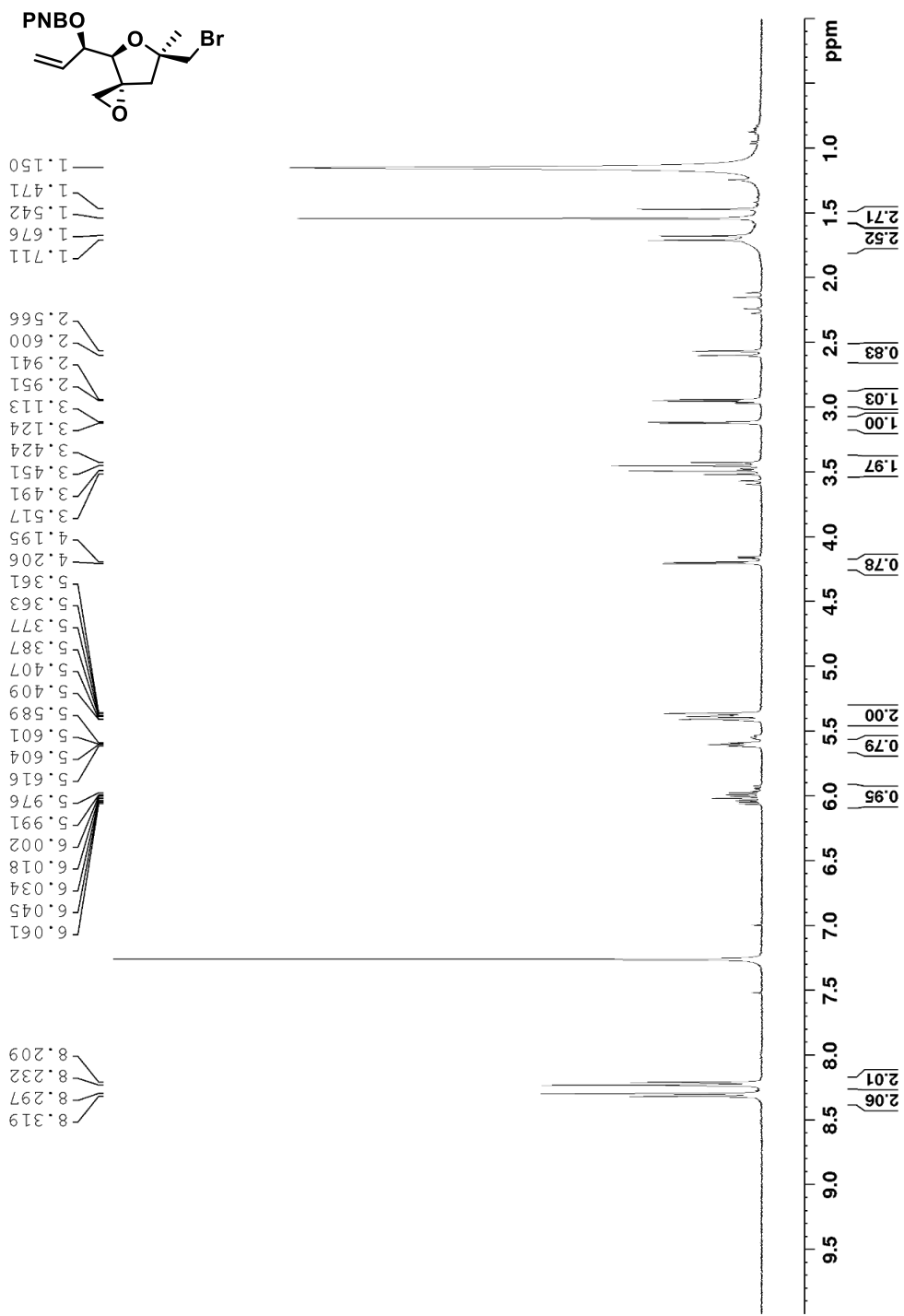
Spectrum 67. ^{13}C NMR spectrum of $((\text{R})\text{-}1\text{-}((3\text{R},4\text{R})\text{-}6,6\text{-dimethyl-}1,5\text{-dioxaspiro}[2.4]\text{heptan-4-yl})\text{allyl})\text{oxytriethylsilane}$ (100 MHz, CDCl_3 , 293K).



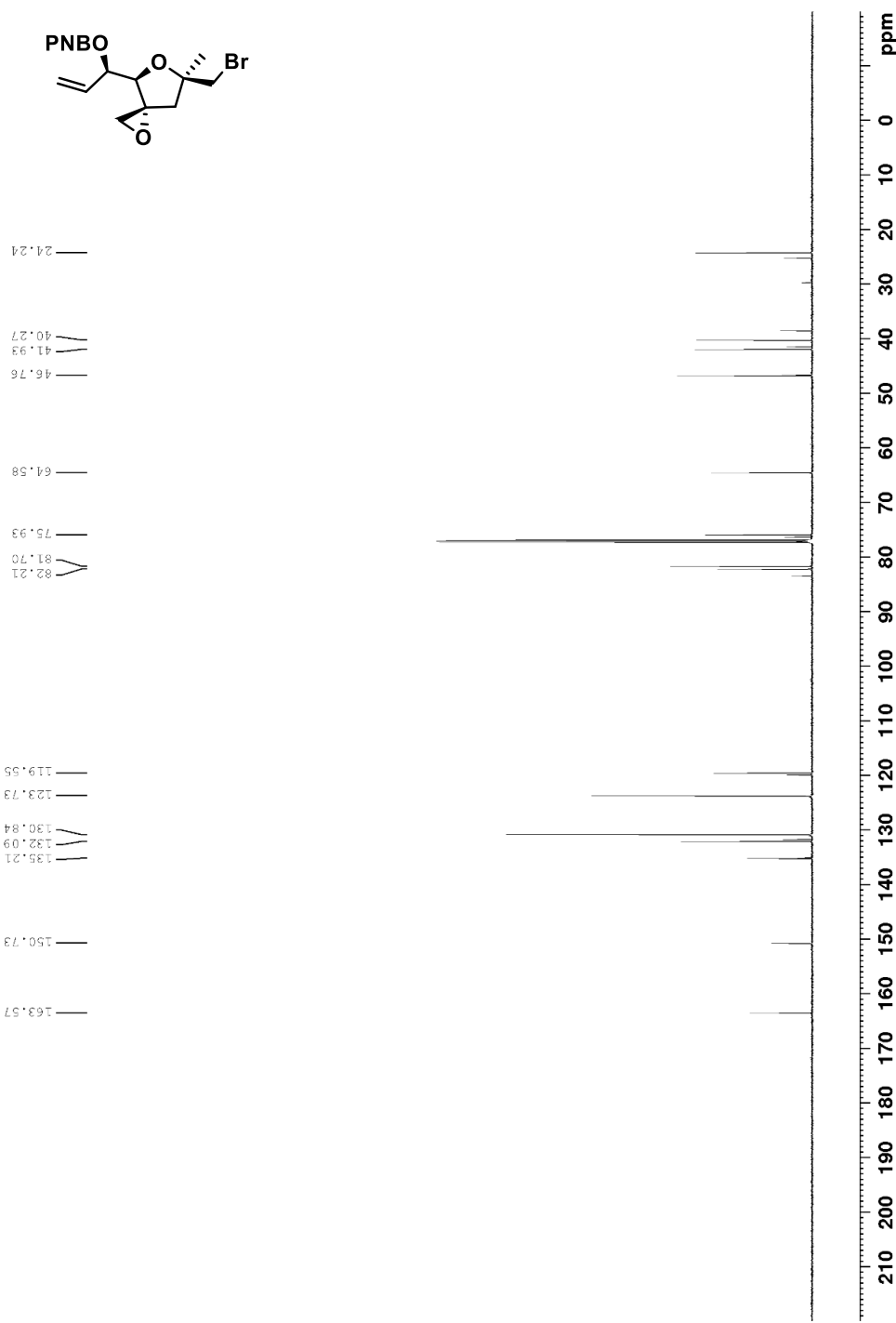
Spectrum 68. ¹H NMR spectrum of (R)-1-((3R,4R)-6,6-dimethyl-1,5-dioxaspiro[2.4]heptan-4-yl)prop-2-en-1-ol (400 MHz, CDCl₃, 293K).



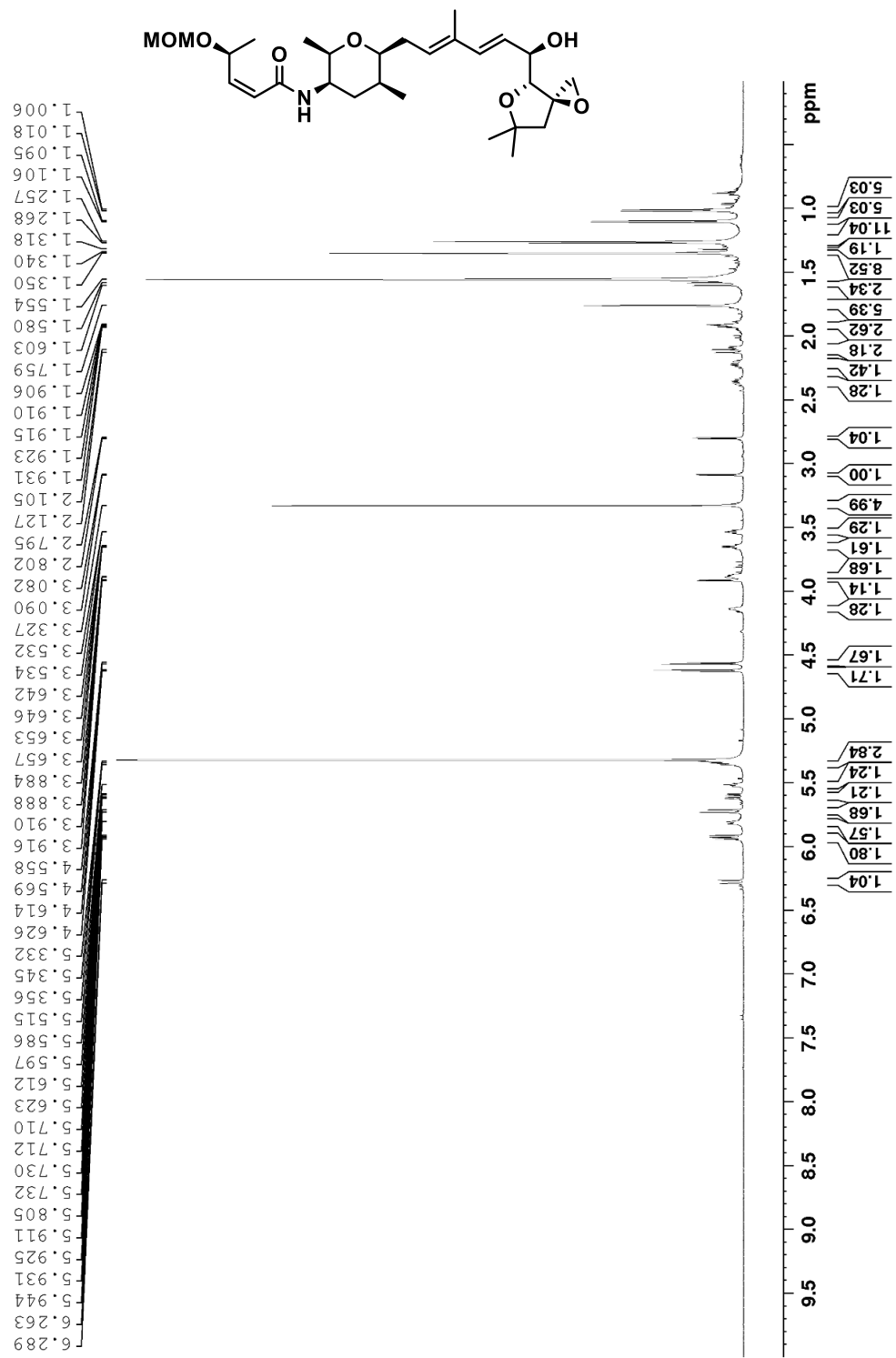
Spectrum 69. ^{13}C NMR spectrum of (*R*)-1-((3*R*,4*R*)-6,6-dimethyl-1,5-dioxaspiro[2.4]heptan-4-yl)prop-2-en-1-ol (100 MHz, CDCl_3 , 293K).



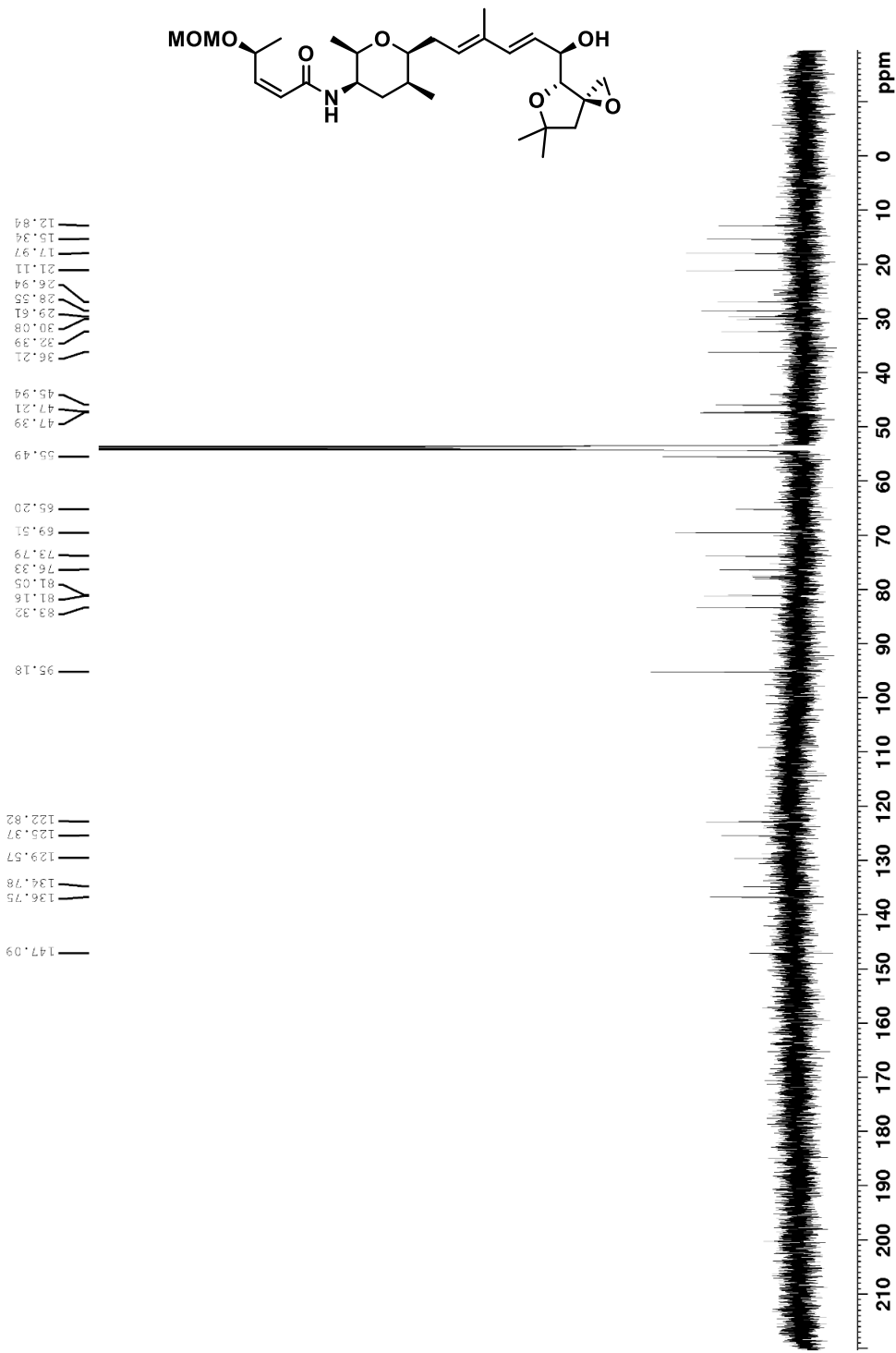
Spectrum 70. ^1H NMR spectrum of (*R*)-1-((3*R*,4*R*,6*R*)-6-(bromomethyl)-6-methyl-1,5-dioxaspiro[2.4]heptan-4-yl)allyl 4-nitrobenzoate (400 MHz, CDCl_3 , 293K).



Spectrum 71. ^{13}C NMR spectrum of (*R*)-1-((3*R*,4*R*,6*R*)-6-(bromomethyl)-6-methyl-1,5-dioxaspiro[2.4]heptan-4-yl)allyl 4-nitrobenzoate (100 MHz, CDCl_3 , 293K).



Spectrum 72. ¹H NMR spectrum of (S,Z)-N-((2R,3R,5S,6S)-6-((R,2E,4E)-6-((3R,4R)-6,6-dimethyl-1,5-dioxaspiro[2.4]heptan-4-yl)-6-hydroxy-3-methylhexa-2,4-dien-1-yl)-2,5-dimethyltetrahydro-2H-pyran-3-yl)-4-(methoxymethoxy)pent-2-enamide (600 MHz, CD₂Cl₂, 293K).



Spectrum 73. ^{13}C NMR spectrum of (*S,Z*)-*N*-((2*R*,3*R*,5*S*,6*S*)-6-((*R*,2*E*,4*E*)-6-((3*R*,4*R*)-6,6-dimethyl-1,5-dioxaspiro[2.4]heptan-4-yl)-6-hydroxy-3-methylhexa-2,4-dien-1-yl)-2,5-dimethyltetrahydro-2*H*-pyran-3-yl)-4-(methoxymethoxy)pent-2-enamide (150 MHz, CD_2Cl_2 , 293K).

Bibliography

- (1) Smidt, J.; Hafner, W.; Jira, R.; Sieber, R.; Sedlmeier, J.; Sabel, A. The Oxidation of Olefins with Palladium Chloride Catalysts. *Angew. Chem., Int. Ed.* **1962**, *1*, 80–88.
- (2) Tsuji, J.; Takahashi, H.; Morikawa, M. Organic Syntheses by Means of Noble Metal Compounds XVII. Reaction of π -Allylpalladium Chloride with Nucleophiles. *Tetrahedron Lett.* **1965**, *6*, 4387–4388.
- (3) Trost, B. M.; Fullerton, T. J. New Synthetic Reactions. Allylic Alkylation. *J. Am. Chem. Soc.* **1973**, *95*, 292–294.
- (4) Trost, B. M.; Crawley, M. L. Asymmetric Transition-Metal-Catalyzed Allylic Alkylations: Applications in Total Synthesis. *Chem. Rev.* **2003**, *103*, 2921–2944.
- (5) Nomura, N.; Tsurugi, K.; Okada, M. Mechanistic Rationale of a Palladium-Catalyzed Allylic Substitution Polymerization—Carbon–Carbon Bond-Forming Polycondensation out of Stoichiometric Control by Cascade Bidirectional Allylation. *Angew. Chem., Int. Ed.* **2001**, *40*, 1932–1935.
- (6) Saitoh, A.; Achiwa, K.; Tanaka, K.; Morimoto, T. Versatile Chiral Bidentate Ligands Derived from A-Amino Acids: Synthetic Applications and Mechanistic Considerations in the Palladium-Mediated Asymmetric Allylic Substitutions. *J. Org. Chem.* **2000**, *65*, 4227–4240.
- (7) Kurosawa, H. Molecular Basis of Catalytic Reactions Involving η^3 -Allyl Complexes of Group 10 Metals as Key Intermediates. *J. Organomet. Chem.* **1987**, *334*, 243–253.
- (8) Trost, B. M.; Van Vranken, D. L. Asymmetric Transition Metal-Catalyzed Allylic Alkylations. *Chem. Rev.* **1996**, *96*, 395–422.
- (9) Kuhn, O.; Mayr, H. Kinetics and Mechanisms of the Reactions of π -Allylpalladium Complexes with Nucleophiles. *Angew. Chem., Int. Ed.* **1999**, *38*, 343–346.
- (10) Andersen, N. G.; Keay, B. A. 2-Furyl Phosphines as Ligands for Transition-Metal-Mediated Organic Synthesis. *Chem. Rev.* **2001**, *101*, 997–1030.
- (11) Trost, B. M.; Kaneko, T.; Andersen, N. G.; Tappertzhofen, C.; Fahr, B. Total Synthesis of Aeruginosin 98b. *J. Am. Chem. Soc.* **2012**, *134*, 18944–18947.
- (12) Evans, L. A.; Fey, N.; Harvey, J. N.; Hose, D.; Lloyd-Jones, G. C.; Murray, P.; Orpen, A. G.; Osborne, R.; Owen-Smith, G. J. J.; Purdie, M. Counterintuitive Kinetics in Tsuji-Trost Allylation: Ion-Pair Partitioning and Implications for Asymmetric Catalysis. *J. Am. Chem. Soc.* **2008**, *130*, 14471–14473.

- (13) Shintani, R.; Tsuji, T.; Park, S.; Hayashi, T. Mechanistic Investigation of the Palladium-Catalyzed Decarboxylative Cyclization of Γ -Methylidene- Δ -Valerolactones with Isocyanates: Kinetic Studies and Origin of the Site Selectivity in the Nucleophilic Attack at a (π -Allyl)Palladium. *J. Am. Chem. Soc.* **2010**, *132*, 7508–7513.
- (14) Negishi, E.; de Meijere, A., *Handbook of Organopalladium Chemistry for Organic Synthesis, 2 Volume Set*. Wiley: 2003.
- (15) Malmberg, C. G.; Maryott, A. A. Dielectric Constant of Water from 0 °C to 100 °C. *J. Res. Nat. Bur. Stand.* **1956**, *56*, 1–8.
- (16) Baeyer, A.; Villiger, V. Einwirkung Des Caro'schen Reagens Auf Ketone. *Ber. Dtsch. Chem. Ges.* **1899**, *32*, 36253633.
- (17) Hofmann, A. W. Ueber Die Einwirkung Des Broms in Alkalischer Lösung Auf Amide. *Chem. Ber.* **1881**, *14*, 2725–2736.
- (18) Wolff, L.; Krüche, R. Über Diazoanhydride (1,2,3-Oxydiazole Oder Diazoxyde) Und Diazoketone. *Liebigs Ann. Chem.* **1912**, *394*, 23–59.
- (19) Buchner, E.; Curtius, T. Synthese Von Ketonsäureäthern Aus Aldehyden Und Diazoessigäther. *Chem. Ber.* **1885**, *18*, 2371–2377.
- (20) Rideout, D. C.; Breslow, R. Hydrophobic Acceleration of Diels-Alder Reactions. *J. Am. Chem. Soc.* **1980**, *102*, 7816–7817.
- (21) Narayan, S.; Muldoon, J.; Finn, M. G.; Fokin, V. V.; Kolb, H. C.; Sharpless, K. B. “On Water”: Unique Reactivity of Organic Compounds in Aqueous Suspension. *Angew. Chem. Int., Ed.* **2005**, *44*, 3275–3279.
- (22) Hang, H. C.; Yu, C.; Kato, D. L.; Bertozzi, C. R. A Metabolic Labeling Approach toward Proteomic Analysis of Mucin-Type O-Linked Glycosylation. *Proc. Natl. Acad. Sci. U. S. A.* **2003**, *100*, 14846–14851.
- (23) Bertozzi, C. R. A Decade of Bioorthogonal Chemistry. *Acc. Chem. Res.* **2011**, *44*, 651–653.
- (24) Sletten, E. M.; Bertozzi, C. R. Bioorthogonal Chemistry: Fishing for Selectivity in a Sea of Functionality. *Angew. Chem., Int. Ed.* **2009**, *48*, 6974–6998.
- (25) Kinoshita, H.; Shinokubo, H.; Oshima, K. Water Enables Direct Use of Allyl Alcohol for Tsuji–Trost Reaction without Activators. *Org. Lett.* **2004**, *6*, 4085–4088.
- (26) Genet, J. P.; Blart, E.; Savignac, M. Palladium-Catalyzed Cross-Coupling Reactions in a Homogeneous Aqueous Medium. *Synlett* **1992**, *1992*, 715–717.

- (27) Sigismondi, S.; Sinou, D.; Pérez, M.; Moreno-Mañas, M.; Pleixats, R.; Villarroya, M. Palladium(0)-Catalyzed Allylation of Uracils and 2-Thiouracils Drastic Effect of an Aqueous Reaction Medium on the Regioselectivity. *Tetrahedron Lett.* **1994**, *35*, 7085–7088.
- (28) Gao, S.; Liu, H.; Wu, Z.; Yao, H.; Lin, A. Palladium-Catalyzed Allylic Alkylation with Internal Alkynes to Construct C–C and C–N Bonds in Water. *Green Chem.* **2017**, *19*, 1861–1865.
- (29) Llevot, A.; Monney, B.; Sehlinger, A.; Behrens, S.; Meier, M. A. R. Highly Efficient Tsuji–Trost Allylation in Water Catalyzed by Pd-Nanoparticles. *Chem. Commun.* **2017**, *53*, 5175–5178.
- (30) Fumiuki, O.; Akihiko, K.; Tamio, H. Generation of Tertiary Phosphine-Coordinated Pd(0) Species from Pd(OAc)₂ in the Catalytic Heck Reaction. *Chem. Lett.* **1992**, *21*, 2177–2180.
- (31) Mason, M. R.; Verkade, J. G. Fluoride-Induced Reduction of Palladium(II) and Platinum(II) Phosphine Complexes. *Organometallics* **1992**, *11*, 2212–2220.
- (32) Wei, C. S.; Davies, G. H. M.; Soltani, O.; Albrecht, J.; Gao, Q.; Pathirana, C.; Hsiao, Y.; Tummala, S.; Eastgate, M. D. The Impact of Palladium(II) Reduction Pathways on the Structure and Activity of Palladium(0) Catalysts. *Angew. Chem., Int. Ed.* **2013**, *52*, 5822–5826.
- (33) Grushin, V. V. Catalysis for Catalysis: Synthesis of Mixed Phosphine–Phosphine Oxide Ligands Via Highly Selective, Pd-Catalyzed Monooxidation of Bidentate Phosphines. *J. Am. Chem. Soc.* **1999**, *121*, 5831–5832.
- (34) McLaughlin, P. A.; Verkade, J. G. Fluoride-Catalyzed Reduction of Palladium(II) to Palladium(0)–Phosphine Complexes. *Organometallics* **1998**, *17*, 5937–5940.
- (35) Schunn, R. A. Preparation and Reactions of Triethylphosphine Complexes of Zerovalent Nickel, Palladium, and Platinum. *Inorg. Chem.* **1976**, *15*, 208–212.
- (36) Tracey, M. P.; Pham, D.; Koide, K. Fluorometric Imaging Methods for Palladium and Platinum and the Use of Palladium for Imaging Biomolecules. *Chem. Soc. Rev.* **2015**, *44*, 4769–4791.
- (37) Li, H.; Fan, J.; Peng, X. Colourimetric and Fluorescent Probes for the Optical Detection of Palladium Ions. *Chem. Soc. Rev.* **2013**, *42*, 7943–7962.
- (38) Snieckus, V. “New Trends in Cross-Coupling: Theory and Applications”. *Johnson Matthey Technol. Rev.* **2016**, *60*, 99–105.
- (39) Baker, M. S.; Phillips, S. T. A Two-Component Small Molecule System for Activity-Based Detection and Signal Amplification: Application to the Visual Detection of Threshold Levels of Pd(II). *J. Am. Chem. Soc.* **2011**, *133*, 5170–5173.
- (40) Chankeshwara, S. V.; Indrigo, E.; Bradley, M. Palladium-Mediated Chemistry in Living Cells. *Curr. Opin. Chem. Biol.* **2014**, *21*, 128–135.

- (41) Völker, T.; Meggers, E. Transition-Metal-Mediated Uncaging in Living Human Cells—an Emerging Alternative to Photolabile Protecting Groups. *Curr. Opin. Chem. Biol.* **2015**, *25*, 48–54.
- (42) Bai, Y.; Chen, J.; Zimmerman, S. C. Designed Transition Metal Catalysts for Intracellular Organic Synthesis. *Chem. Soc. Rev.* **2018**, *47*, 1811–1821.
- (43) Qin, L.-H.; Hu, W.; Long, Y.-Q. Bioorthogonal Chemistry: Optimization and Application Updates During 2013–2017. *Tetrahedron Lett.* **2018**, *59*, 2214–2228.
- (44) King, M.; Wagner, A. Developments in the Field of Bioorthogonal Bond Forming Reactions—Past and Present Trends. *Bioconjugate Chem.* **2014**, *25*, 825–839.
- (45) Yusop, R. M.; Unciti-Broceta, A.; Johansson, E. M. V.; Sánchez-Martín, R. M.; Bradley, M. Palladium-Mediated Intracellular Chemistry. *Nat. Chem.* **2011**, *3*, 239.
- (46) Rautio, J.; Meanwell, N. A.; Di, L.; Hageman, M. J. The Expanding Role of Prodrugs in Contemporary Drug Design and Development. *Nat. Rev. Drug Discov.* **2018**, *17*, 559.
- (47) Song, F.; Garner, A. L.; Koide, K. A Highly Sensitive Fluorescent Sensor for Palladium Based on the Allylic Oxidative Insertion Mechanism. *J. Am. Chem. Soc.* **2007**, *129*, 12354–12355.
- (48) Formica, M.; Fusi, V.; Giorgi, L.; Micheloni, M. New Fluorescent Chemosensors for Metal Ions in Solution. *Coord. Chem. Rev.* **2012**, *256*, 170–192.
- (49) Santra, M.; Ko, S.-K.; Shin, I.; Ahn, K. H. Fluorescent Detection of Palladium Species with an O-Propargylated Fluorescein. *Chem. Commun.* **2010**, *46*, 3964–3966.
- (50) Feng, W.; Liu, D.; Feng, S.; Feng, G. Readily Available Fluorescent Probe for Carbon Monoxide Imaging in Living Cells. *Anal. Chem.* **2016**, *88*, 10648–10653.
- (51) Tian, X.; Liu, X.; Wang, A.; Lau, C.; Lu, J. Bioluminescence Imaging of Carbon Monoxide in Living Cells and Nude Mice Based on Pd(0)-Mediated Tsuji–Trost Reaction. *Anal. Chem.* **2018**, *90*, 5951–5958.
- (52) Feng, S.; Liu, D.; Feng, W.; Feng, G. Allyl Fluorescein Ethers as Promising Fluorescent Probes for Carbon Monoxide Imaging in Living Cells. *Anal. Chem.* **2017**, *89*, 3754–3760.
- (53) Weiss, J. T.; Dawson, J. C.; Macleod, K. G.; Rybski, W.; Fraser, C.; Torres-Sánchez, C.; Patton, E. E.; Bradley, M.; Carragher, N. O.; Unciti-Broceta, A. Extracellular Palladium-Catalysed Dealkylation of 5-Fluoro-1-Propargyl-Uracil as a Bioorthogonally Activated Prodrug Approach. *Nat. Commun.* **2014**, *5*, 3277.
- (54) Weiss, J. T.; Dawson, J. C.; Fraser, C.; Rybski, W.; Torres-Sánchez, C.; Bradley, M.; Patton, E. E.; Carragher, N. O.; Unciti-Broceta, A. Development and Bioorthogonal Activation of Palladium-Labile Prodrugs of Gemcitabine. *J. Med. Chem.* **2014**, *57*, 5395–5404.

- (55) Miller, M. A.; Askevold, B.; Mikula, H.; Kohler, R. H.; Pirovich, D.; Weissleder, R. Nano-Palladium Is a Cellular Catalyst for in Vivo Chemistry. *Nat. Commun.* **2017**, *8*, 15906.
- (56) Yang, Y. W.; Unsworth, L. D.; Semagina, N. Size- and Shape-Controlled Palladium Nanoparticles in a Fluorometric Tsuji-Trost Reaction. *J. Catal.* **2011**, *281*, 137–146.
- (57) Garner, A. L.; Koide, K. Studies of a Fluorogenic Probe for Palladium and Platinum Leading to a Palladium-Specific Detection Method. *Chem. Commun.* **2009**, 86–88.
- (58) Song, F. L.; Carder, E. J.; Kohler, C. C.; Koide, K. Studies toward an Ideal Fluorescence Method to Measure Palladium in Functionalized Organic Molecules: Effects of Sodium Borohydride, Temperature, Phosphine Ligand, and Phosphate Ions on Kinetics. *Chem.-Eur. J.* **2010**, *16*, 13500–13508.
- (59) Koide, K.; Tracey, M. P.; Bu, X.; Jo, J.; Williams, M. J.; Welch, C. J. A Competitive and Reversible Deactivation Approach to Catalysis-Based Quantitative Assays. *Nat. Commun.* **2016**, *7*, 10691.
- (60) Racys, D. T.; Eastoe, J.; Norrby, P. O.; Grillo, I.; Rogers, S. E.; Lloyd-Jones, G. C. Pd- η^3 -C₆H₉ Complexes of the Trost Modular Ligand: High Nuclearity Columnar Aggregation Controlled by Concentration, Solvent and Counterion. *Chem. Sci.* **2015**, *6*, 5793–5801.
- (61) Hale, K. J.; Ridd, H. J. A Reassessment of the Isoinversion Relationship. *J. Chem. Soc., Perkin Trans. 2* **1995**, 1601–1605.
- (62) Hale, K. J.; Ridd, J. H. A Reassessment of the Isoinversion Principle. *J. Chem. Soc., Chem. Commun.* **1995**, 357–358.
- (63) Brown, K. L.; Li, J. Activation Parameters for the Carbon-Cobalt Bond Homolysis of Coenzyme B₁₂ Induced by the B₁₂-Dependent Ribonucleotide Reductase from *Lactobacillus Leichmannii*. *J. Am. Chem. Soc.* **1998**, *120*, 9466–9474.
- (64) Valentine, A. M.; Stahl, S. S.; Lippard, S. J. Mechanistic Studies of the Reaction of Reduced Methane Monooxygenase Hydroxylase with Dioxygen and Substrates. *J. Am. Chem. Soc.* **1999**, *121*, 3876–3887.
- (65) Simões, J. A. M.; Beauchamp, J. L. Transition-Metal Hydrogen and Metal-Carbon Bond Strengths: The Keys to Catalysis. *Chem. Rev.* **1990**, *90*, 629–688.
- (66) Houk, K. N.; Rondan, N. G.; Mareda, J. Theoretical Studies of Halocarbene Cycloaddition Selectivities - a New Interpretation of Negative Activation Energies and Entropy Control of Selectivity. *Tetrahedron* **1985**, *41*, 1555–1563.
- (67) Moss, R. A.; Lawrynowicz, W.; Turro, N. J.; Gould, I. R.; Yuan, C. Activation Parameters for the Additions of Arylhalocarbenes to Alkenes. *J. Am. Chem. Soc.* **1986**, *108*, 7028–7032.

- (68) Benson, S. W.; Dobis, O. Existence of Negative Activation Energies in Simple Bimolecular Metathesis Reactions and Some Observations on Too-Fast Reactions. *J. Phys. Chem. A* **1998**, *102*, 5175–5181.
- (69) Mozurkewich, M.; Benson, S. W. Negative Activation Energies and Curved Arrhenius Plots. 1. Theory of Reactions over Potential Wells. *J. Phys. Chem.* **1984**, *88*, 6429–6435.
- (70) Mozurkewich, M.; Lamb, J. J.; Benson, S. W. Negative Activation Energies and Curved Arrhenius Plots. 2. OH + CO. *J. Phys. Chem.* **1984**, *88*, 6435–6441.
- (71) Shimomura, T.; Tölle, K. J.; Smid, J.; Szwarc, M. Energy and Entropy of Activation of Propagation by Free Polystyryl Anions and Their Ion Pairs. Phenomenon of Negative Activation Energy. *J. Am. Chem. Soc.* **1967**, *89*, 796–803.
- (72) Heller, D.; Buschmann, H.; Neumann, H. Conditions for Maxima and Minima as Inversion Points in the Temperature Dependence of Selection Processes. *J. Chem. Soc., Perkin Trans. 2* **1999**, *175*–181.
- (73) Olson, L. P.; Kuwata, K. T.; Bartberger, M. D.; Houk, K. N. Conformation-Dependent State Selectivity in O-O Cleavage of ONOONO: An "Inorganic Cope Rearrangement" Helps Explain the Observed Negative Activation Energy in the Oxidation of Nitric Oxide by Dioxygen. *J. Am. Chem. Soc.* **2002**, *124*, 9469–9475.
- (74) Rosokha, S. V.; Kochi, J. K. The Preorganization Step in Organic Reaction Mechanisms. Charge-Transfer Complexes as Precursors to Electrophilic Aromatic Substitutions. *J. Org. Chem.* **2002**, *67*, 1727–1737.
- (75) Erden, I.; Alscher, P. E.; Keeffe, J. R.; Mercer, C. Dye-Sensitized Photooxygenation of the C=N Bond. 5. Substituent Effects on the Cleavage of the C=N Bond of C-Aryl-N-Aryl-N-Methylhydrazones. *J. Org. Chem.* **2005**, *70*, 4389–4392.
- (76) Han, X.; Lee, R.; Chen, T.; Luo, J.; Lu, Y. X.; Huang, K. W. Kinetic Evidence of an Apparent Negative Activation Enthalpy in an Organocatalytic Process. *Sci. Rep.* **2013**, *3*, e2557.
- (77) Zhu, X. Q.; Zhang, J. Y.; Cheng, J. P. Negative Kinetic Temperature Effect on the Hydride Transfer from NADH Analogue BNAH to the Radical Cation of *N*-Benzylphenothiazine in Acetonitrile. *J. Org. Chem.* **2006**, *71*, 7007–7015.
- (78) Langhals, H.; Eberspächer, M.; Mayer, P. Uncatalyzed C-H Amination of Aromatic Compounds under Unusually Mild Conditions with Negative Enthalpies of Activation. *Asian J. Org. Chem.* **2017**, *6*, 1080–1085.
- (79) Ruiz-Castillo, P.; Blackmond, D. G.; Buchwald, S. L. Rational Ligand Design for the Arylation of Hindered Primary Amines Guided by Reaction Progress Kinetic Analysis. *J. Am. Chem. Soc.* **2015**, *137*, 3085–3092.

- (80) Niemeyer, Z. L.; Milo, A.; Hickey, D. P.; Sigman, M. S. Parameterization of Phosphine Ligands Reveals Mechanistic Pathways and Predicts Reaction Outcomes. *Nat. Chem.* **2016**, *8*, 610.
- (81) Martin, R.; Buchwald, S. L. Palladium-Catalyzed Suzuki-Miyaura Cross-Coupling Reactions Employing Dialkylbiaryl Phosphine Ligands. *Acc. Chem. Res.* **2008**, *41*, 1461–1473.
- (82) Farina, V.; Krishnan, B. Large Rate Accelerations in the Stille Reaction with Tri-2-Furylphosphine and Triphenylarsine as Palladium Ligands: Mechanistic and Synthetic Implications. *J. Am. Chem. Soc.* **1991**, *113*, 9585–9595.
- (83) Tymonko, S. A.; Smith, R. C.; Ambrosi, A.; Ober, M. H.; Wang, H.; Denmark, S. E. Mechanistic Significance of the Si-O-Pd Bond in the Palladium-Catalyzed Cross-Coupling Reactions of Arylsilanolates. *J. Am. Chem. Soc.* **2015**, *137*, 6200–6218.
- (84) Amatore, C.; Jutand, A.; Khalil, F. Neutral Palladium(0) Complexes from $\text{Pd}(\text{OAc})_2$ and Tri-2-Furylphosphine and Their Reactivity in Oxidative Addition of Iodobenzene. *Arkivoc* **2006**, 38–48.
- (85) Lo, J. C. L.; Gui, J. H.; Yabe, Y. K.; Pan, C. M.; Baran, P. S. Functionalized Olefin Cross-Coupling to Construct Carbon-Carbon Bonds. *Nature* **2014**, *516*, 343–348.
- (86) Calleja, J.; Pla, D.; Gorman, T. W.; Domingo, V.; Haffemayer, B.; Gaunt, M. J. A Steric Tethering Approach Enables Palladium-Catalysed C-H Activation of Primary Amino Alcohols. *Nat. Chem.* **2015**, *7*, 1009–1016.
- (87) Jiang, G.; List, B. Direct Asymmetric α -Allylation of Aldehydes with Simple Allylic Alcohols Enabled by the Concerted Action of Three Different Catalysts. *Angew. Chem., Int. Ed.* **2011**, *50*, 9471–9474.
- (88) Tao, Z. L.; Zhang, W. Q.; Chen, D. F.; Adele, A.; Gong, L. Z. Pd-Catalyzed Asymmetric Allylic Alkylation of Pyrazol-5-ones with Allylic Alcohols: The Role of the Chiral Phosphoric Acid in C-O Bond Cleavage and Stereocontrol. *J. Am. Chem. Soc.* **2013**, *135*, 9255–9258.
- (89) El Maadi, A.; Bennazha, J.; Réau, J. M.; Boukhari, A.; Holt, E. M. New Palladium Phosphate Complexes: $\text{K}_2\text{PdP}_2\text{O}_7$ and $\text{K}_{3.5}\text{Pd}_{2.25}(\text{P}_2\text{O}_7)_2$ Synthesis, Single Crystal Structure and Conductivity. *Mater. Res. Bull.* **2003**, *38*, 865–874.
- (90) Lii, K.-H.; Wang, S.-L.; Liao, F.-L. $\text{Cs}_2\text{Pd}_3(\text{P}_2\text{O}_7)_2$ and $\text{Cs}_2\text{Pd}_3(\text{As}_2\text{O}_7)_2$: A 3D Palladium Phosphate with a Tunnel Structure and a 2D Palladium Arsenate Containing Strings of Palladium Atoms. *Inorg. Chem.* **2004**, *43*, 2499–2502.
- (91) Huo, X. H.; Yang, G. Q.; Liu, D. L.; Liu, Y. G.; Gridnev, I. D.; Zhang, W. B. Palladium-Catalyzed Allylic Alkylation of Simple Ketones with Allylic Alcohols and Its Mechanistic Study. *Angew. Chem., Int. Ed.* **2014**, *53*, 6776–6780.

- (92) Yoshida, T.; Otsuka, S. Reactions of Two-Coordinate Phosphine Platinum(0) and Palladium(0) Compounds. Ligand Exchange and Reactivities toward Small Molecules. *J. Am. Chem. Soc.* **1977**, *99*, 2134–2140.
- (93) Cai, S. T.; Lu, Y.; He, S.; Wei, F. F.; Zhao, L. C.; Zeng, X. S. A Highly Sensitive and Selective Turn-on Fluorescent Chemosensor for Palladium Based on a Phosphine-Rhodamine Conjugate. *Chem. Commun.* **2013**, *49*, 822–824.
- (94) Ahlquist, M. S. G.; Norrby, P.-O. Dispersion and Back-Donation Gives Tetracoordinate [Pd(PPh₃)₄]. *Angew. Chem., Int. Ed.* **2011**, *50*, 11794–11797.
- (95) Lukomski, L.; Pohorilets, I.; Koide, K. Third-Generation Method for High-Throughput Quantification of Trace Palladium by Color or Fluorescence. *Org. Process Res. Dev.* **2020**, *24*, 85–95.
- (96) Wang, J.; Cheng, B.; Li, J.; Zhang, Z.; Hong, W.; Chen, X.; Chen, P. R. Chemical Remodeling of Cell-Surface Sialic Acids through a Palladium-Triggered Bioorthogonal Elimination Reaction. *Angew. Chem., Int. Ed.* **2015**, *54*, 5364–5368.
- (97) Diao, T. N.; White, P.; Guzei, I.; Stahl, S. S. Characterization of DMSO Coordination to Palladium(II) in Solution and Insights into the Aerobic Oxidation Catalyst, Pd(DMSO)₂(TFA)₂. *Inorg. Chem.* **2012**, *51*, 11898–11909.
- (98) Drinkel, E. E.; Wu, L. L.; Linden, A.; Dorta, R. Synthesis, Structure, and Catalytic Studies of Palladium and Platinum Bis-Sulfoxide Complexes. *Organometallics* **2014**, *33*, 627–636.
- (99) Banerjee, S.; Roy, S.; Bagchi, B. Enhanced Pair Hydrophobicity in the Water-Dimethylsulfoxide (DMSO) Binary Mixture at Low DMSO Concentrations. *J. Phys. Chem. B* **2010**, *114*, 12875–12882.
- (100) Ghosh, R.; Banerjee, S.; Chakrabarty, S.; Bagchi, B. Anomalous Behavior of Linear Hydrocarbon Chains in Water-DMSO Binary Mixture at Low DMSO Concentration. *J. Phys. Chem. B* **2011**, *115*, 7612–7620.
- (101) Larsson, J. M.; Szabó, K. J. Mechanistic Investigation of the Palladium-Catalyzed Synthesis of Allylic Silanes and Boronates from Allylic Alcohols. *J. Am. Chem. Soc.* **2013**, *135*, 443–455.
- (102) Amatore, C.; Jutand, A.; M'Barki, M. A.; Meyer, G.; Mottier, L. Importance of the Presence of Chloride Ions in the First Steps of Palladium-Catalyzed Nucleophilic Allylic Substitutions. *Eur. J. Inorg. Chem.* **2001**, 873–880.
- (103) Blackmond, D. G. Reaction Progress Kinetic Analysis: A Powerful Methodology for Mechanistic Studies of Complex Catalytic Reactions. *Angew. Chem., Int. Ed.* **2005**, *44*, 4302–4320.

- (104) O'Brien, A. G.; Luca, O. R.; Baran, P. S.; Blackmond, D. G. In Situ Ftir Spectroscopic Monitoring of Electrochemically Controlled Organic Reactions in a Recycle Reactor. *React. Chem. Eng.* **2016**, *1*, 90–95.
- (105) Mathew, J. S.; Klussmann, M.; Iwamura, H.; Valera, F.; Futran, A.; Emanuelsson, E. A. C.; Blackmond, D. G. Investigations of Pd-Catalyzed ArX Coupling Reactions Informed by Reaction Progress Kinetic Analysis. *J. Org. Chem.* **2006**, *71*, 4711–4722.
- (106) Piechaczyk, O.; Thoumazet, C.; Jean, Y.; le Floch, P. DFT Study on the Palladium-Catalyzed Allylation of Primary Amines by Allylic Alcohol. *J. Am. Chem. Soc.* **2006**, *128*, 14306–14317.
- (107) Mora, G.; Piechaczyk, O.; Le Goff, X. F.; Le Floch, P. Palladium-Catalyzed Deallylation of Allyl Ethers with a Xanthene Phosphole Ligand. Experimental and DFT Mechanistic Studies. *Organometallics* **2008**, *27*, 2565–2569.
- (108) De Luliis, M. Z.; Watson, I. D. G.; Yudin, A. K.; Morris, R. H. A DFT Investigation into the Origin of Regioselectivity in Palladium-Catalyzed Allylic Amination. *Can. J. Chem.* **2009**, *87*, 54–62.
- (109) Keith, J. A.; Behenna, D. C.; Sherden, N.; Mohr, J. T.; Ma, S.; Marinescu, S. C.; Nielsen, R. J.; Oxgaard, J.; Stoltz, B. M.; Goddard III, W. A. The Reaction Mechanism of the Enantioselective Tsuji Allylation: Inner-Sphere and Outer-Sphere Pathways, Internal Rearrangements, and Asymmetric C-C Bond Formation. *J. Am. Chem. Soc.* **2012**, *134*, 19050–19060.
- (110) Frisch, M. J.; Trucks, G. W.; Schlegel, H. B.; Scuseria, G. E.; Robb, M. A.; Cheeseman, J. R.; Scalmani, G.; Barone, V.; Mennucci, B.; Petersson, G. A.; Nakatsuji, H.; Caricato, M.; Li, X.; Hratchian, H. P.; Izmaylov, A. F.; Bloino, J.; Zheng, G.; Sonnenberg, J. L.; Hada, M.; Ehara, M.; Toyota, K.; Fukuda, R.; Hasegawa, J.; Ishida, M.; Nakajima, T.; Honda, Y.; Kitao, O.; Nakai, H.; Vreven, T.; Montgomery, J. A., Jr.; Peralta, J. E.; Ogliaro, F.; Bearpark, M.; Heyd, J. J.; Brothers, E.; Kudin, K. N.; Staroverov, V. N.; Kobayashi, R.; Normand, J.; Raghavachari, K.; Rendell, A.; Burant, J. C.; Iyengar, S. S.; Tomasi, J.; Cossi, M.; Rega, N.; Millam, N. J.; Klene, M.; Knox, J. E.; Cross, J. B.; Bakken, V.; Adamo, C.; Jaramillo, J.; Gomperts, R.; Stratmann, R. E.; Yazyev, O.; Austin, A. J.; Cammi, R.; Pomelli, C.; Ochterski, J. W.; Martin, R. L.; Morokuma, K.; Zakrzewski, V. G.; Voth, G. A.; Salvador, P.; Dannenberg, J. J.; Dapprich, S.; Daniels, A. D.; Farkas, Ö.; Foresman, J. B.; Ortiz, J. V.; Cioslowski, J.; Fox, D. J. Gaussian 09, Revision D.01; Gaussian, Inc.: Wallingford, CT, 2009.
- (111) Marenich, A. V.; Cramer, C. J.; Truhlar, D. G. Universal Solvation Model Based on Solute Electron Density and on a Continuum Model of the Solvent Defined by the Bulk Dielectric Constant and Atomic Surface Tensions. *J. Phys. Chem. B* **2009**, *113*, 6378–6396.
- (112) To properly account for the solvation effects on entropy, molecular dynamics simulations using explicit solvent (water) are typically required. This is beyond the scope of the current study.

See: (a) Levy, R. M.; Gallicchio, E. *Annu. Rev. Phys. Chem.* 1998, 49, 531. (b) Wana, S.; Stote, R. H.; Karplus, M. *J. Chem. Phys.* 2004, 121, 9539.

(113) Plata, R. E.; Singleton, D. A. A Case Study of the Mechanism of Alcohol-Mediated Morita-Baylis-Hillman Reactions. The Importance of Experimental Observations. *J. Am. Chem. Soc.* **2015**, *137*, 3811–3826.

(114) Maddock, S. M.; Finn, M. G. Palladium-Catalyzed Head-to-Head Telomerization of Isoprene with Amines. *Organometallics* **2000**, *19*, 2684–2689.

(115) Brody, M. S.; Finn, M. G. Palladium-Catalyzed Coupling of Functionalized Bromoarenes to a Polystyrene-Bound Aryl Tributylstannane. *Tetrahedron Lett.* **1999**, *40*, 415–418.

(116) Destito, P.; Vidal, C.; López, F.; Mascareñas, J. L. Transition Metal-Promoted Reactions in Aqueous Media and Biological Settings. *Chem.-Eur. J.* **2021**, *27*, 4789–4816.

(117) Soldevila-Barreda, J. J.; Sadler, P. J. Approaches to the Design of Catalytic Metallocdrugs. *Curr. Opin. Chem. Biol.* **2015**, *25*, 172–183.

(118) Ngo, A. H.; Bose, S.; Do, L. H. Intracellular Chemistry: Integrating Molecular Inorganic Catalysts with Living Systems. *Chem.-Eur. J.* **2018**, *24*, 10584–10594.

(119) Martínez-Calvo, M.; Mascareñas, J. L. Organometallic Catalysis in Biological Media and Living Settings. *Coord. Chem. Rev.* **2018**, *359*, 57–79.

(120) Tornøe, C. W.; Christensen, C.; Meldal, M. Peptidotriazoles on Solid Phase: [1,2,3]-Triazoles by Regiospecific Copper(I)-Catalyzed 1,3-Dipolar Cycloadditions of Terminal Alkynes to Azides. *J. Org. Chem.* **2002**, *67*, 3057–3064.

(121) Rostovtsev, V. V.; Green, L. G.; Fokin, V. V.; Sharpless, K. B. A Stepwise Huisgen Cycloaddition Process: Copper(I)-Catalyzed Regioselective “Ligation” of Azides and Terminal Alkynes. *Angew. Chem., Int. Ed.* **2002**, *41*, 2596–2599.

(122) Worrell, B. T.; Malik, J. A.; Fokin, V. V. Direct Evidence of a Dinuclear Copper Intermediate in Cu(I)-Catalyzed Azide-Alkyne Cycloadditions. *Science* **2013**, *340*, 457–460.

(123) Wang, Q.; Chan, T. R.; Hilgraf, R.; Fokin, V. V.; Sharpless, K. B.; Finn, M. G. Bioconjugation by Copper(I)-Catalyzed Azide-Alkyne [3 + 2] Cycloaddition. *J. Am. Chem. Soc.* **2003**, *125*, 3192–3193.

(124) Li, Y.; Fu, H. Bioorthogonal Ligations and Cleavages in Chemical Biology. *ChemistryOpen* **2020**, *9*, 835–853.

(125) Shieh, P.; Hill, M. R.; Zhang, W.; Kristufek, S. L.; Johnson, J. A. Clip Chemistry: Diverse (Bio)(Macro)Molecular and Material Function through Breaking Covalent Bonds. *Chem. Rev.* **2021**, *121*, 7059–7121.

- (126) Uttamapinant, C.; Tangpeerachaikul, A.; Grecian, S.; Clarke, S.; Singh, U.; Slade, P.; Gee, K. R.; Ting, A. Y. Fast, Cell-Compatible Click Chemistry with Copper-Chelating Azides for Biomolecular Labeling. *Angew. Chem., Int. Ed.* **2012**, *51*, 5852–5856.
- (127) Tomás-Gamasa, M.; Martínez-Calvo, M.; Couceiro, J. R.; Mascareñas, J. L. Transition Metal Catalysis in the Mitochondria of Living Cells. *Nat. Commun.* **2016**, *7*, 12538.
- (128) Völker, T.; Meggers, E. Chemical Activation in Blood Serum and Human Cell Culture: Improved Ruthenium Complex for Catalytic Uncaging of Alloc-Protected Amines. *ChemBioChem* **2017**, *18*, 1083–1086.
- (129) Streu, C.; Meggers, E. Ruthenium-Induced Allylcarbamate Cleavage in Living Cells. *Angew. Chem., Int. Ed.* **2006**, *45*, 5645–5648.
- (130) Völker, T.; Dempwolff, F.; Graumann, P. L.; Meggers, E. Progress Towards Bioorthogonal Catalysis with Organometallic Compounds. *Angew. Chem., Int. Ed.* **2014**, *53*, 10536–10540.
- (131) Sasmal, P. K.; Carregal-Romero, S.; Parak, W. J.; Meggers, E. Light-Triggered Ruthenium-Catalyzed Allylcarbamate Cleavage in Biological Environments. *Organometallics* **2012**, *31*, 5968–5970.
- (132) Hsu, H.-T.; Trantow, B. M.; Waymouth, R. M.; Wender, P. A. Bioorthogonal Catalysis: A General Method to Evaluate Metal-Catalyzed Reactions in Real Time in Living Systems Using a Cellular Luciferase Reporter System. *Bioconjugate Chem.* **2016**, *27*, 376–382.
- (133) Labinger, J. A. Platinum-Catalyzed C–H Functionalization. *Chem. Rev.* **2017**, *117*, 8483–8496.
- (134) Basu, U.; Banik, B.; Wen, R.; Pathak, R. K.; Dhar, S. The Platin-X Series: Activation, Targeting, and Delivery. *Dalton Trans.* **2016**, *45*, 12992–13004.
- (135) Johnstone, T. C.; Suntharalingam, K.; Lippard, S. J. The Next Generation of Platinum Drugs: Targeted Pt(II) Agents, Nanoparticle Delivery, and Pt(IV) Prodrugs. *Chem. Rev.* **2016**, *116*, 3436–3486.
- (136) Kenny, R. G.; Marmion, C. J. Toward Multi-Targeted Platinum and Ruthenium Drugs—a New Paradigm in Cancer Drug Treatment Regimens? *Chem. Rev.* **2019**, *119*, 1058–1137.
- (137) Stewart, D. J.; Molepo, J. M.; Green, R. M.; Montpetit, V. A. J.; Hugenholtz, H.; Lamothe, A.; Mikhael, N. Z.; Redmond, M. D.; Gadia, M.; Goel, R. Factors Affecting Platinum Concentrations in Human Surgical Tumour Specimens after Cisplatin. *Br. J. Cancer* **1995**, *71*, 598–604.
- (138) van Hennik, M. B.; van der Vijgh, W. J.; Klein, I.; Elferink, F.; Vermorken, J. B.; Winograd, B.; Pinedo, H. M. Comparative Pharmacokinetics of Cisplatin and Three Analogues in Mice and Humans. *Cancer Res.* **1987**, *47*, 6297–301.

- (139) Jacobs, S.; McCully, C. L.; Murphy, R. F.; Bacher, J.; Balis, F. M.; Fox, E. Extracellular Fluid Concentrations of Cisplatin, Carboplatin, and Oxaliplatin in Brain, Muscle, and Blood Measured Using Microdialysis in Nonhuman Primates. *Cancer Chemother. Pharmacol.* **2010**, *65*, 817–824.
- (140) Klein, A. V.; Hambley, T. W. Platinum Drug Distribution in Cancer Cells and Tumors. *Chem. Rev.* **2009**, *109*, 4911–4920.
- (141) Oliveira, B. L.; Stenton, B. J.; Unnikrishnan, V. B.; de Almeida, C. R.; Conde, J.; Negrão, M.; Schneider, F. S. S.; Cordeiro, C.; Ferreira, M. G.; Caramori, G. F.; Domingos, J. B.; Fior, R.; Bernardes, G. J. L. Platinum-Triggered Bond-Cleavage of Pentyroyl Amide and N-Propargyl Handles for Drug-Activation. *J. Am. Chem. Soc.* **2020**, *142*, 10869–10880.
- (142) Sun, T.; Lv, T.; Wu, J.; Zhu, M.; Fei, Y.; Zhu, J.; Zhang, Y.; Huang, Z. General Strategy for Integrated Bioorthogonal Prodrugs: Pt(II)-Triggered Depropargylation Enables Controllable Drug Activation in Vivo. *J. Med. Chem.* **2020**, *63*, 13899–13912.
- (143) Awuah, S. G.; Zheng, Y.-R.; Bruno, P. M.; Hemann, M. T.; Lippard, S. J. A Pt(IV) Pro-Drug Preferentially Targets Indoleamine-2,3-Dioxygenase, Providing Enhanced Ovarian Cancer Immuno-Chemotherapy. *J. Am. Chem. Soc.* **2015**, *137*, 14854–14857.
- (144) Wang, X.; Guo, Z. Targeting and Delivery of Platinum-Based Anticancer Drugs. *Chem. Soc. Rev.* **2013**, *42*, 202–224.
- (145) Wang, Z.; Xu, Z.; Zhu, G. A Platinum(IV) Anticancer Prodrug Targeting Nucleotide Excision Repair to Overcome Cisplatin Resistance. *Angew. Chem., Int. Ed.* **2016**, *55*, 15564–15568.
- (146) Zhu, G.; Myint, M.; Ang, W. H.; Song, L.; Lippard, S. J. Monofunctional Platinum–DNA Adducts Are Strong Inhibitors of Transcription and Substrates for Nucleotide Excision Repair in Live Mammalian Cells. *Cancer Res.* **2012**, *72*, 790–800.
- (147) Weaver, E. L.; Bose, R. N. Platinum(II) Catalysis and Radical Intervention in Reductions of Platinum(IV) Antitumor Drugs by Ascorbic Acid. *J. Inorg. Biochem.* **2003**, *95*, 231–239.
- (148) Hrabie, J. A.; Keefer, L. K. Chemistry of the Nitric Oxide-Releasing Diazeniumdiolate (“Nitrosohydroxylamine”) Functional Group and Its Oxygen-Substituted Derivatives. *Chem. Rev.* **2002**, *102*, 1135–1154.
- (149) Carpenter, A. W.; Schoenfisch, M. H. Nitric Oxide Release: Part II. Therapeutic Applications. *Chem. Soc. Rev.* **2012**, *41*, 3742–3752.
- (150) Huang, Z.; Fu, J.; Zhang, Y. Nitric Oxide Donor-Based Cancer Therapy: Advances and Prospects. *J. Med. Chem.* **2017**, *60*, 7617–7635.

- (151) Chakrapani, H.; Showalter, B. M.; Citro, M. L.; Keefer, L. K.; Saavedra, J. E. Nitric Oxide Prodrugs: Diazeniumdiolate Anions of Hindered Secondary Amines. *Org. Lett.* **2007**, *9*, 4551–4554.
- (152) Garner, A. L.; Koide, K. Fluorescent Method for Platinum Detection in Buffers and Serums for Cancer Medicine and Occupational Hazards. *Chem. Commun.* **2009**, 83–85.
- (153) Pham, D.; Deter, C. J.; Reinard, M. C.; Gibson, G. A.; Kiselyov, K.; Yu, W.; Sandulache, V. C.; St. Croix, C. M.; Koide, K. Using Ligand-Accelerated Catalysis to Repurpose Fluorogenic Reactions for Platinum or Copper. *ACS Cent. Sci.* **2020**, *6*, 1772–1788.
- (154) Fürstner, A.; Davies, P. W. Catalytic Carbophilic Activation: Catalysis by Platinum and Gold π Acids. *Angew. Chem., Int. Ed.* **2007**, *46*, 3410–3449.
- (155) Li, Z.; Brouwer, C.; He, C. Gold-Catalyzed Organic Transformations. *Chem. Rev.* **2008**, *108*, 3239–3265.
- (156) Gorin, D. J.; Sherry, B. D.; Toste, F. D. Ligand Effects in Homogeneous Au Catalysis. *Chem. Rev.* **2008**, *108*, 3351–3378.
- (157) Dorel, R.; Echavarren, A. M. Gold(I)-Catalyzed Activation of Alkynes for the Construction of Molecular Complexity. *Chem. Rev.* **2015**, *115*, 9028–9072.
- (158) Zi, W.; Dean Toste, F. Recent Advances in Enantioselective Gold Catalysis. *Chem. Soc. Rev.* **2016**, *45*, 4567–4589.
- (159) Liu, X.; He, L.; Liu, Y.-M.; Cao, Y. Supported Gold Catalysis: From Small Molecule Activation to Green Chemical Synthesis. *Acc. Chem. Res.* **2014**, *47*, 793–804.
- (160) Stratakis, M.; Garcia, H. Catalysis by Supported Gold Nanoparticles: Beyond Aerobic Oxidative Processes. *Chem. Rev.* **2012**, *112*, 4469–4506.
- (161) Vericat, C.; Vela, M. E.; Benitez, G.; Carro, P.; Salvarezza, R. C. Self-Assembled Monolayers of Thiols and Dithiols on Gold: New Challenges for a Well-Known System. *Chem. Soc. Rev.* **2010**, *39*, 1805–1834.
- (162) Li, N.; Zhao, P.; Astruc, D. Anisotropic Gold Nanoparticles: Synthesis, Properties, Applications, and Toxicity. *Angew. Chem., Int. Ed.* **2014**, *53*, 1756–1789.
- (163) Daraee, H.; Eatemedi, A.; Abbasi, E.; Fekri Aval, S.; Kouhi, M.; Akbarzadeh, A. Application of Gold Nanoparticles in Biomedical and Drug Delivery. *Artif. Cells Nanomed. Biotechnol.* **2016**, *44*, 410–422.
- (164) Pérez-López, A. M.; Rubio-Ruiz, B.; Sebastián, V.; Hamilton, L.; Adam, C.; Bray, T. L.; Irusta, S.; Brennan, P. M.; Lloyd-Jones, G. C.; Sieger, D.; Santamaría, J.; Unciti-Broceta, A. Gold-

Triggered Uncaging Chemistry in Living Systems. *Angew. Chem., Int. Ed.* **2017**, *56*, 12548–12552.

- (165) Pérez-López, A. M.; Rubio-Ruiz, B.; Sebastián, V.; Hamilton, L.; Adam, C.; Bray, T. L.; Irusta, S.; Brennan, P. M.; Lloyd-Jones, G. C.; Sieger, D.; Santamaría, J.; Unciti-Broceta, A. Gold-Triggered Uncaging Chemistry in Living Systems. *Angew. Chem., Int. Ed.* **2017**, *56*, 12548–12552.
- (166) Jbara, M.; Eid, E.; Brik, A. Gold(I)-Mediated Decaging or Cleavage of Propargylated Peptide Bond in Aqueous Conditions for Protein Synthesis and Manipulation. *J. Am. Chem. Soc.* **2020**, *142*, 8203–8210.
- (167) Egorova, K. S.; Ananikov, V. P. Which Metals Are Green for Catalysis? Comparison of the Toxicities of Ni, Cu, Fe, Pd, Pt, Rh, and Au Salts. *Angew. Chem., Int. Ed.* **2016**, *55*, 12150–12162.
- (168) Dumas, A.; Couvreur, P. Palladium: A Future Key Player in the Nanomedical Field? *Chem. Sci.* **2015**, *6*, 2153–2157.
- (169) Li, J.; Lin, S.; Wang, J.; Jia, S.; Yang, M.; Hao, Z.; Zhang, X.; Chen, P. R. Ligand-Free Palladium-Mediated Site-Specific Protein Labeling inside Gram-Negative Bacterial Pathogens. *J. Am. Chem. Soc.* **2013**, *135*, 7330–7338.
- (170) Chalker, J. M.; Wood, C. S. C.; Davis, B. G. A Convenient Catalyst for Aqueous and Protein Suzuki–Miyaura Cross-Coupling. *J. Am. Chem. Soc.* **2009**, *131*, 16346–16347.
- (171) Dawson, P.; Muir, T.; Clark-Lewis, I.; Kent, S. Synthesis of Proteins by Native Chemical Ligation. *Science* **1994**, *266*, 776–779.
- (172) Weinstock, M. T.; Jacobsen, M. T.; Kay, M. S. Synthesis and Folding of a Mirror-Image Enzyme Reveals Ambidextrous Chaperone Activity. *Proc. Natl. Acad. Sci. U. S. A.* **2014**, *111*, 11679–11684.
- (173) Wang, P.; Dong, S.; Shieh, J.-H.; Peguero, E.; Hendrickson, R.; Moore, M. A. S.; Danishefsky, S. J. Erythropoietin Derived by Chemical Synthesis. *Science* **2013**, *342*, 1357–1360.
- (174) Hackeng, T. M.; Griffin, J. H.; Dawson, P. E. Protein Synthesis by Native Chemical Ligation: Expanded Scope by Using Straightforward Methodology. *Proc. Natl. Acad. Sci. U. S. A.* **1999**, *96*, 10068–10073.
- (175) Canne, L. E.; Botti, P.; Simon, R. J.; Chen, Y.; Dennis, E. A.; Kent, S. B. H. Chemical Protein Synthesis by Solid Phase Ligation of Unprotected Peptide Segments. *J. Am. Chem. Soc.* **1999**, *121*, 8720–8727.
- (176) Ueda, S.; Fujita, M.; Tamamura, H.; Fujii, N.; Otaka, A. Photolabile Protection for One-Pot Sequential Native Chemical Ligation. *ChemBioChem* **2005**, *6*, 1983–1986.

- (177) Jbara, M.; Maity, S. K.; Seenaiah, M.; Brik, A. Palladium Mediated Rapid Deprotection of N-Terminal Cysteine under Native Chemical Ligation Conditions for the Efficient Preparation of Synthetically Challenging Proteins. *J. Am. Chem. Soc.* **2016**, *138*, 5069–5075.
- (178) Li, J.; Yu, J.; Zhao, J.; Wang, J.; Zheng, S.; Lin, S.; Chen, L.; Yang, M.; Jia, S.; Zhang, X.; Chen, P. R. Palladium-Triggered Deprotection Chemistry for Protein Activation in Living Cells. *Nat. Chem.* **2014**, *6*, 352–361.
- (179) Weiss, J. T.; Carragher, N. O.; Unciti-Broceta, A. Palladium-Mediated Dealkylation of N-Propargyl-Floxuridine as a Bioorthogonal Oxygen-Independent Prodrug Strategy. *Sci. Rep.* **2015**, *5*, 9329.
- (180) Bray, T. L.; Salji, M.; Brombin, A.; Pérez-López, A. M.; Rubio-Ruiz, B.; Galbraith, L. C. A.; Patton, E. E.; Leung, H. Y.; Unciti-Broceta, A. Bright Insights into Palladium-Triggered Local Chemotherapy. *Chem. Sci.* **2018**, *9*, 7354–7361.
- (181) Martínez-Calvo, M.; Couceiro, J. R.; Destito, P.; Rodríguez, J.; Mosquera, J.; Mascareñas, J. L. Intracellular Deprotection Reactions Mediated by Palladium Complexes Equipped with Designed Phosphine Ligands. *ACS Catal.* **2018**, *8*, 6055–6061.
- (182) Laps, S.; Satish, G.; Brik, A. Harnessing the Power of Transition Metals in Solid-Phase Peptide Synthesis and Key Steps in the (Semi)Synthesis of Proteins. *Chem. Soc. Rev.* **2021**, *50*, 2367–2387.
- (183) Kamo, N.; Hayashi, G.; Okamoto, A. Triple Function of 4-Mercaptophenylacetic Acid Promotes One-Pot Multiple Peptide Ligation. *Angew. Chem., Int. Ed.* **2018**, *57*, 16533–16537.
- (184) Togashi, D. M.; Ryder, A. G. A Fluorescence Analysis of ANS Bound to Bovine Serum Albumin: Binding Properties Revisited by Using Energy Transfer. *J. Fluoresc.* **2008**, *18*, 519–526.
- (185) Takehara, K.; Yuki, K.; Shirasawa, M.; Yamasaki, S.; Yamada, S. Binding Properties of Hydrophobic Molecules to Human Serum Albumin Studied by Fluorescence Titration. *Anal. Sci.* **2009**, *25*, 115–120.
- (186) Yin, B.-L.; Lai, J.-Q.; Huang, L.; Zhang, X.-Y.; Ji, F.-H. Easy Access to Acetal-Spiroacetal-Enol Ethers by Tandem Dearomatization of a Furan Ring and Acetalization. *Synthesis* **2012**, *44*, 2567–2574.
- (187) Amatore, C.; Jutand, A.; Meyer, G.; Atmani, H.; Khalil, F.; Chahdi, F. O. Comparative Reactivity of Palladium(0) Complexes Generated in Situ in Mixtures of Triphenylphosphine or Tri-2-Furylphosphine and Pd(db₂). *Organometallics* **1998**, *17*, 2958–2964.
- (188) Kühl, O., *Phosphorus-31 Nmr Spectroscopy: A Concise Introduction for the Synthetic Organic and Organometallic Chemist*. Springer-Verlag Berlin Heidelberg: 2008.

- (189) Clark, H. C.; Milne, C. R. Phosphorus-31 Nuclear Magnetic Resonance Spectra of Methylplatinum(II) and Methylpalladium(II) Cations Containing 4-Substituted Pyridine Ligands. *Can. J. Chem.* **1979**, *57*, 958–960.
- (190) Coelho, S. E.; Schneider, F. S. S.; de Oliveira, D. C.; Tripodi, G. L.; Eberlin, M. N.; Caramori, G. F.; de Souza, B.; Domingos, J. B. Mechanism of Palladium(II)-Mediated Uncaging Reactions of Propargylic Substrates. *ACS Catal.* **2019**, *9*, 3792–3799.
- (191) Amatore, C.; Jutand, A.; Thuilliez, A. Formation of Palladium(0) Complexes from $\text{Pd}(\text{OAc})_2$ and a Bidentate Phosphine Ligand (dppp) and Their Reactivity in Oxidative Addition. *Organometallics* **2001**, *20*, 3241–3249.
- (192) Pal, M.; Parasuraman, K.; Yeleswarapu, K. R. Palladium-Catalyzed Cleavage of O/N-Propargyl Protecting Groups in Aqueous Media under a Copper-Free Condition1. *Org. Lett.* **2003**, *5*, 349–352.
- (193) Amatore, C.; Jutand, A.; M'Barki, M. A. Evidence of the Formation of Zerovalent Palladium from $\text{Pd}(\text{OAc})_2$ and Triphenylphosphine. *Organometallics* **1992**, *11*, 3009–3013.
- (194) Amatore, C.; Azzabi, M.; Jutand, A. Role and Effects of Halide Ions on the Rates and Mechanisms of Oxidative Addition of Iodobenzene to Low-Ligated Zerovalent Palladium Complexes $\text{Pd}0(\text{PPh}_3)_2$. *J. Am. Chem. Soc.* **1991**, *113*, 8375–8384.
- (195) Amatore, C.; Carre, E.; Jutand, A.; M'Barki, M. A. Rates and Mechanism of the Formation of Zerovalent Palladium Complexes from Mixtures of $\text{Pd}(\text{OAc})_2$ and Tertiary Phosphines and Their Reactivity in Oxidative Additions. *Organometallics* **1995**, *14*, 1818–1826.
- (196) Lutsenko, S. Human Copper Homeostasis: A Network of Interconnected Pathways. *Curr. Opin. Chem. Biol.* **2010**, *14*, 211–217.
- (197) Koide, K.; Song, F.; de Groh, E. D.; Garner, A. L.; Mitchell, V. D.; Davidson, L. A.; Hukriede, N. A. Scalable and Concise Synthesis of Dichlorofluorescein Derivatives Displaying Tissue Permeation in Live Zebrafish Embryos. *ChemBioChem* **2008**, *9*, 214–218.
- (198) Mottram, L. F.; Boonyarattanakalin, S.; Kovel, R. E.; Peterson, B. R. The Pennsylvania Green Fluorophore: A Hybrid of Oregon Green and Tokyo Green for the Construction of Hydrophobic and Ph-Insensitive Molecular Probes. *Org. Lett.* **2006**, *8*, 581–584.
- (199) Źamojć, K.; Wiczk, W.; Zaborowski, B.; Jacewicz, D.; Chmurzyński, L. Fluorescence Quenching of 7-Amino-4-Methylcoumarin by Different TEMPO Derivatives. *Spectrochim. Acta A* **2015**, *136*, 1875–1880.
- (200) Lanterna, A. E.; González-Béjar, M.; Frenette, M.; Scaiano, J. C. Photophysics of 7-Mercapto-4-Methylcoumarin and Derivatives: Complementary Fluorescence Behaviour to 7-Hydroxycoumarins. *Photochem. Photobiol. Sci.* **2017**, *16*, 1284–1289.

- (201) Nowak, P. M.; Sagan, F.; Mitoraj, M. P. Origin of Remarkably Different Acidity of Hydroxycoumarins—Joint Experimental and Theoretical Studies. *J. Phys. Chem. B* **2017**, *121*, 4554–4561.
- (202) Pohorilets, I.; Tracey, M. P.; LeClaire, M. J.; Moore, E. M.; Lu, G.; Liu, P.; Koide, K. Kinetics and Inverse Temperature Dependence of a Tsuji–Trost Reaction in Aqueous Buffer. *ACS Catal.* **2019**, 11720–11733.
- (203) Iavicoli, I.; Bocca, B.; Fontana, L.; Caimi, S.; Petrucci, F.; Bergamaschi, A.; Alimonti, A. Distribution and Elimination of Palladium in Male Wistar Rats Following 14-Day Oral Exposure in Drinking Water. *J. Toxicol. Environ. Health* **2008**, *72*, 88–93.
- (204) Wang, X.; Liu, Y.; Fan, X.; Wang, J.; Ngai, W. S. C.; Zhang, H.; Li, J.; Zhang, G.; Lin, J.; Chen, P. R. Copper-Triggered Bioorthogonal Cleavage Reactions for Reversible Protein and Cell Surface Modifications. *J. Am. Chem. Soc.* **2019**, *141*, 17133–17141.
- (205) Nakajima, H.; Hori, Y.; Terano, H.; Okuhara, M.; Manda, T.; Matsumoto, S.; Shimomura, K. New Antitumor Substances, FR901463, FR901464 and FR901465. II. Activities against Experimental Tumors in Mice and Mechanism of Action. *J. Antibiot.* **1996**, *49*, 1204–11.
- (206) Nakajima, H.; Hori, Y.; Terano, H.; Okuhara, M.; Manda, T.; Matsumoto, S.; Shimomura, K. New Antitumor Substances, FR901463, FR901464 and FR901465. II. Activities against Experimental Tumors in Mice and Mechanism of Action. *J. Antibiot.* **1996**, *49*, 1196–1203.
- (207) Kaida, D.; Motoyoshi, H.; Tashiro, E.; Nojima, T.; Hagiwara, M.; Ishigami, K.; Watanabe, H.; Kitahara, T.; Yoshida, T.; Nakajima, H.; Tani, T.; Horinouchi, S.; Yoshida, M. Spliceostatin a Targets SF3b and Inhibits Both Splicing and Nuclear Retention of Pre-mRNA. *Nat. Chem. Biol.* **2007**, *3*, 576–583.
- (208) Will, C. L.; Urlaub, H.; Achsel, T.; Gentzel, M.; Wilm, M.; Lührmann, R. Characterization of Novel SF3b and 17S U2 snRNP Proteins, Including a Human Prp5p Homologue and an SF3b DEAD-Box Protein. *Embo J.* **2002**, *21*, 4978–4988.
- (209) Cretu, C.; Gee, P.; Liu, X.; Agrawal, A.; Nguyen, T.-V.; Ghosh, A. K.; Cook, A.; Jurica, M.; Larsen, N. A.; Pena, V. Structural Basis of Intron Selection by U2 snRNP in the Presence of Covalent Inhibitors. *Nat. Commun.* **2021**, *12*, 4491.
- (210) Nilsen, T. W.; Graveley, B. R. Expansion of the Eukaryotic Proteome by Alternative Splicing. *Nature* **2010**, *463*, 457–463.
- (211) Pan, Q.; Shai, O.; Lee, L. J.; Frey, B. J.; Blencowe, B. J. Deep Surveying of Alternative Splicing Complexity in the Human Transcriptome by High-Throughput Sequencing. *Nat. Genet.* **2008**, *40*, 1413–1415.

- (212) Massiello, A.; Roesser, J. R.; Chalfant, C. E. SAP155 Binds to Ceramide-Responsive RNA Cis-Element 1 and Regulates the Alternative 5' Splice Site Selection of Bcl-X Pre-mRNA. *FASEB J.* **2006**, *20*, 1680–1682.
- (213) Gao, Y.; Koide, K. Chemical Perturbation of Mcl-1 Pre-mRNA Splicing to Induce Apoptosis in Cancer Cells. *ACS Chem. Biol.* **2013**, *8*, 895–900.
- (214) Moore, M. J.; Wang, Q.; Kennedy, C. J.; Silver, P. A. An Alternative Splicing Network Links Cell-Cycle Control to Apoptosis. *Cell* **2010**, *142*, 625–636.
- (215) Lee, E. F. *a. e.* Bcl-XI and MCL-1 Are the Key Bcl-2 Family Proteins in Melanoma Cell Survival. *Cell Death Dis.* **2019**, *10*, 342.
- (216) Kollmannsberger, C.; Bjarnason, G.; Burnett, P.; Creel, P.; Davis, M.; Dawson, N.; Feldman, D.; George, S.; Hershman, J.; Lechner, T.; Potter, A.; Raymond, E.; Treister, N.; Wood, L.; Wu, S.; Bukowski, R. Sunitinib in Metastatic Renal Cell Carcinoma: Recommendations for Management of Noncardiovascular Toxicities. *Oncologist* **2011**, *16*, 543–553.
- (217) Campbell, K. J.; Dhayade, S.; Ferrari, N.; Sims, A. H.; Johnson, E.; Mason, S. M.; Dickson, A.; Ryan, K. M.; Kalna, G.; Edwards, J.; Tait, S. W. G.; Blyth, K. MCL-1 Is a Prognostic Indicator and Drug Target in Breast Cancer. *Cell Death Dis.* **2018**, *19*.
- (218) Merino, D.; Whittle, J. R.; Vaillant, F.; Serrano, A.; Gong, J.-N.; Giner, G.; Maragno, A. L.; Chanrion, M.; Schneider, E.; Pal, B.; Li, X.; Dewson, G.; Gräsel, J.; Liu, K.; Lalaoui, N.; Segal, D.; Herold, M. J.; Huang, D. C. S.; Smyth, G. K.; Geneste, O.; Lessene, G.; Visvader, J. E.; Lindeman, G. J. Synergistic Action of the MCL-1 Inhibitor S63845 with Current Therapies in Preclinical Models of Triple-Negative and HER2-Amplified Breast Cancer. *Sci. Transl. Med.* **2017**, *9*, eaam7049.
- (219) Xie, Q.; Wang, S.; Zhao, Y.; Zhang, Z.; Qin, C.; Yang, X. MiR-519d Impedes Cisplatin-Resistance in Breast Cancer Stem Cells by Down-Regulating the Expression of MCL-1. *Oncotarget* **2017**, *8*, 22003–22013.
- (220) Tong, J.; Wang, P.; Tan, S.; Chen, D.; Nikolovska-Coleska, Z.; Zou, F.; Yu, J.; Zhang, L. Mcl-1 Degradation Is Required for Targeted Therapeutics to Eradicate Colon Cancer Cells. *Cancer Res.* **2017**, *77*, 2512–2521.
- (221) Tong, J.; Tan, S.; Zou, F.; Yu, J.; Zhang, L. FBW7 Mutations Mediate Resistance of Colorectal Cancer to Targeted Therapies by Blocking Mcl-1 Degradation. *Oncogene* **2017**, *36*, 787–796.
- (222) Zhang, S.; Zhau, H. E.; Osunkoya, A. O.; Iqbal, S.; Yang, X.; Fan, S.; Chen, Z.; Wang, R.; Marshall, F. F.; Chung, L. W. K.; Wu, D. Vascular Endothelial Growth Factor Regulates Myeloid Cell Leukemia-1 Expression through Neuropilin-1-Dependent Activation of C-Met Signaling in Human Prostate Cancer Cells. *Mol. Cancer* **2010**, *9*, 9.

- (223) Wei, D.; Parsels, L. A.; Karnak, D.; Davis, M. A.; Parsels, J. D.; Marsh, A. C.; Zhao, L.; Maybaum, J.; Lawrence, T. S.; Sun, Y.; Morgan, M. A. Inhibition of Protein Phosphatase 2A Radiosensitizes Pancreatic Cancers by Modulating CDC25C/CDK1 and Homologous Recombination Repair. *Clin. Cancer. Res.* **2013**, *19*, 4422–4432.
- (224) Tron, A. E.; Belmonte, M. A.; Adam, A.; Aquila, B. M.; Boise, L. H.; Chiarparin, E.; Cidado, J.; Embrey, K. J.; Gangl, E.; Gibbons, F. D.; Gregory, G. P.; Hargreaves, D.; Hendricks, J. A.; Johannes, J. W.; Johnstone, R. W.; Kazmirski, S. L.; Kettle, J. G.; Lamb, M. L.; Matulis, S. M.; Nooka, A. K.; Packer, M. J.; Peng, B.; Rawlins, P. B.; Robbins, D. W.; Schuller, A. G.; Su, N.; Yang, W.; Ye, Q.; Zheng, X.; Sechrist, J. P.; Clark, E. A.; Wilson, D. M.; Fawell, S. E.; Hird, A. W. Discovery of Mcl-1-Specific Inhibitor AZD5991 and Preclinical Activity in Multiple Myeloma and Acute Myeloid Leukemia. *Nat. Commun.* **2018**, *9*, 5341.
- (225) Balko, J. M.; Giltnane, J. M.; Wang, K.; Schwarz, L. J.; Young, C. D.; Cook, R. S.; Owens, P.; Sanders, M. E.; Kuba, M. G.; Sánchez, V.; Kurupi, R.; Moore, P. D.; Pinto, J. A.; Doimi, F. D.; Gómez, H.; Horiuchi, D.; Goga, A.; Lehmann, B. D.; Bauer, J. A.; Pietenpol, J. A.; Ross, J. S.; Palmer, G. A.; Yelensky, R.; Cronin, M.; Miller, V. A.; Stephens, P. J.; Arteaga, C. L. Molecular Profiling of the Residual Disease of Triple-Negative Breast Cancers after Neoadjuvant Chemotherapy Identifies Actionable Therapeutic Targets. *Cancer Discov.* **2014**, *4*, 232–245.
- (226) Beroukhim, R.; Mermel, C. H.; Porter, D.; Wei, G.; Raychaudhuri, S.; Donovan, J.; Barretina, J.; Boehm, J. S.; Dobson, J.; Urashima, M.; Mc Henry, K. T.; Pinchback, R. M.; Ligon, A. H.; Cho, Y.-J.; Haery, L.; Greulich, H.; Reich, M.; Winckler, W.; Lawrence, M. S.; Weir, B. A.; Tanaka, K. E.; Chiang, D. Y.; Bass, A. J.; Loo, A.; Hoffman, C.; Prensner, J.; Liefeld, T.; Gao, Q.; Yecies, D.; Signoretti, S.; Maher, E.; Kaye, F. J.; Sasaki, H.; Tepper, J. E.; Fletcher, J. A.; Tabernero, J.; Baselga, J.; Tsao, M.-S.; Demichelis, F.; Rubin, M. A.; Janne, P. A.; Daly, M. J.; Nucera, C.; Levine, R. L.; Ebert, B. L.; Gabriel, S.; Rustgi, A. K.; Antonescu, C. R.; Ladanyi, M.; Letai, A.; Garraway, L. A.; Loda, M.; Beer, D. G.; True, L. D.; Okamoto, A.; Pomeroy, S. L.; Singer, S.; Golub, T. R.; Lander, E. S.; Getz, G.; Sellers, W. R.; Meyerson, M. The Landscape of Somatic Copy-Number Alteration across Human Cancers. *Nature* **2010**, *463*, 899–905.
- (227) Tahir, S. K.; Smith, M. L.; Hessler, P.; Rapp, L. R.; Idler, K. B.; Park, C. H.; Leverson, J. D.; Lam, L. T. Potential Mechanisms of Resistance to Venetoclax and Strategies to Circumvent It. *BMC Cancer* **2017**, *17*, 399.
- (228) Shuang, W.; Hou, L.; Zhu, Y.; Li, Q.; Hu, W. Mcl-1 Stabilization Confers Resistance to Taxol in Human Gastric Cancer. *Oncotarget* **2017**, *8*, 82981–82990.
- (229) Raymond, E.; Dahan, L.; Raoul, J.-L.; Bang, Y.-J.; Borbath, I.; Lombard-Bohas, C.; Valle, J.; Metrakos, P.; Smith, D.; Vinik, A.; Chen, J.-S.; Hörsch, D.; Hammel, P.; Wiedenmann, B.; Van Cutsem, E.; Patyna, S.; Lu, D. R.; Blanckmeister, C.; Chao, R.; Ruszniewski, P. Sunitinib Malate for the Treatment of Pancreatic Neuroendocrine Tumors. *Engl. J. Med.* **2011**, *364*, 501–513.
- (230) Younus, J.; Verma, S.; Franek, J.; Coakley, N. Sunitinib Malate for Gastrointestinal Stromal Tumour in Imatinib Mesylate-Resistant Patients: Recommendations and Evidence. *Curr. Oncol.* **2010**, *17*, 4–7.

- (231) Xin, H.; Zhang, C.; Herrmann, A.; Du, Y.; Figlin, R.; Yu, H. Sunitinib Inhibition of Stat3 Induces Renal Cell Carcinoma Tumor Cell Apoptosis and Reduces Immunosuppressive Cells. *Cancer Res.* **2009**, *69*, 2506–2513.
- (232) Yu, X.; Li, W.; Xia, Z.; Xie, L.; Ma, X.; Liang, Q.; Liu, L.; Wang, J.; Zhou, X.; Yang, Y.; Liu, H. Targeting MCL-1 Sensitizes Human Esophageal Squamous Cell Carcinoma Cells to Cisplatin-Induced Apoptosis. *BMC Cancer* **2017**, *449*.
- (233) Huang, X.-P.; Li, X.; Situ, M.-Y.; Huang, L.-Y.; Wang, J.-Y.; He, T.-C.; Yan, Q.-H.; Xie, X.-Y.; Zhang, Y.-J.; Gao, Y.-H.; Li, Y.-H.; Rong, T.-H.; Wang, M.-R.; Cai, Q.-Q.; Fu, J.-H. Entinostat Reverses Cisplatin Resistance in Esophageal Squamous Cell Carcinoma Via Down-Regulation of Multidrug Resistance Gene 1. *Cancer Lett.* **2018**, *414*, 294–300.
- (234) Wei, S.-H.; Dong, K.; Lin, F.; Wang, X.; Li, B.; Shen, J.-j.; Zhang, Q.; Wang, R.; Zhang, H.-Z. Inducing Apoptosis and Enhancing Chemosensitivity to Gemcitabine Via RNA Interference Targeting Mcl-1 Gene in Pancreatic Carcinoma Cell. *Cancer Chemother. Pharmacol.* **2008**, *62*, 1055–1064.
- (235) Ma, J.; Zhao, Z.; Wu, K.; Xu, Z.; Liu, K. MCL-1 Is the Key Target of Adjuvant Chemotherapy to Reverse the Cisplatin-Resistance in Nsclc. *Gene* **2016**, *587*, 147–154.
- (236) Wang, G.; Nikolovska-Coleska, Z.; Yang, C.-Y.; Wang, R.; Tang, G.; Guo, J.; Shangary, S.; Qiu, S.; Gao, W.; Yang, D.; Meagher, J.; Stuckey, J.; Krajewski, K.; Jiang, S.; Roller, P. P.; Abaan, H. O.; Tomita, Y.; Wang, S. Structure-Based Design of Potent Small-Molecule Inhibitors of Anti-Apoptotic Bcl-2 Proteins. *J. Med. Chem.* **2006**, *49*, 6139–6142.
- (237) Ren, T.; Shan, J.; Qing, Y.; Qian, C.; Li, Q.; Lu, G.; Li, M.; Li, C.; Peng, Y.; Luo, H.; Zhang, S.; Zhang, W.; Wang, D.; Zhou, S.-F. Sequential Treatment with at-101 Enhances Cisplatin Chemosensitivity in Human Non-Small Cell Lung Cancer Cells through Inhibition of Apurinic/Apyrimidinic Endonuclease 1-Activated Il-6/Stat3 Signaling Pathway. *Drug Des. Devel. Ther.* **2014**, *8*, 2517–2529.
- (238) Kotschy, A.; Szlavik, Z.; Murray, J.; Davidson, J.; Maragno, A. L.; Le Toumelin-Braizat, G.; Chanrion, M.; Kelly, G. L.; Gong, J.-N.; Moujalled, D. M.; Bruno, A.; Csekei, M.; Paczal, A.; Szabo, Z. B.; Sipos, S.; Radics, G.; Proszenyak, A.; Balint, B.; Ondi, L.; Blasko, G.; Robertson, A.; Surgenor, A.; Dokurno, P.; Chen, I.; Matassova, N.; Smith, J.; Pedder, C.; Graham, C.; Studeny, A.; Lysiak-Auvity, G.; Girard, A.-M.; Gravé, F.; Segal, D.; Riffkin, C. D.; Pomilio, G.; Galbraith, L. C. A.; Aubrey, B. J.; Brennan, M. S.; Herold, M. J.; Chang, C.; Guasconi, G.; Cauquil, N.; Melchiorre, F.; Guigal-Stephan, N.; Lockhart, B.; Colland, F.; Hickman, J. A.; Roberts, A. W.; Huang, D. C. S.; Wei, A. H.; Strasser, A.; Lessene, G.; Geneste, O. The Mcl1 Inhibitor S63845 Is Tolerable and Effective in Diverse Cancer Models. *Nature* **2016**, *538*, 477–482.
- (239) Mohammad, R. M.; Goustin, A. S.; Aboukameel, A.; Chen, B.; Banerjee, S.; Wang, G.; Nikolovska-Coleska, Z.; Wang, S.; Al-Katib, A. Preclinical Studies of TW-37, a New Nonpeptidic

Small-Molecule Inhibitor of Bcl-2, in Diffuse Large Cell Lymphoma Xenograft Model Reveal Drug Action on Both Bcl-2 and Mcl-1. *Clin. Cancer Res.* **2007**, *13*, 2226–2235.

(240) Zhai, D.; Jin, C.; Shiau, C.-w.; Kitada, S.; Satterthwait, A. C.; Reed, J. C. Gambogic Acid Is an Antagonist of Antiapoptotic Bcl-2 Family Proteins. *Mol. Cancer Ther.* **2008**, *7*, 1639–1646.

(241) Dash, R.; Azab, B.; Quinn, B. A.; Shen, X.; Wang, X.-Y.; Das, S. K.; Rahmani, M.; Wei, J.; Hedvat, M.; Dent, P.; Dmitriev, I. P.; Curiel, D. T.; Grant, S.; Wu, B.; Stebbins, J. L.; Pellecchia, M.; Reed, J. C.; Sarkar, D.; Fisher, P. B. Apogossypol Derivative BI-97C1 (Sabutoclax) Targeting Mcl-1 Sensitizes Prostate Cancer Cells to mda-7/IL-24-Mediated Toxicity. *Proc. Natl. Acad. Sci. U. S. A.* **2011**, *108*, 8785–8790.

(242) Doi, K.; Li, R.; Sung, S.-S.; Wu, H.; Liu, Y.; Manieri, W.; Krishnegowda, G.; Awwad, A.; Dewey, A.; Liu, X.; Amin, S.; Cheng, C.; Qin, Y.; Schonbrunn, E.; Daughdrill, G.; Loughran, T. P.; Sebti, S.; Wang, H.-G. Discovery of Marinopyrrole a (Maritoclax) as a Selective Mcl-1 Antagonist That Overcomes ABT-737 Resistance by Binding to and Targeting Mcl-1 for Proteasomal Degradation. *J. Biol. Chem.* **2012**, *287*, 10224–10235.

(243) Abulwerdi, F.; Liao, C.; Liu, M.; Azmi, A. S.; Aboukameel, A.; Mady, A. S. A.; Gulappa, T.; Cierpicki, T.; Owens, S.; Zhang, T.; Sun, D.; Stuckey, J. A.; Mohammad, R. M.; Nikolovska-Coleska, Z. A Novel Small-Molecule Inhibitor of Mcl-1 Blocks Pancreatic Cancer Growth in Vitro and in Vivo. *Mol. Cancer Ther.* **2014**, *13*, 565–575.

(244) Ohmer, M.; Weber, A.; Sutter, G.; Ehrhardt, K.; Zimmermann, A.; Häcker, G. Anti-Apoptotic Bcl-XL but Not Mcl-1 Contributes to Protection against Virus-Induced Apoptosis. *Cell Death Dis.* **2016**, *7*, e2340–e2340.

(245) Zhao, B.; Sensintaffar, J.; Bian, Z.; Belmar, J.; Lee, T.; Olejniczak, E. T.; Fesik, S. W. Structure of a Myeloid Cell Leukemia-1 (Mcl-1) Inhibitor Bound to Drug Site 3 of Human Serum Albumin. *Bioorg. Med. Chem.* **2017**, *25*, 3087–3092.

(246) Friberg, A.; Vigil, D.; Zhao, B.; Daniels, R. N.; Burke, J. P.; Garcia-Barrantes, P. M.; Camper, D.; Chauder, B. A.; Lee, T.; Olejniczak, E. T.; Fesik, S. W. Discovery of Potent Myeloid Cell Leukemia 1 (Mcl-1) Inhibitors Using Fragment-Based Methods and Structure-Based Design. *J. Med. Chem.* **2013**, *56*, 15–30.

(247) Albert, B. J.; McPherson, P. A.; O'Brien, K.; Czaicki, N. L.; Destefino, V.; Osman, S.; Li, M.; Day, B. W.; Grabowski, P. J.; Moore, M. J.; Vogt, A.; Koide, K. Meayamycin Inhibits Pre-Messenger RNA Splicing and Exhibits Picomolar Activity against Multidrug-Resistant Cells. *Mol. Cancer Ther.* **2009**, *8*, 2308–2318.

(248) Miller-Wideman, M.; Makkar, N.; Tran, M.; Isaac, B.; Biest, N.; Stonard, R. Herboxidiene, a New Herbicidal Substance from Streptomyces Chromofuscus A7847. Taxonomy, Fermentation, Isolation, Physico-Chemical and Biological Properties. *J. Antibiot.* **1992**, *45*, 914–921.

- (249) Sakai, T.; Sameshima, T.; Matsufuji, M.; Kawamura, N.; Dobashi, K.; Mizui, Y. Pladienolides, New Substances from Culture of Streptomyces Platensis Mer-11107. I. Taxonomy, Fermentation, Isolation and Screening. *J. Antibiot.* **2004**, *57*, 173–179.
- (250) Liu, X.; Biswas, S.; Berg, M. G.; Antapli, C. M.; Xie, F.; Wang, Q.; Tang, M. C.; Tang, G. L.; Zhang, L.; Dreyfuss, G.; Cheng, Y. Q. Genomics-Guided Discovery of Thailanstatins A, B, and C as Pre-mRNA Splicing Inhibitors and Antiproliferative Agents from Burkholderia Thailandensis MSMB43. *J. Nat. Prod.* **2013**, *76*, 685–693.
- (251) Kotake, Y.; Sagane, K.; Owa, T.; Mimori-Kiyosue, Y.; Shimizu, H.; Uesugi, M.; Ishihama, Y.; Iwata, M.; Mizui, Y. Splicing Factor SF3b as a Target of the Antitumor Natural Product Pladienolide. *Nat. Chem. Biol.* **2007**, *3*, 570–575.
- (252) Hasegawa, M.; Miura, T.; Kuzuya, K.; Inoue, A.; Won Ki, S.; Horinouchi, S.; Yoshida, T.; Kunoh, T.; Koseki, K.; Mino, K.; Sasaki, R.; Yoshida, M.; Mizukami, T. Identification of SAP155 as the Target of GEX1A (Herboxidiene), an Antitumor Natural Product. *ACS Chem. Biol.* **2011**, *6*, 229–233.
- (253) Thompson, C. F.; Jamison, T. F.; Jacobsen, E. N. Total Synthesis of FR901464. Convergent Assembly of Chiral Components Prepared by Asymmetric Catalysis. *J. Am. Chem. Soc.* **2000**, *122*, 10482–10483.
- (254) Thompson, C. F.; Jamison, T. F.; Jacobsen, E. N. FR901464: Total Synthesis, Proof of Structure, and Evaluation of Synthetic Analogues. *J. Am. Chem. Soc.* **2001**, *123*, 9974–9983.
- (255) Horigome, M.; Motoyoshi, H.; Watanabe, H.; Kitahara, T. A Synthesis of FR901464. *Tetrahedron Lett.* **2001**, *42*, 8207–8210.
- (256) Motoyoshi, H.; Horigome, M.; Watanabe, H.; Kitahara, T. Total Synthesis of FR901464: Second Generation. *Tetrahedron* **2006**, *62*, 1378–1389.
- (257) Albert, B. J.; Sivaramakrishnan, A.; Naka, T.; Koide, K. Total Synthesis of FR901464, an Antitumor Agent That Regulates the Transcription of Oncogenes and Tumor Suppressor Genes. *J. Am. Chem. Soc.* **2006**, *128*, 2792–2793.
- (258) Albert, B. J.; Sivaramakrishnan, A.; Naka, T.; Czaicki, N. L.; Koide, K. Total Syntheses, Fragmentation Studies, and Antitumor/Antiproliferative Activities of FR901464 and Its Low Picomolar Analogue. *J. Am. Chem. Soc.* **2007**, *129*, 2648–2659.
- (259) Ghosh, A. K.; Chen, Z.-H. Enantioselective Syntheses of FR901464 and Spliceostatin A: Potent Inhibitors of Spliceosome. *Org. Lett.* **2013**, *15*, 5088–5091.
- (260) Osman, S.; Albert, B. J.; Wang, Y.; Li, M.; Czaicki, N. L.; Koide, K. Structural Requirements for the Antiproliferative Activity of Pre-mRNA Splicing Inhibitor FR901464. *Chem.-Eur. J.* **2011**, *17*, 895–904.

- (261) Bressin, R. K.; Osman, S.; Pohorilets, I.; Basu, U.; Koide, K. Total Synthesis of Meayamycin B. *J. Org. Chem.* **2020**, *85*, 4637–4647.
- (262) Nicolaou, K. C.; Rhoades, D.; Kumar, S. M. Total Syntheses of Thailanstatins A–C, Spliceostatin D, and Analogues Thereof. Stereodivergent Synthesis of Tetrasubstituted Dihydro- and Tetrahydropyrans and Design, Synthesis, Biological Evaluation, and Discovery of Potent Antitumor Agents. *J. Am. Chem. Soc.* **2018**, *140*, 8303–8320.
- (263) Ghosh, A. K.; Veitschegger, A. M.; Nie, S.; Relitti, N.; MacRae, A. J.; Jurica, M. S. Enantioselective Synthesis of Thailanstatin A Methyl Ester and Evaluation of in Vitro Splicing Inhibition. *J. Org. Chem.* **2018**, *83*, 5187–5198.
- (264) Nicolaou, K. C.; Rhoades, D.; Lamani, M.; Pattanayak, M. R.; Kumar, S. M. Total Synthesis of Thailanstatin A. *J. Am. Chem. Soc.* **2016**, *138*, 7532–7535.
- (265) Pellicena, M.; Krämer, K.; Romea, P.; Urpí, F. Total Synthesis of (+)-Herboxidiene from Two Chiral Lactate-Derived Ketones. *Org. Lett.* **2011**, *13*, 5350–5353.
- (266) Ghosh, A. K.; Li, J. A Stereoselective Synthesis of (+)-Herboxidiene/GEX1A. *Org. Lett.* **2011**, *13*, 66–69.
- (267) Murray, T. J.; Forsyth, C. J. Total Synthesis of GEX1A. *Org. Lett.* **2008**, *10*, 3429–3431.
- (268) Zhang, Y.; Panek, J. S. Total Synthesis of Herboxidiene/GEX1A. *Org. Lett.* **2007**, *9*, 3141–3143.
- (269) Banwell, M.; McLeod, M.; Premraj, R.; Simpson, G. Total Synthesis of Herboxidiene, a Complex Polyketide from Streptomyces Species A7847. *Pure Appl. Chem.* **2000**, *72*, 1631–1634.
- (270) R. Blakemore, P.; J. Kocieński, P.; Morley, A.; Muir, K. A Synthesis of Herboxidiene. *J. Chem. Soc., Perkin Trans. 1* **1999**, 955–968.
- (271) Ghosh, A. K.; Anderson, D. D. Enantioselective Total Synthesis of Pladienolide B: A Potent Spliceosome Inhibitor. *Org. Lett.* **2012**, *14*, 4730–4733.
- (272) Arai, K.; Buonamici, S.; Chan, B.; Corson, L.; Endo, A.; Gerard, B.; Hao, M.-H.; Karr, C.; Kira, K.; Lee, L.; Liu, X.; Lowe, J. T.; Luo, T.; Marcaurelle, L. A.; Mizui, Y.; Nevalainen, M.; O’Shea, M. W.; Park, E. S.; Perino, S. A.; Prajapati, S.; Shan, M.; Smith, P. G.; Tivitmahaisoon, P.; Wang, J. Y.; Warmuth, M.; Wu, K.-M.; Yu, L.; Zhang, H.; Zheng, G.-Z.; Keaney, G. F. Total Synthesis of 6-Deoxypladienolide D and Assessment of Splicing Inhibitory Activity in a Mutant SF3B1 Cancer Cell Line. *Org. Lett.* **2014**, *16*, 5560–5563.
- (273) Kumar, V. P.; Chandrasekhar, S. Enantioselective Synthesis of Pladienolide B and Truncated Analogues as New Anticancer Agents. *Org. Lett.* **2013**, *15*, 3610–3613.

- (274) Müller, S.; Mayer, T.; Sasse, F.; Maier, M. E. Synthesis of a Pladienolide B Analogue with the Fully Functionalized Core Structure. *Org. Lett.* **2011**, *13*, 3940–3943.
- (275) Iwata, M.; Ozawa, Y.; Uenaka, T.; Shimizu, H.; Niijima, J.; Kanada, R. M.; Fukuda, Y.; Nagai, M.; Kotake, Y.; Yoshida, M.; Tsuchida, T.; Mizui, Y.; Yoshimatsu, K.; Asada, M. E7107, a New 7-Urethane Derivative of Pladienolide D, Displays Curative Effect against Several Human Tumor Xenografts. *Cancer Res.* **2004**, *64*, 691–691.
- (276) Kanada, R. M.; Itoh, D.; Nagai, M.; Niijima, J.; Asai, N.; Mizui, Y.; Abe, S.; Kotake, Y. Total Synthesis of the Potent Antitumor Macrolides Pladienolide B and D. *Angew. Chem., Int. Ed.* **2007**, *46*, 4350–4355.
- (277) Hong, D. S.; Kurzrock, R.; Naing, A.; Wheler, J. J.; Falchook, G. S.; Schiffman, J. S.; Faulkner, N.; Pilat, M. J.; O'Brien, J.; LoRusso, P. A Phase I, Open-Label, Single-Arm, Dose-Escalation Study of E7107, a Precursor Messenger Ribonucleic Acid (Pre-mRNA) Splicesome Inhibitor Administered Intravenously on Days 1 and 8 Every 21 Days to Patients with Solid Tumors. *Invest. New Drugs* **2014**, *32*, 436–444.
- (278) Eskens, F. A.; Ramos, F. J.; Burger, H.; O'Brien, J. P.; Piera, A.; de Jonge, M. J.; Mizui, Y.; Wiemer, E. A.; Carreras, M. J.; Baselga, J.; Tabernero, J. Phase I Pharmacokinetic and Pharmacodynamic Study of the First-in-Class Spliceosome Inhibitor E7107 in Patients with Advanced Solid Tumors. *Clin. Cancer Res.* **2013**, *19*, 6296–6304.
- (279) Seiler, M.; Yoshimi, A.; Darman, R.; Chan, B.; Keaney, G.; Thomas, M.; Agrawal, A. A.; Caleb, B.; Csibi, A.; Sean, E.; Fekkes, P.; Karr, C.; Klimek, V.; Lai, G.; Lee, L.; Kumar, P.; Lee, S. C.-W.; Liu, X.; Mackenzie, C.; Meeske, C.; Mizui, Y.; Padron, E.; Park, E.; Pazolli, E.; Peng, S.; Prajapati, S.; Taylor, J.; Teng, T.; Wang, J.; Warmuth, M.; Yao, H.; Yu, L.; Zhu, P.; Abdel-Wahab, O.; Smith, P. G.; Buonamici, S. H3b-8800, an Orally Available Small-Molecule Splicing Modulator, Induces Lethality in Spliceosome-Mutant Cancers. *Nat. Med.* **2018**, *24*, 497–504.
- (280) Ghosh, A. K.; Mishevich, J. L.; Jurica, M. S. Spliceostatins and Derivatives: Chemical Syntheses and Biological Properties of Potent Splicing Inhibitors. *J. Nat. Prod.* **2021**, *84*, 1681–1706.
- (281) Motoyoshi, H.; Horigome, M.; Ishigami, K.; Yoshida, T.; Horinouchi, S.; Yoshida, M.; Watanabe, H.; Kitahara, T. Structure-Activity Relationship for FR901464: A Versatile Method for the Conversion and Preparation of Biologically Active Biotinylated Probes. *Biosci. Biotechnol. Biochem.* **2004**, *68*, 2178–2182.
- (282) Gartshore, C.; Tadano, S.; Chanda, P. B.; Sarkar, A.; Chowdari, N. S.; Gangwar, S.; Zhang, Q.; Vite, G. D.; Momirov, J.; Boger, D. L. Total Synthesis of Meayamycin and O-Acyl Analogues. *Org. Lett.* **2020**, *22*, 8714–8719.
- (283) Lagisetti, C.; Pourpak, A.; Goronga, T.; Jiang, Q.; Cui, X.; Hyle, J.; Lahti, J. M.; Morris, S. W.; Webb, T. R. Synthetic mRNA Splicing Modulator Compounds with in Vivo Antitumor Activity. *J. Med. Chem.* **2009**, *52*, 6979–6990.

- (284) Nicolaou, K. C.; Rekula, S. R.; Kumar, S. M.; Podilapu, A. R.; Matuszak, R. P.; Jung, P. M.; Lam, L. T.; Phillips, A. C.; Lyssikatos, J.; Munneke, S.; Gu, C.; Sarvaiya, H.; Sandoval, J.; Hammond, M.; Aujay, M.; Purcell, J. W.; Reilly, R. M.; Gavriluk, J. Design, Synthesis, and Biological Investigation of Thailanstatin A and Spliceostatin D Analogues Containing Tetrahydropyran, Tetrahydroooxazine, and Fluorinated Structural Motifs. *J. Org. Chem.* **2021**, *86*, 2499–2521.
- (285) Lagisetti, C.; Pourpak, A.; Jiang, Q.; Cui, X.; Goronga, T.; Morris, S. W.; Webb, T. R. Antitumor Compounds Based on a Natural Product Consensus Pharmacophore. *J. Med. Chem.* **2008**, *51*, 6220–6224.
- (286) Beck, A.; Goetsch, L.; Dumontet, C.; Corvaia, N. Strategies and Challenges for the Next Generation of Antibody–Drug Conjugates. *Nat. Rev. Drug Discov.* **2017**, *16*, 315–337.
- (287) Sievers, E. L.; Larson, R. A.; Stadtmauer, E. A.; Estey, E.; Löwenberg, B.; Dombret, H.; Karanes, C.; Theobald, M.; Bennett, J. M.; Sherman, M. L.; Berger, M. S.; Eten, C. B.; Loken, M. R.; van Dongen, J. J.; Bernstein, I. D.; Appelbaum, F. R. Efficacy and Safety of Gemtuzumab Ozogamicin in Patients with Cd33-Positive Acute Myeloid Leukemia in First Relapse. *J. Clin. Oncol.* **2001**, *19*, 3244–3254.
- (288) Modi, S.; Saura, C.; Yamashita, T.; Park, Y. H.; Kim, S.-B.; Tamura, K.; Andre, F.; Iwata, H.; Ito, Y.; Tsurutani, J.; Sohn, J.; Denduluri, N.; Perrin, C.; Aogi, K.; Tokunaga, E.; Im, S.-A.; Lee, K. S.; Hurvitz, S. A.; Cortes, J.; Lee, C.; Chen, S.; Zhang, L.; Shahidi, J.; Yver, A.; Krop, I. Trastuzumab Deruxtecan in Previously Treated HER2-Positive Breast Cancer. *N. Engl. J. Med. Chem.* **2019**, *382*, 610–621.
- (289) Ganapathy-Kanniappan, S.; Geschwind, J.-F. H. Tumor Glycolysis as a Target for Cancer Therapy: Progress and Prospects. *Mol. Cancer* **2013**, *12*, 152.
- (290) Lin, Y.-S.; Tungpradit, R.; Sinchaikul, S.; An, F.-M.; Liu, D.-Z.; Phutrakul, S.; Chen, S.-T. Targeting the Delivery of Glycan-Based Paclitaxel Prodrugs to Cancer Cells Via Glucose Transporters. *J. Med. Chem.* **2008**, *51*, 7428–7441.
- (291) Mikuni, K.; Nakanishi, K.; Hara, K.; Hara, K.; Iwatani, W.; Amano, T.; Nakamura, K.; Tsuchiya, Y.; Okumoto, H.; Mandai, T. In Vivo Antitumor Activity of Novel Water-Soluble Taxoids. *Biol. Pharm. Bull.* **2008**, *31*, 1155–1158.
- (292) Semmelhack, M. F.; Bodurow, C. Intramolecular Alkoxy palladation/Carbonylation of Alkenes. *J. Am. Chem. Soc.* **1984**, *106*, 1496–1498.
- (293) Semmelhack, M. F.; Kim, C.; Zhang, N.; Bodurow, C.; Sanner, M.; Dobler, W.; Meier, M. Intramolecular Alkoxy-Carbonylation of Hydroxy Alkenes Promoted by Pd(II). *Pure Appl. Chem.* **1990**, *62*, 2035–2040.

- (294) Zhong, H. M.; Sohn, J.-H.; Rawal, V. H. Studies toward the Asymmetric Synthesis of the Right Part of the Mycalamides. *J. Org. Chem.* **2007**, *72*, 386–397.
- (295) Chamberlin, A. R.; Dezube, M.; Dussault, P.; McMills, M. C. Iodocyclization of Allylic Alcohol Derivatives Containing Internal Nucleophiles. Control of Stereoselectivity by Substituents in the Acyclic Precursors. *J. Am. Chem. Soc.* **1983**, *105*, 5819–5825.
- (296) Bellucci, G.; Chiappe, C.; Marioni, F. Evidence for a Reversible Electrophilic Step in Olefin Bromination. The Case of Stilbenes. *J. Am. Chem. Soc.* **1987**, *109*, 515–522.
- (297) Bellucci, G.; Bianchini, R.; Ambrosetti, R. Direct Evidence for Bromine-Olefin Charge-Transfer Complexes as Essential Intermediates of the Fast Ionic Addition of Bromine to Cyclohexene. *J. Am. Chem. Soc.* **1985**, *107*, 2464–2471.
- (298) Slebocka-Tilk, H.; Ball, R. G.; Brown, R. S. The Question of Reversible Formation of Bromonium Ions During the Course of Electrophilic Bromination of Olefins. 2. The Crystal and Molecular Structure of the Bromonium Ion of Adamantylideneadamantane. *J. Am. Chem. Soc.* **1985**, *107*, 4504–4508.
- (299) Miura, K.; Hondo, T.; Okajima, S.; Hosomi, A. Stereoselective Synthesis of 2,5-Disubstituted Tetrahydrofurans by Silicon-Directed Cyclization of Vinylsilanes Bearing a Hydroxy Group. *Tetrahedron Lett.* **1996**, *37*, 487–490.
- (300) Baldwin, S. W.; McIver, J. M. Stereoselective Synthesis of (.-.) Methyl Nonactate. *J. Org. Chem.* **1987**, *52*, 320–322.
- (301) Fujioka, H.; Maehata, R.; Wakamatsu, S.; Nakahara, K.; Hayashi, T.; Oki, T. Stereoselective Synthesis of Cis-2,5-Disubstituted THFs: Application to Adjacent Bis-THF Cores of Annonaceous Acetogenins. *Org. Lett.* **2012**, *14*, 1054–1057.
- (302) Leslie, A. K.; Li, D. D.; Koide, K. Amine-Promoted B-Elimination of a B-Aryloxy Aldehyde for Fluorogenic Chemodosimeters. *J. Org. Chem.* **2011**, *76*, 6860–6865.